Design and development of an implantable biohybrid device for muscle stimulation following lower motor neuron injury

Mariann Andrea Angola Rojas

Thesis submitted in fulfilment of the requirements for the degree of

Doctor of Philosophy

School of Pharmacy

University College London

September, 2019

Declaration

I, Mariann Angola Rojas, confirm that the work presented in this thesis is my own. Where information has been derived from other sources, I confirm that these has been indicated in the thesis.

Signed: ____________________________

Date: ____________________________

This thesis is dedicated to the three most
special people in my life:

my mum Ana María,

my nan María,

… and my dad, Eduardo

Acknowledgments

Firstly, I would like to express my appreciation to my supervisor Dr. James Phillips for his support and guidance throughout the last four years. I would also like to thank Prof. Nick Donaldson for his invaluable input, knowledge and helping building a neural amplifier. I am particularly grateful to Dr. Henry Lancashire for his endless patience, kindness, encouragement and enthusiasm throughout this journey, without him this thesis would have not been possible.

Thanks to everyone in the Phillips Group for making the lab a nice and friendly environment to work in. In particular, I would like to thank Rachael Evans for her support, friendship and all the Friday afternoon beers! Furthermore I would also like to thank Callum and Ahmad from the IDG group, and Timea for her support, advice and always putting a smile on my face. Thanks to the maths people: Simao for all his help with MatLab, and Celine for being a good friend and always fun to drink with. A special thank you to Adam, for teaching me how to be SUPER sterile when doing cell culture and for always making me laugh.

Thanks to LIDo, for this great opportunity and giving me the chance to explore new career avenues. Without this opportunity I wouldn't be where I am right now. A special thanks to my LIDo buddies Brynna, Assel and Laura for all the laughter, boozy nights and sharing this journey with me.

I would like to thank Caitriona for her love, guidance and endless support and because finding her has been the best thing that has happened to me.

Finally to my dad for being so loving, caring and supportive. Thanks for being the best example of hard work.

… To my mum and my nan… Because, wherever they are they are always guiding me and so I dedicate this thesis to them. "Cuidate mucho, y sobre todo SE FELIZ MAMI, porque la vida es muy corta y no siempre resulta ser cómo una quisiera que fuera" – Ana María Rojas.

Publications

Conference proceedings:

5th International Symposium of Peripheral Nerve Regeneration – Porto, Portugal July 2019

“Design and development of an implanted biohybrid device for muscle stimulation following lower motor neuron injury”

Authors: Mariann Angola Rojas, Nick Donaldson, Henry T. Lancashire, James B. Phillips

Oral Presentation

Presenting Author: Mariann Angola Rojas

Abstract

In the absence of innervation caused by complete lower motor neuron injuries, skeletal muscle undergoes an inexorable course of degeneration and atrophy. The most apparent and debilitating clinical outcome of denervation is the immediate loss of voluntary use of muscle. However, these injuries are associated with secondary complications of bones, skin and cardiovascular system that, if untreated, may be fatal. Electrical stimulation has been implemented as a clinical rehabilitation technique in patients with denervated degenerated muscles offering remarkable improvements in muscle function. Nevertheless, this approach has limitations and side effects triggered by the delivery of high intensity electrical pulses.

Combining innovative approaches in the fields of cell therapy and implanted electronics offers the opportunity to develop a biohybrid device to stimulate muscles in patients with lower motor neuron injuries. Incorporation of stem cell-derived motor neurons into implantable electrodes, could allow muscles to be stimulated in a physiological manner and circumvent problems associated with direct stimulation of muscle. The hypothesis underpinning this project is that artificially-grown motor neurons can serve as an intermediate between stimulator and muscle, converting the electrical stimulus into a biological action potential and re-innervating muscle via neuromuscular interaction.

Here, a suitable stem cell candidate with therapeutic potential was identified and a differentiation protocol developed to generate motor neuron-like cells. Thick-film technology and laser micromachining were implemented to manufacture electrode arrays with features and dimensions suitable for implantation. Manufactured electrodes were electrochemically characterised, and motor neuron-like cells incorporated to create biohybrid devices. *In vitro* results indicate manufactured electrodes support motor neuron-like cell growth and neurite extension. Moreover, electrochemical characterisation suggests electrodes are suitable for stimulation. Preliminary *in vivo* testing explored implantation in a rat muscle denervation model. Overall, this thesis demonstrates initial development of a novel approach for fabricating biohybrid devices that may improve stimulation of denervated muscles.

Impact Statement

This thesis contributes to translational research in a novel treatment for complete *cauda equina* and *conus medullaris* lesions. Specifically, it provides initial development of the key components for a novel muscle stimulation technology, based on a biohybrid approach, to prevent the muscle wasting associated with these lesions.

Complete *cauda equina* and *conus medullaris* lesions are rare but severely debilitating injuries, affecting 20 people per million EU citizens yearly. The irreversible loss of lower motor neurons characteristic of these lesions, causes secondary complications over and above the lack of mobility leading to increased morbidity and mortality in affected individuals. Currently, electrical stimulation of muscle is used to manage these patients. Although, some remarkable progress has been achieved with such rehabilitation approaches, limitations and side effects associated with the high current pulses used in this treatment, notoriously affect quality of life of these patients.

This work has made progress towards addressing this important unmet clinical need through the development of a potential future therapy to prevent muscle degeneration and atrophy following lower motor neuron lesions and improve outcomes for patients. To this end, this thesis focused on the design and development of an implantable biohybrid device to stimulate denervated muscles. Aspects of this work have contributed towards the field of biohybrid devices/living electronics by: (1) presenting a low-cost technique for the manufacturing of implantable electrode arrays suitable for safe and effective stimulation of cells; (2) implementing human-derived cells suitable for generation of motor neurons and of therapeutic relevance; (3) designing and developing a biohybrid device suitable for implantation in a pre-clinical model; and (4) establishing a rodent muscle denervation model suitable for pre-clinical testing of cell therapies and biohybrid devices.

Overall, this project has made advancements in the development of a new potential treatment for patients bearing muscle denervating injuries. This novel treatment has the potential to enhance the way in which we stimulate denervated muscles by providing a more biologically inspired interface. This would deliver significant benefit to patients by maintaining muscle mass and therefore reducing risks of complications such as pressure sores and reducing associated costs to health services. In the long term such an approach may provide a solution for functional rehabilitation of patients. Furthermore, the findings are also of relevance to the biohybrid device community as they inform the field on alternative methods to fabricate implantable electrodes and the use of synthetic materials and cells adequate for clinical translation. The contributions made here further enhance the potential for closer integration between biology and electronics as well as the unprecedented prospect of replacing lost cells and partly restoring tissue function.

Abbreviations

3D	Three Dimensional
4-OHT	4 Hydroxytamoxifen
ACh	Acetylcholine
AFM	Atomic Force Microscopy
ASIC	Application Specific Integrated Circuit
AP	Action Potential
ATP	Adenosine Triphosphate
Au	Gold
BDNF	Brain-derived Neurotrophic Factor
BMCS	Bone Marrow Mesenchymal Stem Cells
BMP	Bone Morphogenetic Protein
Ca^{2+}	Calcium
cAMP	Cyclic Adenosine Monophosphate
CD4	T-helper Cells
CD8	Cytotoxic T-Cells
CES	*Cauda equina* Syndrome
CH	Conductive Hydrogel
ChAT	Choline Acetyltransferase
CIC	Charge Injection Capacity
Cl^{-}	Chloride
CMAP	Compound Muscle Action Potential
CMS	*Conus medullaris* Syndrome
CNS	Central Nervous System
CSC	Charge Storage Capacity
CSMNs	Cortical Spinal Motor Neurons
CV	Cyclic Voltammetry
DDM	Denervated Degenerated Muscles
DMEM	Dulbecco's Modified Eagle's Medium
DRG	Dorsal Root Ganglion
ECM	Extracellular Matrix
EIS	Electrical Impedance Spectroscopy
EoCG	Electrocorticography
ES	Electrical Stimulation
ESA	Effective Surface Area
ESCs	Embryonic Stem Cells

FBR	Foreign Body Response
FBS	Foetal Bovine Serum
FES	Functional Electrocal Stimulation
FGF	Fibroblast Growth Factors
FINE	Flat Interface Nerve Electrodes
GDNF	Glial cell line-derived Neurotrophic Factor
GFP	Green Fluorescent Protein
GSA	Geometric Surface Area
Hb-9	Homeobox Gene 9
hNPCs	Human Neural Precursor Cells
IC	Integrated Circuit
iPSCs	Indued Pluripotent Stem Cells
IrOx	Iridium Oxide
Isl-1	Islet-1
K^+	Potassium
LFP	Local Field Potential
LIFE	Longitudinal Intrafascicular Electrodes
LMNs	Lower Motor Neurons
MEA	Microelectrode Arrays
MHC	Major Histocompatibility Complex
micro-TENNS	micro Tissue Engineered Neural Networks
MNs	Motor Neurons
MSCs	Mesenchymal Stem Cells
Na^+	Sodium
Nd:YAG	Neodymium-doped Yttrium Aluminium Garnet
NGF	Nerve Growth Factor
NMJ	Neuromuscular Junction
NP	Neural Progenitors
NSCs	Neural Stem Cells
NTF	Neurotrophic Factor
OCT	Optimum Cutting Temperature
PBS	Phosphate Buffer Saline
PDMS	Polydimethylsiloxane
PEDOT	Poly-3,4-ethylenedioxythiophene
PEG	Polyethylene Glycol

PLL	Poly-L-Lysine
PNS	Peripheral Nervous System
PPy	Polypyrrole
PSS	Poly(styrenesulfonate)
Pt/Au	Platinum Gold
PVA-Tyr	Poly Vinyl Alcohol- Tyramine
PVC	Poly Vinyl Chloride
RA	Retionoic Acid
RLU	Relative Luminescence Unit
RT	Room Temperature
SAG	Smoothened Agonist
SCI	Spinal Cord Injury
SEM	Scanning Electron Microscopy
TIME	Transverse Intrfascicular Multichannel Electrodes
TiN	Titanium Nitride
UMNs	Upper Motor Neurons
WNT	Wingless-related Integration Site

Contents

Declaration 2

Acknowledgments 5

Publications 6

Abstract 7

Impact Statement 8

Abbreviations 10

Index of Figures 17

Index of Tables 22

1.0 Introduction 24

  1.1 The nervous system 24

  1.2 Connectivity between CNS and PNS 25

    1.2.1 Upper and lower motor neurons 26

  1.3 Low spinal cord injuries 27

  1.4 Muscle physiology 29

  1.5 Muscle denervation and degeneration 30

  1.6 Electrical stimulation of denervated degenerated muscles 31

    1.6.1 Electrical stimulation of innervated muscles 32

    1.6.2 Electrical stimulation of denervated muscle 33

  1.7 A biohybrid approach to stimulate denervated muscles 36

  1.8 The electrical-neural interface 38

  1.9 Considerations for a biohybrid approach 43

    1.9.1 Electrical considerations 44

    1.9.2 Mechanical and topographical considerations 45

    1.9.3 Biological considerations 46

    1.9.4 Chemical considerations 49

  1.10 Aims of this PhD project 52

2.0 Materials and Methods 53

  2.1 Materials 53

  2.2 Methods 59

    2.2.1 Cell culture 59

    2.2.2 SPC-01 cells seeded on coverslips, alumina plates and electrode construct reservoirs ... 61

2.2.3 Immunocytochemical labelling 61

2.2.4 Delivery of SPC-01 differentiated cells 62

2.2.5 *In vivo* muscle denervation model 62

2.2.6 Preparation of alginate protective hydrogels 66

2.2.7 Cell metabolic activity 67

2.2.8 Scanning electron microscopy 68

Samples were mounted onto aluminium SEM stubs and coated with a thin layer (20 nm) of gold using Quorum Q150T Sputter Coater (Quorum Technologies Ltd, UK) in an argon atmosphere. Subsequently, the materials were imaged with a field emission scanning electron microscope (FEI Quanta 200F, FEI, USA), at an accelerating voltage of 5 kV 2.2.9 Electrode array designs. 68

2.2.10 Manufacturing of electrode arrays 73

2.2.11 Electrode array characterisation 85

2.2.12 Analyses 87

2.2.13 Statistical analysis 89

3.0 Differentiation of human neural stem cells into motor neurons and local delivery *in vivo* 91

3.1 Introduction 91

3.1.1 Motor neuron development 91

3.1.2 Cell origin 92

3.1.3 Directed differentiation of stem cells into motor neurons 95

3.1.4 Injectable cell delivery of MNs into peripheral nerves 96

3.1.5 Host immune response to allogeneic transplants 98

3.1.6 Objectives of this chapter 100

3.2 Results 101

3.2.1 Human neural stem cell differentiation into motor neurons 101

3.2.2 Exploring proliferation of differentiated SPC-01 cells 103

3.2.3 Exploring the effect of different concentrations of retinoic acid (RA) and smoothened agonist (SAG) on motor neuron yield. 107

3.2.4 Delivery of differentiated SPC-01 cells through a syringe needle: exploring needle gauge effect on cell viability to inform cell transplantation *in vivo* 110

3.2.5 Assessing expression of human-specific antibodies on differentiated SPC-01 cells *in vitro* 112

3.2.6 Transplantation of differentiated SPC-01 cells *in vivo*: a pilot experiment 113

3.3 Discussion 122

4.0 Design, development and optimisation of electrode arrays for *in vitro* cell culture experiments 130

4.1. Introduction 130

4.1.1 Thick-film technology for electrode array manufacturing 130

4.1.2 Introducing topographical cues on electrode arrays by substrate micropatterning 133

4.1.3 Electrochemical characterisation of microelectrodes for neural stimulation 135

4.1.4 Objectives of this chapter 139

4.2 Results 140

4.2.1 Exploring optimal groove dimensions to screen print Pt/Au onto laser-structured alumina 140

4.2.2 Manufacturing of microchannel electrode arrays by the laser-structured alumina method 143

4.2.3 Manufacturing of microchannel electrode arrays by unmodified alumina method 149

4.2.4 Exploring cell growth and neurite extension of NG108 cells on microchannel electrode arrays 150

4.2.5 Exploring cell growth and neurite extension of differentiated SPC-01 cells on microchannel electrode arrays 154

4.2.6 Optimised design for *in vitro* experiments 156

4.2.7 Investigating the effect of microgrooves on neurite length and directionality 157

4.2.8 Exploring the effect of laminin coating on electrochemical properties of the optimised electrode arrays designed for *in vitro* experiments. 160

4.3 Discussion 164

5.0 Design, development and optimisation of an implantable biohybrid device to stimulate denervated muscles 173

5.1 Introduction 173

5.1.1 Biohybrid devices to improve implant integration with the host environment 173

5.1.2 Biohybrid devices to restore tissue function 176

5.1.3 The use of hydrogels in bioelectronics and biohybrid devices 178

5.1.4 Hydrogel used for the implantable biohybrid device in this study 184

5.1.5 Objectives of this chapter 186

5.2 Results 187

5.2.1 Manufacture of the prototype implantable device 187

5.2.2 Electrochemical characterisation of implantable device prototype 190

5.2.3 Exploring incorporation of differentiated SPC-01 cells on prototype implantable electrode arrays to create a biohybrid device 194

5.2.4 Implantation of biohybrid device *in vivo:* a pilot experiment 197

5.2.5 Histological analysis of implanted biohybrid device 198

5.2.6 Exploring the use of protective hydrogels to shield differentiated SPC-01 cells on electrode arrays from the host immune system 203

5.3 Discussion 206

6.0 General discussion and proposed future work 215

7.0 References 222

8.0 Appendix 240

8.1 Assessing metabolic activity of differentiated SPC-01 cells with RT-Glo metabolic assay 240

8.2 Investigating the effect of Sigma alginate protective hydrogels on differentiated SPC-01 cells in vitro using RT-Glo metabolic assay 242

8.3 Investigating the effect of NovaMatrix alginate protective hydrogels on differentiated SPC-01 viability using RT-Glo assay 242

8.4 Comparison of differentiated SPC-01 cell metabolic activity using RT-Glo and CT-Glo assays 245

Index of Figures

CHAPTER 1

Figure 1.1 The nervous system

Figure 1.2 Cross section of the spinal cord and nerve connections to the muscle

Figure 1.3 Structure of peripheral nerves

Figure 1.4 The brain and spinal cord (CNS)

Figure 1.5 Structure of skeletal muscle

Figure 1.6 Nerve interfaces classified based on invasiveness and selectivity

Figure 1.7 Functional electrical stimulation (FES) of DDM

Figure 1.8 Biohybrid device to stimulate denervated muscles

Figure 1.9 Schematic depicting the proposed site of implantation of the biohybrid device

Figure 1.10 Electrophysiological signalling at different scales

Figure 1.11 Electrochemical mechanisms underlying electrical stimulation

Figure 1.12 Schematic representation of cathodal stimulation of a nerve fibre

CHAPTER 2

Figure 2.1 SPC-01 differentiation protocol

Figure 2.2 RA/SAG dose response

Figure 2.3 Tibial nerve transection and local delivery of cells

Figure 2.4 Micrographs of electrode arrays

Figure 2.5 Manufacturing process of electrode arrays

Figure 2.6 Laser ablation parameters

Figure 2.7 Wire bonding stainless steel solder pads onto implantable device prototype

Figure 2.8 Setup for electrochemical characterisation of electrode arrays

Figure 2.9 Standardised sampling protocols to analyse cell differentiation, cell death and neurite extension using ImageJ

Figure 2.10 Neurite measurement in cell culture

CHAPTER 3

Figure 3.1 Differentiated SPC-01 cells stained to detect βIII-Tubulin and Isl1

Figure 3.2 Neuron and motor neuron yield following 5, 14 and 21 days of differentiation of SPC-01 cells

Figure 3.3 Phase-contrast microscopy images of differentiated SPC-01 cells at different time points

Figure 3.4 Cell densities of differentiated SCP-01 cells at different time points

Figure 3.4 Differentiated SPC-01 cells in 6-well plates stained to detect Ki67

Figure 3.5 Differentiated SPC-01 cells in 6-well plates stained to detect Ki67

Figure 3.6 Differentiated SPC-01 cells on 6-well plates using different concentrations of RA and SAG stained to detect Isl1

Figure 3.7 Yield of Isl1+ SPC-01 cells exposed to different concentrations of RA and SAG

Figure 3.8 Viability of differentiated SPC-01 cells expelled through a gauge-26 syringe needle

Figure 3.9 Metabolic activity of differentiated SPC-01 cells expelled through a gauge-25 syringe needle

Figure 3.10 Figure 3.10 Differentiated SPC-01 cells stained to detect Nestin *in vitro*

Figure 3.11 Light micrographs of microchannel electrodes manufactured to stimulate the common peroneal and tibial nerves in the *in vivo* pilot experiment

Figure 3.12 Bode plot of frequency-dependent impedance of microchannel electrode arrays used for the *in vivo* pilot experiment

Figure 3.13 Electrophysiology recordings of the uninjured common peroneal nerve

Figure 3.14 Common peroneal rat nerve samples stained to assess cross-reactivity with human-specific markers Nestin and HuNu

Figure 3.15 Nestin^{+ve} cells identified in the transplanted tibial nerve

Figure 3.16 Confocal micrographs of 30 µm longitudinal sections showing three positions along the tibial nerve at 4-weeks post-transplantation of differentiated SPC-01 cells. Nerve sections were stained to detect a host t-cell-mediated immune response

Figure 3.17 Yield of CD4+ve and OX8+ve cells along rat tibial nerve 4 weeks after transplantation with human SPC-01 cells

CHAPTER 4

Figure 4.1 Charge-balanced, current waveforms used in neural stimulation

Figure 4.2 Pt/Au paste screen-printed onto laser-ablated grooves of various dimensions

Figure 4.3 Quantification of the quality of Pt/Au paste filling on screen-printed, laser-ablated grooves of various dimensions

Figure 4.4 Light micrographs of processing steps in the laser-structured alumina manufacturing method

Figure 4.5 Light micrographs of screen printed solder pads following excess paste removal

Figure 4.6 Light micrographs of electrode arrays manufactured using the laser-structured alumina method before and after cleaning in ultrasonic bath

Figure 4.7 SEM micrographs of laser-ablated alumina with and without screen-printed Pt/AU

Figure 4.8 Light micrographs of electrode arrays manufactured using the unmodified alumina method before and after soldering and cleaning in ultrasonic bath.

Figure 4.9 SEM micrographs of unmodified alumina substrate with screen-printed Pt/AU

Figure 4.10 NG108-15 cells seeded on microchannel electrode arrays coated with different molecules

Figure 4.11 Quantification of NG108-15 cell density, neurite density and neurite length of cells seeded on microchannel electrode arrays coated with different molecules

Figure 4.12 NG108-15 cells seeded on PLL-coated microchannel electrode arrays after 5 days *in vitro*

Figure 4.13 Differentiated SCP-01 cells seeded on microchannel electrode arrays

Figure 4.14 Optimised design for *in vitro* experiments

Figure 4.15 Differentiated SPC-01 cells cultured on the optimised design for *in vitro* experiments

Figure 4.16 Assessment of microgrooves on differentiated SPC-01 cells density and neurite extension

Figure 4.17 Bode plots of frequency-dependent impedance of the optimised design for *in vitro* experiments electrode arrays before and after laminin.

Figure 4.18 Cyclic voltammograms of the optimised design for *in vitro* experiments electrode arrays as manufactured (before laminin) and following laminin coating (after laminin).

Figure 4.19 Cyclic voltammetry response of thick-film Pt/Au electrode in nitrogen-purged PBS

Figure 4.20 Cyclic voltammetry response of Au electrode in PBS

CHAPTER 5

Figure 5.1 Light micrographs of the processing steps in the optimisation and manufacturing of the implantable device prototype

Figure 5.2 Bode plots of frequency-dependent impedance of implantable device prototype as manufactured

Figure 5.3 Cyclic voltammograms of implantable device prototype as manufactured

Figure 5.4 Impedance of outer and inner electrodes of unpolished sintered Pt/Au (optimised designed for in vitro experiments) and polished sintered Pt/Au (implantable device prototype)

Figure 5.5 CSC of inner and outer electrodes of unpolished sintered Pt/Au (optimised designed for in vitro experiments) and polished sintered Pt/Au (implantable device prototype)

Figure 5.6 Differentiated SPC-01 cells seeded on implantable device prototypes

Figure 5.7 Quantification of differentiated SPC-01 cell density per seeded implantable device prototype

Figure 5.8 Implantation of biohybrid device in a rat muscle denervation model

Figure 5.9 Visual inspection of the nerve-implant interface after 6 days of surgery showing no fibrotic encapsulation around the biohybrid device

Figure 5.10 Differentiated SPC-01 cells identified on cell-seeding reservoir of biohybrid device 6 days post-implantation

Figure 5.11 Differentiated SPC-01 cells on control biohybrid devices at 3 different time points

Figure 5.12 Differentiated SPC-01 cell density on control biohybrid devices at 3 different time points

Figure 5.13 Standard curve of differentiated SPC-01 cells metabolic activity using CT Glo assay

Figure 5.14 Metabolic activity of differentiated SPC-01 cells in the presence of different acellular alginate hydrogels of different concentrations assessed by CT-Glo assay

APPENDIX

Figure 8.1 Standard curve of differentiated SPC-01 cells metabolic activity using RT-Glo assay

Figure 8.2 Viability of differentiated SPC-01 cells in the presence of different acellular alginate hydrogels of different concentrations assessed by RT Glo assay

Figure 8.3 Percentage change in luminescence recordings at 48 and 72 hrs compared to 24 hrs

Index of Tables

CHAPTER 2

Table 2.1 Cells used in this project

Table 2.2 Consumables used in this project

Table 2.3 Antibodies table

Table 2.4 Summary of microchannel electrode array parameters

Table 2.5 Summary of optimised electrode array design for *in vitro* experiments parameters

Table 2.6 Summary of implantable device prototype parameters

Table 2.7 Silicone rubbers used for the manufacturing of electrode arrays

Table 2.8 Parameters used to laser-ablate grooves of different dimensions

Table 2.9 Laser parameters

Table 2.10 Parameters used for Au bump bonding onto Pt/Au pads of implantable device prototype

CHAPTER 3

Table 3.1 Different concentrations of RA and SAG used to generate a differentiation dose response

Table 3.2 Electrophysiology evaluation of the uninjured common peroneal nerve to validate microchannel electrodes

Table 3.3 Electrophysiology evaluation of the transplanted tibial to nerve to assess muscle reinnervation

CHAPTER 4

Table 4.1 Impedance (|Z|, in kΩ) of thick film Pt/Au electrode arrays manufacured using the unmodified alumina method to create the optimsised design for *in vitro* experiments

Table 4.2 Charge storage capacity (CSC) and cathodic CSC (cCSC) of thick film Pt/Au electrode arrays manufactured using the unmodified alumina method to create the optimised design for *in vitro* experiments

CHAPTER 5

Table 5.1 Hydrogels used in the development of biohybrid devices to improve implant integration with the host environment

Table 5.2 Hydrogels used in the development of biohybrid devices to restore tissue function

Table 5.3 Impedance (|Z|, in kΩ) of thick film Pt/Au electrode arrays manufactured using the unmodified alumina method to create implantable device prototypes

Table 5.4 Charge storage capacity (CSC), cathodic CSC (cCSC) and charge injection capacity (Q_{inj}) of thick film Pt/Au electrode arrays manufactured using the unmodified alumina method to create implantable device prototypes

1.0 Introduction

1.1 The nervous system

The nervous system can be divided into two parts: the central nervous system (CNS) and the peripheral nervous system (PNS). Together, they transmit signals to control the body and ensure communication amongst its parts. The CNS is comprised of the brain and spinal cord and the PNS consists of nerve bundles that connect the CNS to the rest of the body (figure 1.1). Efferent (motor) nerves transmit signals from the brain to muscles, glands and organs to regulate their function and afferent (sensory) nerves transmit information from sensory receptors to the brain.

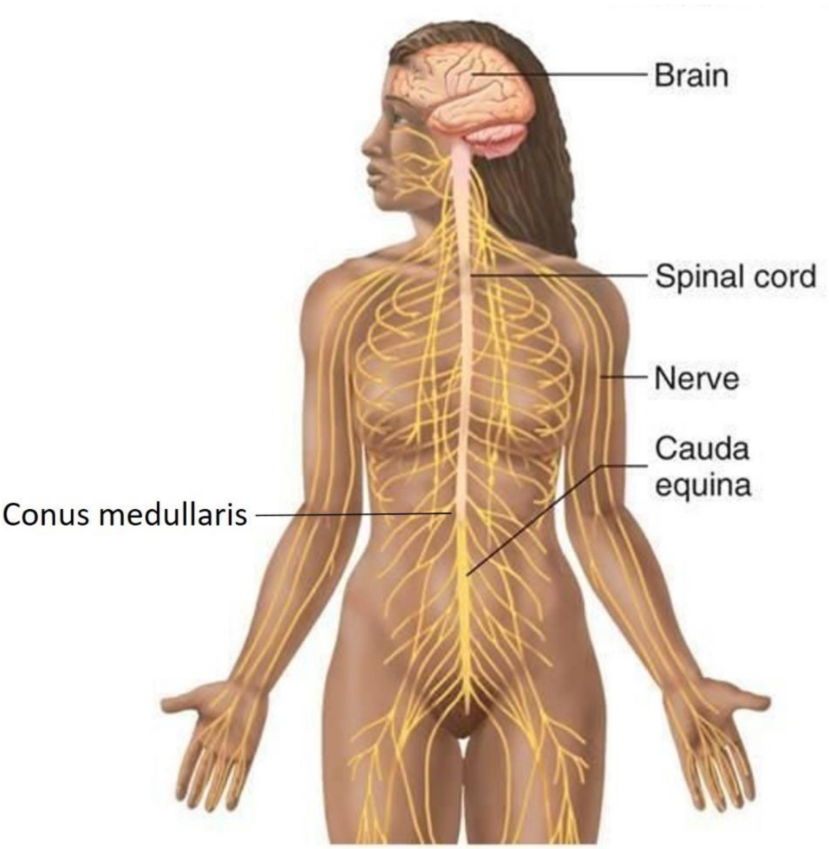

Figure 1.1 The nervous system

Diagram depicting the CNS (brain and spinal cord) and the PNS (nerves that innervate the rest of the body). Injuries to the most distal areas of the spinal cord (*cauda equina* and *conus medullaris*) are the focus of this research. Image modified from (Patton, 2012)

1.2 Connectivity between CNS and PNS

Transmission of signals in efferent and afferent nerves is mediated by electrically excitable cells, or neurons. Neurons are composed of three elements: a cell body (soma), one or more dendrites and a single axon. The cell body contains the cell's organelles, dendrites receive information from sensory receptors or other neurons and axons are long thin fibres that transmit this information to effector organs or other neurons. Cell bodies of PNS neurons reside in the spinal cord (motor neurons) or within ganglia (sensory neurons). Motor neurons receive information from the brain and transmit this signal along the axons towards the periphery while sensory neurons receive information from sensory receptors and transmit the signal to neurons located in the spinal cord (figure 1.2). Axons branch into multiple terminals, allowing a single neuron to communicate with multiple cells.

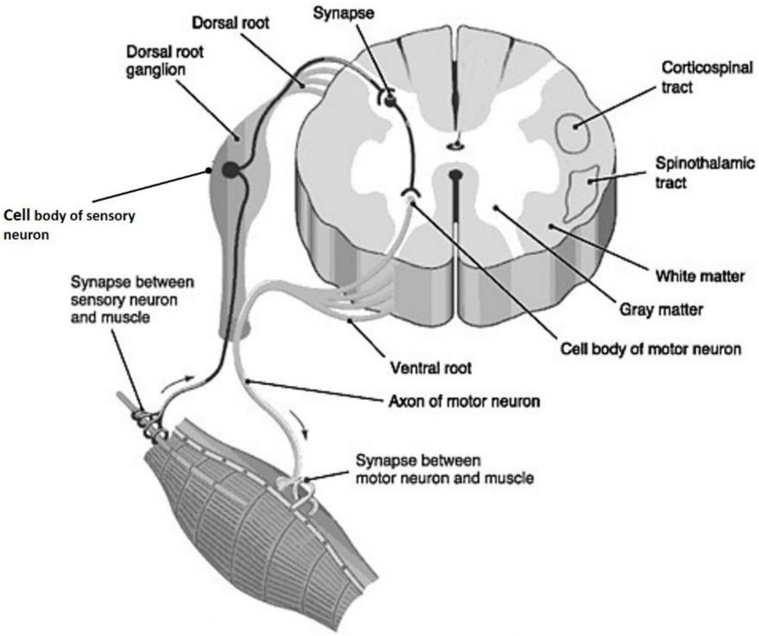
Dorsal root
Synapse
Dorsal root ganglion
Corticospinal tract
Spinothalamic tract
Cell body of sensory neuron
White matter
Synapse between sensory neuron and muscle
Gray matter
Cell body of motor neuron
Ventral root
Axon of motor neuron
Synapse between motor neuron and muscle

Figure 1.2 Cross section of the spinal cord and nerve connections to the muscle

The image depicts sensory and motor nerve fibres connecting the spinal cord to muscles. Image reproduced from (Catharyn *et al*., 2005)

Peripheral nerves serve as conduits for axons projecting towards the periphery and to the spinal cord (Biazar *et al*., 2010). These nerves are comprised of bundles of fascicles surrounded by a connective tissue sheath, the epineurium. Individual fascicles are enclosed within the perineurium, a sheath that controls the influx of substances into fascicles (Zochodne, 2008). Each fascicle is formed by bundles of axons (the endoneurium)(figure 1.3). Apart from neurons, glial cells are also found within peripheral nerves where they provide structural and metabolic support to neurons (Burnett and Zager, 2004). Peripheral nerve axons can be myelinated or unmyelinated. The myelin sheath is a multilamellar structure produced by Schwann cells that surrounds axons and provides insulation (Taveggia, 2016). Myelin wraps along the length of the nerve forming internodes, separated by nodes of Ranvier where a portion of the axon is exposed. Here, the movement of ions through the axon membrane allows transmission of axon potentials in what is known as 'saltatory' conduction. Myelin increases the speed of conduction (up to 80 m/s) (Zochodne, 2008) without a large increase in metabolic cost or axon diameter, whereas conduction of unmyelinated axons is between 0.5-2 m/s (Zochodne, 2008).

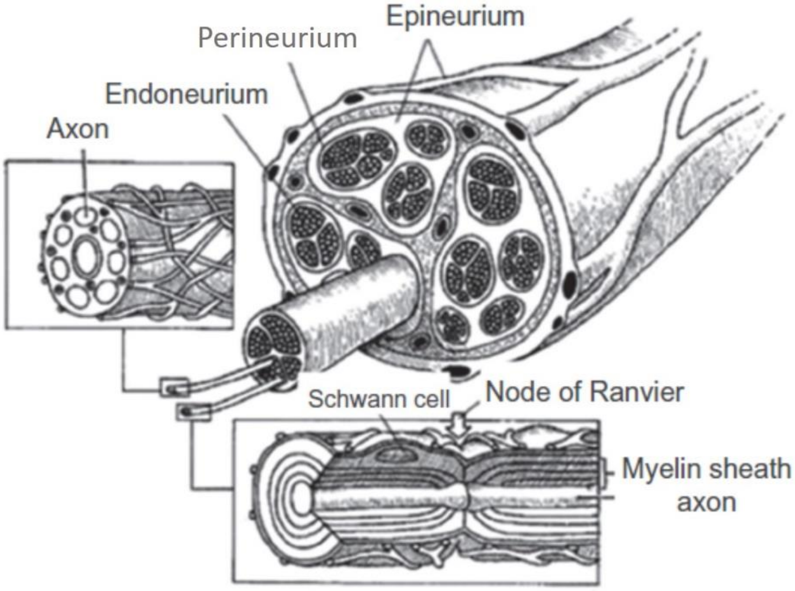

Figure 1.3 Structure of peripheral nerves

Physiology of peripheral nerves. Image adapted from (Biazar *et al*., 2010).

1.2.1 Upper and lower motor neurons

Pathways between the brain and muscle can be arranged into two groups based on the neurons that populate them: upper motor neurons (UMNs), or corticospinal MNs (CSMNs) and lower MNs (LMNs). LMNs originate from the brainstem, cranial nerve nuclei and anterior horn cell of the spinal cord. They are the final efferent common motor pathway linking brain and muscles (Doherty *et al*., 2002).

Although most of the axons of LMNs reside in the PNS, their cell bodies and initial axonal segment originate in the CNS. Injuries to LMNs cause denervation of peripheral skeletal muscles. Clinically, this is manifested as weakness or paralysis of muscles, loss of muscle tone (flaccidity), loss of reflexes (areflexia) and muscle atrophy. Injuries to LMNs at the most distal part of the spinal cord (*cauda equina* and *conus medullaris*) (figure 1.4) result in paralysis and flaccidity of the lower limbs, loss of bladder and bowel control and erectile dysfunction (Podnar, 2006, Lavy *et al*., 2009).

UMNs reside in the cerebral cortex and brain stem, where they project axons towards interneurons or LMNs. In patients bearing UMN lesions, muscles remain innervated as LMNs remain intact. Lesions to UMNs are clinically manifested by: muscle spasticity, muscle paralysis or weakness (depending on the severity of the injury) and, contrary to LMN injuries, local reflexes are preserved (Trompetto *et al*., 2014). Both, symptoms and treatment management of UMN and LMN lesions are different, therefore, it is important to distinguish the predominant type of neuron affected by the injury.

This thesis will focus on the most distal part of the spinal cord, specifically a novel therapeutic approach for patients bearing injuries to LMNs in the *cauda equina* and *conus medullaris*.

1.3 Low spinal cord injuries

The human spinal cord extends from the base of the brain to the first lumbar vertebra (L1) (Silva *et al*., 2014). The terminal end of the spinal cord, most typically at the level of L1 for the average adult, is known as the *conus medullaris* (Brouwers *et al*., 2017). The *cauda equina* is comprised of a group or nerves that stem from the distal end of the spinal cord, typically between L1 and L5, and provide motor and sensory innervation to the legs, anus, bladder and perineum (Quaile, 2019) (figure 1.4). Traumatic injuries of the thoracolumbar spine can lead to *conus medullaris* syndrome (CMS) or *cauda equina* syndrome (CES), rare and serious conditions caused by pressure to these areas (Brouwers *et al*., 2017). Approximately 15% of spinal cord injuries occur at this level. Out of this 15%, only 10-38% affect the *cauda equina* or *conus medullaris*, which are mostly attributed to lumbar disc herniations. The clinical symptoms of patients with CES or CMS due to incomplete lesions include: low back pain, lower limb weakness, bowel and/or bladder dysfunction, reduced sensation in the saddle area, reduction of sexual function, sensory loss in the perineum, buttocks and upper posterior thighs (Brouwers *et al*., 2017) (Kapetanakis *et al*., 2017). Surgical decompression (a type of surgery used to treat compressed nerves in the lower spine) is the treatment of choice, after which most patients fully or partially recover from the above symptoms.

A subset of patients bear complete lesions of the *cauda equina* and/or *conus medullaris*. This type of lesion causes denervation of the entire lower extremity musculature, due to irreversible loss of lower motor neurons residing in the *cauda equina* and *conus medullaris*. As a result, patients present with flaccid paraplegia. The incidence of this type of lesion is extremely rare yet incredibly debilitating and potentially fatal. Indeed, injuries that result in muscle denervation have secondary complications over and above the lack of voluntary use of muscle leading to increased morbidity and mortality in affected individuals (Handschin and Spiegelman, 2008, Furrer and Handschin, 2019). As a result of paraplegia, patients are prone to developing secondary complications of bones and skin. The lack of cushioning over bony areas due to the loss of muscle tone and the loss of skin condition, increase the risks of developing pressure sores and septicaemia (Salmons and Jarvis, 2008). Furthermore, lack of physical activity makes patients susceptible to developing osteoporosis and life-threatening conditions like pulmonary thromboembolisms (Hagen, 2015). It is estimated that approximately 20 people per million EU citizen are affected by complete *cauda equina*/ *conus medullaris* lesions every year (Mayr *et al*., 2004).

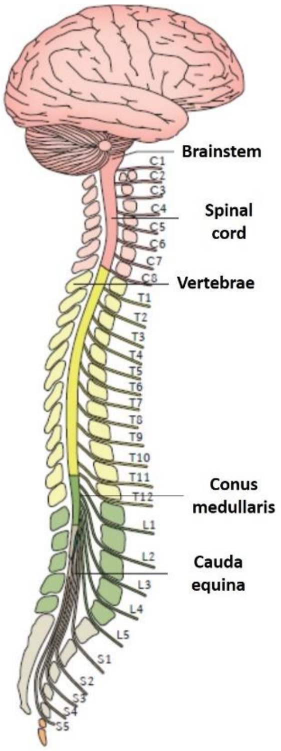

Figure 1.4 The brain and spinal cord (CNS)

Image of the CNS showing the different regions of the spinal cord; cervical (C), thoracic (T), lumbar (L) and sacral (S). The most distal areas of the spinal cord (*conus medullaris* and *cauda equina*) are labelled. Image modified from (Ahuja *et al*., 2017).

1.4 Muscle physiology

There are three types of muscles in the body: skeletal, cardiac and smooth muscle (Matthews and Matthews, 2013). Skeletal muscles, are responsible for voluntary movement and posture, and will be considered in this body of work.

Skeletal muscles are composed of bundles of individual cells known as muscle fibres, or myocytes. These are long, tubular multinucleated cells that extend the full length of the muscle. Each muscle fibre is comprised of bundles of smaller fibres, or myofibrils, which are surrounded by a plasma membrane known as the sarcolemma. Myofibrils are cylindrical structures containing two types of filaments: myosin and actin, which form repeated units known as the sarcomere. The sarcomere is the contractile machinery of skeletal muscles which is also responsible for their characteristic striated appearance (Matthews and Matthews, 2013). Individual myofibrils are surrounded by a basement membrane known as the endomysium. Tens to hundreds of muscle fibres form a fascicle which is enclosed within a connective layer, or perimysium. Bundles of fascicles enclosed within the perimysium form a muscle (figure 1.5).

Skeletal muscles are closely controlled by the nervous system (Greig and Jones, 2016) through synapses between nerves and muscle known as neuromuscular junctions (NMJs). A NMJ is formed between an individual motor neuron (MN) and a single muscle fibre where the action potential (AP) is transmitted to the muscle by the release of the neurotransmitter acetylcholine (ACh). The point at which a motor neurons synapses with a muscle fibre is known as the motor endplate, formed of multiple NMJs. Individual muscle fibres can only be innervated by a single MN axon, however a single motor neuron may innervate multiple muscle fibres (motor unit).

In a similar manner to neurons, muscles elicit APs upon stimulation. ACh released from the nerve terminal binds to ACh receptors which elicits an intracellular cascade leading to the release of Ca^{2+} from intracellular stores. Intracellular Ca^{2+} elicits changes in the binding of myosin and actin on microfilaments in an adenosine triphosphate (ATP)-dependent manner, leading to contraction of the sarcomere.

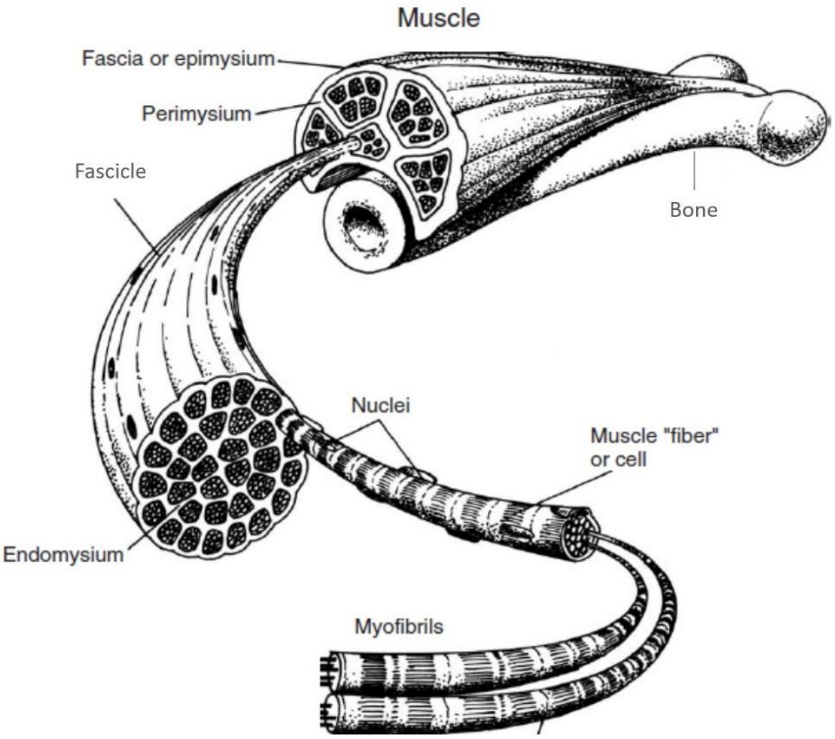

Figure 1.5 Structure of skeletal muscle

The physiology of skeletal muscle with its different layers and cellular elements labelled. Image reproduced from (Lamb, 1984).

1.5 Muscle denervation and degeneration

In the absence of innervation caused by lower motor neuron injuries, skeletal muscle undergoes atrophy. Three main stages have been described throughout the process of muscle decline following denervation (Carlson, 2014). First, and perhaps the most apparent clinical observation of denervation, is the immediate loss of voluntary and reflex function of the muscle, followed by loss of muscle weight and atrophy of muscle fibres. The second phase is characterised by the disorganisation of the muscle contractile apparatus and severe muscle 'wasting'. By the third stage, a significant number of muscle fibres have been replaced by adipose and fibrotic tissue with those remaining bearing little or no resemblance to healthy muscle fibres. A study following a cohort of patients with *cauda equina* and/or *conus medullaris* injuries taking part in EU project ‘RISE’ (described in section 1.6.2), characterised the time course of morphological changes in denervated muscles. Within weeks to months, disorganisation of the cellular structure of muscles can be detected, muscle deterioration leads to severe atrophy 3 to 6 years post injury and muscle fibre loss is estimated to occur over 3 years after injury (Kern *et al*., 2017). At the molecular level, denervation is associated with increased turnover of ACh receptors (Wong and Pomerantz, 2019) and loss of motor end plates (Apel *et al*., 2009).

In clinical practice, it is accepted that significant recovery of motor function in patients with denervated muscles caused by UMN lesions, is highly unlikely if reinnervation does not occur within 12 to 18 months post-injury (Wong and Pomerantz, 2019). Pertinent to muscle tissue, the barriers associated with reinnervation of muscles are: muscle fibrosis, severe atrophy of muscle fibres, loss of myonuclei, changes in ACh receptors and decreased density and proliferative capacity of muscle stem cells (satellite cells) (Carlson *et al*., 2002).

In contrast to previous literature, recent evidence suggests that muscle fibres in humans survive years of denervation following complete and irreversible loss of motor neurons (Kern *et al*., 2017). Indeed, Carraro and Kern (2016) reported human muscle fibres survived denervation at least 3 to 6 years after injury. Moreover, atrophic muscle fibres can be rescued by electrical stimulation (ES) using custom-made electrodes and stimulators (discussed in further detail in section 1.4.2) (Kern *et al*., 2010, Kern *et al*., 2017). Clinically, this translates in patients being able to perform stand-up, sit-down exercises supported by parallel bars (figure 1.7).

1.6 Electrical stimulation of denervated degenerated muscles

For many years there has been a dearth of effective treatment options for the severe wasting and secondary complications that arise from LMN injuries (Salmons and Jarvis, 2008). Stimulators and training parameters used for patients with UMN lesions (that is, patients in which intact lower motor neurons still innervate muscles) can successfully stimulate paralysed muscles via their nerves. However, such stimulators and training parameters are characterised by electrodes which are too small, stimulation amplitudes and pulse widths too low, and time and regularity of treatment sessions too short (Kern *et al*., 1999) to functionally activate denervated muscles in patients with LMN injuries. The substantially different technical requirements needed to stimulate denervated degenerated muscles (DDM) following LMN lesions compared to those implemented for nerve stimulation following UMN lesions are due to the absence of neuromuscular junctions, leading to decomposition of motor units. Therefore, muscle contraction can only be elicited by depolarising the cellular membrane of individual muscle fibres. The excitability of the muscle membrane is directly correlated to the degree of muscle degeneration; however, even well preserved muscles are less excitable than nerves (Mayr *et al*., 2004). In order to understand the different technical requirements to stimulate denervated muscles compared to muscles with intact motor units via their nerves, it is appropriate to first describe the basic properties of electrodes for nerve stimulation

1.6.1 Electrical stimulation of innervated muscles

To generate muscle contraction by electrical stimulation, the stimulus is generally applied to peripheral nerves (provided that the neuromuscular system is intact) instead of directly to muscles (Ragnarsson, 2008). Because of the differences in excitability, it is estimated that more than 100 times stronger stimuli are required to stimulate muscles compared to nerves (Ragnarsson, 2008).

The electrical stimulus may be applied at different locations along the nerve, from its origin in the spinal cord to the point where it connects with the muscle, using different electrodes. When choosing the type of electrode, a trade-off between invasiveness and selective stimulation is required. Moreover, the current density required for stimulation increases with distance of electrodes from the nerve. The most basic, least invasive and least selective form of stimulation is achieved through electrodes placed on the surface of the skin. Slightly more invasive and a precursor to implantable electrodes, are needle electrodes placed subcutaneously (Agarwal *et al*., 2003). Implantable electrodes placed in close proximity to the nerve, provide increased selectivity and require lower current densities than surface electrodes to elicit APs, therefore reducing the risk of tissue damage due to stimulation (Ho *et al*., 2014). A variety of implantable electrode array designs has been reported; out of these, the least invasive are cuff electrode arrays, which wrap around the nerve (Brunton *et al*., 2016). Selective recruitment of different nerve fascicles has been achieved by flat interface nerve electrodes (FINE), cuffs which reshape the structure of the nerve into a flat geometry, therefore increasing the surface area and positioning central axons closer to electrode surfaces (Tyler and Durand, 2002). Subsets of neurons can be individually stimulated using intrafascicular electrodes, which can be inserted parallel (longitudinal intrafascicular electrodes, LIFE) or perpendicular (transverse intrafascicular multichannel electrodes, TIME) with respect to nerve fascicles (Badia *et al*., 2011). Furthermore, regenerative electrodes, allow for regenerating nerves to grow around the electrode, therefore avoiding puncturing nerve structures (Thompson *et al*., 2016) (figure 1.6). Alternatively, groups of lower motor neurons can be directly stimulated from the spinal cord by intraspinal microstimulation (Bamford and Mushahwar, 2011).

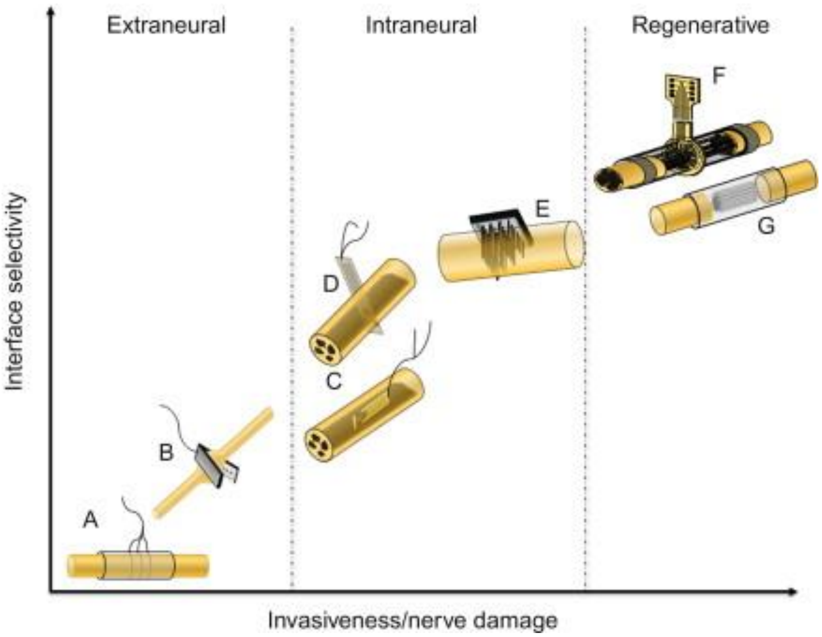

Figure 1.6 Nerve interfaces classified based on invasiveness and selectivity

(A) Cuff electrode, (B) FINE, (C) LIFE, (D) TIME, (E) multielectrode array, (F) sieve electrode and (G) microchannel electrode. Image reproduced from (del Valle and Navarro, 2013).

1.6.2 Electrical stimulation of denervated muscle

In 2002, the "RISE" project adapted existing neuromuscular stimulation protocols used for nerve stimulation and developed new equipment to directly activate muscle fibres in patients with chronic denervated muscles caused by complete *cauda equina* and *conus medullaris* lesions (Kern *et al*., 2002a). This clinical rehabilitation therapy, referred to as 'Functional Electrical Stimulation (FES)' in project 'RISE' publications, is based on an intensive regime of electrical stimulation (ES) applied through large-size (200 cm^2), anatomically shaped electrodes placed across the skin over denervated muscles[1] (figure 1.7).

The rationale behind the use of large size electrodes is two-fold: first, it ensures homogenous distribution of the electric field to allow even contraction of the entire muscle (Kern *et al*., 2002b) and second, it allows safe injection of high stimulation currents by keeping current density at a low level to prevent skin damage (Kern *et al*., 2002a). The researchers developed a stimulator unit able to generate biphasic charge-balance pulses between 1 and 300 ms in duration, with an amplitude of up to ± 80 V and stimulation current up to 250 mA (Hofer *et al*., 2002). This is in contrast to Odstock Dropped Foot Stimulator (ODFS®) Pace, a common commercial system used for footdrop which uses a pulse width between 0 to 360 µs in 3.6 ms steps with and output amplitude between 10 to 100 mA (Rehab, 2018) to stimulate the peroneal nerve in patients with gait dysfunction due to dropping of the forefoot.

---

[1] Readers should note, however, that the term 'FES' refers to the process of pairing the stimulation simultaneously or intermittently with a functional task as initially described by MOE, J. & POST, H. 1962. Functional electrical stimulation for ambulation in hemiplegia. *Lancet,* 82**,** 285-288.
It is not quite appropriate to use 'FES' to describe the early phases of the rehabilitation training program implemented in the "RISE" project, as these only consisted of applying electrical pulses to muscles in the absence of a functional task. Therefore, I shall use 'Electrical Stimulation (ES)' to describe the early phases of the programme.

The equipment and stimulation regime in the project "RISE" were tested in 14 patients with complete *cauda equina* or *conus medullaris* lesions between 1 and 3 years post-injury. During the first 4 to 6 months of therapy, pulse durations 1,500 times longer than those implemented during nerve stimulation were required to elicit single muscle twitches. The training regime consisted of stimulating individual muscle for 15-20 minutes each, 5 times a week. Furthermore, taking into consideration donning and doffing the electrodes, ES training took approximately 2 hours a day (Kern *et al*., 2002a). Muscle excitability progressively increased with daily stimulation of individual muscles (*m. gluteus*, *m. quadriceps*, hamstrings and *m. triceps surae*) which therefore required stimulation pulses of shorter duration and decreased amplitude. Muscle force measurements and CT scans of muscles showed increased muscle force and muscle mass. Specifically, the authors reported knee extension torque between 0 and 5% in patients with DDM at the beginning of ES training compared to that of healthy individuals. Knee extension torque increased after ES training to up to 20% of maximum torque in healthy participants. Similarly, mean cross-sectional area of the *m.quadriceps* increased by 26.7% and muscle biopsies revealed a lack of adipocytes (a sign of muscle wasting) after 1 year of ES training (Kern *et al*., 2002a).

Once the force produced in muscles was sufficient to allow stabilisation of the knee joint in the standing position, the functional rehabilitation aspect of "RISE" ES programme was initiated. Functional rehabilitation in the "RISE" project consisted of pairing ES of muscles involved in standing with sit-to-stand exercises. Overall, this training program reported improved excitability of denervated tissue and an increase in muscle mass and contraction force which, in some patients, was significant enough to allow them to stand up using their own power and to support themselves in parallel bars for 20-40 seconds (Kern *et al*., 2010). However, although some remarkable improvements have been achieved by direct ES of denervated muscle, this approach has multiple limitations;

(1) Functional response of DDM to the ES regime is directly correlated with the extent of degeneration and atrophy, with late onset of therapy after injury negatively impacting on the ability

of patients to rebuild muscles and achieve functional outcomes. Indeed, a long lag phase (4-6 months) to restore enough muscle mass and force to allow knee flection and standing up exercises (12 months) was reported in the study (Kern *et al*., 2002a). Moreover, it is estimated that by 6 years post-injury, degeneration is so far progressed that nearly all muscle fibres have been substituted by connective and fat tissue.

(2) Energy per stimulation pulse exceeds that used by conventional stimulators and is higher than that allowed by regulatory bodies to ensure patient safety. Because fat and connective tissue act as an electrical shunt, and because muscle is less electrically excitable than nerve, higher charge injection is required to induce muscle excitation, therefore requiring an increase in current amplitudes.

(3) Applying stimulation pulses of high intensity and long duration to maintain large muscle groups can only be safely achieved through large size electrodes. As a result, discomfort and skin burns, are some of the negative side effects experienced by patients (Pieber *et al*., 2015) (figure 1.7).

(4) Training regimes to achieve optimal clinical outcomes are long, time-consuming, highly regimented, and fully dependent on patient compliance. Based on training parameters (Kern *et al*., 2002a), patients attended an estimated 250 hours of rehab over 4 to 6 months.

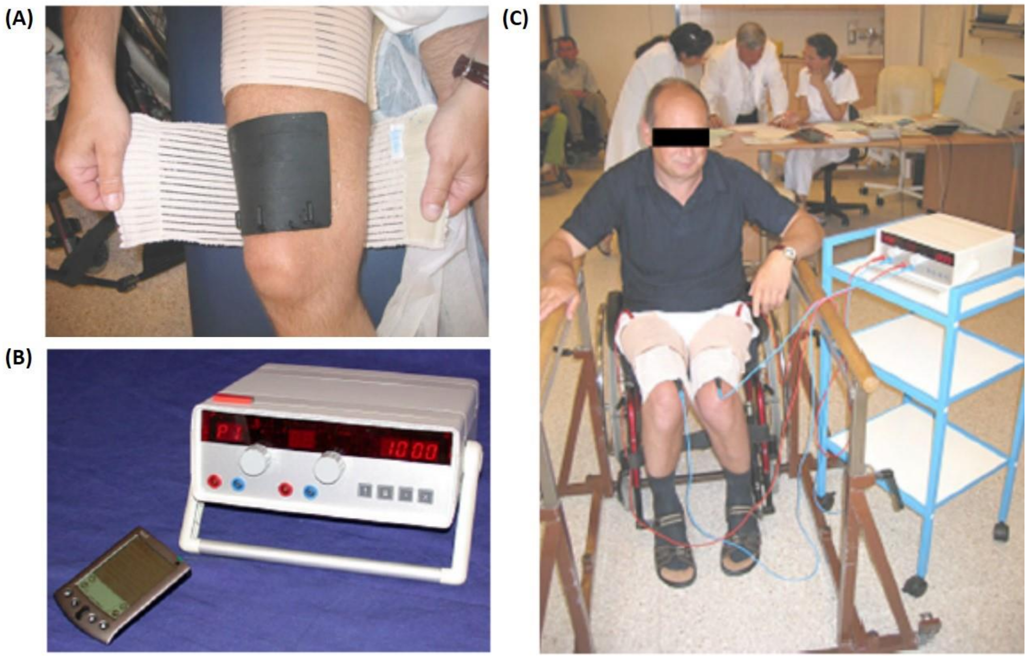

Figure 1.7 Functional electrical stimulation (FES) of DDM

Equipment utilised by Kern *et al*. (2002a) to stimulated DDM in patients with low spinal cord injuries. (A) Surface electrodes wrapped with a bandage to prevent accidental peel off, (B) FES stimulation device, (C) patient undergoing FES training. Parallel bars are for stability when performing sit-to-stand exercises. Images reproduced from (Kern *et al*., 2002a).

Fundamentally, eliciting muscle contraction via electrical stimulation is inherently less efficient than achieving contraction via physiological APs. During electrically-evoked muscle contractions, motor units are recruited based on their size and proximity to electrodes, leading to non-selective, random activation of motor units which can lead to muscle fatigue. In contrast, voluntary contractions are characterised by the recruitment of smaller, fatigue-resistant motor units before activation of large motor units (Martin *et al*., 2012b). Furthermore, electrical pulses cause simultaneous activation of motor fibres unlike the highly organised recruitment and de-recruitment of muscle fibres underlying physiological contractions. As a result, muscle contractions achieved through electrical pulses can produce sudden, un-coordinated and inefficient movement patterns (C. L and M. R, 2008) (Martin *et al*., 2012a).

1.7 A biohybrid approach to stimulate denervated muscles

A novel paradigm to stimulate denervated muscles consists of adopting a biohybrid approach, whereby motor neurons and electrodes are combined to develop an artificial nerve tissue, therefore providing a more biologically inspired interface to reinnervate muscles. In recent years, the field of bioelectronics has focused research efforts on the development of implantable electrode arrays housing living cells (see Chapter 5, section 5.1 for more detail on biohybrid devices). The fabrication of such devices offers the potential for ever closer integration between biology and electronics as well as the unprecedented prospect of replacing lost cells and partly restoring tissue function.

A biohybrid approach tailored to patients with complete *cauda equina* and *conus medullaris* lesions aims to elicit muscle contraction through the integration of cells between the ES device and the muscle, so that the current applied by the electrodes, evokes an action potential (AP) in MNs which is conveyed to muscle fibres via neuromuscular junctions (figure 1.8). Because the activation threshold of neurons is lower than that of muscles, a lower current density is required to cause neural activation, thus circumventing side effects associated with the substantially high current demands of direct ES of muscle.

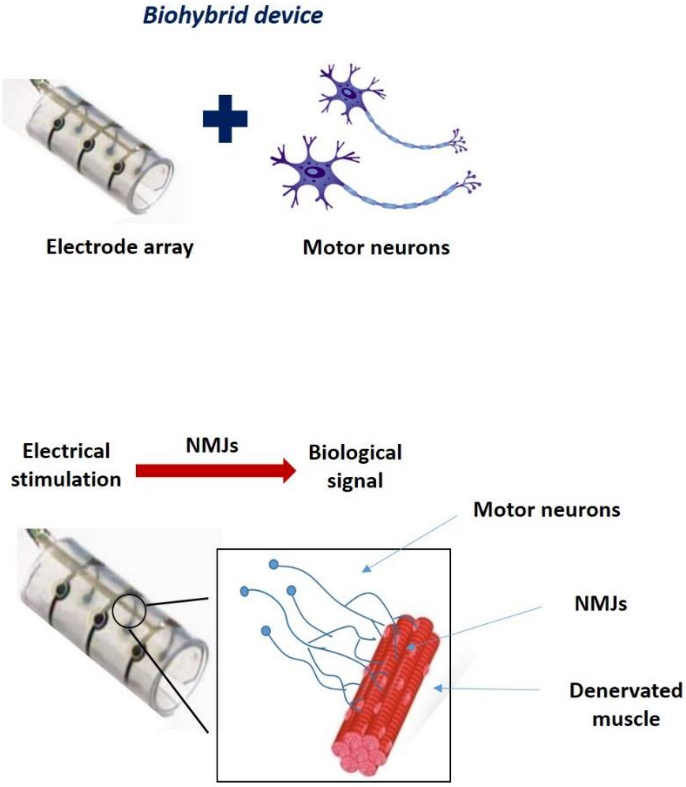

Figure 1.8. Biohybrid device to stimulate denervated muscles

Diagram of a biohybrid approach for muscle stimulation following LMN lesions. MNs can be incorporated into implantable electrode arrays to develop an artificial nerve tissue. This artificial nerve tissue serves as an intermediate between electrodes and muscle, converting the electrical signal into a biological AP, therefore reinnervating muscle through physiological neuromuscular interaction and circumventing side effects linked to the high current demands of direct ES of muscle.

The manufactured biohybrid device will be interfaced to a denervated muscle through the remaining distal stump of the nerve (figure 1.9). In this approach, MNs seeded on the device will be in direct contact with the lumen of the nerve in order to allow these cells to grow down the distal stump of the nerve towards the muscle.

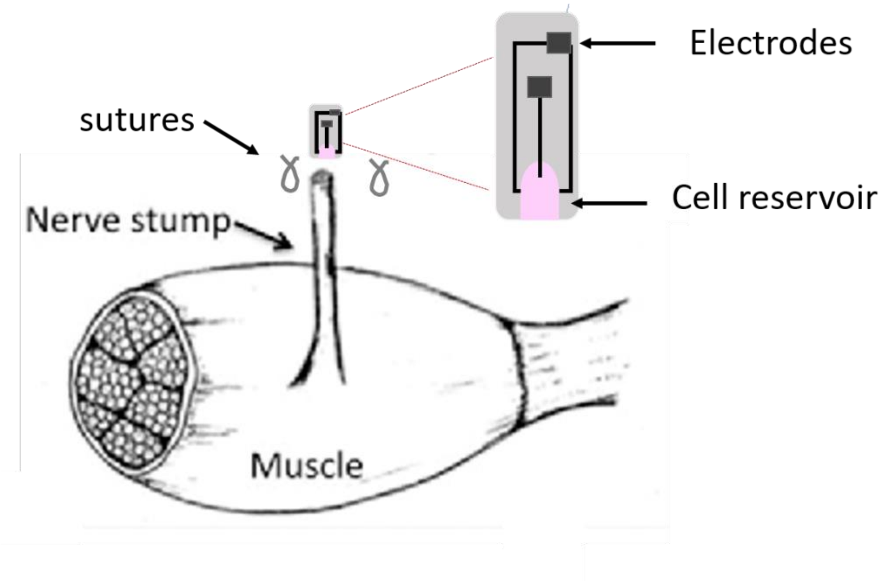

Figure 1.9. Schematic depicting the proposed site of implantation of the biohybrid device

The proposed approach to interface biohybrid device and denervated muscle is to utilize the distal stump that remains following lower motor neuron injuries. The device can be sutured to the nerve stump, so that MNs seeded on the cell-reservoir are in direct contact with the nerve lumen. The rationale behind this approach is that the nerve can provide the structure and guidance needed for motor neurons on the device to grow towards the muscle. A potential limitation of this approach is that, as motor neurons fire action potentials and activate the muscle, the force produced by muscle contraction may result in detachment of the device from the nerve stump. Image adapted from (Cederna et al., 2015)

1.8 The electrical-neural interface

This section examines the fundamental mechanisms underpinning bioelectronics communication between biological and electronic systems. Electrodes communicate with biological tissue in a bidirectional manner. In one way electrodes can stimulate neurons by delivering electrical pulses. Alternatively, the activity from firing neurons can be sensed and recorded by electrodes (Cogan, 2008, Yuk *et al.*, 2019). Neuronal cell communication relies on the movement of ions through a cellular membrane, whereas almost all conventional electrodes use free electrons as mobile charge carriers. As such, bioelectronics creates an interface where ion-based current and electron-based currents are exchanged (figure 1.10E).

Neurons communicate via spikes of ionic currents known as action potentials (APs). The flux of sodium (Na^+), potassium (K^+), calcium (Ca^{2+}) and chloride (Cl^-), in and out of the cell soma dictates the transmembrane potential of cells. At rest, this potential is approximately -60 to -75 mV, with a more negative internal potential, due to the concentration gradient of ions across the membrane (figure 1.10A). Typically the gradient is characterised by an excess of intracellular K^+ and extracellular Na^+ by energy dependent ion pumps. Other ionic pumps, regulate the intracellular pH through the outflow of Ca^{2+} and Cl^- (Ruffin *et al*., 2014). Excitatory inputs at synapses with other neurons cause the transmembrane potential to fluctuate to a more positive potential (depolarisation) whereas inhibitory inputs result in the transmembrane potential becoming more negative (hyperpolarisation). If the excitatory signal is enough to depolarise the membrane beyond threshold level (-50 to -55 mV), an AP is generated. This is triggered by the opening of voltage-gated Na^+ channels to allow the intracellular influx of Na^+, driving the membrane to depolarisation. Once the membrane reaches a potential between 30 to 40 mV, voltage-gated Na^+ channels close, and the opening of voltage-gated K^+ channels promotes the extracellular flow of K^+, driving the membrane back to the resting potential (Hodgkin and Huxley, 1952). This ion flux generates APs across the cell membrane (nm scale) as well as the extracellular space (µm scale) (Yuk *et al*., 2019). In the extracellular space, this potential difference declines rapidly with increasing distance from the cell body or axon where it is generated, therefore, requiring electrodes to be placed within 100 µm of a cell if single unit activity is to be detected (figure 1.10B,D) (Ferro and Melosh, 2018). Concurrent activity of neurons firing together, generates what is known as a local field potential (LFP), which can be recorded over a tissue range of mm to cm (figure 1.10C). Electrodes can detect signals from more than one neuron at the same time, thus requiring the use of algorithms to distinguish signals from individual neurons (Harris *et al*., 2016).

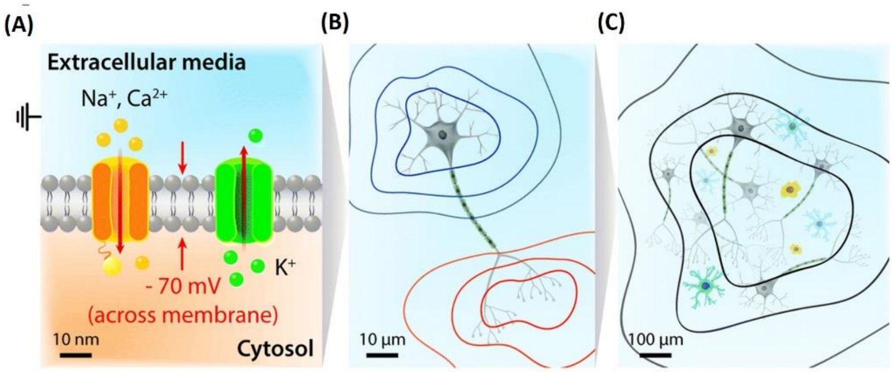

Transmembrane potential

Extracellular potential

Local field potential

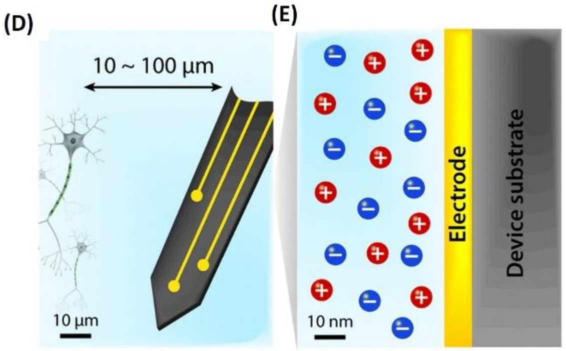

Implantable electrodes

Electrolyte-electrode interface

Figure 1.10 Electrophysiological signalling at different scales

(A) Ligand-gated ion channels allow the movement of ions in and out of the cell, generating a transmembrane potential (nm scale). (B) Electrically active neurons produce an extracellular potential (µm scale; blue line represents negative and red line positive values for local field potentials). (C) Concurrent activity of populations of electrically active neurons generate a local field potential (mm to cm scale; black lines). (D) Electrodes are required to be within 100 µm distance from neurons in order to stimulate or record from individual cells. (E) The exchange between ionic-based and electron-based current occurs at the electro-electrolyte interface (nm scale). Image adapted from (Yuk *et al*., 2019).

For electrodes to stimulate neurons, a transduction of charge carriers from electrons in the metal to ions in the electrolyte is required (figure 1.10E). This transduction is underpinned by two types of reactions occurring at the surface of the electrode: capacitive (non-faradaic) reactions and reduction-oxidation (Redox or faradaic) reactions (Merrill *et al*., 2005) (see Chapter 4, section 4.1.3 for more details). Capacitive reactions (figure 1.11A) are based on the charging and discharging of the double layer above the surface of the electrode with the corresponding oppositely charged carriers accumulating in the extracellular space adjacent to the electrode. Because this type of reaction is purely capacitive and does not entail transfer of electrons to the extracellular space or change in chemical species, capacitive reactions are more desirable in bioelectronics stimulation. However, in practice, only small charges can be transferred by non-faradaic means due to a low capacitive charge per unit area.

Reduction-oxidation reactions involve electron transfer across the electrode-electrolyte interface, therefore leading to the formation of new chemical species (figure 1.11B). The disadvantage of these reactions is that they must be kept within a potential range that prevents water electrolysis or the formation of other hazardous species. The limits of water electrolysis, known as the water window, is a potential range dependent on the electrode material. Further limits on charge injection occur due to other irreversible redox reactions, where the reaction products do not remain available at the electrode surface for the reverse reaction during biphasic stimulation.

Electrodes stimulate neurons by means of current injection which generates a change in potential in the extracellular environment that can depolarise cell membranes, leading to APs, and alter the LFP. Low impedance electrodes are preferred as they allow injection of higher currents at lower voltages avoiding irreversible chemical reactions and the formation of toxic by-products (Ferro and Melosh, 2018). Electrochemical characterisation of electrodes *in vitro* allows measurement of the amount of charge electrodes can safely inject per unit area at a voltage within the water window that is within the limits of water electrolysis. This parameter is known as the charge injection capacity (CIC) (Cogan, 2008).

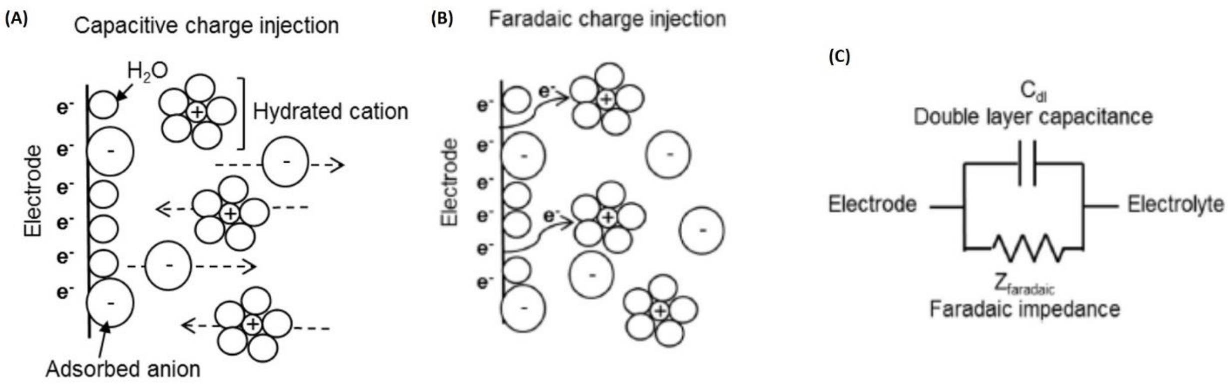

Figure 1.11 Electrochemical mechanisms underlying electrical stimulation

Charge injection mechanisms can be (A) capacitive (non-faradaic), where redistribution of charged chemical species leads to charging and discharging of the double-layer and (B) Faradaic (Redox), where electron transfer occurs and reduction-oxidation reaction takes place. The inherent formation of new chemical species can be irreversible. (C) Charge transfer mechanisms between electrode and electrolyte can be modelled by an electrical capacitor (double-layer capacitance) and a resistor (Impedance (Z) encountered by electron transfer). Image reproduced from (Bareket-Keren and Hanein, 2012).

The clinical usefulness of electrical stimulation relies on the ability to chronically provide safe levels of therapeutic stimulation. For most neural stimulation purposes, pulses with a cathodic and anodic phase that result in overall zero net charge (charge-balanced) are used (Cogan 2008). These waveforms play a crucial role in maintaining the electrode potential within a range that guarantees the reversibility of reduction and oxidation reactions that would otherwise degrade electrodes and cause tissue damage (Merrill *et al*., 2005) (see Chapter 4, section 4.1.3). Electrical stimulation causes a redistribution of charge on the axon membrane. When the cathode is used as the working electrode, current flows from the cathode into the tissue and back to the anode. Negative charge accumulates extracellularly adjacent to the cathode, causing depolarisation of the membrane. This depolarisation is associated with a movement of positive charge inside the cell membrane to the region under the cathode and hyperpolarisation of the cell membrane under the anode (Merrill *et al*., 2005) (figure 1.12). Single neurons can be stimulated by both anodal and cathodal stimulation depending on their orientation and the strength of stimulation (Caldwell *et al*., 2019). Anodal pulses best stimulate dendrites and terminals whereas cathodal pulses best stimulate axons (McIntyre and Grill, 2000). In both instances, depolarisation occurs at the level of the axon either a short initial segment or at nodes of Ranvier – where the outward flowing current is propagated as an AP. When the anode is used as the working electrode, the area directly beneath the anode becomes hyperpolarised but regions further away are depolarised and an AP is initiated, this is known as the virtual cathode (Merrill *et al.*, 2005). For instance, anodal surface stimulation of neocortical cells in the brain leads to hyperpolarisation of dendrites. Associated with the accumulation of negative charges inside the membrane is the congregation of positive charges distally, at the level of the cell body or axon thus causing depolarisation of this region (Caldwell *et al.*, 2019). It is estimated that depolarisation achieved through anodal stimulation is between one-seventh and one-third of the depolarisation caused by cathodal stimulation of the same amplitude (Merrill *et al.*, 2005). As such, cathodic stimulation requires lower charge injection to elicit APs (Brocker and Grill, 2013, Voigt and Kral, 2019).

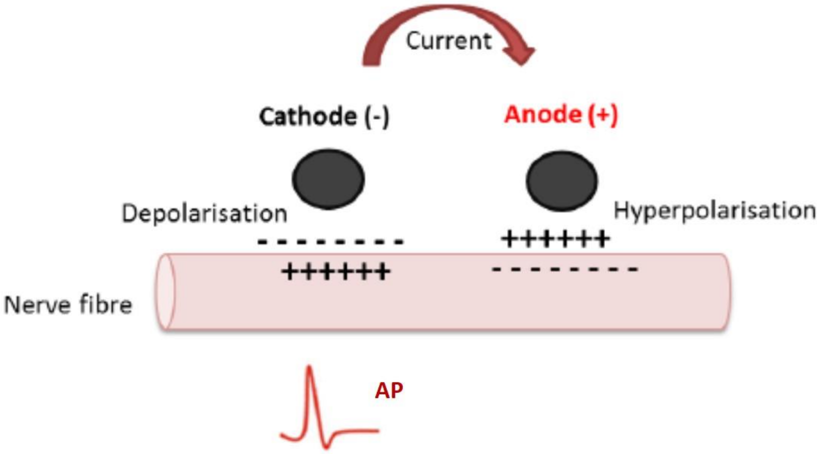

Figure 1.12 Schematic representation of cathodal stimulation of a nerve fibre

Cathodal stimulation causes depolarisation of excitable cells through the flow of current from the cathode (negative polarity) into the anode (positive polarity). The cathode is the working electrode that causes nerves to depolarise and generate APs, whereas the anode is the counter-electrode that causes membrane hyperpolarisation (as a result of returning charge), thus rendering the nerve membrane directly under it more resistant to becoming depolarised.

1.9 Considerations for a biohybrid approach

The ideal biohybrid device would consist of a suitable substrate that provides mechanical support and electrical insulation for the electrode array while also serving as a carrier for the cellular component. To this end, the substrate must be able to support cell growth and neurite extension of incorporated cells. Moreover, incorporated cells should be capable of extending neurites from the electrode to the muscle, forming functional NMJs and being able to survive long-term in the host environment. In addition, it is highly desirable that the mechanical properties of the biohybrid device match those of the native tissue in order to promote seamless integration with the host environment and mitigate the foreign body response. Finally, a successful biohybrid approach must support the formation of synaptic connections between transplanted and endogenous cells while also maintaining long-term connections between the electrodes and the cells within the device. To achieve the ideal biohybrid device electrical, mechanical, biological and chemical considerations need to be taken into account during the design phase of development.

1.9.1 Electrical considerations

Manufacturing electrodes capable of effective stimulation is one of the main considerations when choosing conductors and designing a biohybrid device. One of the main challenges in implantable electrodes is the associated miniaturisation of devices to achieve dimensions suitable for implantation. Reducing electrode size causes an increase in impedance and poses a limit on CIC, consequently requiring injection of greater charge density in order to achieve clinical efficacy. This increased charge density increases the risks of pushing electrodes outside their safe limits (e.g. the 'water window') which can cause damage to the tissue and the environment. To meet this requirement, the electrode material is an aspect of the device which can be modified. Indeed metal alloys have been shown to increase CIC compared to pure metals. This is due to their ability to inject charge through capacitive reactions as well as reduction-oxidation reactions. Deposition of metal compounds such as iridium oxide (IrOx) and titanium nitride (TiN) on the metallic surface is commonly reported in the literature as a means of achieving greater CIC (Cogan *et al*., 2009, Chung *et al*., 2018). One main disadvantage of IrOx coating is that the benefits it provides in term of charge transfer are achieved through a potential bias across the electrode when reduction-oxidation reactions occur (Cogan *et al*., 2009). Although the impact of a constant potential bias in the *in vivo* environment is not fully understood, it has been suggested that it may cause changes in the extracellular environment due to shifts in the ion concentration (Goding *et al*., 2018). Another proposed approach to overcome issues with miniaturisation is roughening of the metal (see chapter 4, section 4.1.1 for more detail). Briefly, this strategy increases the effective surface area (ESA) of the electrode, therefore increasing the surface available for charge transfer to occur.

Another point for consideration is the requirement to stimulate cells on the device without causing charge transfer to endogenous cells. Previous research using microelectrode arrays (MEAs) *in vitro* has shown that cells located within a short distance of electrodes require a lower threshold of activation that those located afar (Kim *et al*., 2016b). Therefore, seeding cells directly in contact with electrode sites will likely decrease the charge injection required to stimulate these cells while preventing unwanted activation of endogenous cells due to charge injection below clinically effective levels.

1.9.2 Mechanical and topographical considerations

It is well documented in the literature that developing biohybrid devices that match the stiffness of the *in vivo* environment helps prevent a mechanical mismatch between implant and tissue that would otherwise aggravate the foreign body response (FBR) (Nguyen *et al*., 2014) (Sohal *et al*., 2016, Zheng *et al*., 2019). Softer materials with stiffness values within the range reported for nerves (0.04 – 20 kPa) (Borschel *et al*., 2003) results in a decrease in scar tissue formation around the device. For a biohybrid device, the implications of a less severe FBR, translates into increased likelihood of long-term synaptic connections with endogenous cells and chronic interface between the cellular component and the electrodes on the device. Incorporating hydrogels into biohybrid devices is a commonly used solution in the field of bioelectronics to improve the interface between implant and tissue (see Chapter 5, section 5.1.4 for further details).

The matrix stiffness of hydrogels can be tuned to more closely resemble that of the local *in vivo* environment. Indeed, natural hydrogels like alginate can be controlled by systematically altering the ratio of alginate to ionic cross linker, thus varying the mechanical properties of these hydrogels (Freeman and Kelly, 2017). The incorporation of a hydrogel within the biohybrid device poses multiple further considerations. A variety of hydrogels with different properties have been used previously, depending on the intended function of the biohybrid device (refer to Chapter 5, tables 5.1 and 5.2 for examples of hydrogels used in the biohybrid field). The function served by the biohybrid device will dictate the choice of material. In selecting a hydrogel with the most suitable properties, the following considerations should be assessed: degradation parameters, viability of cells in the device, effect of stiffness on cell differentiation, impact on electrochemical properties of electrodes and the effect of embedding cells and electrodes on their ability to extend neurites to form synaptic connections with endogenous cells. With respect to the latter, previous research has shown that the neuronal-like cells, PC12, are capable of extending neurites when embedded in a poly (vinyl alcohol) tyramine (PVA-Tyr) hydrogel cross-linked with sericin and gelatine; however, in the absence of topographical or chemical cues to provide neurite guidance, neurites extended around cell bodies instead of growing outside the hydrogel (Aregueta-Robles *et al*., 2015).

Topographical cues can be incorporated on biohybrid devices as a means of guiding extending neurites towards target endogenous cells. To this end, microchannels can be implemented to structures that compartmentalise cell bodies and neurites, so as to retain the former in close proximity to electrodes while guiding the latter towards the target tissue. A wealth of literature has been reported on the use of grooved substrates to provide directionality to neurons *in vitro* (refer to Chapter 4, section 4.1.2 for further details). Furthermore, a similar approach has been successfully implemented to guide regenerating nerves and facilitate reconnection of neurons in damaged nerves. In line with this, Lacour *et al*. (2009) reported the use of microchannel electrode arrays with a channel cross-section of approximately 10,000 μm^2 can support axon guidance *in vivo* over a distance of 2 mm. Similarly, Srinivasan *et al*. (2015) reported successful guidance of regenerating nerves using PDMS microchannels of equal dimensions. Implanting the biohybrid device in close proximity to the target tissue will decrease the distance MNs have to traverse to form NMJs with denervated muscle.

Overall, multiple mechanical and topographical characteristics require careful assessment when designing a biohybrid device. The choice of substrate, presence and composition of hydrogel components, hydrogel and surface topographical cues will vary according to the intended purpose of the biohybrid approach. It is highly likely that the best match for the desired approach will have some limitations, therefore, creating the need to compromise on individual aspects based on what is prioritised.

1.9.3 Biological considerations

The following aspects should be taken into account when incorporating cells into implantable electrodes: cell source, developmental stage at which cells will be incorporated, cell survival and protection against the host immune system and means of tracking cells once implanted in order to assess integration with the host environment.

The ideal type of cell to develop a biohybrid device with therapeutic potential will be originated from a source with no to minimal ethical concerns with sufficient supply and with minimal tumorigenic potential. Furthermore, if the main application of the biohybrid approach is to partly restore lost tissue function (refer to Chapter 5, section 5.1.2), the cell of choice must be able to differentiate into cells with molecular and functional characteristics that match those of endogenous cells. The various different cells with therapeutic potentials currently being investigated to replace MNs are discussed in greater detail in Chapter 3, section 3.1.2.

The question of whether incorporated cells will be differentiated or undifferentiated will directly depend on whether a specific neural subtype is required for the intended function of the device; or whether a mixed population of neural stem cells is more appropriate. In the case of adopting a biohybrid approach to replace LMNs, a subset of specific neurons will be required. However, incorporating a mixed population of neurons, including the desired type of neuron alongside supporting glial cells may be more beneficial for long-term survival and integration of the device with the host environment. Magown *et al*. (2017) reported improved functional connections with denervated muscles in mice upon transplantation of mouse embryonic stem cell-derived motor neurons (MNs) containing a mixed population of cells compared to purified MNs. The transplanted cells consisted of a mixed population of MNs and interneurons, which formed microcircuits *in vivo* leading to the generation of rhythmic activity required for muscle contraction. This study suggests that a mixed population of neurons, as opposed to MNs alone, is a better approach to facilitate neuromuscular innervation. Moreover, the use of a mixed population of cells better resembles the physiology of tissues and may promote the development of complex tissues that are self-supporting. This is likely to be beneficial in promoting cell survival and integration in the challenging wound microenvironment, where the presence of the implant and surgical site injury create an immunological response detrimental for the survival of transplanted cells (Woolley *et al*., 2011).

In the development of a biohybrid device, cells can be differentiated at three different stages: *in vitro* before incorporation into the device, *in vitro* once seeded on the device or undifferentiated (or partially differentiated) progenitor cells can be incorporated on the device to differentiate once implanted *in vivo* (Goding *et al*., 2018). Differentiation of neural stem cells *in vitro* provides better control over the neural phenotype adopted by terminally differentiated cells than spontaneous differentiation *in vivo*. Fortin *et al*. (2016) reported that undifferentiated human neural precursor cells (hNPCs) transplanted into mouse brains had higher proliferation activity and showed a preference for astrocytic differentiation compared to hNPCs differentiated into a neural progeny prior to transplantation. Another important aspect to take into consideration is whether differentiating cells prior to implantation affects their viability. There is disagreement in the literature with regards to this subject, with some studies reporting a difference in viability of cells transplanted *in vivo* at different stages of differentiation and others suggesting developmental stage of transplanted cells does not impact on their viability. In line with the former, Huang *et al*. (2017) reported improved survival rate of iPSC-derived neural crest stem cells (NCSC) compared to iPSC-derived NCSC differentiated into Schwann cells when implanted into a rat sciatic nerve transection model. In contrast, Fortin *et al*. (2016) showed purified neurons obtained from hNPCs survived as well as their undifferentiated counterparts when transplanted in mice brains. Poor survival of both, undifferentiated and pre-differentiated human striatal neural stem cell line (STROC05) into GABAergic neurons was reported by El-Akabawy *et al*. (2012) upon transplantation in a transgenic mouse model of Huntington's disease. Overall, there is no consensus on the optimal level of differentiation or the benefits of implanting a mixed population of cells to support cell survival, mitigate tumorigenicity and encourage integration with the local environment.

Means by which implanted cells can be protected from the host are essential for the success of a biohybrid approach. To this end, cells require protection against the host immune response but also against the challenging microenvironment resulting from injury caused by the underlying condition and by implantation of the device. To protect cells against the host immune system, proposed strategies include the use of hydrogels to shield cells from the host immune system while allowing access of oxygen and nutrients to cells. Indeed, most research in the field of biohybrid devices incorporates hydrogels to match mechanical properties of the device with the host environment, to protect cells against the host immune response or both (Purcell *et al*., 2009, Richter *et al*., 2011a, Green *et al*., 2013b, Cullen *et al*., 2011a) (refer to Chapter 5, tables 5.1 and 5.2 for further details on hydrogels implemented in existing biohybrid devices). Other proposed approaches include the release of anti-inflammatory drugs from the device. To this end, dexamethasone was incorporated into the polymer polyterthiophene during its manufacturing (Stevenson *et al*., 2010). The authors reported release of the drug at therapeutic levels over a period of 24 hours. However, the study did not assess release of the drug over longer periods of time. Other examples in the literature include drug entrapment within a degradable material. Abidian *et al*. (2006) reported entrapment of dexamethasone within biodegradable PEDOT nanotubes. In this study, controlled release of the drug at therapeutic levels was achieved over 54 days. Although drug entrapment and successful release over time has been achieved in electrode arrays, the incorporation of these agents in devices housing cells may pose further challenges. First, the size of biohybrid devices is a limiting factor in the amount of drug that can be stored. Therefore, this approach may fail to provide anti-inflammatory effects at therapeutic levels over the time period required. It is estimated that anti-inflammatory agents need to be supplied for 14 days to exceed the neuronal wound healing phase (Green and Abidian, 2015). Furthermore, storing the required amount of pharmacological agent required to achieve the desired effect may cause cytotoxicity to cells within the device.

The microenvironment in which the biohybrid device is implanted is characterised by ischaemia, extracellular matrix (ECM) degradation, inflammatory agents, oxidative stress and acute immune reactions product of surgical injury (Sart *et al*., 2014). This microenvironment poses a challenge for cell survival, therefore, to optimise survival of transplanted cells some studies have explored the benefits of pre-conditioning cells when cultured *in vitro* to similar conditions to those that would be encountered within the implant environment. Indeed, pre conditioning of cardiac progenitor cells to ischaemia and oxidative stress prior to implantation improved their survival once implanted in the heart of rats (Pendergrass *et al*., 2013). Similarly, culturing mesenchymal stem cells (MSCs) at hypoxic levels improved their survival once implanted in a model of cerebral ischaemia in rats (Wei *et al*., 2012). Indeed, high post-transplantation cell mortality has been partly linked to the differences in oxygen level used during cell culture (approximately 20% in atmospheric air) compared to physiological oxygen levels cells experience once implanted (between 0.5 and 8% in the adult brain) (reviewed in Sandvig *et al*. (2017)). With regards to denervated muscles, capillary loss is one of the most prominent features associated with this type of injury (Carlson, 2014). Understanding the level of hypoxia in denervated muscles is highly desirable in order to pre-condition MNs prior to transplantation.

Finally, it is highly desirable to be able to trace cells within the biohybrid device to assess their viability and level of integration with the endogenous cells. Furthermore, from a clinical perspective it allows for early intervention in cases of tumour formation (Goding *et al*., 2018). For pre-clinical testing purposes, transduction of cells with a fluorescent protein like green fluorescent protein (GFP), allows their localisation upon histological endpoint tissue analysis. Nevertheless, their use within a clinical setting is currently not feasible. An alternative approach to trace implanted cells in patients consists of incorporating nanoparticles within cells that can be visualised through imaging techniques. To this end, Wan *et al*. (2016) reported successful tagging of bone marrow mesenchymal stem cells (BMSCs) with gold nanoparticles, modified to improve their biocompatibility. Using dual energy computer tomography, the researchers were able to perform real-time tracking of BMSCs implanted in rabbits. Similarly, Jendelová *et al*. (2004) were able to identify bone marrow and ESCs labelled with iron oxide nanoparticles, once transplanted in rat spinal cord and brain, using magnetic resonance imaging.

Although, several biological considerations need to be taken into account when incorporating cells into implantable electrode arrays, this biohybrid approach offers the potential to replace endogenous cells and restore lost tissue function following injury.

1.9.4 Chemical considerations

Biocompatibility and non-toxicity of all materials and elements incorporated within the device must be ensured at all stages of the development life cycle, including manufacturing, sterilisation, implantation and in some materials degradation (e.g. of hydrogels encapsulating the cellular component).

Substrate, conductors and insulators on electrode arrays should be manufactured using non-toxic materials, preferably with a long clinical record to ensure these materials can withstand exposure to the *in vivo* environment for long periods of time without causing any adverse reactions. If potential toxic components are used, it is necessary to ensure these are not released in the body. Based on toxicity concerns, implementing inert inorganic metals such as platinum, gold, iridium and titanium, with a good medical record may be more desirable (Cogan, 2008). Furthermore, adopting these well-established metals for the production of electrodes on biohybrid devices, will increase the likelihood of faster clinical translation if the device is successful.

Research on the use of novel conductors like carbon nanotubes (Simon *et al*., 2019), graphene (Reina *et al*., 2017, Dasari Shareena *et al*., 2018), and intrinsic conducting polymers such as poly-3,4-ethylenedioxythiophene (PEDOT) (Green *et al*., 2013d, Pranti *et al*., 2018) and polypyrrole (PPy) (Kim *et al*., 2018a) in the manufacturing of biomedical implants has rapidly increased in recent years. The benefits of these conductors in increasing the charge injection capacity of implantable electrodes is indisputable (Gabay *et al*., 2007, Keefer *et al*., 2008, Green *et al*., 2013c, Kim *et al*., 2018b). Although, these materials have been shown to be biocompatible, their use in a clinical setting has not yet been approved. In fact some issues related to safety and toxicity of graphene derivatives were highlighted during preliminary biological applications (Yang *et al*., 2013). For translation of these materials into a therapeutic setting, it is necessary to fully understand the impact of carbon derivatives, like graphene oxide, on the body and how long these derivatives take to be metabolised and excreted (Zhu *et al*., 2010).

Implementing biodegradable hydrogels to encapsulate cells, requires considerations of two aspects. First, the rate of degradation should be slow enough to allow the embedded cells to form their own ECM but fast enough so as to not interfere with cell development and differentiation. Second, the safety of by-products released during degradation needs to be ensured as well as the ability of the body to metabolise such products (refer to Chapter 5, section 5.1.4 for further details on the use of hydrogels in bioelectronics).

Where cells are not embedded within hydrogels, coating of the implant may be used to promote cell attachment to the surface. It has been suggested that ECM molecules provide structural and chemical cues to encourage regeneration at the neural interface (Chan and Mooney, 2008). To this end, molecules like collagen, laminin and fibronectin have been reported in the literature. Laminin has been shown to reduce microglia and macrophage accumulation near electrode arrays after 4 weeks post-implantation in the rodent brain compared to uncoated probes (He *et al*., 2006). Furthermore, Righi *et al*. (2018) reported coating polyimide electrodes with a laminin-derived peptide (CAS-IKVAV-S) promoted neuronal cell adhesion and neurite elongation as well as supporting peripheral glial cell viability while reducing fibroblast migration *in vitro*. More recently, Bas *et al*. (2019) reported laminin-coated arrays improved Schwann cell migration towards cochlear implants promoting neurite outgrowth and guidance as well as survival of spiral ganglion neurons in the inner ear compared to uncoated arrays. It has been suggested that adsorption of these molecules to the surface of electrodes does not produce a stable interface when transplanted *in vivo*, as competitive protein binding within this environment may displace the adsorbed layer (Aregueta-Robles *et al*., 2014). Based on this, covalent binding of attachment biomolecules to the surface of implants has been adopted by various researchers to produce more stable interfaces (Nguyen-Vu *et al*., 2007, Green *et al*., 2010). Choice of coating and the potential impact in the *in vivo* environment warrant consideration. The use of biomolecules as opposed to synthetic polymers is preferred as they are native to the *in vivo* environment and therefore tend to be biocompatible.

1.10 Aims of this PhD project

There is a dearth of treatment options for patients bearing complete *cauda equina*/ *conus medullaris* injuries. The lack of mobility causes development of secondary health-related complications that increase the morbidity and mortality rates in these individuals. Thus far, the ES approach developed by the EU project 'RISE' has made considerable progress in partly restoring muscle function. However, direct ES of muscle results in several limitations and side effects associated with this rehabilitation therapy. Advances in stem cell therapy research and bioelectronics offers the opportunity to develop new therapeutic approaches. By incorporating MNs into implantable electrodes an artificial motor nerve can be developed, therefore allowing stimulation of denervated muscles in a more physiological manner similar to the neuromuscular interaction *in vivo*. Because nerves require less charge density to evoke muscle contraction, it is hypothesised that directly stimulating MNs on implantable electrodes will elicit muscle contraction and mitigate side effects associated with direct ES of muscles. Therefore, the overall aim of this PhD project is to start to develop the components of a biohybrid device to stimulate denervated muscles following lower motor neuron lesions, which could ultimately be used to mitigate the onset of secondary complications associated with muscle denervation. This was divided into the following objectives:

1. To identify cells with therapeutic potential capable of adopting a motor neuron (MN)-like phenotype upon induced differentiation.
2. To design and manufacture electrode arrays with the following characteristics; (1) suitable for implantation, (2) with an allocated area for the incorporation of MN-like cells; (3) supportive of MN-like cell growth and neurite extension and (4) capable of effective stimulation.
3. To manufacture electrode arrays at appropriate scale for implantation and to assess the feasibility of implanting this biohybrid device in a rodent muscle denervation model.

2.0 Materials and Methods

2.1 Materials

The following tables list the cell lines (table 2.1) the consumables (table 2.2) and the antibodies (table 2.3) used for this project.

Table 2.1 Cells used in this project

This table includes the names of the cell lines, suppliers and catalogue numbers.

Cell lines	Supplier	Catalogue Number
NG108-15 mouse neuroblastoma x rat	Sigma-Aldrich, UK	88112302-1VL
SPC-01 cells, human	Supplied by ReNeuron, UK	N/A

Table 2.2 Consumables used in this project

This table includes the names of the reagents, solutions, materials and other, the supplier and catalogue numbers, which were used in this project.

Reagent/solution/material/other	Supplier	Catalogue number
Dulbecco’s modified Eagle’s medium (DMEM)	Sigma-Aldrich, UK	D6429
Foetal Bovine Serum (FBS/FCS)	Fisher-Scientific, UK	26140079
Penicilin-streptomycin (P/S)	Sigma-Aldrich, UK	P0781
DMEM-complete is DMEM supplemented with 10% FBS and 1% P/S		
DMEM-differentiation is DMEM supplemented with 1% P/S		
Trypsin-EDTA solution (TE)	Fisher-Scientific, UK	R001100
Poly-L-lysine	Sigma-Aldrich, UK	P6282
Collagen Type I	First Link, UK	60-30-810
Mouse laminin-I	Amsbio, UK	3400-010-02
Alginic acid sodium salt	Sigma Aldrich, UK	180947
PRONOVA™ SLM100 Sodium Alginate	NovaMatrix, Norway	420306
Calcium chloride hexahydrate	Sigma Aldrich, UK	21108
Dulbecco's Modified Eagle Medium:Nutrient Mixture F-12 (DMEM/F-12)	Fisher-Scientific, UK	21331020
Human serum albumin (HSA)	Octapharma, UK	Albunorm 20%
Human recombinant transferrin	Millipore, UK	9701-10
Putrescine dihydrochloride	Sigma-Aldrich, UK	P7505
Human insulin	Sigma-Aldrich, UK	I9278

Progesterone	Sigma-Aldrich, UK	P6149
GlutaMAX supplement	Fisher- Scientific, UK	35050038
Sodium Selenite	Sigma-Aldrich, UK	S9133
Recombinant Human FGF-basic (bFGF)	Preprotech, UK	AF-100-18B
Recombinant Human EGF	Preprotech, UK	100-15
4-hydroxytamoxifen (4-OHT)	Supplied by ReNeuron, UK	N/A
Expansion media is DMEM-F12 DMEM-F12 supplemented with HSA (0.03%), human transferrin (5 µg/ml), putrescine dihydrochloride (16.2 µg/ml), human insulin (5 µg/ml), progesterone (60ng/ml), GlutaMAX (2mM), sodium selenite (40ng/ml), bFGF (10 ng/ml), EGF (20 ng/ml) and 4-OHT (100nM)		
Basal differentiation media is expansion media minus bFGF (10 ng/ml), EGF (20 ng/ml) and 4-OHT (100nM)		
Retinoic acid (RA)	Sigma-Aldrich, UK	R2625
Smoothened ligand (SAG)	Enzo, UK	ALX-270-426-M001
Supplemented differentiation media is basal differentiation media supplemented with RA and SAG		
TrypZean-EDTA (1X)	Lonza, UK	BE02-034E
Defined Trypsin Inhibitor (DTI)	Fisher-Scientific, UK	R007100
Hank's balanced salt sodium (HBSS)	Fisher- Scientific, UK	14170138
Phosphate buffered saline (PBS)	Sigma-Aldrich, UK	P4417
Paraformaldehyde (PFA)	Fisher-Scientific, UK	P/0840/53
Dimethyl Sulfoxide (DMSO)	Sigma-Aldrich, UK	D5879
Hoechst 33258 (Bisbenzimide)	Sigma-Aldrich, UK	861405

Propidium Iodide (PI)	Sigma-Aldrich, UK	81845
Syto 9 Green Fluorescent Nucleic Acid Stain	Fisher-Scientific, UK	S34854
CellTiter-Glo® Luminescent Cell Viability Assay	Promega, UK	G7572
Trypan blue solution (0.4%)	Sigma-Aldrich, UK	T8154
Triton X-100	Sigma-Aldrich, UK	T9284
Normal goat serum	Dako, Denmark	X0907
Normal horse serum	Vector Laboratories, UK	S-2000
Isoflurane anaesthetic	Minrad Inc, UK	From the pharmacist
Rimadyl analgesic	Pfizer, US	From the pharmacist
Lacri-lube	Allergan, UK	From the pharmacist
Battles veterinary wound powder	Fearing, UK	AH07045
10-0 sutures	eSutures	2830G
Sucrose	Fisher-Scientific, UK	S/8600/60
Hamilton® syringe, 7000 series, knurled hub	Sigma-Aldrich, UK	20750
OCT embedding matrix	Fisher Scientific, UK	12678646
CeramTec Rubalit® 708S Alumina, 96%	CeramTec, US	Ribalit 708S
Platinum/Gold conductor (Pt/Au)	ElectroScience, US	5837-G
Fibreglass Bristle PCB and Flux Brush	RS Pro, UK	514-868
Stainless Steel foil	Advent Research Materials, UK	FE6920

Silicone elastomer Sylgard 184	Farnell, UK	101697
Silicone elastomer MED-6015	Nusil, US	MED-6015
Silicone 734 Dow Corning	Farnell, UK	2289632
Color masterbatch (black)	Nusil, US	MED-4800-2
Acetone	Honeywell, UK	40289H
Propan-2-ol	Fisher-Scientific, UK	P/7500/17
Poly (4-styrenesulfonic acid)	Sigma-Aldrich, UK	561223
Sodium Phosphate	Alfa Aesar, UK	7601-54-9
Teepol	N/A	N/A
Hydro-X FLUX	Loctite, UK	HYDX 60EN 3C 0.7MMS
Hook-up wire	Mouser Electronics, Germany	602-2840/7-100-02

Table 2.3 Antibodies table. This table includes the names, dilutions, supplier and catalogue numbers of the primary and secondary antibodies used in this project

Primary Antibody	Dilution	Supplier	Catalogue Number	Secondary Antibody	Dilution	Supplier	Catalogue Number
Antibodies for Immunocytochemistry							
Rabbit, polyclonal anti-β-Tubulin III	1:400	Sigma-Aldrich, UK	T3952	DyLight 488 or 549, goat anti-rabbit IgG (H + L)	1:600	Vector Laboratories, US	DI-1488 or DI-1549
Mouse, monoclonal anti-β-Tubulin III	1:400	Sigma-Aldrich, UK	T8660	DyLight 488 or 549, horse anti-mouse IgG (H +L)	1:600	Vector Laboratories, US	DI-2488 or DI-2549
Mouse, monoclonal anti-Isl1	1:100	DSHB, US	40.3A4				
Mouse, monoclonal anti-Nestin	1:200	Millipore, US	MAB5326				
Mouse, monoclonal anti-nuclei AlexaFluor® 488 conjugate	1:100	Millipore, US	MAB1281A4	N/A			
Rabbit, polyclonal anti-Ki67	1:300	Abcam, UK	Ab15580	Dylight 488, goat anti-rabbit IgG (H + L)	1:600	Vector Laboratories, US	DI-2488
Antibodies for Immunohistochemistry							
Mouse, monoclonal anti-Nestin	1:200	Millipore, US	MAB5326	DyLight 488 or 549, horse anti-mouse IgG (H +L)	1:600	Vector Laboratories, US	DI-2488 or DI-2549
Mouse, monoclonal anti-nuclei AlexaFluor® 488 conjugate	1:100	Millipore, US	MAB1281A4	N/A			
Mouse, monoclonal OX-8	1:500	BIO-RAD, UK	MCA48GA	DyLight 549, horse anti-mouse IgG (H +L)	1:600	Vector Laboratories, US	DI-2488
Mouse, monoclonal CD4	1:500	Hycult Biotech, The Netherlands	HM3001	DyLight 549, horse anti-mouse IgG (H +L)	1:600	Vector Laboratories, US	DI-2549

2.2 Methods

2.2.1 Cell culture

2.2.1.1 NG108-15 cell line

NG108-15 is a hybrid cell line formed by the fusion of mouse neuroblastoma and rat glioma cells with cholinergic motor-neuron like characteristics. These cells were chosen for initial experiments due to their resemblance to motor neurons in order to optimise manufacturing of electrode constructs for *in vitro* experiments.

Cells were cultured on standard tissue culture flaks in DMEM complete medium (DMEM supplemented with 10% FBS and 1% P/S). Media was replaced every 2-3 days until cells were approximately 80% confluent, as observed under phase-contrast microscopy, at which point they were either sub-cultured or used for experiments. Cells were dissociated from the culture dishes by gently knocking the flask and recovered by centrifugation at 400 x g for 5 minutes. When used for experimental studies, FBS was removed from the media to promote cell differentiation and neurite extension (DMEM-differentiation media).

2.2.1.2 Human neural stem cells (SPC cell line)

Spinal Cord cell (SPC) is a conditionally immortalised human neural stem cell line with the ability to differentiate into ventral spinal cord neural subtypes. SPC clones were originally generated from 10-week-old human foetal spinal cord tissue.

Undifferentiated spinal cord clonal line 1 (SPC-01) cells were obtained from ReNeuron and routinely cultured as previously described in (Pollock *et al*., 2006). Cells were seeded on 75 cm^2 tissue culture flasks coated freshly with mouse laminin (10 µg/ml in DMEM-F12) for 1 h at 37 ^{0}C, 5% CO_2. Cells were grown in expansion media consisting of: DMEM-F12 supplemented with human serum albumin (HSA) (0.03%), human transferrin (5 µg/ml), putrescine dihydrochloride (16.2 µg/ml), human insulin (5 µg/ml), progesterone (60ng/ml), L-glutamine (2mM), sodium selenite (40ng/ml), basic fibroblast growth factor (bFGF) (10 ng/ml), epidermal growth factor (EGF) (20 ng/ml) and 4-OHT (100 nM). Media was replaced every 2-3 days until cells reached 70-80% confluency, as observed under phase-contrast microscopy, at which point cells were passaged using 2.5ml TrypZean/EDTA for 3 min at 37 ^{0}C, 5%CO_2 followed by an equivalent volume of Defined Trypsin Inhibitor (1X) (DTI). Cells were spun down (400 x g for 5 min at room temperature), resuspended at an appropriate density in DMEM-F12 and reseeded for expansion or experimental use. SPC-01 cells from passages 13 through 29 were used in all experiments.

2.2.1.2.1 Differentiation of SPC-01 into spinal motor neurons

Cells were seeded in laminin-coated 25 cm^2 tissue culture flaks. Spinal motor neuron differentiation was triggered by the removal of growth factors (bFGF and EGF) and 4-OHT from the media and the addition of RA (1 µM) and SAG (500 nM) for the first 5 days of differentiation (herein, referred to as supplemented differentiation media) (Wichterle, Lieberam *et al*. 2002, Miles 2004, Magown, Brownstone *et al*. 2016). After 5 days cells were either fixed in 4% paraformaldehyde for immunocytochemical characterisation or differentiation was continued by the removal of RA (1 µM) and SAG (500 nM) supplemented media and addition of expansion media lacking growth factors and 4-OHT (herein, referred to as basal differentiation media) (figure 2.1). In order to compare spinal motor neuron yield at various differentiation time points, cells were differentiated for 5, 14 and 21 days.

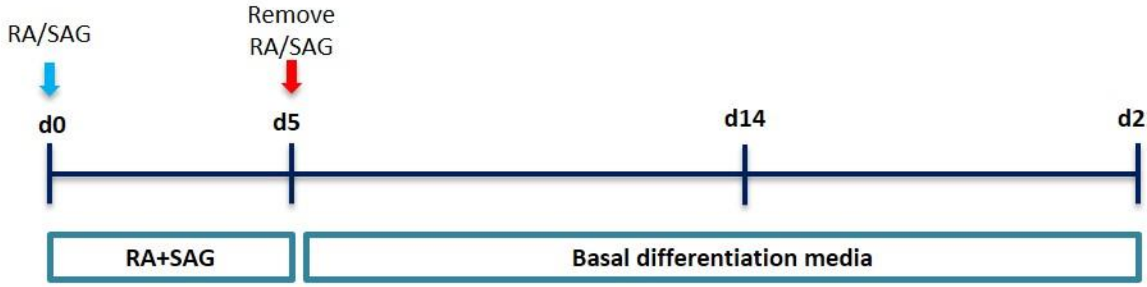

Figure 2.1 SPC-01 differentiation protocol
This diagram illustrates the protocol used to induce differentiation of SPC-01 cells into spinal motor neurons. RA and SAG were added to basal differentiation medium at day 0, removed from the medium at day 5 and cells either fixed or maintained in basal differentiation medium until day 14 and day 21.

2.2.1.2.2 RA/SAG differentiation dose response

A dose response of RA and SAG was performed to establish optimal concentration for spinal motor neuron differentiation. The initial concentrations of RA and SAG (1 µM and 500 nM, respectively) were individually increased and decreased by 10 fold (figure 2.2). After 5 days, RA/SAG supplemented media was removed and replaced by basal differentiation media until day 14 when cells were fixed for immuocytochemical characterisation. Day 14 was chosen as the yield of spinal motor neurons obtained using the protocol described in figure 2.1 was greater than at day 5 and similar to day 21.

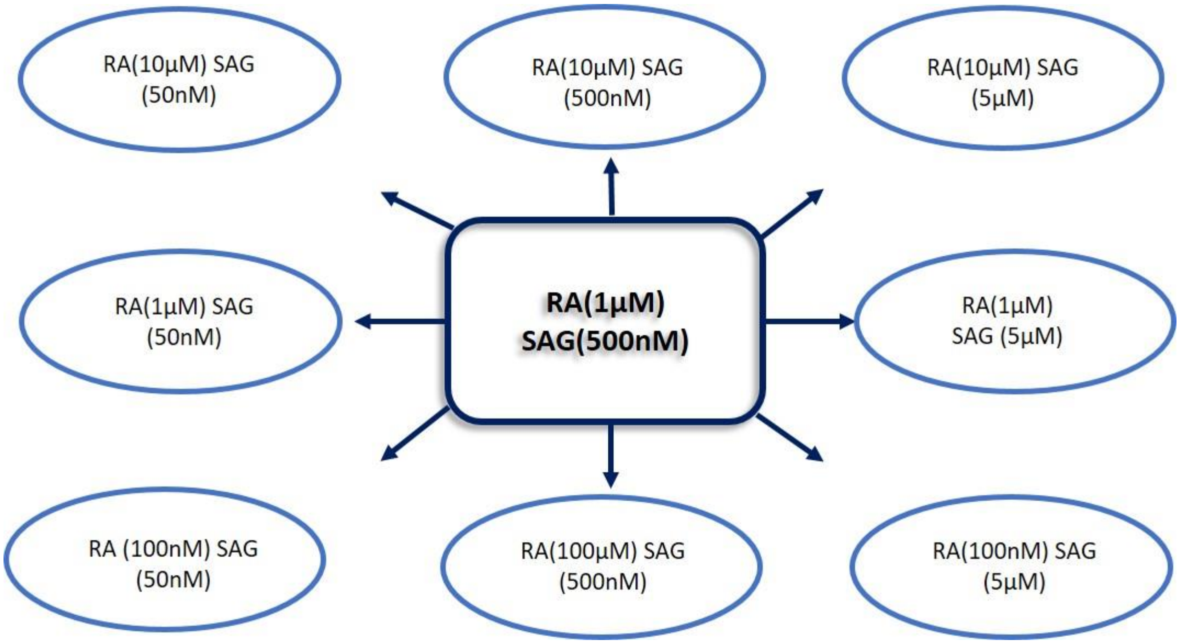

Figure 2.2 RA/SAG dose response
This diagram shows the 9 different concentrations of RA and SAG used to generate a spinal motor neuron differentiation dose response. RA (1 µM) SAG (500 nM) was used as the initial concentration based on previous literature to obtain spinal motor neurons and investigate different stages of differentiation.

2.2.2 SPC-01 cells seeded on coverslips, alumina plates and electrode construct reservoirs

Glass coverslips, alumina plates and electrode constructs (see section 2.2.9) were placed in 24 well-plates, 6 well-plates and petri dishes, respectively to accommodate for different sizes. Samples were coated with mouse laminin (10 µg/ml in DMEM-F12) for 1 hour at 37 ^{o}C, 5% CO_2, laminin removed and surfaces washed once with DMEM-F12. The volume of cellular solution was determined by the size of the reservoirs on the electrode-array constructs, cells seeded at the required density and incubated at 37 ^{o}C, 5% CO_2 for 45 minutes to allow cells to adhere to the surface. Following cell attachment, media was added to each well and petri dish to cover the samples.

2.2.3 Immunocytochemical labelling

Cell immunostaining was performed in order to identify neurons and differentiated motor neurons. The following protocol was carried out in 25 cm^2 tissue culture flasks, coverslips, alumina plates and electrode array constructs.

After a defined period in culture, media was removed, cells briefly washed in HBSS, and fixed in 4% paraformaldehyde (PFA) made in PBS for 20 min at room temperature (RT). Following fixation, PFA was removed, cells washed 3x 5 min in PBS and permeabilised with 0.5% Triton-X for 15 min at room temperature (RT). Non-specific binding was blocked in 5% normal goat or horse serum diluted in PBS for 30 min at RT. The choice of blocking serum was matched to the species in which the secondary antibody was raised. Cells were then probed with primary antibody(s) at the appropriate dilution(s) in PBS at 4 ^{0}C overnight (see table 2.3). Apart from 25 cm^{2} tissue culture flasks, all other samples were stored in a humidified box during incubations. Primary antibodies were washed off x5 in PBS and cells incubated with secondary antibody(s) for 90 min at RT at the appropriate dilution(s), as seen on table 2.3. Cells were then washed x3 in PBS and counterstained with Hoechst 33258 (1 µg/ml), a nuclear marker, at a dilution of 1:1000 for 10 minutes at RT. Finally, samples were washed and stored in PBS ready for microscopy.

2.2.4 Delivery of SPC-01 differentiated cells

14-day differentiated SPC-01 cells were dissociated from tissue culture flasks and recovered by centrifugation as previously described. Following cell trypsinisation, the density of recovered cells was determined using a haemocytometer and cells resuspended in the appropriate volume of basal differentiation media to achieve a final cell density of 1x10^{8} cells/ml. To assess the needle-gauge effect on cell survival, 1 µl of cellular content was drawn up a 25-gauge Hamilton™ syringe, as used in *in vivo* studies (see section 2.2.5.1), and expelled onto laminin-coated coverslips contained within 24 well-plates. Cells were incubated at 37 ^{0}C, 5% CO_2 for 24 hours. For *in vivo* experiments cells were kept in a sterile Eppendorf tube at RT until ready for transplantation.

2.2.5 *In vivo* muscle denervation model

2.2.5.1 Surgery

All experimental procedures involving animals were conducted in accordance with the UK Animals (Scientific Procedures) Act (1986)/the European Communities Council Directives (86/609/EEC) and approved by the UCL Animal Welfare and Ethics Review Board. 3 adult male (200-220g) Sprague-Dawley rats were deeply anesthetised by inhalation of isoflurane and oxygen, and maintained under anaesthetic with a gas mask throughout surgery. During surgery animals were placed on a heated table set to 40^{0}C. Respiration was monitored throughout the procedure as an indication of depth of anaesthesia and the anaesthetic dose was adjusted accordingly. Lacri-lube eye ointment was applied to both eyes of the rat to prevent drying during the surgery. The skin over the left femur was shaved and a 3 cm lateral skin incision was made parallel to and approximately 5 mm dorsal to a straight line between the knee and hip joint, to reveal the intermuscular plane, which was then separated using blunt dissection to expose the sciatic nerve and its branches (i.e. tibial, common peroneal and sural nerves). Viewed with a Zeiss Stemi DV4 spot stereomicroscope the sciatic nerve and its branches were released from surrounding tissue and the tibial, common peroneal and sural nerves carefully separated. Using a 25-gauge Hamilton™ syringe, $1x10^5$ differentiated SPC-01 cells suspended in 1 µl of media were transplanted into the tibial nerve approximately 7 mm distal to the sciatic nerve trifurcation. Following cell transplantation, a 10/0 non-absorbable nylon suture was used as a ligature around the nerve 2-3 millimetres proximal to the injection site to prevent any leakage of cells from the distal nerve stump following transection (figure 2.3). In order to achieve complete muscle denervation, the tibial nerve was then transected a few millimetres proximal to the suture site and the proximal stump was reflected proximally and sutured to the biceps femoris muscle to prevent spontaneous reinnervation of the gastrocnemius muscle. Wounds were closed in layers using 2x 4/0 vicryl sutures to close the muscle then stainless steel wound clips to close the skin. 0.1 ml Rimadyl analgesic was administered sub-cutaneously to the injury site and veterinary wound powder placed over the sutured skin wound to reduce the risk of infection and the animal disrupting the wound.

During recovery animals were kept separately in a heated chamber and monitored closely until they had regained consciousness before being returned to their previous social group. Animals had free access to food and water after recovery from anaesthesia. All rats were kept in ventilated cages with room temperature maintained at 21 ± 0.5 ^{0}C and a lighting condition of 12 hour light/dark cycle. The weight of the animals was monitored throughout the experiment.

A sham intervention was carried out in one animal in which all experimental procedures were replicated and an equivalent volume of cell-free media delivered.

2.2.5.2 Microchannel electrodes for nerve stimulation

Microscope glass slides were used as a carrier for the samples. Slides were spin-coated with polystyrene sulfonic acid (PSS) at 2000 rpm for 10 sec and baked in an oven at 80° for 15 min. PSS is a release layer that allows detachment of the sample when placed in distilled water. A two part Polydimethylsiloxane (PDMS) (Sylgard 184) was used as a structural material and an insulator. PDMS preparation is discussed in more detail in section 2.2.9.3. A 12.5 µm thick stainless steel foil was cleaned with isopropyl alcohol and placed over the PDMS surface. An Nd:YAG laser was used to ablate the electrode design onto the stainless steel foil (ablation parameters described in table 2.9) and tweezers used to remove the excess foil. A second layer of PDMS was spin-coated onto the sample and cured as previously described. Laser ablation was used to expose solder pads and electrode sites (see table 2.9 for ablation parameters) and a 2 mm diameter PDMS channel was mounted above the electrode sites to create a microchannel. Finally, the channel was sealed with a PDMS sheet attached on top at one side and samples placed in distilled water to be detached from the microscope slide carrier.

2.2.5.3 In vivo electrophysiology

After 4 weeks animals were anaesthetised and the tibial nerve on the injury side exposed. Muscle reinnervation was assessed electrophysiologically (using a Sapphire 4ME system) by comparing the cell-transplanted nerve to the undamaged common peroneal nerve on the same side in each animal. Manufactured microchannel electrodes (see section 2.2.5.2) were connected to the electrophysiology system and placed around the nerve of interest. The uninjured common peroneal nerve was stimulated first in order to validate the manufactured stimulation electrodes. Functional reinnervation of muscle was assessed based on the protocol previously described by O'Rourke *et al*. (2018). Electrodes (Natus) were attached to the animal; a grounding electrode was placed onto the tail of the animal and a reference electrode was placed above the hip bone. A monopolar recording needle (Ambu®Neuroline concentric) was placed into the gastrocnemius muscle. Electrophysiological stimulation of the nerve was performed using a bipolar stimulation constant voltage configuration and muscle response recorded. Stimulation threshold was determined by increasing the stimulus amplitude in 0.1 V steps (200 µs pulses) until a reproducible, stimulus-correlated compound muscle action potential (CMAP) was recorded and a significant twitch of the animal's hind paw could be seen. The latency was measured from the time of stimulus to the first deviation from the baseline, and the amplitude of the CMAP was measured from baseline to the greatest peak. Immediately following electrophysiological analysis, animals were culled using terminal anaesthesia.

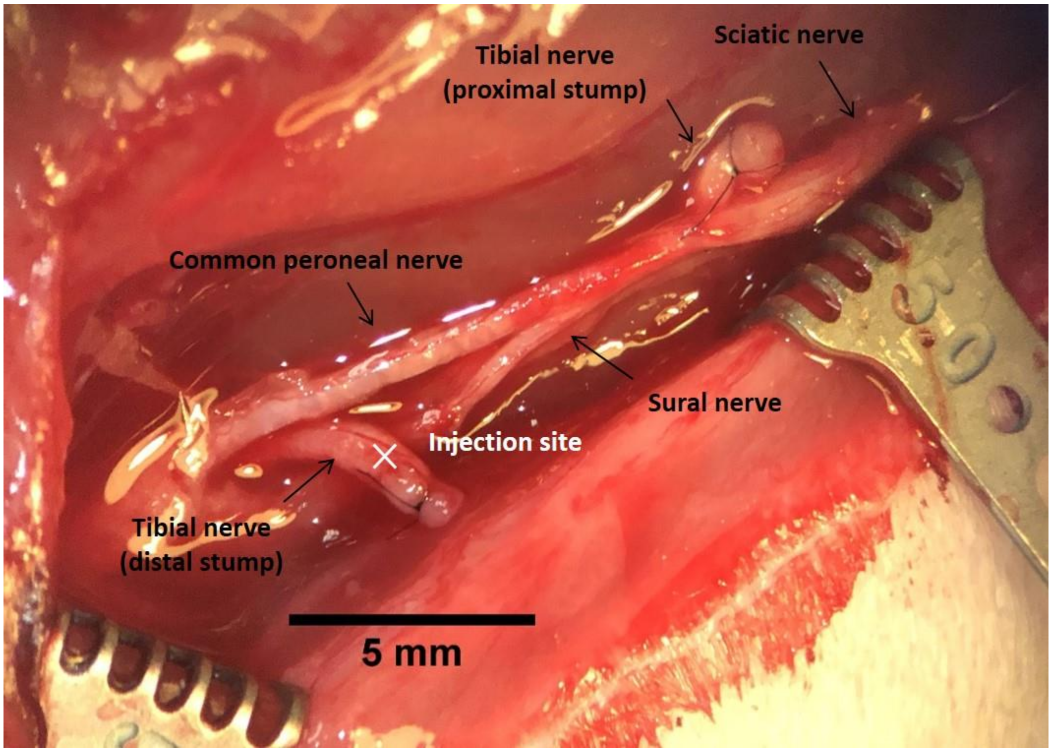

Figure 2.3 Tibial nerve transection and local delivery of cells
Image of tibial nerve transection depicting the distal tibial nerve stump, injection site where differentiated SPC-01 cells were delivered and the proximal tibial nerve stump ligated to an upstream muscle to avoid spontaneous reinnervation.

2.2.5.4 Nerve harvest

Transplanted nerves were excised under a dissecting microscope and stored in 4% PFA using a card frame to keep the nerve at the same length during fixation.

2.2.5.5 Cryo-sectioning

Following fixation by immersion in 4% PFA overnight at 4°C, the fixative was removed, samples washed in PBS and incubated in 30% sucrose in PBS overnight at 4°C. Immersion in a hypertonic sucrose solution removes water from the cells to ensure the morphology and cellular organisation of the tissue is preserved after freezing. Samples were then placed in rectangular plastic moulds and overlaid with FSC22 Frozen Section Compound in 30% Sucrose for 2 hours at RT before snap freezing in liquid nitrogen. The frozen block containing the tissue was removed from the mould and secured to the specimen holder with optimum cutting temperature (OCT) embedding matrix in the required orientation in the -25 ^{o}C cutting chamber of a Leica CM1900 Cryostat. 30 µm longitudinal sections were cut and collected on glass slides ready for immunostaining (refer to section 2.2.3.2). PBS was used to wash off any remaining OCT before staining samples.

2.2.5.6 Immunohistochemistry of tibial nerve transplanted with differentiated SPC-01 cells

Rat tissue samples (section 2.2.5) were stained in order to identify the transplanted SPC-01 differentiated cells and the host immune response elicited in response to the transplanted cells.

A PAP pen was used to draw a hydrophobic circle around the slide-mounted tissue in order to keep liquids pooled around the samples. A single PBS wash was performed before permeabilising and blocking the tissue sections in 10% goat or horse serum + 0.3% Triton-X diluted in PBS for 2 hours at RT. The choice of blocking serum was matched to the species in which the secondary antibody was raised. Following permeabilisation and blocking, the tissue sections were incubated with primary antibody(s) at the appropriate dilutions (refer to table 2.3) in 10% goat or horse serum in PBS and stored in a humidified box at 4 ^{o}C overnight. After incubation with primary antibody, slide-mounted tissue was washed 3x 15 min in PBS and incubated with secondary antibody(s) at the appropriate dilutions (refer to table 2.3) in 10% goat or horse serum in PBS for 2 hours at RT. Samples were washed 3x 15 min in PBS and counterstained with Hoechst 33258 (1 µg/ml) at a dilution of 1:1000 for 10 min at RT. Finally, a single PBS wash was performed and sections mounted using Vectashield HardSet mounting medium ready for microscopy.

2.2.5.7 Assessment of SPC-01 transplanted cells and host immune response in vivo

Confocal microscopy (Zeiss LSM 710) was used to capture images from immunostained longitudinal sections. Three field of view (proximal, middle and distal) were sampled using a x20 lens. Image analysis was conducted using ImageJ software to count number of CD8 and CD4 positive cells.

2.2.6 Preparation of alginate protective hydrogels

Alginate hydrogels were made to cover cell-seeding reservoirs of implantable devices in order to protect transplanted differentiated SPCs from the host immune response.

Two types of alginate were used to manufacture the hydrogels; alginate acid sodium salt (Sigma-Aldrich) and Novamatrix alginate 1.5% (w/v). The alginate acid sodium salt was diluted in DMEM:F12 media to make up a 2 % (w/v) stock concentration, which was then further diluted in DMEM:F12 to achieve 1% (w/v) and 1.5% (w/v) concentrations. The Novamatrix alginate was used at the 1.5% (w/v) stock concentration and diluted in DMEM:F12 to achieve a 1% (w/v) concentration. Gels were manufactured in 24-well plates using transwells with 0.1 µm ϕ pore size. 1ml of 102 mM $CaCl_2$/DI H_20 was aliquoted in each well to cross-link 100 µl of alginate expelled into each transwell, gels were allowed to set at 37 ^{o}C, 5% CO_2 for an hour and washed 3x in DMEM:F12 to remove any $CaCl_2$ before experimental use.

2.2.7 Cell metabolic activity

Cell metabolic assays were performed using the CellTiter-Glo® Luminescent Cell Viability Assay (Promega G7572) and the RealTime-Glo™ MT Cell Viability Assay (Promega G9711).

2.2.7.1 CellTiter-Glo assay

100 ml of CellTiter-Glo® Buffer was added to the CellTiter-Glo® Substrate to reconstitute the lyophilised enzyme/substrate mixture. The resulting CellTiter-Glo® Reagent was aliquoted and stored at -20 ^{o}C until ready to use.

Cells were seeded in 96-well plates freshly coated with mouse laminin (10 µg/ml in DMEM-F12) for one hour and incubated at 37°C, 5% CO_2 for different time points. Once ready to be analysed, well plates and CellTiter-Glo® Reagent were equilibrated at RT for 30 minutes. A volume of CellTiter-Glo® Reagent equal to the volume of cell medium was added to each well, mixed for 2 minutes in an orbital shaker to induce cell lysis and incubated at RT for 10 minutes to stabilise the luminescent signal. The contents of each well were transferred to a white opaque-walled 96-well plate to record luminescence.

2.2.7.2 RealTime-Glo assay

Cells were seeded in sterile white opaque-walled 96-well plates freshly coated with mouse laminin (10 µg/ml in DMEM-F12) for one hour. Laminin was washed off in DMEM-F12 and cells seeded at a range of densities to determine optimal culture density for a 72-hour assay.

Once optimal cell-seeding density was determined, the assay was run to test cell viability in the presence of acellular alginate hydrogels of different concentrations.

Cells were seeded at a density of $5x10^3$ under the conditions previously described and incubated at 37 ^{o}C, 5% CO_2 for 30 minutes to allow the cells to attach to the bottom of the well. Culture medium, MT Cell Viability Substrate and NanoLuc® Enzyme were equilibrated to 37 ^{o}C before use. The reagents were diluted in culture medium to achieve a concentration of 2X and an amount of culture medium containing 2X RealTime-Glo™ reagents equal to the volume of cell suspension added to each well. 96-well plates were incubated at 37 ^{o}C, 5% CO_2 for one hour before the first luminescence reading to ensure sufficient penetration of RealTime-Glo reagents to yield a strong signal above background. Following the first luminescence reading, alginate hydrogels were placed inside wells and monitored every 24 hours over a period of 72 hours to track changes in metabolic activity. To obtain readings from wells containing hydrogels, the hydrogel was removed using a spatula and placed in a 24-well plate in basal differentiation media at 37 ^{o}C, 5% $CO_{2.}$ Once luminescence was recorded, hydrogels were returned to their corresponding wells. Plates were returned to the cell culture incubator between readings to maintain a consistent temperature at each measurement.

For both assays, luminescence was recorded using a microplate reader (Synergy HTX, BioTek) controlled by Gen 5 3.03 software (BioTek). Wells containing culture medium without cells were used as controls to obtain values for background luminescence.

2.2.8 Scanning electron microscopy

The interface between alumina plates and Pt/Au electrode arrays was characterised using scanning electron microscopy (SEM). Electrode array samples were coated with an EPOXY resin in order to preserve the screen printed electrodes before transverse sections were made with a diamond blade cutter.

Samples were mounted onto aluminium SEM stubs and coated with a thin layer (20 nm) of gold using Quorum Q150T Sputter Coater (Quorum Technologies Ltd, UK) in an argon atmosphere. Subsequently, the materials were imaged with a field emission scanning electron microscope (FEI Quanta 200F, FEI, USA), at an accelerating voltage of 5 kV 2.2.9 Electrode array designs.

All electrode array patterns were designed using LibreCAD software with pragmatically selected electrode size and geometry. An initial basic prototype was designed for *in vitro* experiments and optimised throughout this project to design an electrode array with dimensions suitable for implantation. For the purposes of this thesis, microelectrode arrays are defined as interconnected electrodes belonging to the same metal layer where at least one of the surface dimensions of individual electrodes is ≤ 500 µm.

2.2.9.1 Microchannel electrode array

The microchannel electrode array design is based on previous literature reporting neurite extension and cell alignment in microfluidic chambers and microchannel structures (Mahoney *et al*., 2005, Mobasseri *et al*., 2014, Honegger *et al*., 2016a). Each construct consists of 3 open reservoirs for seeding cells. At one end of the reservoirs, 2 electrode sites are exposed to electrically stimulate cells and at the opposite end of reservoirs, microchannels provide physical cues to guide developing neurites across recording electrodes organised in a tripolar configuration. Optical micrographs of the microchannel-electrode array are shown in figure 2.4A and the parameters of this design are summarised in table 2.4.

Table 2.4 Summary of microchannel electrode array parameters

This table shows the dimensions of the microchannel electrode array.

Parameters	Values (width x length)
Construct	25.4 x 25.4 mm
Electrode array size	15.01 x 16.16 mm
Stimulation electrode site	50 x 200 µm
Recording electrode site	50 x 30 µm
Solder pads dimensions	2 x 1.44 mm
Track width	50 µm
Reservoir area	4.91 mm^2
Top microchannel	30 µm x 700 µm
Middle microchannel	30 µm x 500 µm
Bottom microchannel	30 µm x 300 µm

2.2.9.2 Optimised design for *in vitro* experiments

In order to guide neurite extension down the channel and towards the end of the construct, microgrooves were laser-ablated on the surface of the cell seeding reservoir. Each construct consist of one open reservoir for seeding cells with 3 electrodes sites equally spaced across the reservoir to provide stimulus pulses to cell bodies. At the opposite end of the reservoir a channel guides cells towards the end of the construct. Optical micrographs of the optimised design for *in vitro* experiments are shown in figure 2.4B and the parameters of this design are summarised in table 2.5.

Table 2.5 Summary of optimised electrode array design for *in vitro* experiments parameters

This table shows the dimensions of the optimised electrode array design for *in vitro* experiments.

Parameters	Values (width x length)
Construct	25.4 x 25.4 mm
Electrode array size	7.71 x 15.89 mm
Electrode site	1 x 250 µm
Solder pads dimensions	3.4 x 1.4 mm
Tracks width	200 µm
Reservoir area	7.07 mm^2
Channel	1 x 1.58 mm
Microgroove width	30 µm

2.2.9.3 Implantable device prototype

A scaled down version of the previous optimised *in vitro* construct was designed with suitable dimensions for *in vivo* implantation. Taking into consideration space limitations and the diameter of rat sciatic nerve branches (≤ 1 mm diameter), the device was designed to be 2 mm in diameter. Corners were coated in silicone to avoid sharp endings. Optical micrographs of the implantable device prototype are shown in figure 2.4C and the parameters of this design are summarised in table 2.6.

Table 2.6 Summary of implantable device prototype parameters

This table shows the dimensions of the implantable device prototype.

Parameters	Values (mm) (width x length)
Construct	2 x 3.83 mm
Electrode array size	1.2 x 3.22 mm
Outer Electrode	400 X 150 µm
Inner electrode	150 x 200 µm
Pt/Au pad dimensions	360 x 490 µm
Tracks width	200 µm
Reservoir area	0.43 mm^2
Stainless steel connectors holes	70 µm
Stainless steel pads dimensions	1.02 x 1.02 mm

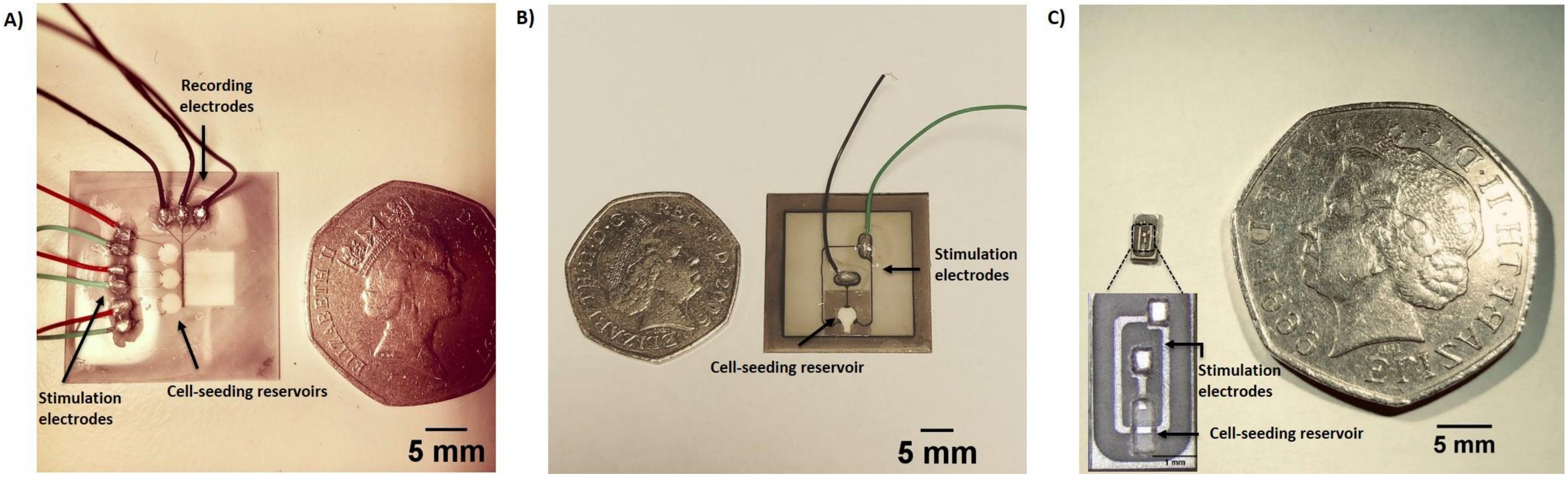
A)
Recording electrodes
Stimulation electrodes
Cell-seeding reservoirs
5 mm
B)
Stimulation electrodes
Cell-seeding reservoir
5 mm
C)
Stimulation electrodes
Cell-seeding reservoir
1 mm
5 mm

Figure 2.4 Micrographs of electrode arrays

This figure shows images of the three designs of electrode arrays used in this project. A) Microchannel electrode array, B) Optimised design for in vitro experiments and C) Implantable device prototype. Electrodes and cell-seeding reservoirs are labelled. Scale bar = 5 µm. Inset of zoomed in implantable device shown (scale bar = 1 µm).

2.2.10 Manufacturing of electrode arrays

The electrode array fabrication process was performed in multiple stages (figure 2.5). These are broadly summarised as:

- Thick film screen printing
- Polydimethylsiloxane (PDMS) coating
- Soldering and wire bonding

All stages of the manufacturing process were performed in an IO 6 class cleanroom (class 1000 equivalent) where particle count, temperature, humidity and vibration are all controlled. These conditions limit traces of dust and contaminants during the microfabrication process ensuring reliable and repeatable processing.

The electrode sites, tracks, and connectors are composed of a single layer of platinum/gold (Pt/Au) alloy screen-printed on an alumina ceramic substrate (Rubalit, 708S, 96% Aluminium Oxide, CeramTec). Different silicone rubbers (see table 2.7) were used as a structural material and insulator.

2.2.10.1 Thick film screen printing

Alumina substrates were cleaned in an ultrasonic bath before screen printing to remove any contaminants from the surface. Samples were placed in glass beakers inside the ultrasound bath and cleaned in aqueous solution of 25 % w/v Na_3PO_4 and 5% w/v detergent (Teepol-L, Teepol) for 5 minutes. Samples were then washed in deionised water 3 times for 5 minutes, and finally rinsed in isopropyl alcohol (IPA) for 5 minutes. Alumina substrates were air dried at RT. All electrode array designs were manufactured using a screen printing machine (model 1202, DEK) and a screen bearing an open stainless steel mesh designed with equal dimensions to the alumina substrate (1” x 1” square). The open mesh contained apertures of 200 µm oriented at a 45 ^{o} angle. Alumina samples were held on a vacuum chuck and the screen fitted inside the machine. The screen was lowered to approximately 550 µm away from the sample. This distance was chosen to match the thickness of the sample onto which ink was being transferred. To test this distance an alumina substrate was briefly fitted between the screen and the sample and the screen adjusted on the Z plane accordingly. Once the Z position of the screen was established, the screen was adjusted on the X and Y planes to align the mesh with the alumina substrate. Using a teflon rod, a small amount of Pt/Au conductor paste (5837-G, ESL) was spread below the open mesh covering the diameter of the mesh. A squeegee was fitted in the machine and placed at the opposite end of the screen. A double print was carried out with the squeegee. During the first stroke the squeegee fills the open mesh aperture with Pt/Au paste and during the second stroke the paste makes contact with the alumina substrate causing the ink to wet the substrate and be pulled out of the mesh apertures as the screen moves back to its initial position once the squeegee has passed. Screen-printed samples were allowed to level by resting at RT for 15 minutes, the paste was dried in an oven at 125°C for 15 minutes, and sintered in a thick-film belt furnace (model 840, DEK) at peak temperatures of 850°C for 10 minutes with 1 hour ramp up and 1 hour ramp down. During sintering organic carrier compounds in the paste are removed by oxidation. The remaining glass and metal particles undergo sintering: atomic diffusion in particles of the same material in contact cause necks to form between particles and total surface area to reduce. Sintering of metal particles create an electrically conductive path, while sintering of glass particles adheres the paste to the alumina substrate.

2.2.10.2 Microchannel electrode array

Microchannel electrode arrays were manufactured via two different mechanisms. The electrode array was either screen printed onto alumina substrates previously modified with a laser (herein referred to as laser-structured alumina manufacturing process) or the electrode array pattern was laser-ablated onto screen-printed, sintered alumina substrates (herein referred to as unmodified alumina manufacturing process).

2.2.10.3.Laser-structured alumina manufacturing process

The rationale behind this manufacturing process was to create a flush surface for cells to grow atop and minimise any potential effects protruding Pt/Au structures could have on neurite outgrowth and cell behaviour.

A preliminary experiment in which grooves of varying depth and width were laser-ablated onto alumina substrates was performed to establish the optimal electrode array dimensions to ensure robust and reproducible printing of Pt/Au paste onto grooves. Grooves of 1 mm length and different width were designed on LibreCAD software and laser-ablated onto alumina substrates. Different number of laser passes were used to create grooves of different depth (see table 2.8 for details on laser parameters). Samples were screen printed as previously described and the paste located outside the grooves was removed by the manual passage of a squeegee across the alumina substrate. Samples were imaged under a light microscope, analysed on ImageJ and the optimal dimensions for robust screen printing of grooves determined (refer to section 2.2.11.6 for details on the analysis method).

Microchannel electrode array patterns were transferred onto alumina substrates using a laser (Nd-YAG, Laservall Violino 2, Laservall) controlled by Laservall Smartist 4.1 software on Windows PC.

Alumina samples were rinsed in deionized water using an ultrasonic cleaner to remove any particles left behind by the laser ablation process and samples air dried at RT. Once dried, Pt/Au paste was screen printed onto substrates and the paste outside the electrode array pattern removed manually by the passage of a squeegee in a 45° orientation with respect to (w.r.t) the long dimension of the test structures. Screen-printed samples were allowed to level at RT for 15 minutes, the Pt/Au paste dried in an oven at 125°C for 15 minutes and fired at 850°C as previously described (see section 2.2.9.1) (refer to figure 2.5A for a diagram of the manufacturing process).

Due to issues with paste detachment from the laser-ablated electrode array patterns in the final stages of the manufacturing process, the protocol was adjusted by drying the paste at 50°C overnight to improve paste adherence onto the alumina cavities and placing the samples under vacuum prior to the levelling step in order to rupture any entrapped bubbles generated during the screen printing process.

2.2.10.4 Unmodified alumina manufacturing process

The rationale behind this manufacturing process was to compare the robustness and reproducibility of thick-film screen printed electrodes with that achieved by the laser-structured alumina manufacturing process. This manufacturing process was implemented to produce the optimised electrode arrays for *in vitro* experiments and the implantable device prototype.

Alumina substrates were cleaned and screen-printed as previously described (refer to section 2.2.9.1 Thick-film screen printing). Once sintered, the desired electrode array pattern was laser-ablated onto samples (see table 2.9 for details of laser ablation parameters) (refer to figure 2.5B for a diagram of the manufacturing process). Figure 2.6 depict laser ablation parameters.

2.2.10.5 PDMS coating - Insulation of metal tracks

Insulation of Pt/Au tracks was achieved by spin coating a single layer of Polydimethylsiloxane (PDMS, silicone rubber) on top of screen-printed samples. The silicone rubbers used for each electrode array prototype are summarised in table 2.7. Once the metal layer was sintered, electrode arrays cleaned with IPA in ultrasonic bath for 5 min to remove any debris generated by the laser-ablation process. Silicone rubbers were prepared in a syringe by mixing base and curing agents at the appropriate ratios (refer to table 2.7). Additionally, 1:44 ratio black pigment (Med-4800-2, Polymer Systems Technology Limited) was added to the clear mix in order to make the silicone opaque to the laser light thus, improving visualisation when laser-cutting the silicone layer to expose areas of interest. The syringe was placed in a Speedmixer (Dual Asymmetric Centrifugal Laboratory Mixer System, DAC 150 FVZ-K, Synergy Devices Ltd) and the silicone mixed at 2500 rpm for 3 minutes or until a homogenous mixture was achieved. Screen-printed alumina substrates were placed in a custom polytetrafluoroethylene (PTFE) holder inside a WS-400E-NPP-Lite spin coater (Laurell Technologies). Silicone was dispensed on the middle of the sample and spin coated using different parameters to achieve different thickness. Samples were removed from the spin coater and heat cured (refer to table 2.7 for details of curing times and temperatures). Finally, silicone was laser-ablated to expose electrode sites and cell-seeding reservoirs (refer to table 9 for details of laser ablation parameters). The electrode array manufacturing process is summarised in figure 2.5. A diagram to explain different laser ablation parameters is presented in figure 2.6.

2.2.10.6 PDMS coating - Structural support for cell-seeding reservoir

To optimise the initial microchannel electrode array design, a layer of Sylgard 184 silicone was added around the cell–seeding reservoir areas of the optimised design for *in vitro* experiments. This structural layer of silicone was used to contain the cell suspension within the reservoir area of the device.

The silicone mix was prepared as previously described. Standard glass microscope slides (75 mm × 25 mm, 1 mm thick) were used as carriers for the structural support layer manufacture. First, microscope slides were plasma treated in a radio-frequency plasma chemistry unit (Zepto low cost plasma laboratory unit, Diener electronic) to achieve a hydrophilic surface. Slides were placed inside the unit and subjected to air (O_2) plasma for 2 min at 2 mbar using a forward and reflective power of 50W and 10W, respectively. Samples were removed from the plasma chemistry unit and spin coated with a release layer of polystyrene sulfonic acid (PSS, 561223 Sigma, UK) at 2000 rpm for 10 seconds, then baked at 80 ^{o}C for 15 minutes. Silicone was then spin coated on slides at 500 rpm for 45 seconds and cured in an oven at 85 ^{o}C for 30 minutes (refer to table 2.7 for details on silicone used). Finally samples were laser-ablated (see table 2.9 for details of laser ablation parameters) with the desired pattern and glass slides placed in distilled water to allow swelling and dissolution of the PSS layer, thus facilitating the removal of the structural support silicone layer from the carrier slides.

Table 2.7 Silicone rubbers used for the manufacturing of electrode arrays

This table shows the silicone type, components, mix ratio, spin coating parameters, curing parameters and application for each silicone elastomer used in this project.

Silicone type	Components	Mix ratio	Spin coating parameters		Curing parameters		Application
			Speed (rpm)	Time (seconds)	Temperature (^{o})	Time	
Sylgard 184	Base/Curing agent	10:1	1000	40	85	30 min	Insulation of electrode array tracks for *in vitro* experiments designs
			500	45			Provide structural support to cell-seeding reservoir
MED-6015	Part A/ Part B		1000	40	150	15 min	Insulation of electrode array tracks for implantable device prototype
Sylgard 3140	One part	N/A	N/A	N/A	RT	24 hrs	Solder joint insulation
							Stainless steel insulation of implantable device prototype
							Cover sharp corners of implantable device prototype

Table 2.8 Parameters used to laser-ablate grooves of different dimensions

This table shows the number of laser passes and their corresponding depth in microns ablated from alumina samples to create grooves of different dimensions.

Number of passes per groove	Approximate depth (μm)
Grooves of 1,10,30,50,70 and 100 μm width	
3	7.2
5	12.0
7	16.8
8	19.2
9	21.6
11	26.4
15	36.0
20	48.0

Table 2.9 Laser parameters. This table shows the materials laser ablated, power, frequency, speed, number of laser passes, if the material was hatched, the ablation angle, ablation type, spacing between each laser cut and application for the three electrode array designs manufactured in this project.

Microchannel electrode array									
Material	**Power (%)**	**Frequency (kHz)**	**Speed (mm/seconds)**	**Number of passes**	**Hatching (Yes/No)**	**Ablation angle (°)**	**Ablation type**	**Spacing (µm)**	**Application**
Alumina	90	10	200	20	Yes	0	Single line Bidirectional	10	Create electrode array design before screen printing Pt/Au (laser structured alumina manufacturing process)
Sylgard 184 silicone	90	10	200	1	Yes	0	Single line Bidirectional	10	Remove silicone layer to expose areas of interest
Sintered Pt/Au	50	60	120	8	Yes	0	Single line Bidirectional	10	Ablate electrode array pattern on Pt/Au screen printed alumina (unmodified alumina manufacturing process)

Optimised design for in vitro experiments

Material	Power (%)	Frequency (kHz)	Speed (mm/seconds)	Number of passes	Hatching (Yes/No)	Ablation angle (^{o})	Ablation type	Spacing (µm)	Application
Sintered Pt/Au	90	10	200	6	Yes	90	Single line Bidirectional	10	Ablate electrode array pattern on Pt/Au screen printed alumina (unmodified alumina manufacturing process)
Alumina	90	10	200	6	No	N/A	N/A	N/A	Ablate microgrooves on cell-seeding reservoir
Sylgard 184 silicone	40	10	30	18	No	N/A	N/A	N/A	Remove silicone layer to expose cell-seeding reservoir
	40	10	30	8	No	N/A	N/A	N/A	Remove silicone layer to expose electrode sites and solder pads
	40	10	30	70	No	N/A	N/A	N/A	Ablate silicone layer used to provide structural support for cell-seeding reservoir

Implantable device prototype

Material	Power (%)	Frequency (kHz)	Speed (mm/seconds)	Number of passes	Hatching (Yes/No)	Ablation angle (^{o})	Ablation type	Spacing (µm)	Application
Sintered Pt/Au	90	10	200	6	Yes	90	Single line Bidirectional	10	Ablate electrode array pattern on Pt/Au screen printed alumina (unmodified alumina manufacturing process)
MED 6015 Silicone	40	10	200	18	No	N/A	N/A	N/A	Remove silicone layer to expose cell-seeding reservoir
		10	200	8	No	N/A	N/A	N/A	Remove silicone layer to expose electrode sites and solder pads
Alumina	90	10	200	225	Yes	45	Cross lines Bidirectional	10	Snap alumina substrate to separate individual samples
Stainless Steel	40	10	2.1	1	No	N/A	N/A	N/A	Stainless steel point of contact with Pt/Au solder pads

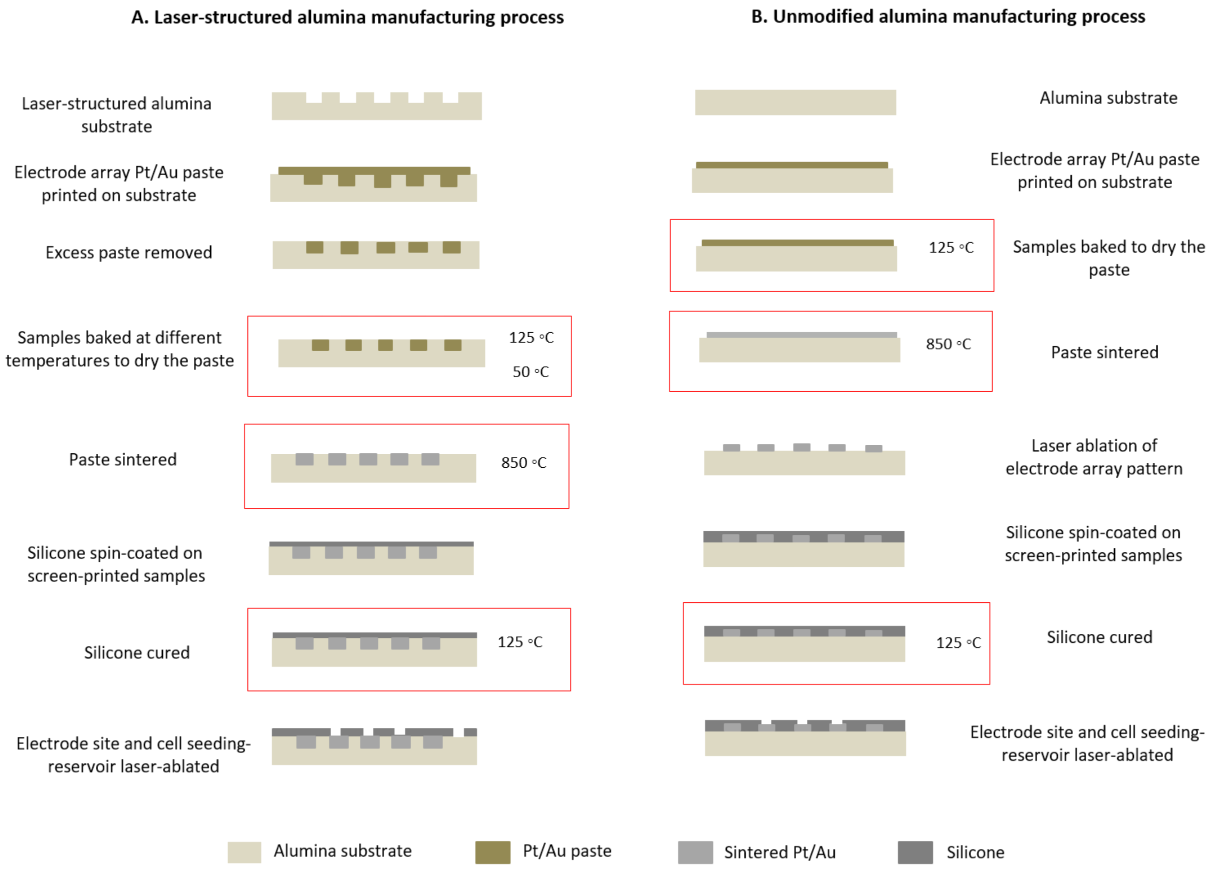
A. Laser-structured alumina manufacturing process
B. Unmodified alumina manufacturing process
Laser-structured alumina substrate
Electrode array Pt/Au paste printed on substrate
Excess paste removed
Samples baked at different temperatures to dry the paste
125 °C
50 °C
Paste sintered
850 °C
Silicone spin-coated on screen-printed samples
Silicone cured
125 °C
Electrode site and cell seeding-reservoir laser-ablated
Alumina substrate
Electrode array Pt/Au paste printed on substrate
125 °C
Samples baked to dry the paste
850 °C
Paste sintered
Laser ablation of electrode array pattern
Silicone spin-coated on screen-printed samples
125 °C
Silicone cured
Electrode site and cell seeding-reservoir laser-ablated
Alumina substrate
Pt/Au paste
Sintered Pt/Au
Silicone

Figure 2.5 Manufacturing process of electrode arrays

A) Laser-structured alumina manufacturing process. Method implemented to manufacture the microchannel electrode array design. B) Unmodified alumina manufacturing process. Method implemented to manufacture the optimised electrode array for *in vitro* experiments and implantable device prototype designs.

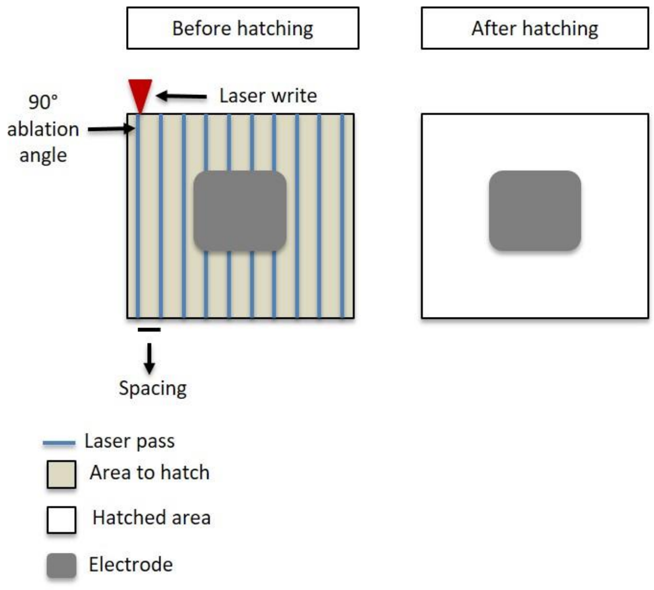

Figure 2.6 Laser ablation parameters

The diagram illustrates laser hatching, a type of laser ablation whereby parallel laser cuts (passes) are used to ablate a desired area. The spacing between each laser pass, angle at which the laser ablates the sample and the type of ablation (unidirectional, bidirectional, cross-lines or single lines) are all parameters that can be customised.

2.2.10.7 Electrical connections to solder pads

When passing of electrical current through the electrode arrays was required, soldering was implemented to connect soldered pads to copper wires. Due to the small dimensions of solder pads on the implantable device prototype, wire bonding was performed to connect the small pads on the device to larger external pads, which were then soldered to copper wires.

2.2.10.8 Soldering

Samples were placed on a mini hot plate at 121 ^{0}C. Using a soldering iron, solder was used to connect insulated tinned copper wires to solder pads. Samples were thoroughly cleaned in an ultrasonic bath, as previously described, to remove flux residues generated during the process. A one part silicone rubber (see table 2.7) was manually applied to insulate soldered pads and left to cure under pressure in a humidified chamber for 24 hours. Finally, samples were leached in ethanol for 48 hours to remove any uncured silicone and ready to be used for electrochemical testing or cell culture experiments.

2.2.10.9 Bump bonding

The Kulicke & Soffa (K&S) Model 4524 Manual Gold Ball Bonder was used to connect solder pads on the implantable device prototype to external stainless steel pads. This thermosonic machine operates by applying heat, pressure and ultrasonic forces to generate gold bonds. To improve bonding of Au onto Pt/Au pads, electrode arrays were polished using a fibreglass brush. Samples were clamped on a heated workholder set at 130°C and solder pads manually positioned under the bonding head as observed under the integrated microscope. The machine was operated on the bumping mode for the first bond and second bond. Once the sample was set in the right position, a semi-manual micromanipulator was used to bring the capillary down a few millimetres away from the bonding pad. The search function was finely adjusted to further lower the capillary to approximately 100 µm vertical distance from the bonding surface as observed through the overhead microscope. A ball bump was formed on the pad with the following bonding using the parameters shown in table 2.10. The stainless steel interconnects were carefully aligned on top of the first bond and the same process repeated to generate a second bond immediately above the first bond. A diagram of the bonding head piece and gold bonds used to connect stainless steel pads to the implantable device prototype are shown in figure 2.7.

Table 2.10 Parameters used for Au bump bonding onto Pt/Au pads of implantable device prototype

The table shows the power, time force and ball size used for the first and second bonds.

Bump bond	Power	Time	Force	Ball size
First	4.5	5	4	4.8
Second	2.5	5	2	4.8

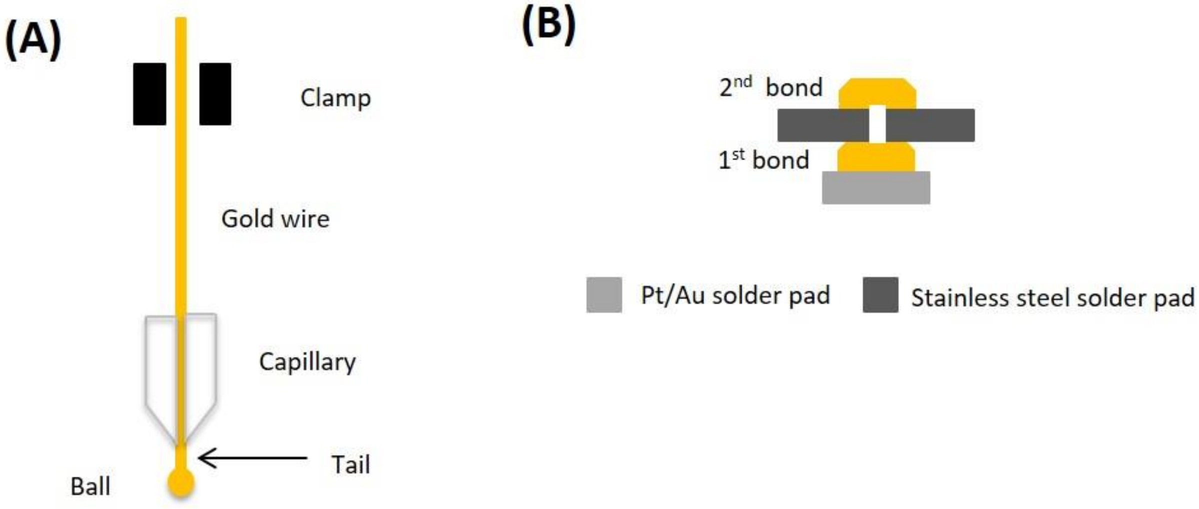

Figure 2.7 Wire bonding stainless steel solder pads onto implantable device prototype
A) Bonding head piece showing the clamp used to secure the gold wire in place and a capillary through which a gold wire is fed and used to apply pressure onto the bonding surface. B) First, a gold bump bond is created on the Pt/Au pads of the implantable device prototype, the point of contact on the stainless steel pads is carefully aligned over the first bond and a second gold bump bond is created on atop the stainless steel metal foil securing it to the implantable device prototype.

2.2.11 Electrode array characterisation

2.2.11.1 Surface Topography

The interface between alumina plates and Pt/Au electrode arrays was characterised using scanning electron microscopy (SEM). Electrode array samples were coated with an EPOXY resin in order to preserve the screen printed electrodes before transverse sections were made with a diamond blade cutter. Samples were mounted on aluminium SEM stubs with double-sided carbon sticky tabs (Agar Scientific, UK), spur coated with gold/palladium (Polaron E5000, Quorum Technology, UK) and examined in a JEOL 5410LV scanning electron microscope (JEOL, UK) operating at 15 kV.

2.2.11.2 Electrochemical analysis: Electrical Impedance Spectroscopy (EIS) and Cyclic Voltammetry (CV)

Electrode arrays were placed in plastic wells filled with phosphate buffered saline (PBS) to simulate the physiological environment. The solution was purged with nitrogen gas (N_2) in order to remove dissolved oxygen form the testing environment and the system was allowed to settle for 30 minutes before testing. The experimental setup was composed of three electrodes; the reference electrode, the counter electrode and the working electrode (see figure 2.8). A saturated silver/silver chloride (Ag/AgCl) or calomel electrode was used as reference, a 1 cm^2 platinum electrode as a counter electrode and individual Pt/Au electrodes from the array as the working electrode. All three electrodes were connected to a ModulabXM Potentiostat (Solartron Analytical, USA) and measurements recorded using ModulabXM ECS software (version 2.2.x, Solartron Analytical). This setup and instruments were used for electrical impedance spectroscopy and cyclic voltammetry measurements described below

2.2.11.3 Electrical Impedance Spectroscopy (EIS)

Impedance of Pt/Au electrodes was measured by sweeping a sinusoidal voltage of 50 mV peak-peak at different frequencies, ranging from 20 Hz to 100 kHz.

2.2.11.4 Cyclic Voltammetry (CV)

CV characterisation was performed at a scan rate of 50mV sec^{-1} for a total of 30 cycles. Voltage limits of -0.6V to +0.8V w.r.t Ag/AgCl or calomel reference electrode were chosen as these are commonly considered to be the 'water window' of platinum in a neutral buffer solution (Cogan, 2008).

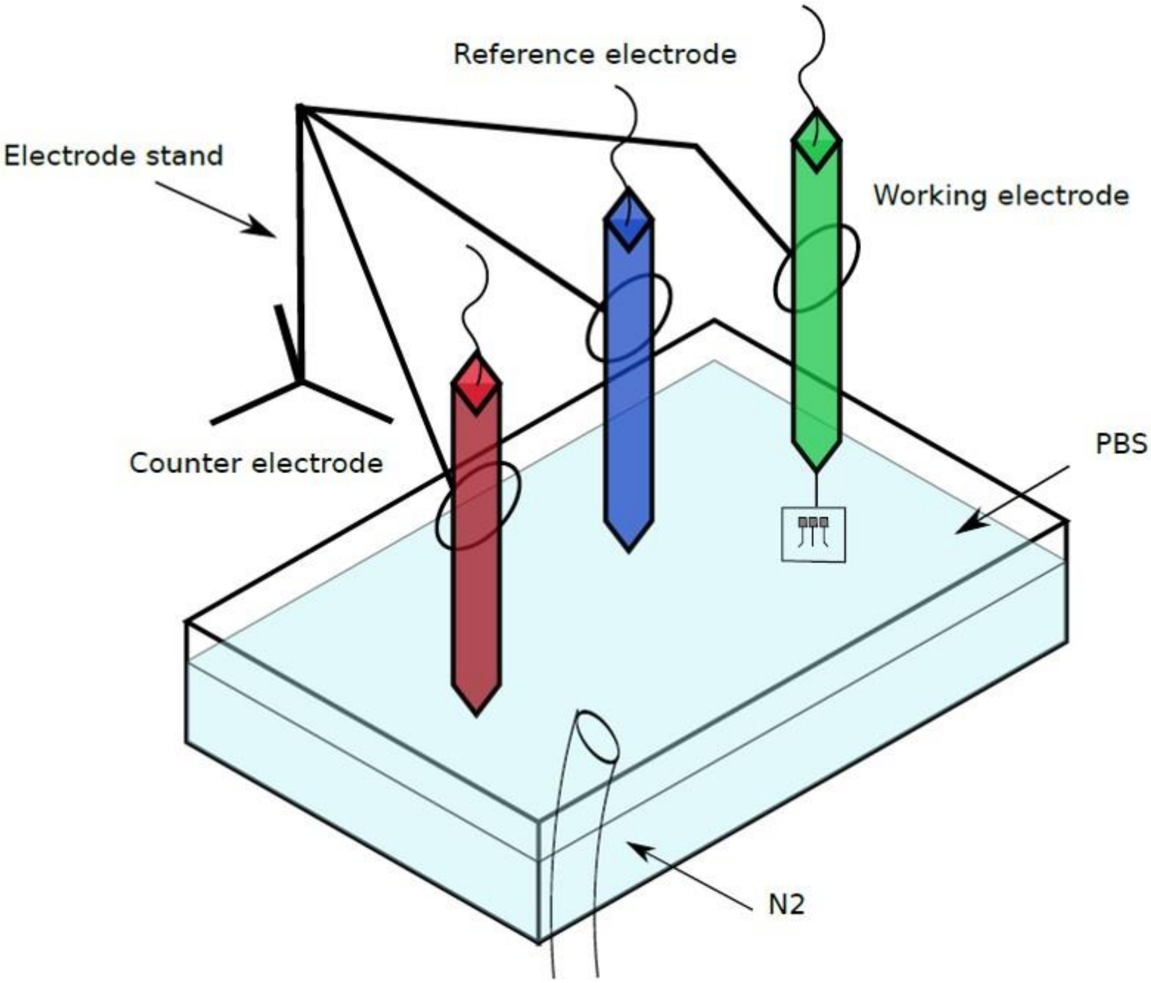

Figure 2.8 Setup for electrochemical characterisation of electrode arrays

This diagram shows the three electrodes used to perform EIS and CV on the manufactured electrode arrays. A plastic well was filled with PBS and purged with N_2 where 3 electrodes were immersed. A 1 cm^2 platinum electrode (counter electrode; red), a saturated Ag/AgCl electrode (reference electrode; blue) and the manufactured electrode array in which each electrode was tested individually (working electrode; green).

2.2.12 Analyses

2.2.12.1 Cell differentiation analysis

Fluorescence microscopy (Leica DM IRB) was used to capture images from immunostained cells. Equivalent fields between flasks were analysed using a standardised sampling protocol (figure 2.9A). Images were captured using a x20 lens and ImageJ was used to count the total number of cells, number of βIII-Tubulin positive cells and number of Isl1 positive cells per field of view.

2.2.12.2 Cell death quantification

Live/dead analysis was performed using propidium iodide (PI) exclusion and Syto-9 as a counter stain to establish the number of live cells. PI is commonly used as a marker of cell death as it only penetrates cells with damaged plasma membranes as a result of late apoptotic and necrotic death. Dead cells can be identified by their condensed, bright red PI-stained nuclei. Syto-9, is a cell permeant dye that exhibits bright green fluorescence upon binding to nucleic acids of live cells. Cells were incubated with PI (20 µg/ml) and Syto-9 (5 mM) both used at 1:1000 dilution in cell culture media for 10 minutes at 37°C, 5% CO_2. Equivalent fields were analysed per sample using a standardised sampling protocol (figure 2.9B)

2.2.12.3 Neurite extension and cell proliferation analyses

Fluorescence microscopy was used in the assessment of cell proliferation and neurite outgrowth. Equivalent fields were analysed on cover slips and electrode array samples using a standardised sampling protocol (figure 2.8B). Images were captured using a 20X lens with a (Zeiss Axiolab A1, Axiocam Cm1). Using ImageJ software, the number of cells (Hoechst stained nuclei) and length of individual neurites (βIII-tubulin stained processes) measured in each field (figure 2.10).

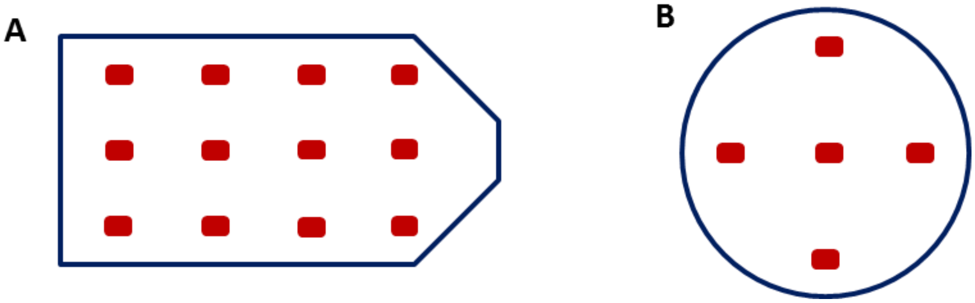

Figure 2.9 Standardised sampling protocols to analyse cell differentiation, cell death and neurite extension using ImageJ

Sampled fields of 25 cm^2 tissue culture flasks looking down at the surface on which SPC-01 cells were differentiated (A); sampled fields of coverslips, alumina plates and reservoirs on electrode arrays on which cells were seeded (B).

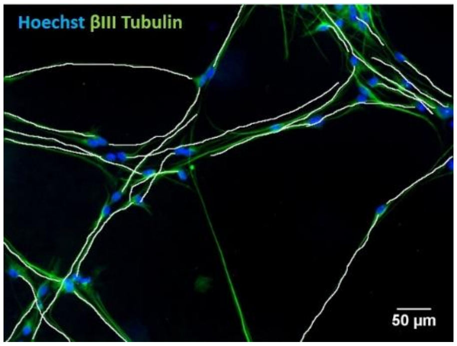

Figure 2.10 Neurite measurement in cell culture
Samples were stained to detect βIII-Tubulin (green) and Hoechst (blue) in order to identify neurons. Neurites were traced (white lines) and length measured on ImageJ software. For the purposes of these experiments, neurites were defined as any projection extending from the cell body, longer in length than the diameter of the cell body. Representative image of differentiated SPC-01 cells cultured on alumina substrate. Scale bar 0 = 50 µm.

2.2.12.4 Screen printing of laser-ablated grooves analysis

Optical micrographs of samples were analysed to determine optimal groove dimensions required to completely fill laser-ablated patterns with Pt/Au paste. Micrographs were converted into binary images (black and white) and intensity was measured. A threshold was set and applied to all images. A value of 255 was assigned to black pixels corresponding to Pt/Au paste and a value of 0 to white pixels corresponding to the unfilled alumina substrate background.

2.2.12.5 EIS analysis

Graph Pad software was used to generate Bode plots to display impedance and phase angle against frequency and allow the determination of absolute values of impedance $|Z|$ and phase shift (φ).

2.2.12.6 CV analysis

Graph Pad software was used to analyse the last voltammetry cycle of each electrode tested. Cathodic charge storage capacity (cCSC) was calculated by integrating the current response with respect to time and normalised to the electrode geometric area using MATLAB (R2015a, The MathWorks, Inc).

2.2.13 Statistical analysis

Shapiro-Wilk test was performed on all data to determine normality. One-way ANOVA and t-tests were performed when data followed a Gaussian distribution. One-way ANOVA was followed by Dunnett’s post hoc test to determine pairwise significant difference between groups.

When data did not follow a Gaussian distribution or number of samples was too small to test for normality ($n < 4$), a Friedman’s non-parametric test was performed instead of a one-way ANOVA, followed by Dunn’s post hoc test corrected for multiple comparisons. A Mann-Whitney non-parametric test was performed in place of a t-test.

When comparing the mean differences between groups that have been split on two independent variables a two-way ANOVA was performed.

For all tests, *$p < 0.05$, **$p < 0.01$ and ***$p < 0.001$ were considered to be significant.

3.0 Differentiation of human neural stem cells into motor neurons and local delivery *in vivo*

3.1 Introduction

Stem cells are characterised by two broad properties: their ability to differentiate into various cell types and their capacity to maintain a self-renewing population (Donnelly *et al*., 2012). There are different classes of stem cells based on their differentiation potential. Pluripotent stem cells have the ability to generate any type of cells derived from the three germ layers (ecto-, meso- and endoderm); such is the case with cells of embryonic origin. Multipotent cells, on the other hand, originate once the three germ layers are separated, as such their differentiation capacity is restricted to the lineages of the tissue from which they are derived (Adeeb *et al*., 2015).

In the context of spinal cord injury, the drive to regenerate motor pathways to restore muscle function has prompted the use of stem cells to produce motor neurons (MNs) for translational applications (Yan *et al*., 2007, Yousefi *et al*., 2017). To this end, stem cell-derived MNs have been extensively tested *in vivo* as a potential replacement for endogenous MNs following spinal cord lesions (Wyatt *et al*., 2011, Amemori *et al*., 2013, Khazaei *et al*., 2016, Gazdic *et al*., 2018).

In order to generate cells that mimic the behaviour and characteristics of endogenous MNs, it is essential to understand the neurodevelopmental events that command the specification and differentiation of MNs during embryogenesis.

3.1.1 Motor neuron development

MNs are efferent neurons located in the central nervous system (CNS) that project axons into specific targets in the periphery. According to the location of their cell bodies, MNs can be divided into two categories; upper or cortical spinal motor neurons (CSMNs) and LMNs. Upper MNs, are located in the cerebral cortex where they project axons down the spinal cord. Lower MNs – located in the brainstem and spinal cord - receive inputs from upper MNs and convey these signals to their target muscles through a synaptic connection known as the neuromuscular junction (NMJ) (Davis-Dusenbery *et al*., 2014). Upper MN lesions typically result in muscle spasticity (Ivanhoe and Reistetter, 2004) whereas lower MN lesions can lead to complete paralysis in the most severe cases as there is no alternative route to convey signals to muscles.

Among lower MNs, spinal MNs – residing in the ventral horn of the spinal cord – have been extensively studied thus, the developmental biology mechanisms underlying their origin are relatively well understood. During spinal cord development, different types of neurons are generated by various signalling factor gradients along the dorsoventral and rostrocaudal axes. Such factors render progenitors with a positional identity which is critical in determining the subclass of neurons these precursors will become at a later stage. Following neural induction in the ectoderm, the regulation of BMP, WNT and FGF signalling renders neural precursors a rostral positional identity. These rostral neural precursors become spinal progenitors in response to caudalising signals mediated by retinoic acid (RA). Sequentially, spinal progenitors are exposed to ventralising signals mediated by sonic hedgehog (Shh) which results in the generation of motor neuron progenitors (Wichterle *et al*., 2002).

An increasing wealth of literature is focusing on generating MNs by recapitulating these endogenous cues *in vitro*, using stem cells from different developmental stages and tissue sources. The therapeutic value of each stem-cell type varies according to their cellular behaviour, differentiation potential, engraftment post-transplantation, safety profile and ethical concerns (Khazaei *et al*., 2016).

3.1.2 Cell origin

Embryonic stem cells (ESCs), are PSCs derived from the inner cell mass of the blastocyst. Over the last two decades extensive research using mouse ESCs has provided insights into the molecular and functional properties of MNs generated *in vitro*. These differentiated cells express the same proteins and genes characteristic of endogenous MNs (Hynek Wichterle, 2002, Soundararajan, 2006), when in co-culture with muscle cells they from NMJs and become electrophysiologically active (Miles, 2004) and following transplantation *in vivo*, they reinnervate muscle providing some functional improvement after injury (Yohn *et al*., 2008, Bryson *et al*., 2014). These findings have paved the way into human ESC (hESCs) research. Rodent cells have limitations of physiological accuracy in medical research as important differences may exist between mouse and human stem cell-derived motor neurons (Qu *et al*., 2014). As such, human ESCs (hESCs) enable the generation of MNs with features likely to be more relevant to human physiology.

Due to their endlessly self-renewing nature and a stable genetic background (Rugg-Gunn *et al*., 2007), hESCs are commonly reported in the literature as a source of MNs for developmental studies and a potential therapeutic tool in regenerative medicine (Adeeb *et al*., 2015). However, limited supplies and ethical concerns in relation to cell source are linked to their use. Moreover, their tumorigenic potential (Ramot *et al*., 2017) represents another challenge in their clinical adoption.

Human induced pluripotent stem cells (hiPSCs) bypass many of the ethical concerns associated with hESCs as they are obtained from adult tissue and reprogrammed, by introducing transcription factors, which induce pluripotency. These cells express PSC markers (Pomeroy *et al*., 2016) and have the ability to generate cells from all three germ layers. hiPSCs can be patient-derived thus, circumventing issues associated with immune system rejection of graphed cells. Since their discovery in 2006 (Takahashi and Yamanaka, 2006), there has been a growing interest in the use of hiPSCs-based cell therapies in different areas of regenerative medicine, including spinal cord injury patients. hiPSCs have been successfully produced from different somatic cell types including: fibroblasts, keratinocytes, melanocytes, CD34$^+$ cells, hepatocytes, umbilical cord blood cells and adipocytes (Khazaei *et al*., 2016). Therefore providing different tissue sources, some of which offer the opportunity to isolate these cells in a non or minimally invasive manner.

Several published papers have effectively differentiated hiPSCs into MNs (Qu *et al*., 2014, Shimojo *et al*., 2015, Jha *et al*., 2014) and shown the functional recovery benefits in animals transplanted with these differentiated cells following nerve injury (Pepper *et al*., 2017). However, the induction technology to generate iPSCs needs further optimisation as safety concerns regarding incomplete differentiation or purification to remove undifferentiated cells, remain. Once this technology has been refined to meet the required safety standards, iPSCs have the potential to become a clinical-grade cell therapy to treat patients with lower MN lesions.

Multipotent stem-cells have also been implemented as a source of MN production *in vitro*. Among these, mesenchymal stem cells (MSC) are a popular choice. There is discrepancy in the literature regarding the nomenclature of MSCs. Some studies describe them as stem cells of bone marrow origin capable of differentiating into osteoblasts, adipocytes and chondrocytes. Alternatively, MSCs appear in the literature as stromal progenitors derived from different tissues with the ability to differentiate into various lineages beyond cells of skeletal origin (Wilson *et al*., 2019). Stromal MSCs have been differentiated into MN-like cells; for example: human olfactory ectomesenchymal stem cells (OE-MSCs) expressed molecular and morphological characteristics of MNs following 2-week incubation in a MN differentiation cocktail (Bagher *et al*., 2018). More recently, human tonsil-derived MSCs were found to express MN-markers after 2-weeks of differentiation and formed NMJs when co-cultured with a muscle cell line (Park *et al*., 2019). Although, differentiation of human bone marrow-derived MSCs is restricted to skeletal tissue, Park and colleagues overcame this limitation by genetically engineering MSCs with transcription factors expressed by MNs and incubating these cells in MN induction medium (Park *et al*., 2012).

Overall, as a source of MNs, MSCs are a desirable choice as they can be obtained from different tissues and provide an autologous source for cell replacement therapy, therefore, circumventing issues of limited availability and immune rejection. Nevertheless; there is evidence on the extensive variation among populations of MSCs - reviewed in (Wilson *et al.*, 2019) - arising from different tissues as well as within tissue from a single donor. This translates into a challenge to produce a consistent population of cells for therapeutic purposes.

3.1.2.1 Cell source for this study

In choosing a cell source with therapeutic potential to generate MNs; three factors were considered: ethical concerns, ability of the cell source to be differentiated into motor neuron like cells – that is cells with molecular and functional characteristics that match those of endogenous MNs- and cell fate upon implantation.

Neural stem cells (NSCs) or neural progenitors (NPs) are cells of multipotent origin capable of differentiating into neurons, oligodendrocytes and astrocytes. They are found in the adult and developing CNS where they can be isolated from and expanded *in vitro* (Lee *et al*., 2014). The ethical concerns in obtaining NSCs from foetal spinal cord, as well as the limited availability of this tissue, has prompted the development of immortalised cell lines. These cells can proliferate indefinitely and be cultured *in vitro* over several generations. However, the use of immortalised cell lines in the clinic is constrained by a tendency to tumour formation and genetic instability product of long-term expansion (Nikitina *et al*., 2018). To overcome the issue of scalability, safety and genetic stability a conditionally immortalised cell line from human foetal neuroepithelium was developed (Pollock *et al*., 2006). The conditional growth of these cells allows for the downregulation of the immortalising gene upon transplantation into the host tissue, thus, circumventing concerns over tumorigenicity. The technology employed for the manufacturing of this cell line is *c*-mycER^{TAM}, a fusion protein. Primary cells were dissociated from foetal tissue and transduced with a retrovirus containing a growth-promoting gene (c-myc) fused to a mutated form of the oestrogen receptor. The resulting fusion protein is controlled by 4-hydroxy-tamoxifen (4-OHT), a synthetic drug. More specifically, cells proliferate only in the presence of 4-OHT. One of these cell lines, is CTX0E03, a clinical-grade cell line derived from human foetal brain cortical tissue, which has recently been approved in the UK for Phase II (https://clinicaltrials.gov/ct2/show/NCT02117635) and in the U.S for Phase IIb (https://clinicaltrials.gov/ct2/show/NCT03629275) clinical trials in stroke patients. The clinical stage this stem cell line has achieved prompted the adoption of spinal cord clonal line 01 (SPC-01) for this study. SPC-01, a conditionally immortalised cell line generated using the technology described above, is derived from human foetal spinal cord (Cocks *et al*., 2013); as such it has the potential to be differentiated into MNs. Indeed, when karyotyped and transcriptionally profiled, these cells remained genetically stable and retained the transcriptional identity of ventral spinal cord progenitors, which was not altered following extensive propagation *in vitro.* Moreover, upon removal of growth factors and 4-OHT from culture conditions; SPC-01s differentiated into a mixed population of interneurons (10%) and astrocytes (79%) with a low yield of oligodendrocytes. When cultured in the presence of RA, SPC-01 cells gave rise to motor neurons, albeit they represented less than 5% of the neuron population (Cocks *et al*., 2013). Further, research from another group has demonstrated significant early functional recovery in rats transplanted with SPC-01 cells following SCI, good survival of grafted cells 8 weeks after transplantation and no sign of hyperproliferation or tumour formation (Amemori *et al*., 2013). Recently, it has been shown that SPC-01s have strong immunomodulatory properties achieved through the inhibition of the nuclear factor κB (NF-κB) signalling pathway, which underlies much of the inflammatory response associated with SCI (Karova *et al*., 2019). Overall, the strong evidence highlighting the translational potential of conditionally immortalised cell lines and the ability of SPC-01s to differentiate into MNs and promote functional recovery following SCI, makes these cells a promising candidate for cell replacement therapy following lower MN lesions.

3.1.3 Directed differentiation of stem cells into motor neurons

Several well-established protocols can reliably and reproducibly achieve MN production from stem cells in defined culture conditions (Patani, 2016). For human NSCs the timeline for differentiation into MNs is typically 1 week (Lee *et al*., 2014), whereas for human pluripotent stem cells differentiation protocols are more protracted and, depending on the one implemented, can take an additional 2-4 weeks after neural induction to obtain electrophysiologically active MNs (Faravelli *et al*., 2014). Following neural induction, NPs can be patterned based on developmental principles. Treatment with RA and recombinant Shh or small molecule agonists of the Shh pathway - such as smoothened agonist (SAG) and purmorphamine - are commonly used to generate MNs (Frank-Kamenetsky *et al*., 2002, Shimojo *et al*., 2015). Although, research in mouse and human cells have shown generation of MNs is possible in the absence of RA by either endogenous Wnt and FGF signalling or inhibition of BMP/Activin/Nodal signalling pathways (Patani *et al*., 2011). Many other differentiation cocktails have been reported; for example, adding B27 (Hu and Zhang, 2009), brain-derived neurotrophic factor (BDNF), glial cell line-derived neurotrophic factor (GDNF) and cyclic adenosine monophosphate (cAMP) to the RA/Shh supplemented media (Takazawa *et al*., 2012). There are disparities in the literature as to whether neurotrophic factors like BDNF play a role in the directed differentiation of MNs (Amoroso *et al*., 2013) or contribute to the survival of differentiated MNs (Karumbayaram *et al*., 2009).

Heterogeneity in differentiation protocols generates highly variable data on the yield of MNs produced. Studies have reported 20% (Lee *et al*., 2007), 50% (Shimojo *et al*., 2015), 70% (Qu *et al*., 2014, Bianchi *et al*., 2018) and up to 90% (Du *et al*., 2015) - yield of MNs obtained following directed differentiation *in vitro*. Efficiency of differentiation is assessed by specific marker expression, morphological and electrophysiological analyses and transplantation into animals (Faravelli *et al*., 2014).

Among the markers most commonly used to detect MNs are: Islet-1 (Isl-1), homeobox gene 9 (Hb9) and Choline acetyltransferase (ChAT). Isl-1, a member of the LIM/homeodomain family transcription factors, is expressed by terminally differentiated MNs. Indeed, this transcription factor is expressed by prospective MNs once they exit the cell cycle. Qu and colleagues (2014) studied the function of Isl-1 in human cells and found it to be required for the induction of mature and functional MNs. MN and pancreas homeobox 1 (MNX1, better known as Hb9) is expressed selectively by MNs in the developing CNS. Hb9-knockout mice have shown the pivotal role this homeobox gene serves in consolidating the identity of post-mitotic MNs (Arber *et al*., 1999). ChAT, is an enzyme responsible for the synthesis of acetylcholine (Ach); the neurotransmitter released from MNs at the NMJ that triggers depolarisation and subsequent contraction of muscle fibres. ChAT is considered a definitive marker of cholinergic neurons and is reliably expressed in mature MNs (Sances *et al*., 2016).

Successful directed differentiation and characterisation of MNs *in vitro*, has prompted research into transplantation of these cells *in vivo*, thus, posing new challenges regarding suitable cell delivery methods.

3.1.4 Injectable cell delivery of MNs into peripheral nerves

A successful MN replacement therapeutic strategy relies on the ability of the transplanted cells to extend axons from the site of implantation to the target muscle. Previous studies in animals have reported MN survival following transplantation in spinal cord injury models, axonal outgrowth down peripheral nerves and improvements in motor function. This functional recovery is mostly attributed to transplanted MNs releasing growth factors that aid in the survival of endogenous cells and promote regeneration and sprouting of severed axons (Rossi *et al*., 2010, Amemori *et al*., 2013). A limited number of studies have reported formation of NMJs by transplanted MNs in the spinal cord. The inability of transplanted cells to form functional neural connections in the adult mammalian nervous system is in part attributed to myelin-derived proteins restricting axonal growth (Hu and Strittmatter, 2004). Deshpande *et al*. (2006) implemented a combination paradigm consisting of administration of neurotrophic factors and immune suppressors to promote survival of transplanted MNs and axonal growth by mitigating the inhibitory effect of myelin and the host immune response. This resulted in only 3% of transplanted cells forming NMJ (Deshpande *et al*., 2006). Translating these results into humans, however, may have additional limitations due to the long distance MNs will have to traverse and the long time it would take for them to reach the appropriate muscle. As an alternative, Zhang *et al*. (2018) have reported peripheral nerve cell transplantation as a therapeutic strategy for spinal cord injury (SCI). Moreover, transplanting NSCs have yielded promising results for the treatment of peripheral nerve injuries (Yohn *et al*., 2008). In 1993 Erb and colleagues first reported the reinnervation of denervated muscles by embryonic MNs transplanted into peripheral nerves (Erb *et al*., 1993). In light of this evidence, it is possible that delivering MNs into peripheral nerves may have a potential therapeutic effect in restoring function of paralysed muscles following lower MN injuries.

MNs can be delivered *in vivo* via microinjections into peripheral nerves. Promising pre-clinical data have been obtained using this delivery platform leading to clinical studies; nevertheless many challenges still remain. Overall, the mechanical forces implicated when passing cells through a needle often affect the viability and function of the transplanted cells (Aguado *et al*., 2012). Indeed, numerous studies have shown less than 5% of injected cells *in vivo* remain at the site of injection within days of transplantation (Amer *et al*., 2017). Furthermore, damage to the nerve at the site of the delivery is also a consequence of microinjections; this can cause physical damage and also elicit inflammation in response to injury. In rodent models of nerve injury, the tibial branch can be transected and used as the site of cell transplantation. Tibial nerve transection is a well-tolerated, validated and reproducible model of muscle denervation (Batt *et al*., 2006). The tibial nerve is one of the three terminal branches of the sciatic nerve, therefore transection of this nerve, rather than the more proximal sciatic nerve, results in less morbidity allowing animals to ambulate easily as the weight bears almost equally on both hind limbs (Batt and Bain, 2013). Because the remaining branches of the sciatic nerve (i.e. sural and common peroneal) remain intact, their target muscles and sensory functions are preserved. Tibial nerve transection causes denervation of the posterior calf musculature (gastrocnemius, soleus and plantaris) whereas sciatic nerve transection, a muscle denervation model commonly used in rodents, results in loss of function of all the muscles of the leg (below the knee) and foot (Batt and Bain, 2013).

MN microinjections are performed using syringe needles from a range of different gauges (25-gauge, being the largest size reported in the literature thus far (Erb *et al*., 1993) and 31-gauge needle size being the smallest (Pepper *et al*., 2017) used for MN transplantation into the tibial nerve). Typically, needle gauge size is chosen according to cell type, site of transplantation, injection speed and the viscosity of the suspension (Amer *et al*., 2017). Other key considerations for MN transplantation are cell density and injection rate. In regards to cell density, $1x10^5$ cells/µl is commonly reported in the literature (Yohn *et al*., 2008, Kurimoto *et al*., 2016, Pepper *et al*., 2017), anything above is considered highly concentrated. These highly-concentrated suspensions can lead to adverse effects like needle clogging and uneven injection flow. Moreover, it increases the risks of cell death due to limited availability of oxygen and nutrients (Amer *et al*., 2017). Injection speed has been found to have an impact in delivery of cells in the CNS (Amer *et al*., 2015), however, this parameter is not always specified in publications related to MN transplantation in peripheral nerves.

Survival of MNs post-transplantation is influenced by pre-delivery factors (cell density), injection protocols and cell retention post-delivery. Providing cells engraft initially following transplantation, the inflammatory microenvironment and host immune response play a key role in determining subsequent cell survival.

3.1.5 Host immune response to allogeneic transplants

Concerns regarding immune rejection are raised when the transplanted cells do not match the immune system of the recipient (host). In the clinic, such situations arise when donor cells are derived from unrelated donor tissue (allogeneic transplants). Preclinical studies test allogeneic transplantation in rodent models by sourcing cells from a different strain. Alternatively, transplanted cells are derived from a different species (xenograft); this is often the case when testing the therapeutic potential of human-derived stem cells. In order to avoid immune rejection and protect the transplanted cells, immunosuppression is often reported in stem-cell xenograft studies.

Immune rejection is mediated through T-cell and humoral immune mechanisms. T-cells become activated, undergo clonal expansion, differentiate into effector cells and migrate to the transplantation site where they mediate destruction of transplanted cells (Ingulli, 2010). T-cells are activated in response to antigens known as major histocompatibility complex (MHC), which present antigens recognised by T-cell receptors. Two classes of MHC molecules activate different t-cells; MHC-I is expressed in almost all nucleated cells and is recognised by cytotoxic T-cells (CD8), whereas T-helper cells (CD4) recognise MHC-II molecules expressed on the surface of antigen presenting cells. Previous published papers have reported the immunobiology of nerve allografts. In 1990, Ansselin *et* *al*. reported a gradual increase of T-helper and cytotoxic T-cell infiltration following rat peripheral nerve allograft , with both cells types reaching peak numbers at day 7 (Ansselin and Pollard, 1990). Similarly, another publication described an intense invasion of CD4$^+$ and CD8$^+$ cells 2-weeks post-surgery in the allograft group compared to the animals receiving an isograft (where donor and recipient are genetically identical). Peak numbers of both cell types, however, were reported by week 4 (Gulati, 1998). Equally, peak numbers of infiltrating CD8$^+$ cells were reported at 28 days following peripheral nerve allograft transplantation (Hellenbrand *et al*., 2016). In all of the previously mentioned papers, nerve regeneration was superior in the autograft groups. A recent publication quantified the abundance of host derived CD4$^+$ cells following peripheral nerve allograft implantation in rats with and without local immunosuppression. The number of CD4$^+$ cells in the immunocompetent animals was significantly higher 3, 7, 14 and 21 days post-op than that observed in animals subjected to localised immunosuppression. Furthermore, CD4$^+$ infiltration was found to peak 14 days after allograft transplantation. The sustained reduction of CD4$^+$ cells in immunosuppressed animals was correlated with the improvement in functional and regenerative outcomes (Santos Roballo *et al*., 2019). Based on these publications, T-cells seem to play an important role in the rejection of allogeneic peripheral nerve transplants, thus hindering nerve regeneration and contributing to poor muscle functional outcomes. This evidence suggests that the same immunobiological mechanisms may play a role following allogeneic stem cell transplantation. Notably, low expression of MHC-I and II proteins has been reported for CTX0E03, the conditionally immortalised human neural stem cell line. Furthermore, pre-clinical studies using this cell line reported no evidence to suggest that immunosuppression was required in order to obtain cell survival and efficacy (Kalladka *et al*., 2016).

3.1.6 Objectives of this chapter

The aims of this chapter were two-fold:

First, to establish a protocol for the differentiation of SPC-01 cells to a motor neuron phenotype and to measure their proliferative activity as part of an overall *in vitro* assessment of differentiation.

Second, to establish an *in vivo* model and conduct initial tests to explore the potential of transplanted differentiated SPC-01 cells to restore muscle function following *in vivo* transplantation. This was tested by a series of experiments with the following objectives:

(i) To quantify the expression of MN marker Isl-1 in differentiated SPC-01 cells *in vitro*

(ii) To assess proliferative activity of differentiated SPC-01 cells *in vitro* via expression of Ki67 in order to inform the differentiation capacity of these cells

(iii) To implement an *in vivo* model in which potential MN cell replacement therapy could be tested.

(iv) To conduct initial tests using SPC-derived MNs in the *in vivo* model, to investigate whether survival, engraftment and host immune response could be measured.

3.2 Results

3.2.1 Human neural stem cell differentiation into motor neurons

The conditionally immortalised human neural stem cell line, SPC-01 (Cocks *et al*., 2013) was differentiated into motor neurons by the addition of RA (1µM) and SAG (500nM) to basal differentiation media for 5 days (refer to Materials and Methods, section 2.2.1.2 for more detail). Cells were differentiated for 5, 14 and 21 days. After each of the three differentiation time points, cells were fixed and stained to test the proportion of cells that were βIII-Tubulin and Isl1 positive, markers for neurons and motor neurons, respectively (figure 3.1). The yield of neurons after each differentiation time point was quantified and expressed as a percentage of the total number of cells per field of view, as determined by the nuclear stain Hoechst. Similarly, the yield of motor neurons was quantified and expressed as a percentage of the total number of neurons per field of view, as determined by the neuronal marker βIII-Tubulin. There was no significant difference in the percentage of neurons calculated between day 5 (96% ± 1% βIII-Tubulin$^+$ cells), day 14 (98% ± 1% βIII-Tubulin$^+$ cells) and day 21 (98% ± 2% βIII-Tubulin$^+$ cells). There was a significant increase over time in the percentage of motor neurons obtained at day 5 and day 14 (3% ± 1% compared with 24% ± 5% Isl1$^+$ cells) and at day 5 and day 21 of differentiation (3% ± 1% compared with 27% ± 5% Isl1$^+$ cells). The difference in motor neuron yield between days 14 and 21 post differentiation was not significant (figure 3.2).

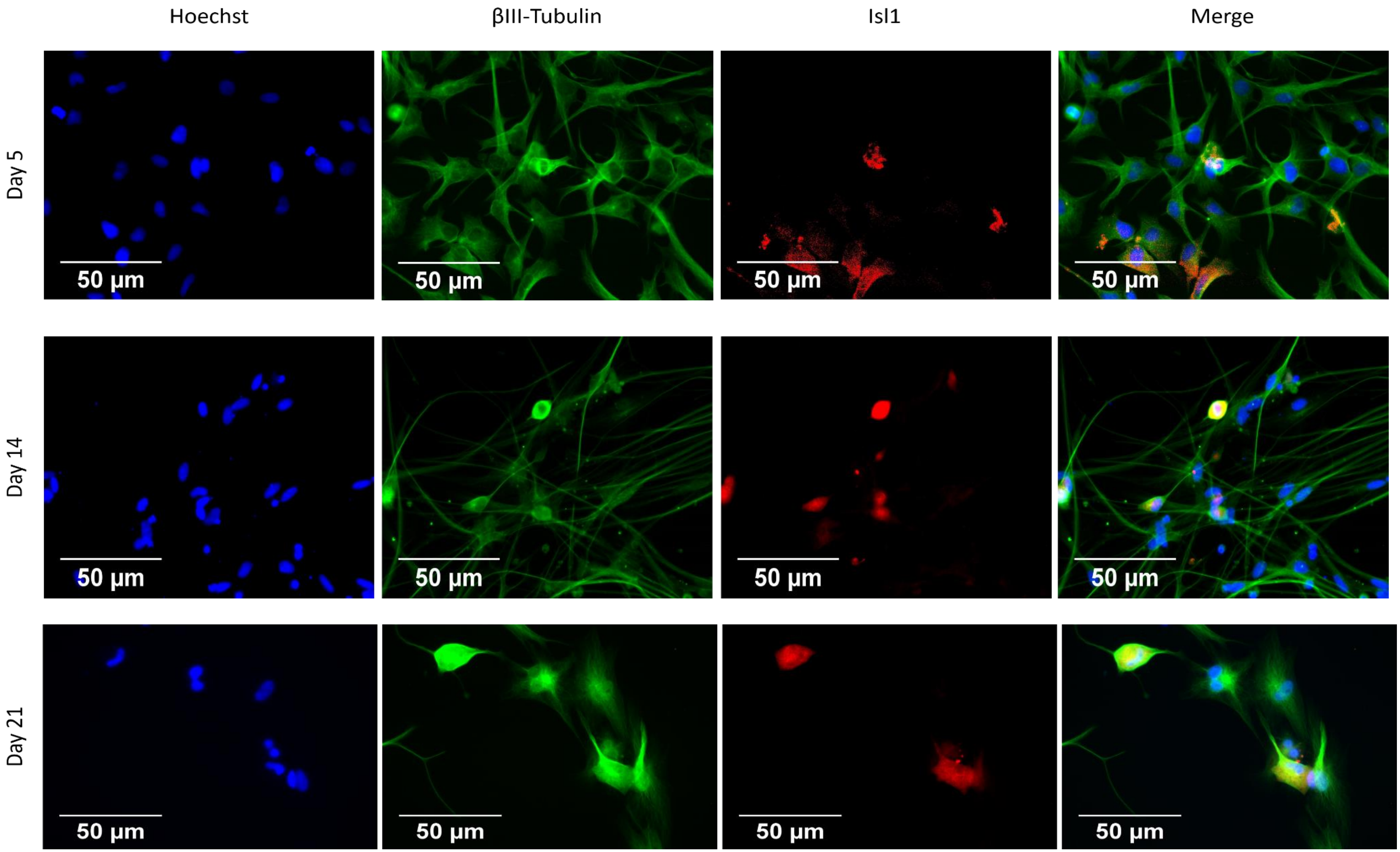
Hoechst
βIII-Tubulin
Isl1
Merge
Day 5
Day 14
Day 21
50 µm

Figure 3.1 Differentiated SPC-01 cells stained to detect βIII-Tubulin and Isl1

Representative fluorescence microscopy images showing SPC-01 cells differentiated in 25 cm^2 tissue culture flasks for 5, 14 and 21 days, respectively. After each differentiation time point cell were stained to detect βIII-Tubulin (green), Isl1 (red) and Hoechst (blue)

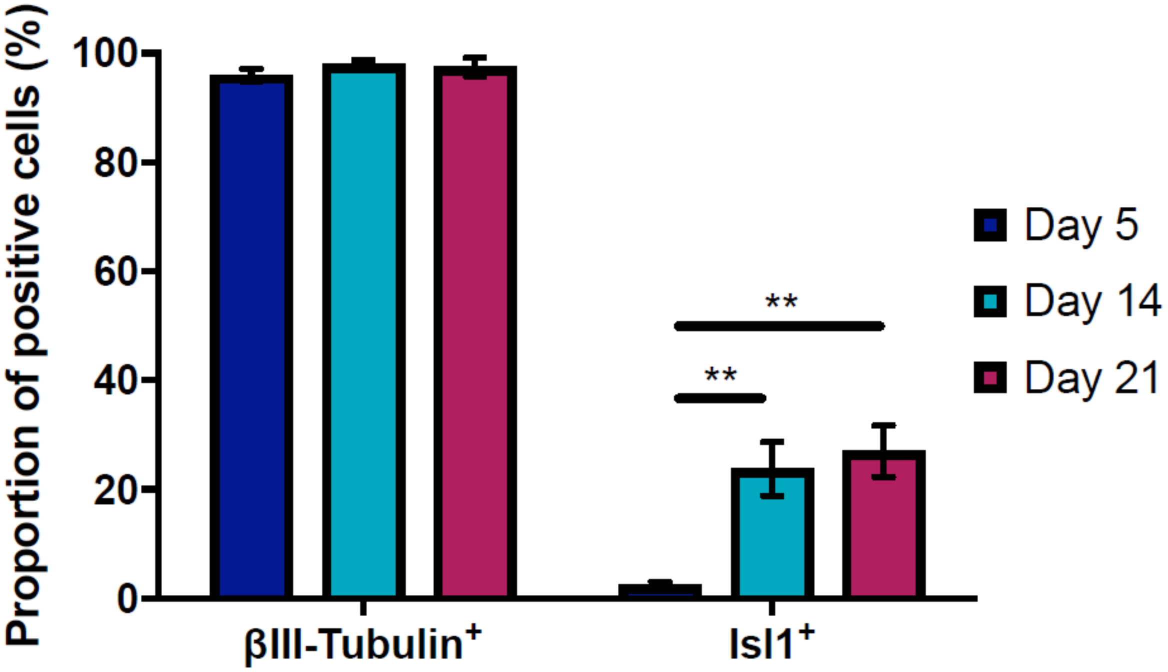

Figure 3.2 Neuron and motor neuron yield following 5, 14 and 21 days of differentiation of SPC-01 cells

Quantification of the yield of neurons (βIII-Tubulin$^+$) and motor neurons (Isl1$^+$) after 5, 14 and 21 days of differentiation. The number of nuclei was quantified to determine the total number of cells per field of view. The number of neurons is expressed as a percentage of total number of cells and the number of motor neurons as a percentage of the total number of neurons per field of view. One field of view = 0.003 cm^2. Data presented as means ± SD for n=4, 12 regions sampled per flask.**p <0.01, Friedman test with Dunn's post-test.

3.2.2 Exploring proliferation of differentiated SPC-01 cells

SPC-01 cells were seeded at a density of 1.25 x 10^5 in 25 cm^2 tissue culture flasks, where differentiation was induced. Once a differentiation time point was reached, flasks were viewed under a microscope and phase contrast images taken. At day 5 of differentiation cells reached 80-90% confluency, similar to undifferentiated cells. In contrast, cells were less confluent at day 14 and day 21, with density similar to that estimated at day 0 (45 minutes after cells were seeded and allowed to attach to the surface of the flask) (figure 3.3)

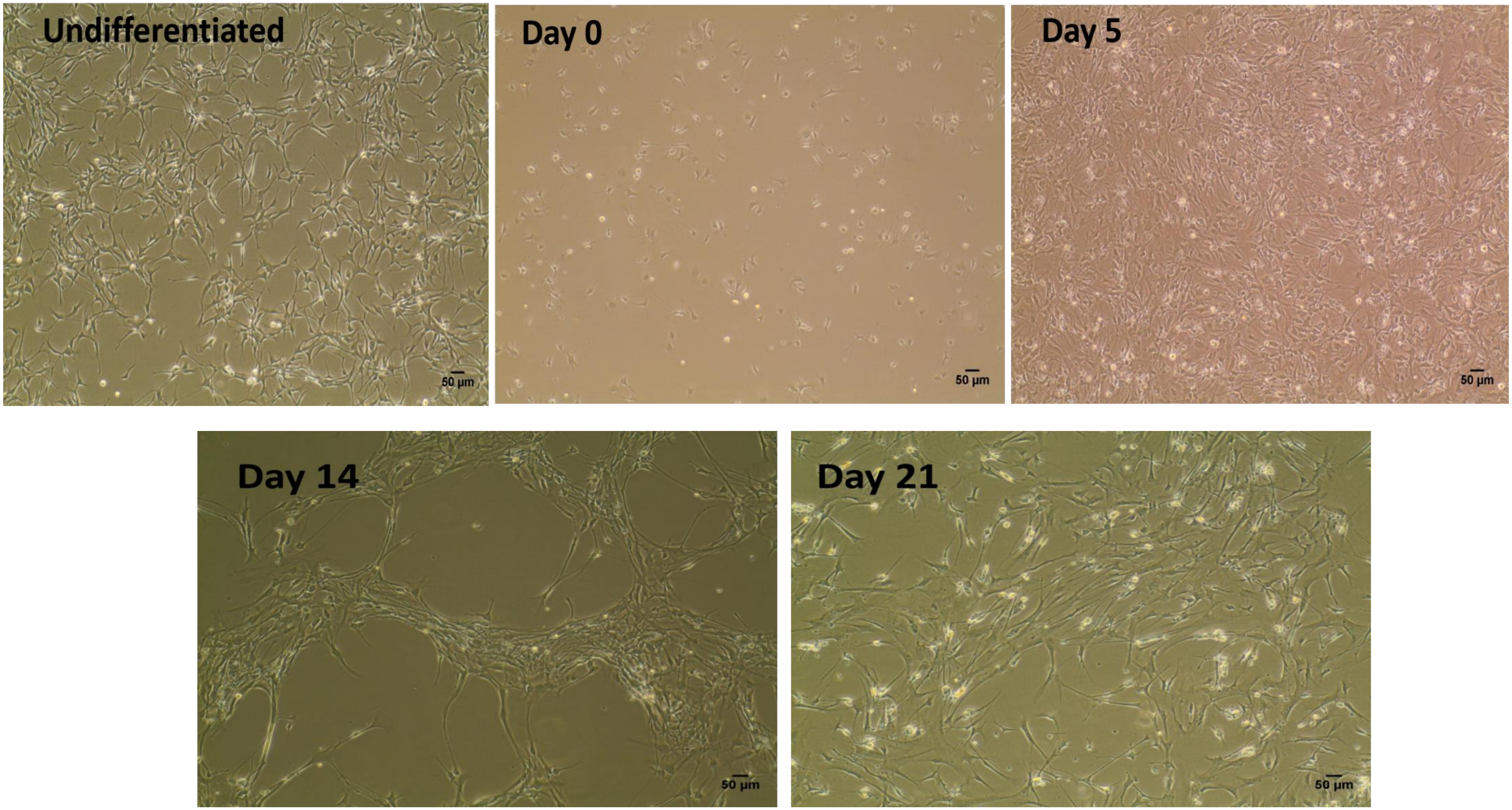
Undifferentiated

Day 0

Day 5

Day 14

Day 21

Figure 3.3 Phase-contrast microscopy images of differentiated SPC-01 cells at different time points

Micrographs showing cell confluency 45 minutes after seeding in supplemented differentiation media (day 0), at day 5, day 14 and day 21 of differentiation. The right hand panel shows an image of undifferentiated cells before passaging. Scale bars are 50 µm.

In order to quantify cell density, samples were fixed, stained with Hoechst and the total number of cells in 12 fields of view (0.03 cm^2) quantified. Day 0 was included to determine the number of cells originally seeded in each flask. Cell density at day 0 was significantly smaller (11,134 ± 496 cells counted per flask) than cell density at day 5 of differentiation (50,534 ± 8,083 cells counted per flask). Both, cell densities at day 14 (15,825 ± 3,806 cells counted per flask) and day 21 (17,667 ± 4,703 cells counted per flask) of differentiation, were significantly smaller than that observed at day 5 of differentiation (50,534 ± 8,083 cells counted per flask). There was no significant difference in cell density between day 0, day 14 and day 21 of differentiation (figure 3.4).

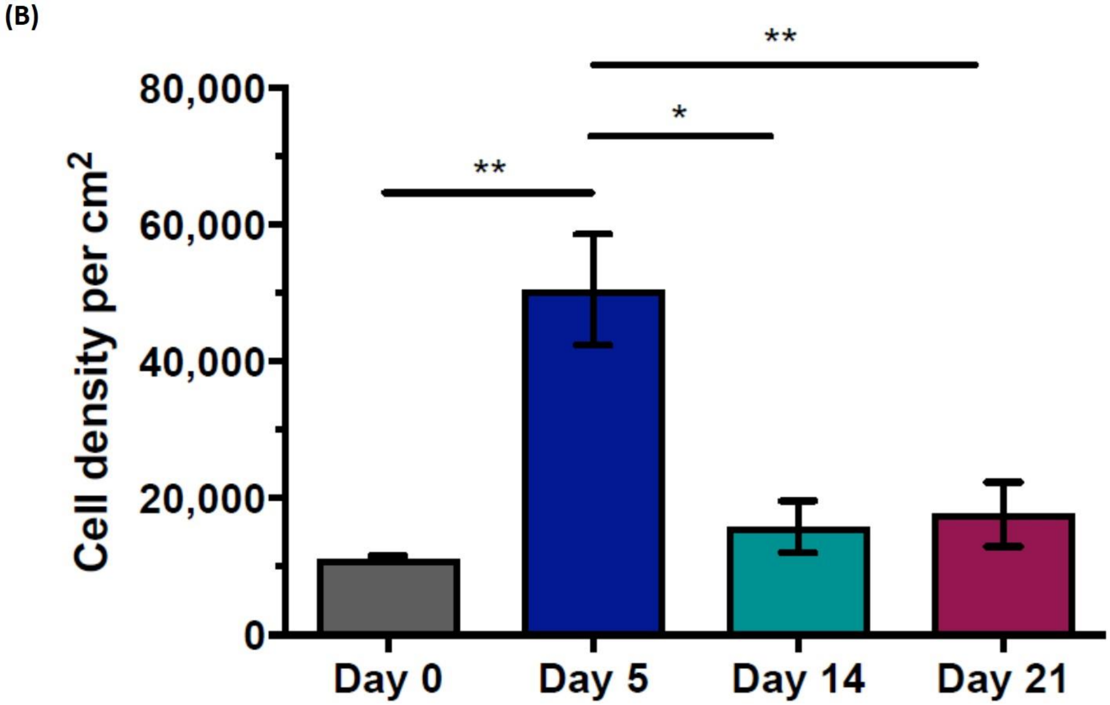

Figure 3.4 Cell densities of differentiated SCP-01 cells at different time points

SPC-01 cell density at day 5, day 14 and day 21 of differentiation and 45 minutes post-seeding (day 0). Samples were stained with Hoechst and the number of nuclei quantified to determine total number of cells per field of view (0.003 cm^2). Data presented as means ± SD for n=4, 12 regions sampled per flask. *p <0.05, **p <0.01, one-way ANOVA with Tukey's post-test.

To further investigate cell proliferation under differentiation conditions, SPC-01 cells were differentiated in 6-well plates for 5, 14 and 21 days. Following fixation, cells were immunostained to detect Ki67, a marker of proliferation (figure 3.5A). Hoechst nuclear stain was quantified in 5 fields of view to determine the total number of cells per field of view and Ki67 positive cells quantified to assess the number of cells proliferating per field of view. There was a significant difference in the percentage of Ki67$^+$ cells at day 5

(30% ± 11 cells per flask) compared with day 14 (3% ± 3 cells per flask) and day 21 of differentiation (1% ± 1%) (figure3.5B)

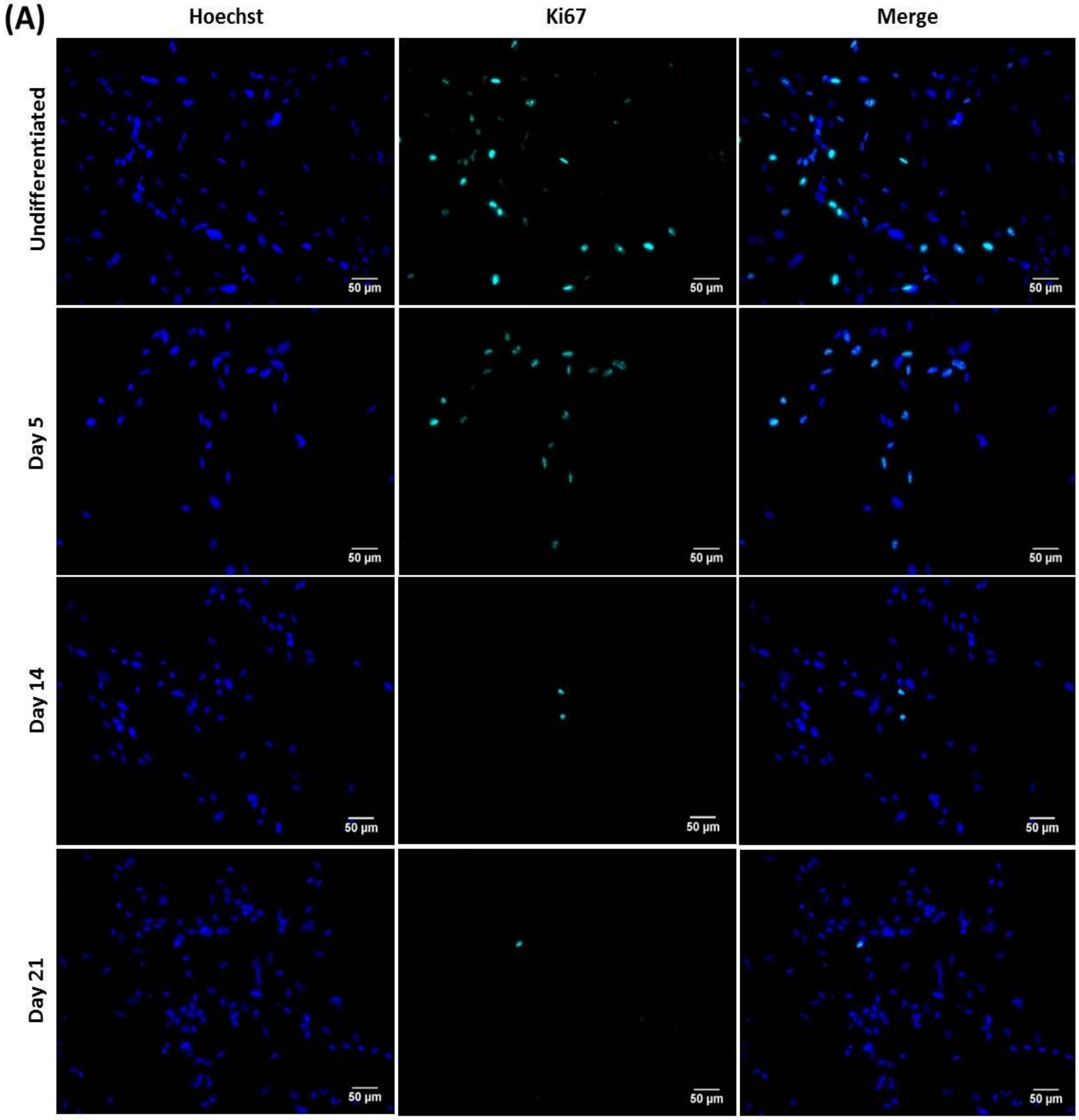
(A)
Hoechst
Ki67
Merge
Undifferentiated
Day 5
Day 14
Day 21
50 µm

Figure 3.5A Differentiated SPC-01 cells in 6-well plates stained to detect Ki67

Representative fluorescence images showing SPC-01 cells differentiated for 5, 14 and 21 days and stained to detect Ki67 (cyan) and Hoechst (blue). Scale bars are 50 µm

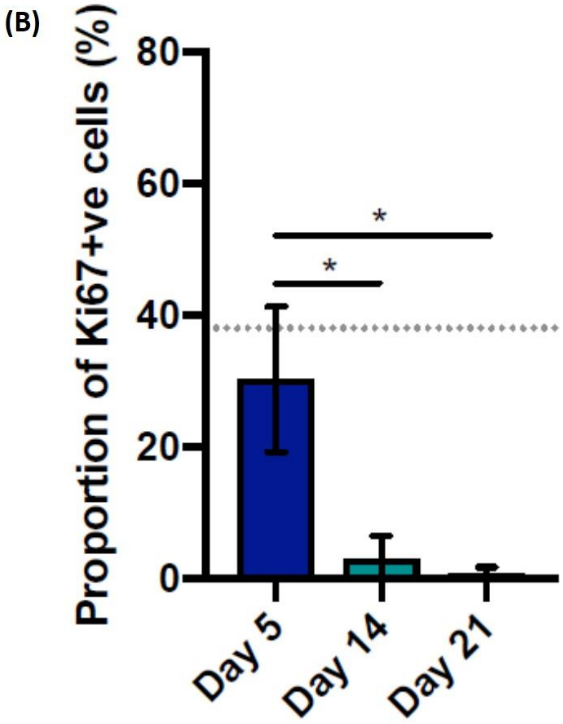

Figure 3.5B Differentiated SPC-01 cells in 6-well plates stained to detect Ki67

Quantification of the yield of proliferating cells (Ki67$^+$) after day 5, day 14 and day 21 of differentiation. The number of nuclei was quantified to determine the total number of cells per field of view. The number of proliferating cells is expressed as a percentage of total number of cells per field of view. The dotted line represents mean proliferation of undifferentiated cells (38% for n=1). One field of view = 0.003 cm^2. Data presented as means ± SD for n=4, 5 regions sampled per well. *$p < 0.05$, one-way ANOVA with Tukey's post-test.

Based on the results thus far presented, day 14 of differentiation was adopted as the time point to differentiate SPC-01 cells into motor neurons (Isl1) for the remaining experiments described in this body of work. This was due to the similarities in the yield of Isl1$^+$ cells and minimal proliferation identified between day 14 and day 21.

3.2.3 Exploring the effect of different concentrations of retinoic acid (RA) and smoothened agonist (SAG) on motor neuron yield.

In a bid to increase the yield of motor neurons, SPC-01 cells were differentiated using various concentrations of RA and SAG. To this end, the initial concentrations of each factor was changed 10 fold, resulting in 9 different concentrations used to generate a differentiation dose response (table 3.1).

Cells were seeded in 6-well plates at a density of 4.5x10^4 cells per well and incubated in basal differentiation media supplemented with the various concentrations of RA and SAG. At day 14, cells were fixed and immunostained to detect βIII-Tubulin and Isl1 (figure 3.5A). The yield of motor neurons was quantified as previously described (refer to section 3.2.1).

Table 3.1. Different concentrations of RA and SAG used to generate a differentiation dose response

This table shows the various concentrations of RA and SAG used to supplement basal differentiation media in a bid to increase the yield of motor neurons obtained from SPC-01 cells.

Condition	Concentration
A	RA (0.1 µM) SAG (50 nM)
B	RA (0.1 µM) SAG (500 nM)
C	RA (0.1 µM) SAG (5 µM)
D	RA (1 µM) SAG (50 nM)
E (control)	RA (1 µM) SAG (500 nM)
F	RA (1 µM) SAG (5 µM)
G	RA (10 µM) SAG (50 nM)
H	RA (10 µM) SAG (500 nM)
I	RA (10 µM) SAG (5 µM)

Cells exposed to 5 µM SAG (conditions C, F and I) died within the first 48 hrs of differentiation. No significant difference in the yield of motor neurons was detected between the control condition (E) and the remaining conditions used to differentiate SPC-01 cells (figure 3.6). Indeed, the yield of motor neurons obtained in 3 of the conditions - A (19% ± 6 motor neurons per well), B (20% ± 7 motor neurons per well) and G (18% ± 6 motor neurons per well) - was comparable to that of the control (see figure 3.1A) (E; 20% ± 8 motor neurons per well). A slight decrease in the number of motor neurons was detected in cells differentiated in condition D (14% ± 3 motor neurons per well). Overall, out of the 9 concentrations tested, cells subjected to condition H produced the highest yield of motor neurons (27% ± 11 motor neurons per well) (figure 3.7).

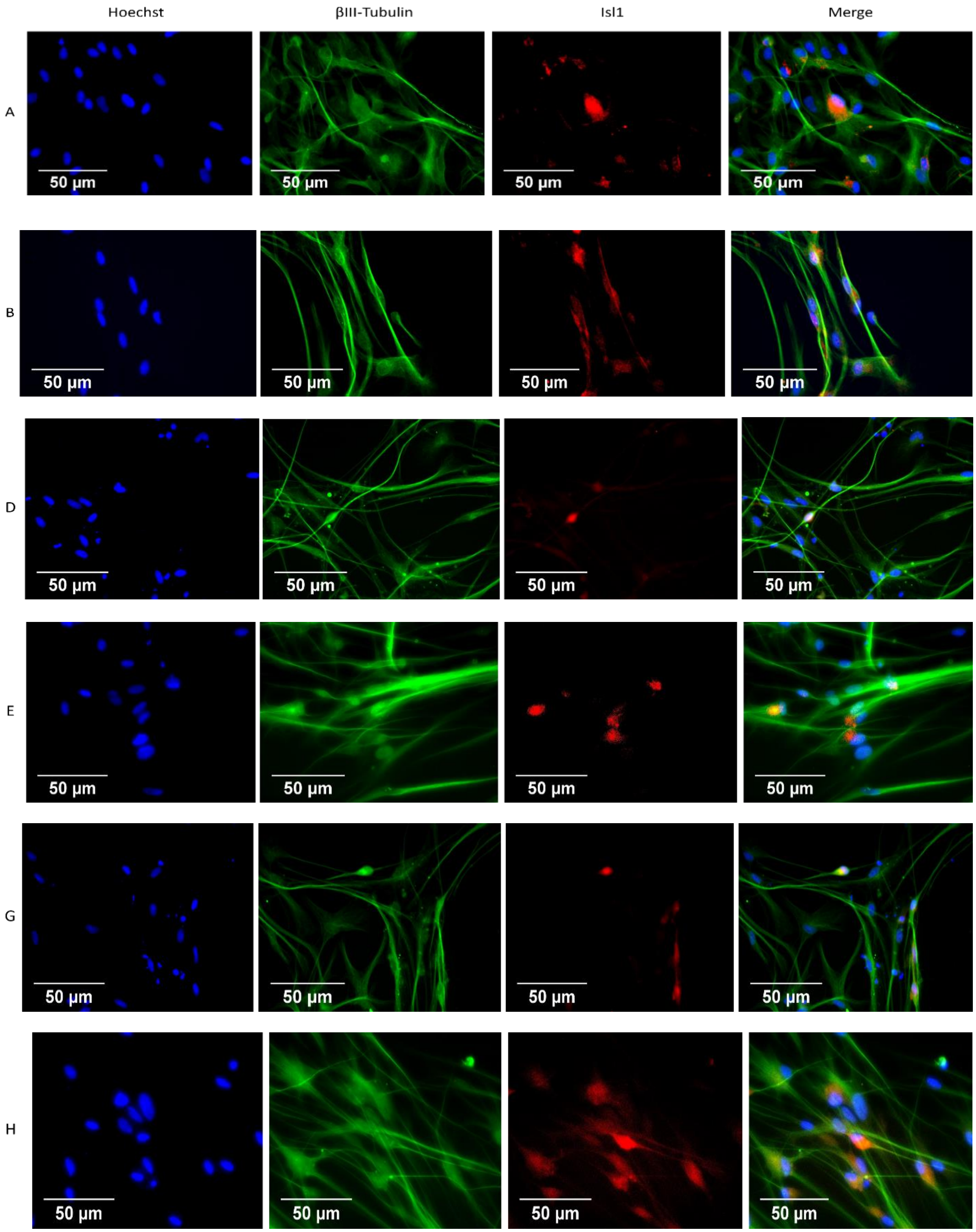
Hoechst
βIII-Tubulin
Isl1
Merge
A
B
D
E
G
H
50 µm

Figure 3.6 Differentiated SPC-01 cells on 6-well plates using different concentrations of RA and SAG stained to detect Isl1

Representative fluorescence microscopy images showing SPC-01 cells differentiated using different concentrations of RA and SAG. Cells stained to detect βIII-Tubulin (green), Isl1 (red) and Hoechst (blue).

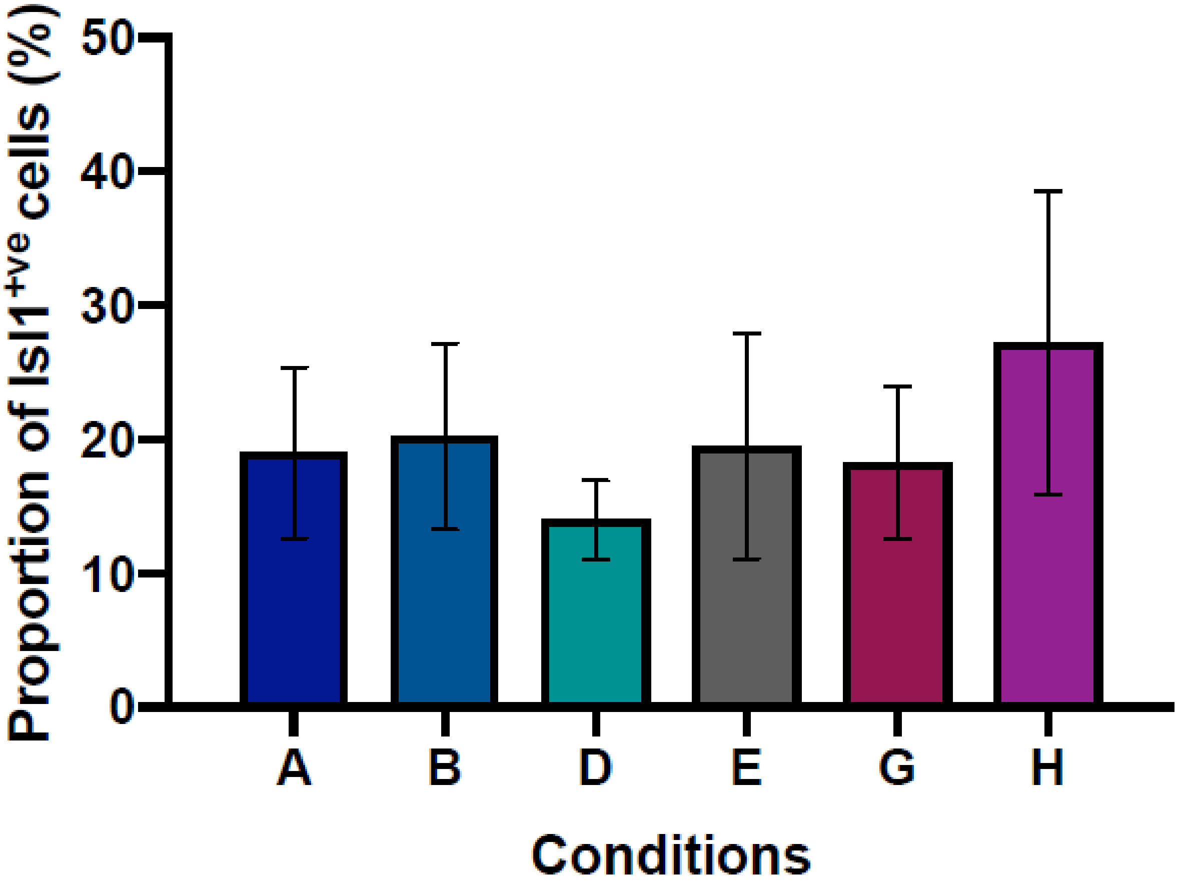

Figure 3.7 Yield of Isl1+ SPC-01 cells exposed to different concentrations of RA and SAG

Quantification of the yield of motor neurons (Isl1^{+}) after 14 days of differentiation using 6 different concentrations of RA and SAG. The number of nuclei was quantified to determine the total number of cells per field of view. Cells co expressing βIII-Tubulin and Isl1 were quantified and expressed as a percentage of the total number of neurons. One field of view = 0.003 cm^{2}. Data presented as means ± SD for n=4, 5 regions sampled per well. ns, one-way ANOVA with Tukey's post-test, all conditions were compared to condition E (control).

3.2.4 Delivery of differentiated SPC-01 cells through a syringe needle: exploring needle gauge effect on cell viability to inform cell transplantation *in vivo*

Cell viability assays were performed on differentiated SPC-01 cells expelled through a gauge 25 (25G) syringe needle to assess the efficacy of this delivery approach prior to cell transplantation in an *in vivo* muscle denervation model. 1x10^{5} cells suspended in 1 µl of media were drawn up a 25-gauge Hamilton™ syringe and expelled onto laminin-coated coverslips for live/dead cell viability assay or 96-well plates for CellTiter-Glo metabolic assays (refer to Materials and Methods chapter, sections 2.2.11.2 and 2.2.11.4, respectively). In both assays, cells seeded using a 0.2-2 µl Gilson pipette were included as controls. Less than 5% cell death was detected at 24 hours post-seeding when using both the control method and when expelling cells through a 25-gauge syringe needle. Furthermore, no significant difference was found between control (4% ± 3.5 of cells per coverslip) and syringe needle (4% ± 3 of cells per coverslip) (figure 3.8). Although not significant, the metabolic activity was slightly higher in cells expelled through a 25G syringe needle (14,665 ± 3,014 RLU per well) than in cells seeded using a Gilson pipette (control; 11,712 ± 2,648 RLU per well) (figure 3.9).

Overall, delivering differentiated SPC-01 cells through a 25G syringe needle did not affect viability or metabolic activity of the cells compared to the control method.

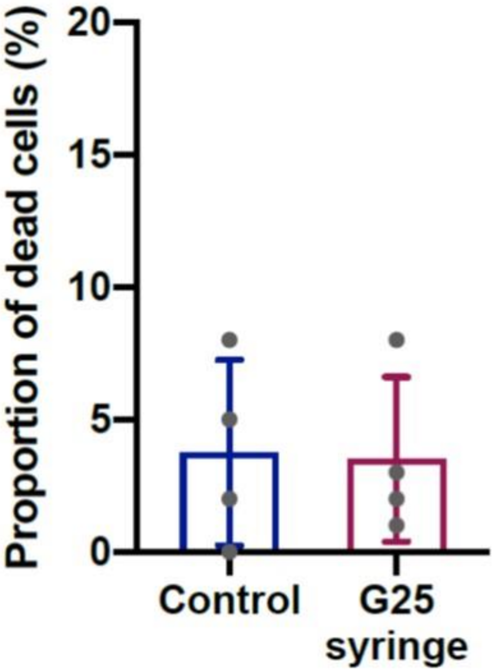

Figure 3.8 Viability of differentiated SPC-01 cells expelled through a gauge-26 syringe needle

Quantification of the percentage of dead cells expelled through a pipette tip (ϕ 0.8 mm) (control) and expelled through a gauge-25 (ϕ 0.2 mm) syringe needle 24 hours after seeding. The number of live and dead cells was quantified to determine the total number of cells per field of view. The number of dead cells is expressed as a percentage of total number of cells per field of view (0.003 cm^2). Data presented as mean ± SD for n=4 with individual values displayed.

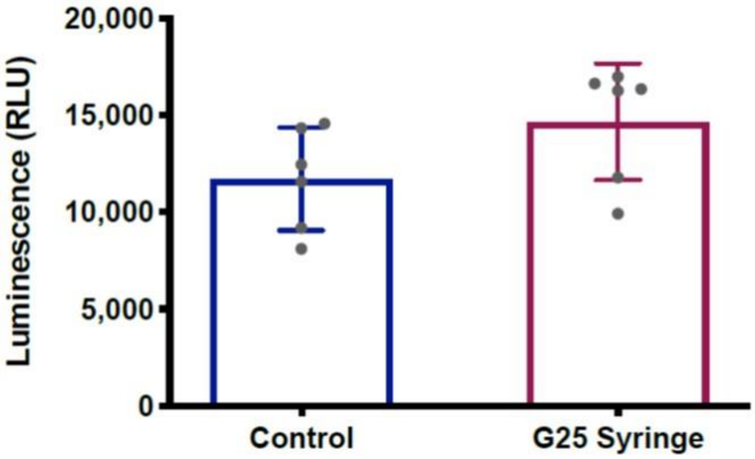

Figure 3.9 Metabolic activity of differentiated SPC-01 cells expelled through a gauge-25 syringe needle

Metabolic activity of cells expelled through a pipette tip and cells expelled through a gauge-25 syringe needle 24 hours after seeding. One field of view = 0.003 cm^2. Data quantified as luminescence in relative light units (RLU) and presented as mean ± SD for n=6 with individual values displayed.

In order to track cells after implantation into an animal model, it is useful to distinguish implanted cells from host cells using immunostaining. Since in this case the implanted cells are human and animal model is a rat, human-specific antigens were selected which can be detected using antibodies that do not cross-react with rat cells

3.2.5 Assessing expression of human-specific antibodies on differentiated SPC-01 cells *in vitro*

Expression of Nestin - a human-specific neural stem cell progenitor marker – and human anti-nuclear antibody (HuNu) were assessed by immunocytochemistry on differentiated SPC-01 cells. At day 14 of differentiation, cells were seeded in laminin-coated cover slips contained within 24-well plates at a density of $5x10^4$ cells per well. Cells were left to attach and extend neurites overnight before fixing and staining with Nestin and HuNu (figure 3.10). The yield of $Nestin^+$ cells was quantified and expressed as a percentage of the total number of cells per field of view, as determined by the nuclear stain Hoechst. 84% ± 4 of differentiated SPC-01 cells expressed Nestin. All differentiated SPC-01 cells expressed HuNu.

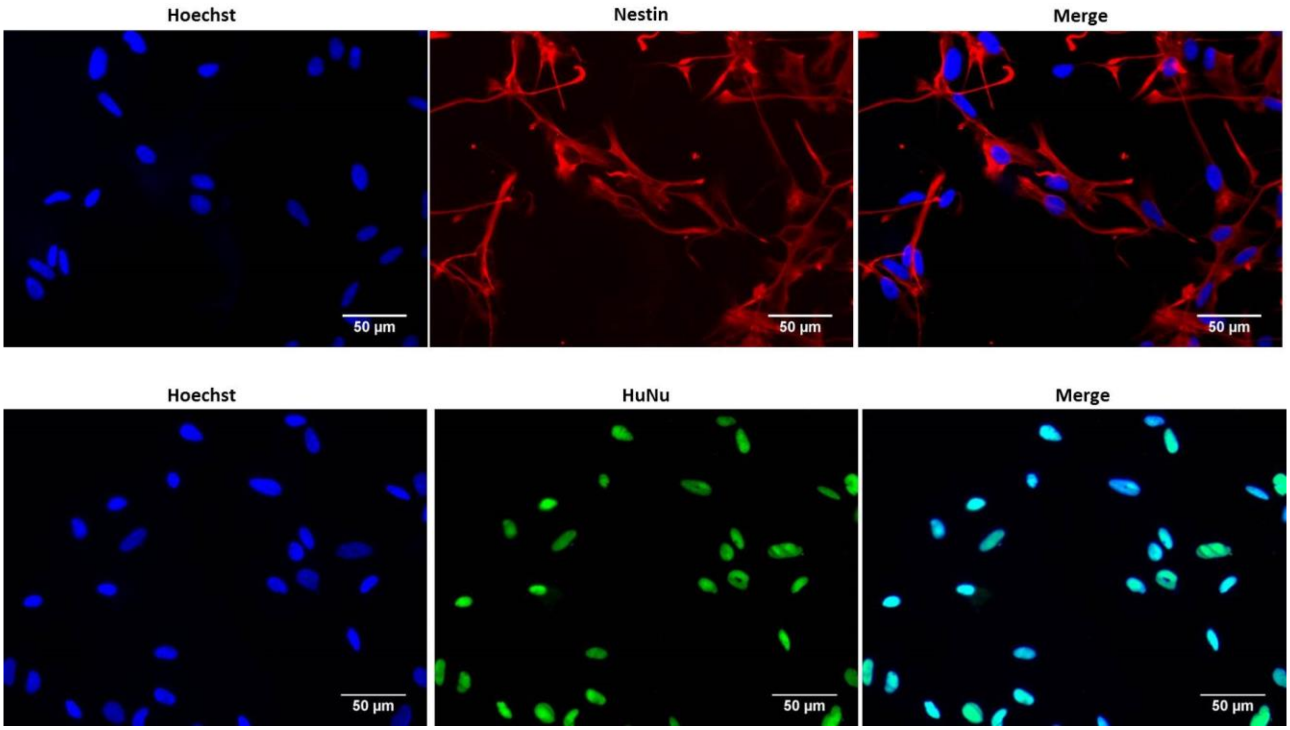

Figure 3.10 Differentiated SPC-01 cells stained to detect Nestin *in vitro*

Representative fluorescence microscopy images showing Nestin expression on SPC-01 cells differentiated for 14 days. Cells were stained to detect Nestin (red) and Hoechst (blue). Scale bars are 50 µm. 84% ± 4 of cells per field of view were Nestin$^+$. One field of view = 0.003 cm^2. Data presented as mean ± SD for n=5.

The *in vitro* results described thus far show presence of Isl 1$^+$ cells upon directed differentiation of SPC-01s, minimal cell proliferation after 14 days of differentiation, viable and metabolically active cells following delivery through a 25G syringe needle and the ability to detect these cells through human-specific markers. In light of these results, a pilot experiment (n=2) was performed to test the experimental design protocol used to administer these cells *in vivo* and to evaluate their functional properties in a muscle denervation rat model.

3.2.6 Transplantation of differentiated SPC-01 cells *in vivo*: a pilot experiment

Using a 25-gauge Hamilton™ syringe, 1x10^5 differentiated SPC-01 cells suspended in 1 µl of media were transplanted into the tibial nerve approximately 7 mm distal to the sciatic nerve trifurcation. In order to achieve complete muscle denervation, the tibial nerve was then transected proximal to the injection site and the proximal stump was reflected proximally and ligated to the hip muscle to avoid spontaneous reinnervation. The sham animal underwent the same surgical procedure but 1 µl of cell-free media was injected instead. After 4 weeks of recovery, electrophysiology was implemented to investigate muscle reinnervation by transplanted cells and the distal tibial nerves excised for histological analysis.

3.2.6.1 Low impedance microchannel electrodes for nerve stimulation

Microchannel electrodes with suitable dimensions to interface with the tibial nerve were manufactured to assist in the electrophysiological testing for this *in vivo* pilot experiment (figure 3.11). A 12.5 µm stainless steel foil was embedded between two layers of PDMS to provide electrical insulation, electrode sites were exposed by laser-ablation of the top PDMS layer and a 2 mm diameter channel was mounted above the electrode sites. This diameter was chosen to accommodate individual branches of the rat sciatic nerve. Finally, the channel was sealed with a PDMS sheet attached on top at one side (refer to section 2.2.5.2 for manufacturing method). Electrode impedance was tested prior to their use *in vivo* to assess their ability to support nerve stimulation. At 1 kHz, the impedance value recorded was 3.9 kΩ (figure 3.12).

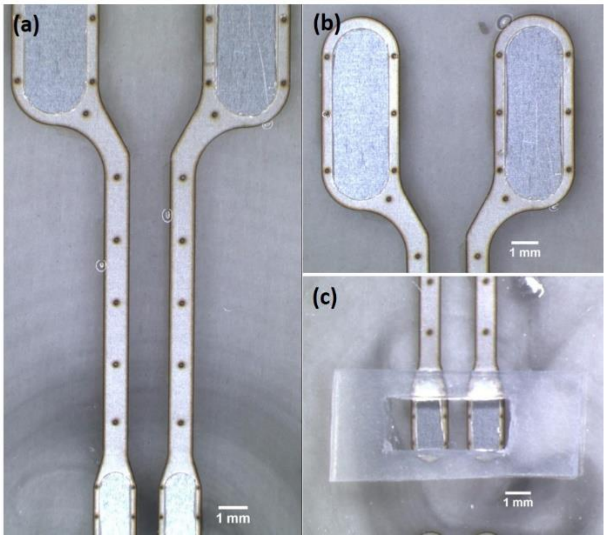

Figure 3.11 Light micrographs of microchannel electrodes manufactured to stimulate the common peroneal and tibial nerves in the *in vivo* pilot experiment

(a) Laser-ablated electrode array pattern embedded within 2 PDMS layers showing exposed pads and electrode sites; (b) Higher magnification of exposed pads achieved by laser-cutting the top PDMS layer and (c) PDMS layer stacked onto electrode sites with a 2 mm diameter opening to expose electrode sites. Both ends of the PDMS layer were cut to create a channel (not shown in micrograph).

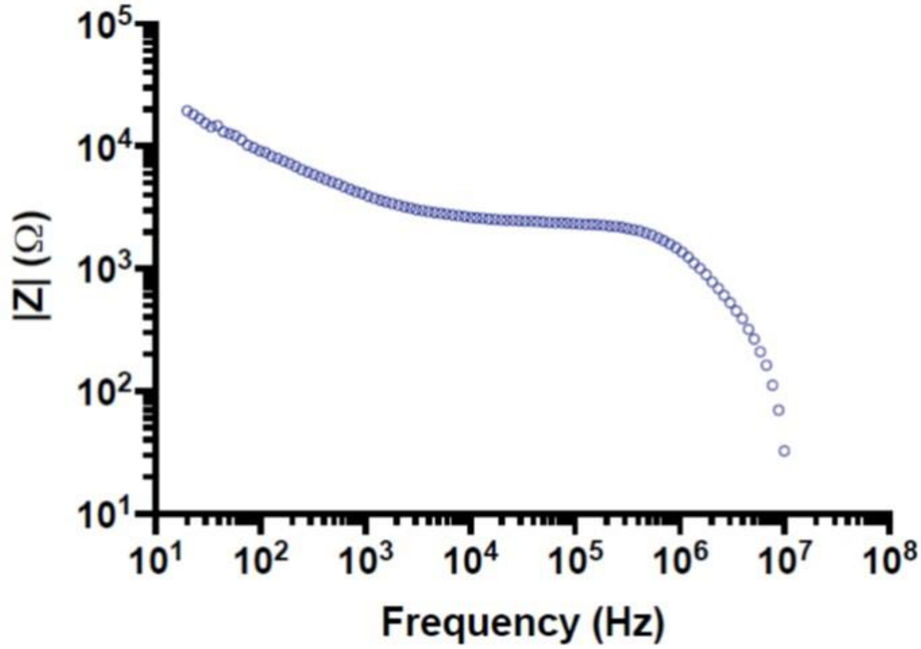

Figure 3.12 Bode plot of frequency-dependent impedance of microchannel electrode arrays used for the *in vivo* pilot experiment

Impedance measurements were taken at different frequencies ranging from 20 Hz to 10 million Hz prior to using the electrodes for nerve stimulation *in vivo.* Data presented as individual values for n=1.

3.2.6.2 Investigating functional reinnervation of muscle in animals transplanted with differentiated SPC-01 cells.

To determine whether transplanted cells reinnervated the host muscle, the gastrocnemius muscle response to electrical stimulation of the cell-transplanted nerve was investigated. Prior to this, compound muscle action potentials (CMAP) were recorded in response to stimulating the uninjured common peroneal nerve on the transplanted side in all 3 animals in order to validate the manufactured microchannel electrodes (table 3.2). Muscle contraction was observed and recorded in all animals upon stimulation of the common peroneal nerve (figure 3.13B-C), except for the sham animal where a muscle response was observed but the CMAP was below the threshold of detection (figure 3.13A). Once the manufactured stimulation electrodes were validated, the distal tibial nerves of the cell-transplanted animals and the sham were stimulated. No muscle response was observed upon stimulation of the distal tibial nerve stumps (table 3.3).

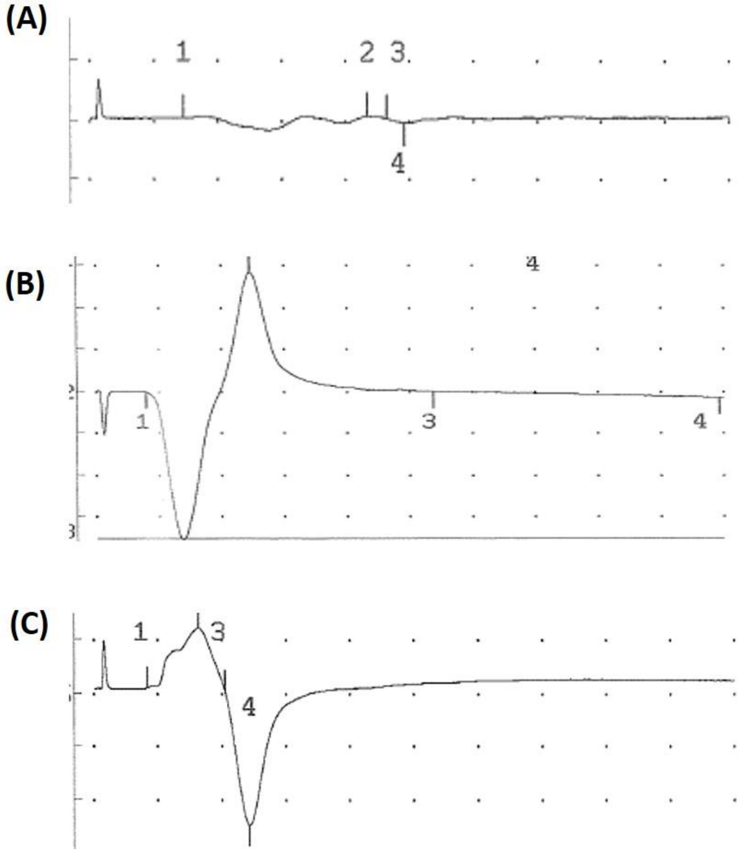

Figure 3.13 Electrophysiology recordings of the uninjured common peroneal nerve

Recording obtained from the gastrocnemius muscle upon electrical stimulation of the common peroneal nerve. (A) Sham, (B) experimental 1 and (C) experimental 2. X axis depicts latency (ms), Y axis depicts CMAP (mV). Scale = 2 units

Table 3.2 Electrophysiology evaluation of the uninjured common peroneal nerve to validate microchannel electrodes

This table shows the stimulus intensity used to elicit muscle contraction, amplitude of CMAP and latency of response in all three animals upon electrical stimulation of the uninjured common peroneal nerve to validate the manufactured microchannel electrodes. Muscle contraction was observed in the sham animal but the CMAP was below the threshold of detection and could not be recorded.

Common peroneal nerve stimulation				
Subject	**Muscle response (Yes/No)**	**Stimulus intensity (mA)**	**CMAP (mV)**	**Latency (ms)**
Sham	Yes	1.2	N/A	N/A
Experimental 1	Yes	2.2	14.1	1.56
Experimental 2	Yes	1.1	12.6	1.64

Table 3.3 Electrophysiology evaluation of the transplanted tibial to nerve to assess muscle reinnervation

This table shows absence of muscle response observed in all three animals upon electrical stimulation of the tibial nerve to assess muscle reinnervation by the transplanted SPC-derived MNs.

Tibial nerve stimulation	
Subject	**Muscle response (Yes/No)**
Sham	No
Experimental 1	No
Experimental 2	No

In order to determine the fate of transplanted cells, distal tibial nerve stumps in all animals were excised for immunohistochemical analysis.

3.2.6.3 Histological analysis of excised cell-transplanted nerves

Distal tibial nerves were excised from all three animals, longitudinally cryosectioned (30 µm thick) and stained with human-specific Nestin antibody and HuNu to identify the transplanted cells. Rat nerve tissue with no human transplanted cells was immunostained with both markers to assess cross-reactivity in this species (figure 3.14). No nestin$^+$ or HuNu$^+$ rat cells were detected in stained rat nerve tissue. These results validate the use of HuNu and nestin as human-specific markers to localise differentiated SPC-01 cells transplanted in rats. In the cell-transplanted nerves, no HuNu$^+$ cells were identified in either of the experimental animals. In contrast, two nestin$^+$ cells were identified in one of the transplanted animals (experimental 1) (figure 3.15). No nestin$^+$ cells were detected in experimental animal 2. Based on these results, the remaining tissue sections in experimental 1 and sham were stained with rat-specific CD4 antibody (a marker of T-helper cells) and rat-specific OX8 antibody (a marker of cytotoxic T-cells) in order to investigate a potential T-cell mediated host immune response elicited against the transplanted cells. Nerve immunostaining revealed the presence of both types of T-cells in sham and experimental animal (figure 3.16). However, the number of CD4$^+$ cells was lower in the experimental animal (105 ± 34 cells per nerve section) compared with the sham animal (183 ± 55 cells per nerve section). Regarding cytotoxic T-cell presence, there was a slightly higher number of OX8$^+$ cells detected in the experimental animal (178 ± 37 cells per nerve section) compared with the sham animal (164 ± 76 cells per nerve section) (figure 3.17A). In a bid to understand if T-cell presence was correlated to the site of cell transplantation, the distribution of CD4$^+$ and OX8$^+$ cells along the nerve section was assessed. The majority of CD4$^+$ cells were located at the proximal end of the nerve, near the site of injection. This trend was observed in both, sham (84 ± 44 cells per proximal end, 56 ± 10 cells per middle section and 43 ± 33 cells per distal end of the nerve) and experimental 1 (48 ± 21 cells per proximal end, 25 ± 8 cells per middle section 32 ± 18 cells detected per distal end of the nerve) (figure 3.17B). In contrast, a different trend was observed between sham and experimental 1 in the distribution of OX8$^+$ cells. In experimental 1, approximately 75% of cells expressing OX8 were identified at the proximal end of the nerve (132 ± 35 cells per proximal end), the remaining 25% of cytotoxic T-cells were equally distributed between middle position (22 ± 11 cells per middle section) and distal end (23 ± 23 cells per distal end) (figure 3.17C). In the sham animal the distribution of T-helper cells across the nerve was very similar with the majority of cells localised distally (64 ± 38 cells per distal end compared to 54 ± 29 cells per middle section and 46 ± 12 cells per proximal end).

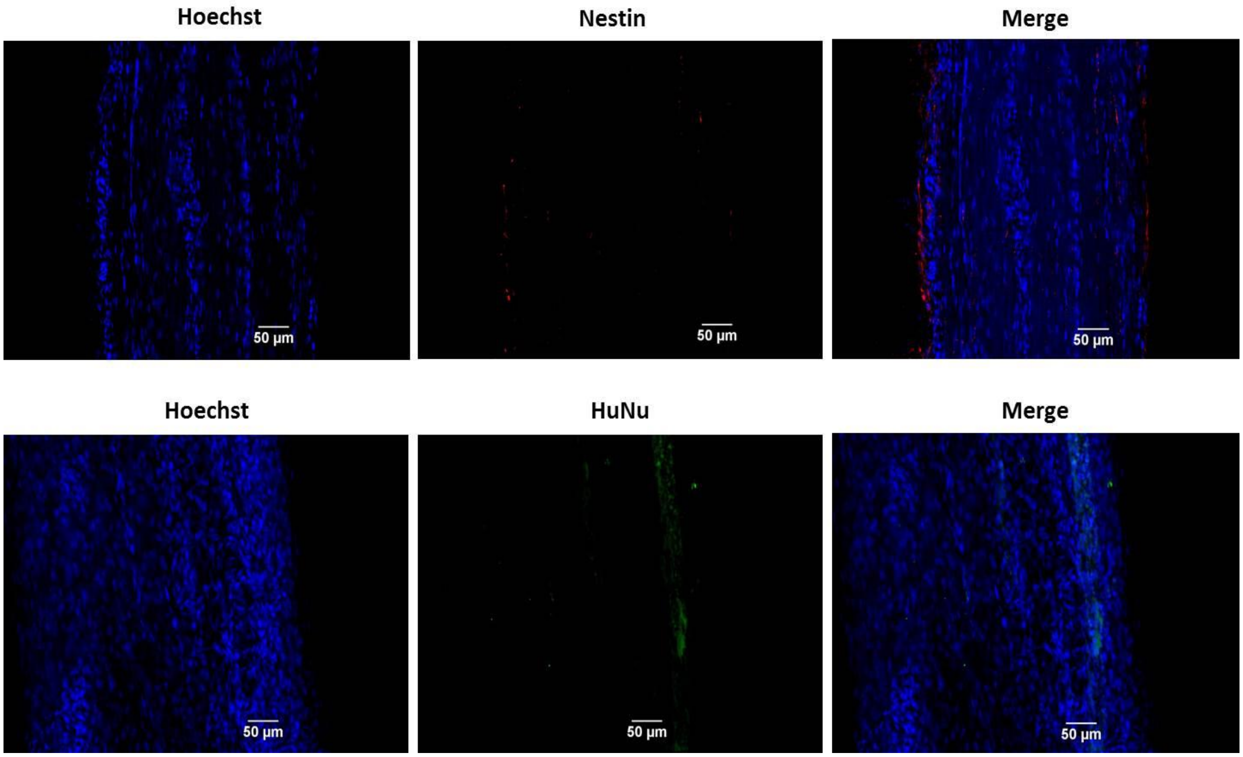

Figure 3.14 Common peroneal rat nerve samples stained to assess cross-reactivity with human-specific markers nestin and HuNu

Representative fluorescence microscopy images showing no nestin (top panel) or HuNu (bottom panel) expression on rat longitudinal nerve sections of the common peroneal nerve. Cells were stained to detect nestin (red), HuNu (green) and Hoechst (blue). Scale bars are 50 µm.

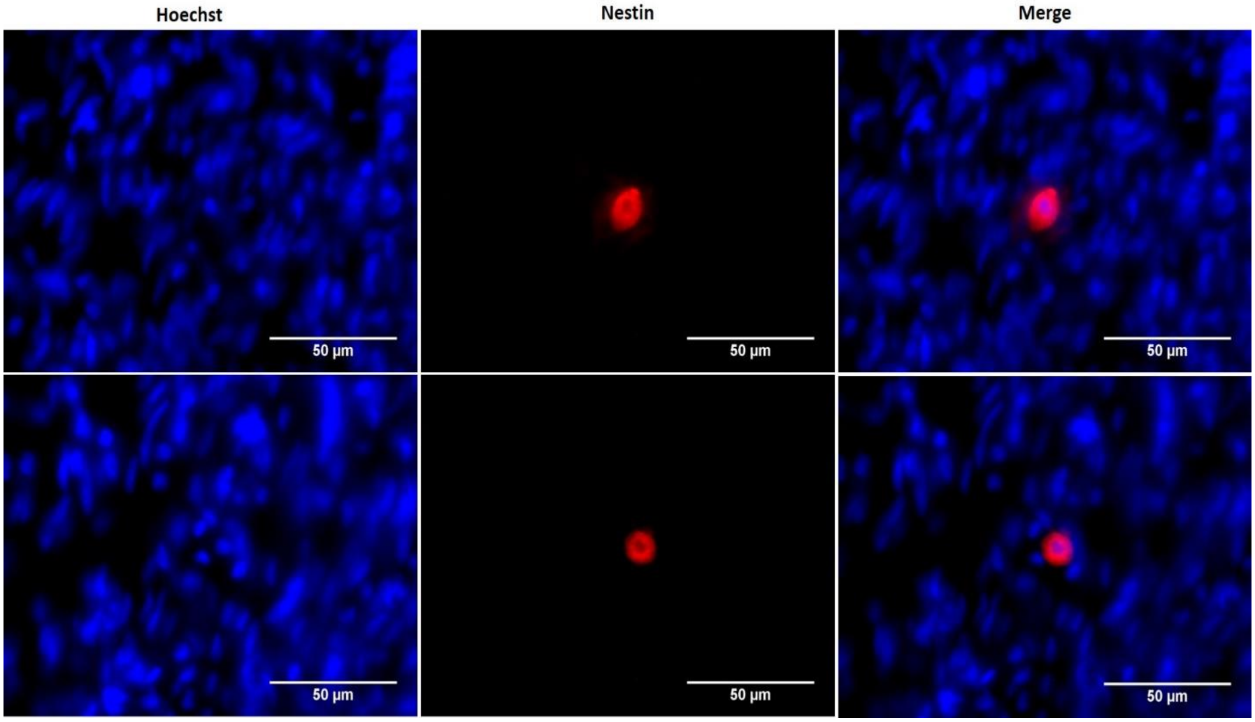
Hoechst
Nestin
Merge
50 µm
50 µm
50 µm
50 µm
50 µm
50 µm

Figure 3.15 Nestin^{+ve} cells identified in the transplanted tibial nerve

Fluorescence microscopy images of the two Nestin^{+} cells identified in one of the transplanted animals (experimental 1). Scale bars are 50 µm.

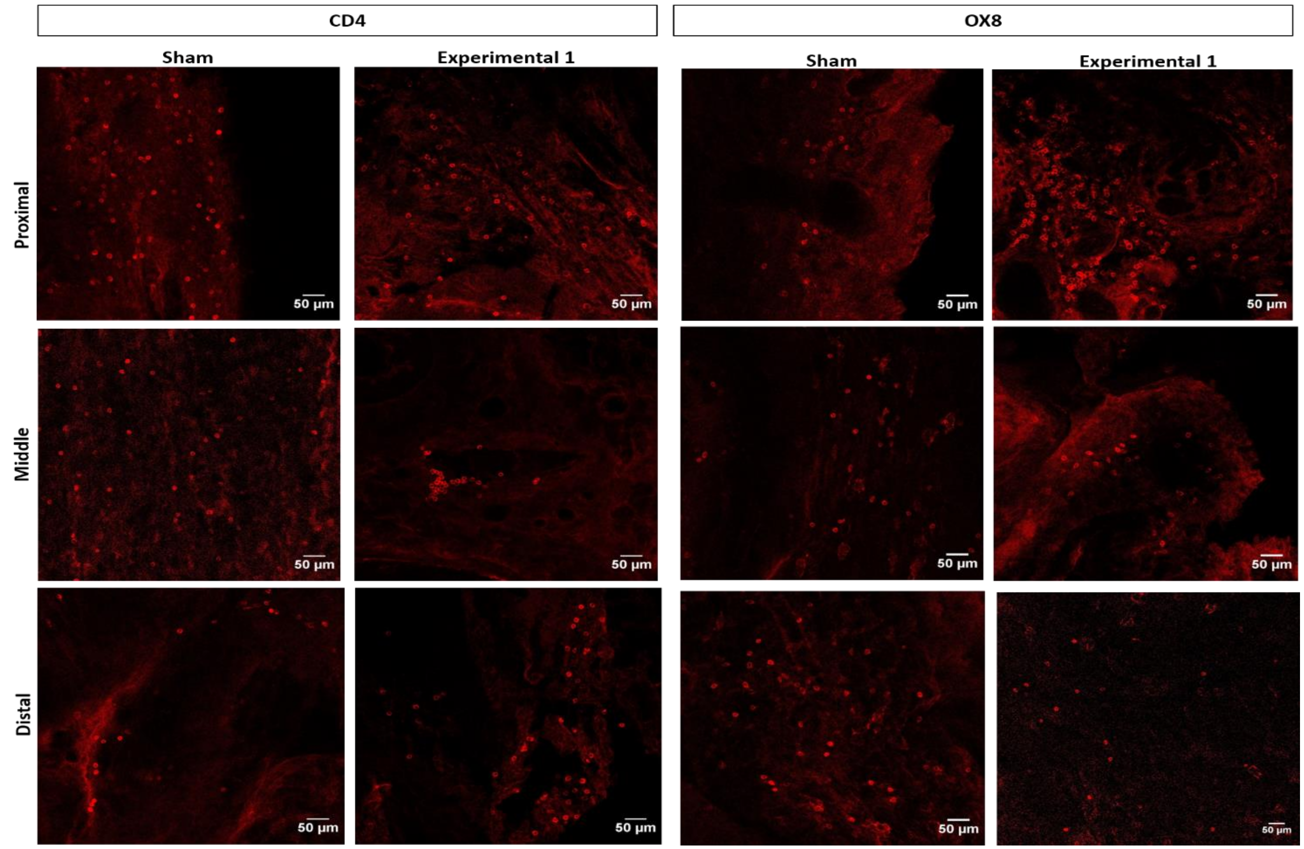

Figure 3.16 Confocal micrographs of 30 µm longitudinal sections showing three positions along the tibial nerve at 4-weeks post-transplantation of differentiated SPC-01 cells. Nerve sections were stained to detect a host t-cell-mediated immune response

Representative confocal microscopy images of rat CD4$^+$ cells (red; left panel) and OX8$^+$ cells (red; right panel) at proximal, middle and distal positions of the tibial nerve 4-weeks after pilot *in vivo* experiment. Sham animal was subjected to tibial nerve transection followed by injection of 1 µl of media. Experimental animal was subjected to tibial nerve transection followed by transplantation of 1x10^5 differentiated SPC-01 cells suspended in 1 µl of media. Scale bars = 50 µm.

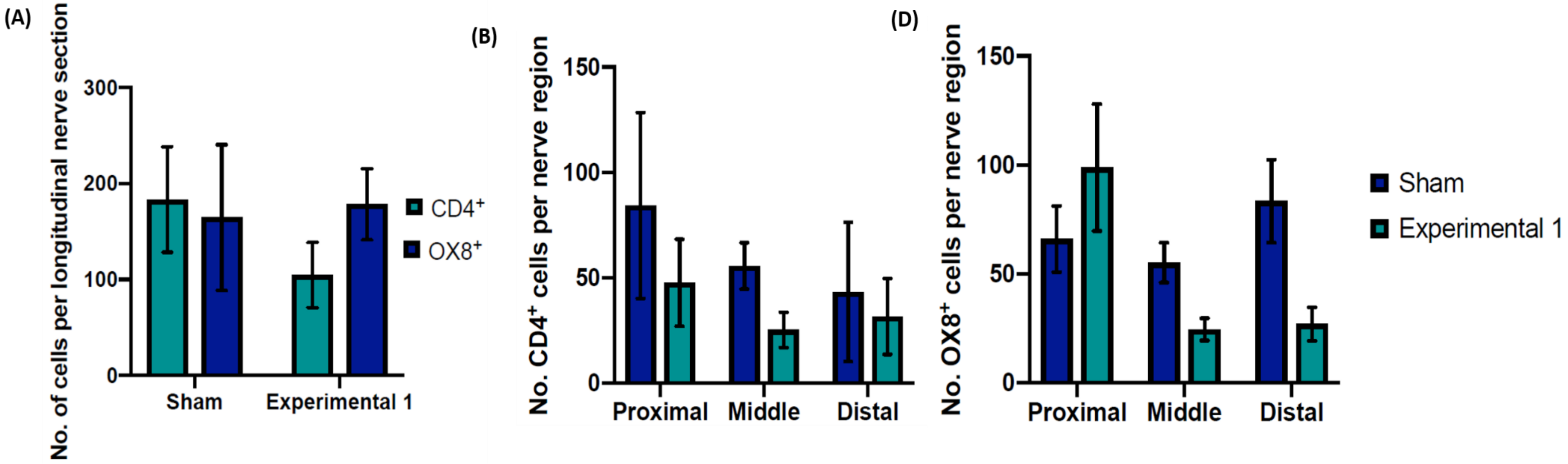

Figure 3.17 Yield of CD4+ve and OX8+ve cells along rat tibial nerve 4 weeks after transplantation with human SPC-01 cells

(A)Quantification of the mean number of T-helper cells ($CD4^+$) and cytotoxic T-cells ($OX8^+$) per tibial nerve longitudinal sections in sham and experimental (B) Distribution of $CD4^+$ cells and (D) $OX8^+$ cells across 3 regions (proximal, middle and distal) of the excised tibial nerves for both, sham and experimental 1. Data presented as mean ± SD for n=1; 3 tibial nerve longitudinal sections stained for each cell marker per animal.

3.3 Discussion

The growing interest in neuronal cell replacement therapies to restore muscle function following injury, is undisputable. Over the last two decades, research efforts in the field of regenerative medicine have generated evidence on the successful differentiation of stem cells into motor neuron-like cells that mimic the molecular, electrophysiological and functional properties of endogenous MNs. Moreover, the extensive preclinical data on the ability of transplanted human-derived MNs to promote regeneration and aid in muscle functional recovery following injury (Cummings *et al*., 2005, Amemori *et al*., 2013, Pepper *et al*., 2017, Jang *et al*., 2018) highlights the potential use of exogenous MNs in the clinic. The choice of source of cell is of critical importance to advance MN cell replacement strategies towards the clinic. Advantageous criteria include: non to minimal ethical concerns, favourable safety profile, large availability, high expandability, ease and efficacy of differentiation into MN-like cells and low immunogenicity.

Here, the suitability of a hNSC line, SPC-01, was investigated as a potential source of therapeutic MNs. The ability of these cells to differentiate into MNs, was assessed by exploring the expression of mature MN marker Isl-1 in cells exposed to various differentiation conditions over different time points. Overall, SPC-01 cells were differentiated into Isl 1^+ cells - indicative of a MN phenotype - when exposed to all differentiation conditions tested. 14 days of differentiation was shown to be the most efficient length of time in which to generate Isl 1^+ neurons. Indeed, this time point generated a significantly higher proportion of Isl 1^+ cells than earlier time points and the difference in the number of Isl 1^+ cells between 14 and 21 days was minimal, therefore; adoption of a 14-day differentiation protocol was favoured to reduce cell culture costs, which is an important factor from a manufacturing prospect. In regards to the yield of putative MNs obtained, this study shows 24% of Isl 1^+ neurons after 5 days of incubation in RA (1 µM) SAG (500 nM) and a further 9 days of exposure to basal differentiation media (figure 3.1). The first published paper on SPC-01 cells, reported less than 5% Isl 1^+ neurons following 2 day incubation with RA (100 nM) and a further 5 days of differentiation (Cocks *et al*., 2013). The difference in MN yield reported using the same cell source can most likely be attributed to differences in RA concentration, time length of differentiation and the effect of ventralising cues provided by activation of sonic hedgehog signalling used here. Regarding protocol efficiency, based on previous studies using the same concentrations of RA and SAG/Shh, the percentage of Isl 1^+ cells here reported is in line with some of the literature which used other starting cell sources. For example, Wada *et al*. (2009) showed just over 20% of hESCs differentiated into putative MNs – assessed by the expression of Isl 1 – after exposure to RA for 7 days following neural induction. Evidence provided by Qu and colleagues (2014) shows that yield of Isl 1^+ cells and therefore

MN specification, can be improved by a more precise temporal modulation of the factors involved in neural patterning. Indeed, RA signalling precedes Shh activation during embryogenesis. When recapitulating this temporal sequence in hiPSCs *in vitro*, the authors showed a difference in Isl-1 marker expression observed when introducing RA to the culture medium at different stages of their differentiation protocol. A high yield - 76% Isl 1^+ cells - was achieved by the addition of RA at day 3 of their neural induction protocol compared to less than 10% efficiency reported when adding RA at the early (day 1) and late (day 6) phases of neural induction (Qu *et al*., 2014). Similarly, another group adopted the same differentiation strategy, whereby RA signalling and Shh activation are triggered in a temporal manner, leading to approximately 50% of hESCs expressing Isl-1 after 2 weeks (Shimojo *et al*., 2015). Albeit, using different concentration of both factors, the yield reported by both publications is higher than the one described in this chapter. Here, different concentrations of RA and SAG were tested in a bid to increase MN yield assessed by Isl 1^+ expression. The results obtained (figure 3.5) show a similar percentage of Isl 1^+ cells to that obtained with the control condition – RA (1 µM) SAG (500 nM) – thus suggesting that temporal patterning of cells into MNs by RA and Shh agonists might have a bigger impact in efficiency of differentiation than concentrations of such factors. Future work should explore how implementing a differentiation approach based on the activation of RA and Shh signalling in a temporal manner affect the proportion of SPC-01 derived MNs. To this end, SPC-01 cells could be incubated in basal differentiation media supplemented with RA during the initial stages of differentiation before triggering activation of the Shh pathway by addition of SAG.

Overall, the high heterogeneity in factors (i.e. Shh, purmorphamine, SAG) and concentrations used to generate MNs, the various differentiation strategies so far employed in the field as well as the diversity of cell source reported in the literature, pose a challenge when comparing efficiency of MN generation amongst protocols.

One of the concerns with regards to cell transplantation therapies is the risk of indefinite cell division. To mitigate this risk - and for a cell-based regenerative medicine treatment to be considered beneficial - transplantation of a relatively small number of cells should result in sufficient functional restoration (Kato *et al*., 2015). As part of an overall assessment of differentiation, the proliferation potential of differentiated SPC-01 cells was assessed by the expression of Ki67 – a proliferation marker – at various points of differentiation.The results presented in this chapter indicate that proliferation of SPC-01 cells after 2 and 3 weeks of differentiation is minimal (3% and 1%, respectively). The proportion of $Ki67^+$ cells at day 5 of differentiation, however, is comparable to that of undifferentiated cells. As previously discussed (refer to introduction, section 3.1.2.1), the conditional immortalisation of SPC-01 cells translates in an inability of cells to proliferation in the absence of 4-0HT. The removal of 4-OHT and growth factors as well as addition of RA and SAG patterning factors to the differentiation cocktail implemented in this study, triggers cell cycle exit and the generation of post-mitotic cells. High expression of Ki67, indicative of cell proliferation, 5 days after initiation of differentiation could be reasoned by retention of 4-OHT intracellularly, thus allowing for further cell division. Amemori and colleagues (2013) transplanted $5x10^5$ undifferentiated SPC-01 cells in a rat spinal cord injury model. The researchers showed no tumour formation during the entire period of observation; however, they reported 3% of grafted cells expressed Ki67 after 8 weeks *in vivo*. This confounding result does not reflect the findings reported in this chapter, suggesting factors in the spinal cord environment could be promoting cell division even in the absence of 4-OHT. In summary, the data presented here validates the conditional immortalisation of SPC-01 as well as the generation of post-mitotic neurons following *in vitro* differentiation.

Other criteria to determine the success of cell therapies is the effective and reproducible delivery of viable cells to the transplantation site. Here, a syringe-based delivery approach was implemented to test the cellular component of the biohybrid device *in vivo.* To this end, this chapter assessed the delivery of 14 day-differentiated SPC-01 cells through a 25G Hamilton syringe *in vitro* in order to inform cell transplantation *in vivo*. A 25G syringe needle was chosen based on the protocol reported by Erb and colleagues (1993) who, for the first time, showed successful muscle reinnervation following MN transplantation into the tibial nerve of rats.

To assess the impact of expelling cells through a syringe needle of this size, viability and metabolic activity were quantified. The results obtained showed no difference in cell death or metabolic activity using this delivery method compared to the standard Gilson pipette used for cell culture. Indeed, literature on injectable cell therapies have reported a wide range of needle sizes used as delivery methods, nevertheless contradictory results have been published on the potential effect that delivering cells in this fashion may have on their survival. For instance, there are publications reporting no impact on cell viability post-injection (Walker *et al*., 2010), whereas other papers report 40% cell death following syringe-based transplantation methods (Aguado *et al*., 2012). Furthermore, the effect (if any) that injecting cells may have on survival of different cell types has not yet been researched. As cell-based therapies advance onto clinical trials with the potential of being adopted to treat diseases and injuries, it is pivotal that the effect(s) of syringe-based delivery platforms on cell survival and functional properties are investigated in more detail. Moreover, the development of a robust and standardised cell-delivery method is warranted in order to accomplish the transition of cell-based treatments from bench-side to clinic.

Overall, the *in vitro* findings here described, support the use of 25G syringe needles as delivery platforms for the transplantation of SPC-01-derived MNs *in vivo* with the aim to assess the cellular component of the biohybrid approach developed in this project.

The next line of investigation in this chapter was focused on assessing the expression of human-specific markers on differentiated SPC-01 cells that would allow tracing of these cells once implanted in a rat. To this end, it was important to select markers that would not cross react with rat cells. The expression of nestin, a human-specific neural stem cell progenitor marker, was tested *in vitro* on day 14-differentiated SPC-01 cells by immunocytochemistry. The results here reported indicate 84% of differentiated SPC-01 expressed nestin. Similarly, the expression of HuNu antibody was assessed *in vitro*, showing expression in all differentiated SPC-01 cells (figure 3.7). Notably, use of nestin within this body of work was limited for the purpose of distinguishing cells of human origin from cells of rat origin and not with the aim of identifying stage of cell development. Indeed the reliability of nestin as a stem cell marker is questionable as research papers have reported nestin expression in a variety of human cells independent of proliferation status (Hendrickson *et al*., 2011, Dusart *et al*., 2018).

In light of the results obtained *in vitro*, a pilot *in vivo* experiment (n=2) was performed, in which 14-day differentiated SPC-01 cells were transplanted in rats with the aim to establish a model in which the functional properties of potential MN therapy candidates could be explored. To this end the tibial nerve transection model was favoured over the sciatic nerve transection model. This is a robust, well tolerated and less severe approach to induce muscle denervation (Batt and Bain, 2013). Transection of the tibial nerve results in denervation of the gastrocnemius, soleus and plantaris muscles, however, because the common peroneal and sural branches of the sciatic nerve are preserved, animals can easily ambulate as footprint and weight bearing is better preserved compared to sciatic nerve transection; therefore significantly decreasing morbidity. Transplanting MN candidates for cell replacement therapies in one of the sciatic nerve branches of rat muscle denervation models, allows duration of *in vivo* studies to be reduced as the length MNs have to traverse to reach the gastrocnemius muscle is shorter compared to using the more proximal sciatic nerve for transplantation.

At 4 weeks post-transplantation, electrophysiological testing was performed to assess whether this technique could be implemented to test functional reinnervation of muscle in this model. To this end, microchannel electrodes were manufactured (figure 3.8) based on the protocol previously reported by Lancashire *et al*. (2016). The focus for this *in vivo* experiment was to create a channel of suitable dimensions to accommodate rat sciatic nerve branches (approx. 1 mm diameter) that would allow for selective stimulation of individual branches by confining axons within a long, small diameter, electrically insulating channel.

Electrical impedance measured at 1 kHz was 3.9 kΩ (figure 3.9). Overall, the microchannel electrodes herein manufactured were successful at supporting nerve stimulation as observed by contraction of the gastrocnemius muscle and quantification of CMAPs generated following stimulation of unoperated common peroneal nerve (figure 3.10). These microchannel electrodes can overcome limitations associated with standard stimulation electrodes (i.e. Neurosign Bipolar Probe 2 × 100 mm × 0.75 mm electrode). The dimensions of this bipolar probe pose a challenge when stimulating these small nerve branches. Therefore increasing the technical difficulties of electrophysiology tests in tibial nerve transection models and limiting its use to skilled surgeons. The ease of stimulation of small nerve branches with the microchannel electrodes here described, allows for increased adoption of the tibial nerve transection model as a means to induce gastrocnemius muscle denervation and electrophysiologically assess functional muscle reinnervation following treatment.

Electrical stimulation of cell-transplanted nerves, however, yielded no muscle contraction; therefore suggesting a lack of functional connections between the transplanted cells and the muscle (table 3.1). Histological assessment of excised nerves at 4-weeks showed 2 nestin$^+$ cells present in the same experimental animal and a lack of HuNu expression (figure 3.11).

In order to demonstrate implanted cells can be detected in this model, future studies should include an earlier time point to perform histology of the cell-transplanted nerve immediately after cell delivery. Albeit no conclusions can be drawn from this pilot data, this *in vivo* study allowed to evaluate two key aspects of this experimental design. First, it served to test the feasibility of cell delivery into the rat tibial nerve using the equipment and methodology herein reported. Second it allowed histology analysis of the transplanted distal tibial nerve stump to assess whether xenograft transplantation of differentiated SPC-01 cells is viable in immunocompetent rats.

With regards to the first aspect; optimisation of the injection procedure is warranted to ensure robust, reliable and reproducible cell administration. An injector system that allows flow rate to be controlled would be beneficial in standardising cell administration protocols. Indeed, it has been previously documented that injection rate has an impact on cell viability, apoptosis and senescence (Amer *et al*., 2017).

In terms of the second aspect; the expression of host-derived T-helper and cytotoxic cells was quantified in the experimental animal in which nestin$^+$ cells were detected. Histology results showed slightly minor differences between experimental and sham in the expression of both T-cell markers (figure 3.12B). Assessment of the distribution of T-cells along different regions of the nerve showed the vast majority of cytotoxic T-cells in the experimental animal were localised at the proximal stump, near the site of cell transplantation; this pattern was not observed in the sham animal (figure 3.12D). High variability observed across longitudinal nerve sections, however, posed a challenge in identifying a clear T-cell mediated response against transplanted cells at 4 weeks.

Overall, various explanations could be proposed to account for the minimal expression of human-specific nestin. Given the small sample size and the lack of repeats, however, this experiment should only be taken as a preliminary study to evaluate the different factors that need to be optimised in a future study.

In order to understand whether differentiated SPC-01 cells can evade the host-immune system when transplanted into immunocompetent animals, assessment of T-cell expression at earlier time points is required. Indeed, Santos Roballo *et al*. (2019) reported peak expression of T-helper cells at day 7 following allograft nerve transplants in immunocompetent rats. By 4 weeks, the expression of this cell marker declined to match that seen in the autograft nerve transplant group. With regards to cytotoxic T-cells, the authors observed a peak increase between day 7 and day 14, with a decline in their expression by day 28. A critique of this work is the 4-week time point chosen to evaluate the host immune response following cell transplantation. Based on previous literature, future experiments should assess the host immune response between day 7 and day 14 post-transplantation.

In summary, the results presented in this chapter highlight the ability of SPC-01 cells to generate Isl1$^+$ cells following directed differentiation. Furthermore, the differentiation protocol implemented here shows efficient and rapid differentiation of cells with minimal proliferation activity after 14 days. SPC-derived MNs can be transplanted using a syringe delivery platform with the needle gauge size described here, as no effect was found in metabolic activity or cell survival.

Finally, preliminary *in vivo* data suggests the tibial nerve transection model is a useful approach to induce muscle denervation with minimal morbidity. This was validated by the CMAPs generated upon stimulation of the unoperated common peroneal nerve compared to the absence in muscle activity observed following stimulation of the transected tibial nerve. Furthermore, this model can be successfully implemented to deliver MN cell therapy candidates via injection. The ability of these transplanted cells to reinnervate muscle can be electrophysiologically tested using microchannel electrodes to stimulate small diameter nerve branches.

In conclusion, this chapter presents a protocol for the differentiation of SPC-01 cells into Isl1^{+} cells and describes an *in vivo* muscle denervation model suitable for cell transplantation and testing muscle reinnervation

Notably, the adoption of a purely histological approach to identify MNs following directed differentiation is open to criticism and a limitation of the body of work here presented. Moreover, the use of βIII-tubulin and Isl-1 to evaluate the presence of MNs in the differentiated culture is certainly a major limitation of this study. Co-expression of at least 2 or 3 motor neuron markers represents a more reliable criteria to identify this cell type in differentiated cultures. To this end, previous research had relied on Isl1 and Isl2 antigens or a combination of Hb9 and Isl1/2 immunostaining (Sances et al., 2016). However, these LIM-homeodomain transcription factors are downregulated during motor neuron development, therefore presenting a challenge when characterising MNs. Choline Acetyltransferase (ChAT) is expressed by all cholinergic neurons including MNs, however, its expression is only detectable in mature MNs. Given the developmental stage of ISL1+ cells detected in this study was not explored, future work should stain for a combination of young and mature motor neuron markers in order to provide more reliability to the differentiation results here presented.

Additionally, an indispensable property of MNs is their ability to form neuromuscular junctions and mediate muscle contraction. Without this functional evidence, the differentiated cells here described and further implemented in the remaining chapters of this work can only be described as putative MNs.

Future work should focus on investigating the morphological characteristics of differentiated SPC-01 cells (for motor neurons, one would expect to see a multipolar cell, with a large soma, single axon and multiple dendrites). SIM-32, an antibody that stains MN- enriched Neurofilament Heavy Chain (NFH) could be used to stain MN processes and facilitate morphological analysis of these cells.

Implementing electrophysiological techniques such as patch clamping would allow to evaluate the excitability of this differentiated culture. Furthermore, performing co-culture experiments with muscle cells to evaluate the ability of differentiated SPC-01 cells to form NMJs, is crucial to reliably identify the presence of MNs among differentiated SPC-01 cells. These thorough characterisation allows to determine if the differentiated cells used throughout this body of work are indeed motor neurons.

The lack of characterisation of the full population of differentiated SPC-01 cells warrants further investigation. With only a small proportion of cells expressing both βIII-tubulin and Isl-1, it is unclear what other cell types are present in the culture. Future work should seek to characterise the overall population of differentiated cells. Based on previous work by Cocks *et al.* (2013), SPC-01 cells differentiate into a mixed population of astrocytes, oligodendrocytes and interneurons. To detect astrocytes, glial fibrillary acidic protein (GFAP) should be used in future experiments. The presence of oligodendrocytes in the culture could be detected with anti-olig2 antibody, a transcription factor necessary for oligodendrocyte development. Additionally, the presence of these glia cells could be further corroborated by co-staining with sox 10, a transcription factor directing NSCs towards a glial lineage. Finally, staining for Chx10 (transcription factor expressed in V2a interneruons) could help elucidate the presence of spinal cord glutamatergic interneurons.

4.0 Design, development and optimisation of electrode arrays for *in vitro* cell culture experiments

4.1. Introduction

Culturing neurons on electrode arrays for extracellular stimulation *in vitro* is a crucial step towards the development of an implantable biohybrid device for muscle stimulation. To this end, an ideal electrode array must have the following properties: made from biocompatible materials; be durable; support cell growth; and have electrodes which can apply effective stimulation.

Currently, the most commonly used manufacturing techniques to produce this type of electrode arrays include: photolithography, wet etching and thin-film deposition (Grumet *et al*., 2000, Heuschkel *et al*., 2002, Gholmieh *et al*., 2006, Ordonez *et al*., 2012). These techniques have so far been successfully implemented to produce high-density electrode arrays with features in the micrometre scale that support cell growth and stimulation; however, they require the use of specialised materials and equipment available to few research labs. Access costs for suitable facilities at UCL are estimated at ~£10,000 per annum. Additionally, typical microelectrode array systems are commercialised at prices in the range of tens to thousands of euros, with a considerable increase if electrical stimulation needs to be added to the system (Rolston *et al*., 2009). Furthermore, their implementation entails multiple production stages, thus rendering the process laborious and limiting the widespread use of these technologies for custom made devices (Green *et al*., 2013a, Carnicer-Lombarte *et al*., 2017). As an alternative, thick-film technology was implemented throughout this body of work to manufacture electrode arrays. This is a simple, versatile, and low-cost manufacturing technique that allows batch production of robust, reproducible and biocompatible electrode arrays (Carnicer-Lombarte *et al*., 2017) to be implemented in the development of biohybrid devices. This approach would also potentially reduce the 'cost of goods' in a final product, thus making it more suitable for future clinical and commercial translation.

4.1.1 Thick-film technology for electrode array manufacturing

Thick-film technology (refer to Materials and Methods chapter, figure 2.5) is an established method for effective manufacturing of hybrid microelectronic circuits (White, 2017). This technology is being implemented by corporations like Cortec® for packaging of implantable microelectronics (Cortec, 2017). Furthermore, Ordonez *et al*. (2012) reported the manufacturing of retinal vision prostheses using this technology.

The fabrication process is based around screen printing a desired ink paste on a substrate followed by a sintering stage. Specifically, an ink paste is transferred through a mesh screen with the desired pattern onto a substrate by the passage of a flexible blade (known as squeegee). The ink paste is then sintered to develop the electrical properties of the material and permanently bond this film onto the substrate. Ink pastes comprise three components: the active material (e.g. a metal conductor); a glass binder; and a viscous organic fluid. During sintering the organic fluid is first evaporated by drying at low temperatures, then in a high temperature firing stage the glass binder forms an adhesive layer to the substrate and interdiffusion between adjacent particles of active material produces a continuous (e.g. conductive) phase (White, 2017). This technique is widely used in many industries, including the pharmaceutical sector, where commercialised chemical and biosensors have been developed through this manufacturing process (e.g. glucose biosensors used by patients with diabetes) (Hu, 1998).

Notably, although the term thick-film is used, the conductive layer produced is in the order of a few micrometres. In contrast thin-film processes are in the nanometres scale.

Various materials have been reported in the manufacturing of thick-film electrodes. Appropriate choice of substrate and conductor is crucial in the development of a biocompatible device with electrode properties suitable for neural stimulation. The following section describes some of the most common substrates and conductor pastes used in thick-film technology.

4.1.1.1 Substrates

A substrate serves the function of providing mechanical support and electrical insulation for the printed circuit. The most commonly used substrates for thick-film technology are the ceramics, specifically alumina (Al_20_3) (White, 2017). Alumina of 96% purity and 4% silica and magnesia is commonly implemented in microelectronics (White, 2017, Carnicer-Lombarte *et al*., 2017). This type of ceramic has desirable physical and chemical properties, such as inertness, high electrical resistivity, thermal conductivity and high chemical resistance (Preusch *et al*., 2014), all of which are desirable for this body of work. Furthermore, from a clinical perspective, alumina resistance to wear and biocompatibility has led to the adoption of this material for orthopaedic (Zeng, 2013) and dental applications (A Al-Sanabani *et al*., 2014).

Stainless steel is another substrate implemented in the manufacturing of thick-film circuits. Desirable properties of stainless steel include: strength, elasticity and relatively high thermal conductivity (White, 2017). However, because of its good electrical conductivity, stainless steel requires coating with a glass insulating layer before it can be used as a substrate for thick film circuit, therefore, adding further steps and materials in the development of electrode arrays.

Polymers are also implemented as substrates for thick-film technology, their main desirable property for medical applications, and especially for devices implanted in a soft environment, is their flexibility. Most of these materials are soft, light-weight and low cost (Chen *et al*., 2018b). Polymer materials commonly used in the development of thick-film circuits include: polyesters, polycarbonates and polyimide plastics (White, 2017). However, issues related with biocompatibility of some polymers presents a challenge in their wide use for biomedical applications. Indeed polymer-based biomaterials and medical devices currently used have been associated with bacterial infections (Busscher *et al*., 2012). Furthermore, plasticised poly (vinyl chloride) (PVC), a polymer commonly used in the manufacturing of blood bags, intravenous infusion sets and tubing (George *et al*., 2011) has generated wide concerns due to documented toxicity in the liver and reproductive organs in some animal species (Tickner *et al*., 2001). Research efforts are being made to modify these materials in order to mitigate biosafety concerns associated with polymer-based devices for clinical applications (Yin and Luan, 2016).

4.1.1.2 Conductors

Conductors provide interconnections between the components in the circuit. Metals such as gold (Au), platinum (Pt) and silver (Ag) and their alloys are commonly implemented. The emerging biomedical applications of electrode arrays and the development of implantable electrical devices requires the fabrication of smaller electrodes. These microelectrodes are characterised by high impedance and limited charge injection capacity, which for some therapeutic applications, may not be suitable. Amongst the metals used in the manufacturing of permanently implantable electronic devices, Pt and Pt alloys are a popular choice. Pt is a reliable metal with desirable properties such as: biocompatibility, inertness, relative stability within the body, durability, good electrical conductivity and radiopacity (Woodward, 2014). Over the last four decades, Pt electrodes have been incorporated in implantable devices used to treat heart diseases (Cowley and Woodward, 2011), chronic pain (Keifer *et al*., 2014), stroke (Kil *et al*., 2018) and other neurological disorders. More recently, its use has been reported in neuromodulation devices like cochlear implants for hearing loss (Lee *et al*., 2018), retinal implants for vision prostheses (Allen *et al*., 2013) and deep brain stimulation devices for patients with Parkinson's disease (Petrossians *et al*., 2016).

Work by Green *et al*. (2013a) and more recently by Carnicer-Lombarte *et al* (2017) suggests thick-film technology can be implemented in the manufacturing of circuits for use in the neuroscience and tissue engineering fields. In this paper, the authors report customisable, high-density electrode arrays manufactured by thick-film technology using commercially available Pt/Au alloy and insulator inks printed on alumina substrates. The resulting arrays had electrical and topological features comparable to those obtained using more complex and expensive manufacturing methods. Furthermore, when tested *in vitro*, the electrode arrays were found to be biocompatible and to support growth of neuronal cell lines. The electrodes produced by thick-film printing have unusually highly porous surfaces due to the composition of the paste ink. This porosity translates into a bigger surface area over which charge transfer may occur, thereby compensating for the limitations of microelectrodes by decreasing impedance and improving the amount of charge that can be injected (Green *et al*., 2012, Carnicer-Lombarte *et al*., 2017). Roughening of electrodes is widely reported in the literature as a means of increasing charge injection capacity. Roughening has been achieved by altering the metallic surface of electrodes through laser micromachining (Green *et al*., 2012) or through coating electrodes with materials like the conductive polymer poly(ethylene dioxythiophene) PEDOT and carbon nanotubes (reviewed in Aregueta-Robles *et al*. (2014)).

Overall, thick film technology is a promising technique for the manufacturing of microelectrode arrays for biomedical applications. Although, initially developed to produce robust electronic devices such as hybrid integrated circuits and sensors, recent research suggests this technique can be adopted to manufacture electrode arrays for biological research and clinical applications.

The adaptation of micro-fabricated devices to biology has created the unprecedented possibility of studying multiple neurons and their network activity *in vitro.* Indeed, devices like microelectrode arrays (MEAs) have been implemented *in vitro* to assess electrophysiological properties of neuronal networks (Obien *et al*., 2014, Aqrawe *et al*., 2018). Over the years, MEAs have evolved from a standard culture dish with electrodes to more complex designs that integrate topographical cues to guide cell growth. Previous research has successfully combined microelectrode arrays with topographical cues to allow for the stimulation of cell bodies located outside microchannels and recording from axons growing inside microchannels (Habibey *et al*., 2017).

4.1.2 Introducing topographical cues on electrode arrays by substrate micropatterning

In designing the optimal biohybrid device to stimulate denervated muscles, one of the desired features is to guide neurite outgrowth on the shortest route to reinnervate muscles. To this end, a proposed solution is the incorporation of topographical cues on electrode arrays.

A wealth of literature has been reported on the use of micro-patterned surfaces to guide neuronal cell growth (Curtis and Wilkinson, 1997, Hoffman-Kim *et al*., 2010, Chen *et al*., 2018a). The concept of 'contact guidance' was first introduced by Weiss (1934) to describe how nerve fibres follow a topographic pattern of oriented fibrin micelles *in vitro*. Since then, research has shed light on the complex guidance system cells employ to project axons to their specific targets. As part of this process, growth cones located at the tip of axons, explore their surroundings and direct axons along a defined path (Wen and Zheng, 2006).

Contact guidance of neurons can be achieved through microfabrication techniques by introducing surface features that allow the control of the direction of growth. To this end, dimensions of surface topographies should be in the cell (20-95 µm in diameter) (Lee *et al*., 1986) and axon (2-20 µm in diameter) ranges (Wieringa *et al*., 2018). Grooved substrates are one of the most common imposed topographies, partly because it resembles the topography of the nervous system but also due to their relative ease of fabrication (Roach *et al*., 2010). Topographical cues have been shown to impact various aspects of neuronal behaviour (Simitzi *et al*., 2018); this section will evaluate literature focused on neuronal cell alignment and neurite length in response to distinct microgroove dimensions.

Microgrooves of various depths (0.2 to 69 µm) and widths (5 to 350 µm) have been implemented as a mean of providing directional cues to neurons (Nikkhah *et al*., 2012). There is a high variability between studies, which can be attributed to different types of neurons and surfaces used, therefore, the precise features that result in a particular desired response are yet to be determined. Generally, the trend observed is that greater neurite alignment is induced by deeper and narrower grooves (larger aspect ratio).

For the purpose of simplicity, all groove dimensions are referred to as width x depth in µm (e.g. 10 x 4 µm means 10 µm wide by 4 µm deep groove). A study on PC-12 neuronal-like cells reported improved cell orientation in response to 20-30 x 11 µm grooves compared to wider grooves (Mahoney *et al*., 2005). Rajnicek *et al*. (1997) reported rat hippocampal neurons had a greater preference to grow parallel to 4 x 0.5 - 1 µm grooves compared to narrower and shallower grooves where perpendicular orientation was observed. MN-muscle co-cultures using micro-fluidic culture systems have reported the successful compartmentalisation of neuron cell bodies and muscle cells with neurites extending along 10 x 3 µm microgrooves (Park *et al*., 2012, Zahavi *et al*., 2015). Furthermore, research on murine cortical neurons has shown that deeper grooves (22 – 69 µm) rather than shallower grooves (2.5 – 4.6 µm) can cause neurites to turn following contact with the edge of the groove to remain inside the delineated channel rather than crossing over the groove wall, preserving the intended direction of growth (Li and Folch, 2005). Increased alignment induced by deeper grooves has also been reported on chicken embryonic spinal cord cells (Weigel *et al*., 2012). Additionally, there is evidence to suggest that functionalising these topographies with biomolecules such as nerve growth factor (NGF) and laminin further enhances the effect on alignment and promotes a higher degree of neurite extension (Gomez *et al*., 2007, Kang *et al*., 2011). Interestingly, there is a limit on the effect of narrow grooves on inducing alignment as < 1 µm wide structures promote perpendicular neurite outgrowth in most kinds of CNS neurons but not PNS neurons (Nagata *et al*., 1993).

Regarding the effect of topographical cues on neurite length, Li *et al*. (2008) reported increased neurite length of chick sympathetic neurites growing along 1-2 x 0.1 µm grooves compared to those in an unpatterned, relatively flat control group. PC-12 cells have also been shown to extend longer neurites when aligned to 0.8 x 1.2 µm grooves; however, this effect was observed only when NGF was added to the culture media (Su *et al*., 2013). This reinforces that the synergistic effect of topographical and chemical cues on guidance and neurite extension is more effective than individual cues. Recently, Terryn *et al*. (2018) showed improved neurite outgrowth of hiPSCs differentiated into cortical neurons when cultured on 4 x 3 µm microgrooves.

Overall, there is compelling evidence in the literature that suggests the incorporation of microgrooves on substrates for neuronal cell culture induces alignment of neurites in a desired direction and promotes longer neurite outgrowth, both of which are desirable features when engineering a biohybrid device.

4.1.3 Electrochemical characterisation of microelectrodes for neural stimulation

An understanding of the electrochemical properties of manufactured electrode arrays is essential for any device manufactured with the aim to be implanted. The ability to electrically stimulate MNs to induce biological action potentials is paramount for the success of this biohybrid approach to muscle stimulation and recording. Electrochemical techniques like cyclic voltammetry (CV) and electrical impedance spectroscopy (EIS) are commonly employed to characterise electrodes for neural stimulation and recording. These techniques provide an understanding of the electrode properties and of the electrochemical mechanisms underlying stimulation. For effective stimulation to occur, current density at an electrode needs to be sufficient to inject the required charge that will initiate the desired effect (i.e. MN cell depolarisation) (Cisnal *et al*., 2018). Charge injection, in most neural applications, is commonly performed using a current-controlled method, whereby a two phase-charge balanced electric pulse injects the same amount of anodic and cathodic charge, thus resulting in zero net charge transfer as direct current during a stimulation pulse (figure 4.1) (Cisnal *et al*., 2018). For physiological reasons, the leading phase is usually cathodic and is used to achieve the desired physiological function. This is followed by the anodic phase which reverses the electrochemical processes that took place during the cathodic phase (Merrill *et al*., 2005, Voigt and Kral, 2019).

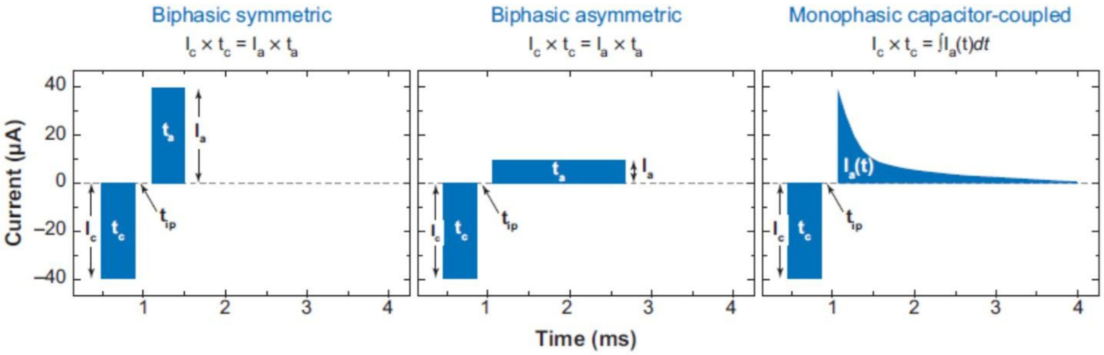
Biphasic symmetric $I_c \times t_c = I_a \times t_a$

Biphasic asymmetric $I_c \times t_c = I_a \times t_a$

Monophasic capacitor-coupled $I_c \times t_c = \int I_a(t)dt$

Figure 4.1 Charge-balanced, current waveforms used in neural stimulation

Examples of charge-balanced current waveforms used in neural stimulation leading to zero net charge transfer. I_c (cathodic current), I_a (anodic current), t_c (cathodic half-phase period), t_a (anodic half-phase period), t_{ip} (interphase dwell) (Cogan, 2008).

During CV measurements, a voltage is swept in a cyclical manner at a constant rate between two potential limits, causing current flow between two electrodes. This applied potential promotes reactions to occur at the electrode and the current measured is proportional to the rate of these reactions. CV measurements allow the investigator to assess the amount of electroactive surface area on the electrode and the electrochemical processes that the surface undergoes during charge transfer. Indeed, it is common practice in this field to characterise stimulation electrodes by their cathodic charge storage capacity (cCSC) (Cogan, 2008). This parameter, quantifies the maximum total amount of reversible charge available for the cathodic phase of a stimulation pulse and is calculated by integrating the cathodic current in a slow sweep-rate voltammogram over a potential range that falls within the limits of water electrolysis ('water window'). It has been previously reported by Cogan (2008) that charge transfer properties vary with electrode size and geometry due to current being distributed in a non-uniform manner. Similarly previous literature, has shown that charge injection is also dependent on electrode material (Merrill *et al*., 2005).

The development of electrodes with smaller geometric surface area (GSA) of suitable size for implantation results in increased electrode impedance and limitations in the amount of charge that can be safely delivered to achieve clinical benefits. To overcome this challenge, coating technologies such as Iridium oxide (Wang *et al*., 2009), conducting polymers like poly (3,4-ethylene dioxythiophene) (PEDOT) (Venkatraman *et al*., 2011) and generally other alloys or coatings with high surface roughness are used (Cisnal *et al*., 2018). These strategies cause an increase in the effective surface area (ESA) of the electrodes where charge transfer can take place and, therefore, the amount of charge that can be safely delivered.

Porous electrodes have a similar effect with regards to increasing ESA and decreasing impedance. Electrodes produced by thick-film printing are characterised by their highly porous surface. Carnicer-Lombarte *et al*. (2017) reported lower impedance values with Pt/Au porous electrodes (~8 kΩ at 1 kHz for GSA of ~0.0295 mm^2) compared to Pt foil (26 kΩ at 1 kHz) and thin-film smooth Au electrodes (59.1 kΩ at 1 kHz) of similar sizes. Fundamentally, porosity of electrically active surfaces determines the available surface area for electrochemical reactions to occur. Higher surface area increases surface capacitance which leads to a decrease in electrical impedance. However, geometry of the electrodes may impose a limitation on the increased charge injection capacity that results from having larger surface areas. This is particularly evident with narrow and deep pores, where access to all available charge is limited by the increased resistance on the interior of the pore (Norlin *et al*., 2005).

The electrochemical reactions occurring to support electrical stimulation are well documented in the literature. When a metal is immersed in a solution, or in more general electrochemical terms, *the electrolyte*, a transduction of charge carriers from electrons in the metal to ions in the electrolyte occurs (Merrill *et al*., 2005). Two types of reactions are known to underlie this transduction and therefore support stimulation: non-Faradic or capacitive reaction and Faradic reaction or reduction-oxidation reactions. The former is characterised by the lack of electron transfer between electrode and electrolyte, instead a redistribution of charged chemical species in the electrolyte occurs, which creates of plane of charge on the surface of the electrode and a plane of opposite charge in the electrolyte, like the charges on the plates of a capacitor. This state between the electrode and electrolyte can be modelled by an electrical capacitor and is known as the double layer capacitance. During stimulation when the charge of the electrode is altered, a redistribution of charge at the electrode/electrolyte interface occurs. Faradic reactions are characterised by electron transfer and the reduction or oxidation of chemical species at the electrode-electrolyte interface. During Faradic charge transfer, reduction and oxidation reactions lead to formation of new chemical species. Upon reversing the direction of current, these reactions are only reversible if the species formed are available at the electrode during the reverse current pulse (Merrill *et al*., 2005). Species can become unavailable due to processes including precipitation, diffusion, and off-gassing, causing a permanent chemical change to the electrode or electrolyte. For this reason, it is thought that the safest mechanism for neural stimulation with Pt electrodes will mostly rely on double layer charging (capacitive reactions) to minimise chemical changes in the electrolyte (Rose and Robblee, 1990, Merrill *et al*., 2005, Green *et al*., 2013a).

In addition, some metals like Pt, have the property of charge injection by pseudocapacitance. This is a process whereby Faradic electron transfer occurs. However, species in the electrolyte receiving electrons remain bound to the electrode metal surface; therefore, these reactions are more likely to be reversible upon changing the current direction. Although electron transfer occurs as in Faradic reactions, pseudocapacitance is better modelled as a capacitive reaction because charge is being stored at the electrode rather than dissipated in the electrolyte. An example of pseudocapacitance is hydrogen adsorption to platinum electrodes during the cathodic phase of stimulation and desorption once the potential is moved to a positive direction (anodic phase) (Kumsa *et al*., 2016).

4.1.4 Objectives of this chapter

The aims of this chapter were two-fold:

First, to manufacture electrode arrays suitable for: supporting differentiated SPC-01 cells, supporting neurite elongation and guiding neurite outgrowth *in vitro*.

Second, to characterise the electrochemical properties of manufactured electrodes with the purpose to determine their suitability for effective stimulation of differentiated SPC-01 cells. This was tested by a series of experiments with the following objectives:

(i) To design and manufacture Pt/Au electrodes using thick-film technology

(ii) To incorporate topographical features using laser micromachining methods to promote neurite guidance and increase neurite length of differentiated SPC-01 cells

(iii) To culture differentiated SPC-01 cells on laminin-coated electrode arrays and assess neurite elongation *in vitro*

(iv) To electrochemically characterise manufactured electrodes by CV and EIS measurements and to assess how these properties change following laminin-coating.

4.2 Results

4.2.1 Exploring optimal groove dimensions to screen print Pt/Au onto laser-structured alumina

The optimal dimensions for robust and reproducible electrode array manufacture using the laser-structured alumina manufacturing process were determined (refer to methods chapter section 11.1.1). Grooves of equal length and varying width, controlled by design pattern, and depth, controlled by number of laser passes, were laser-ablated onto an alumina substrate. Pt/Au was screen-printed onto the laser-structured sample, excess paste (i.e. paste located outside grooves) was removed by the manual passage of a squeegee (figure 4.2). The quality of groove filling was quantified with ImageJ using a region of interest brightness scale from 0 (white, empty) to 255 (black, fully filled). Samples across all widths tested obey the same trend; grooves ablated using 9 laser passes (approximately 22 µm deep) or less remained only partially filled. Grooves manufactured using 3 laser passes (approximately 7 µm deep) retained near to none Pt/Au paste and optimal paste filling was achieved in grooves ablated using 20 laser passes (approximately 48 µm deep) (figure 4.3). Equivalent depth of laser passes was calculated based on the thickness of the alumina substrate (550 µm) and the number of laser passes required to ablate a hole (225).

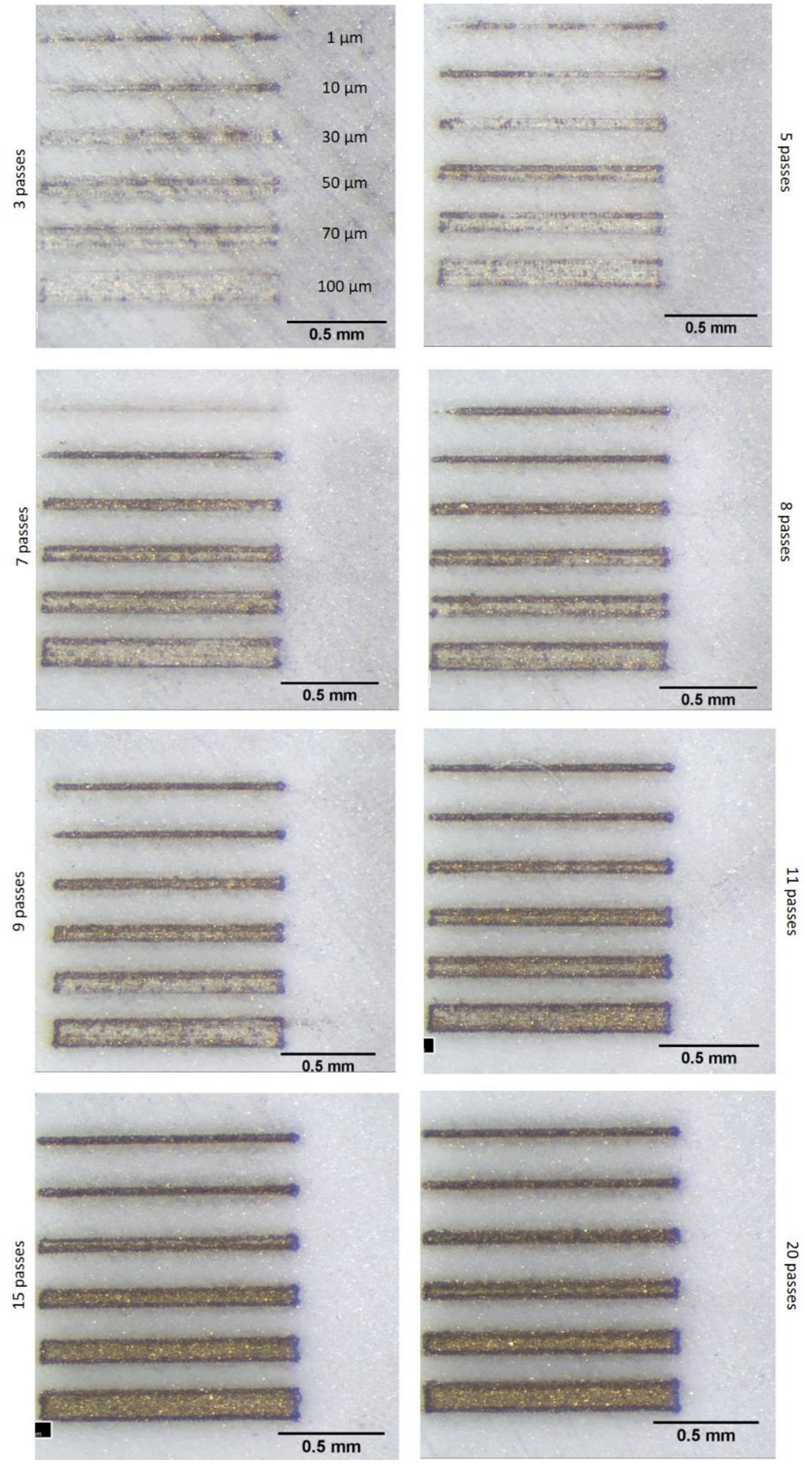
1 µm
10 µm
30 µm
50 µm
70 µm
100 µm
3 passes
5 passes
7 passes
8 passes
9 passes
11 passes
15 passes
20 passes
0.5 mm

Figure 4.2 Pt/Au paste screen-printed onto laser-ablated grooves of various dimensions

Representative micrographs of a Pt/Au screen-printed alumina sample with laser-ablated grooves of various width manufactured using a different number of laser passes. Each image in the panel depicts 6 grooves of 1, 10, 30, 50, 70 and 100 µm width produced using 3, 5, 7, 8, 9, 11, 15 and 20 laser passes

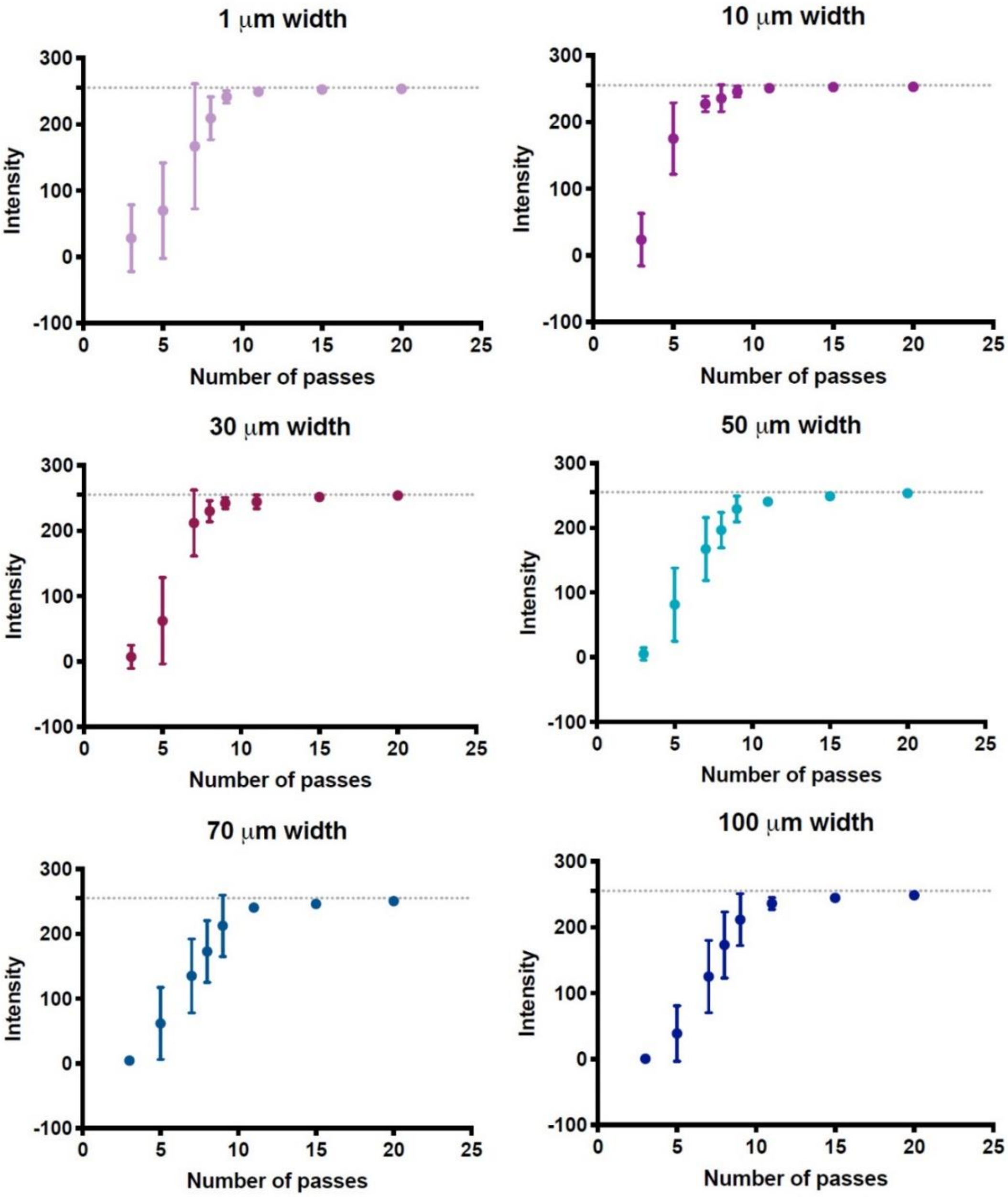

Figure 4.3 Quantification of the quality of Pt/Au paste filling on screen-printed, laser-ablated grooves of various dimensions

Quantification of quality of Pt/Au paste filling for each width tested. Dotted lines on each graph represent fully filled grooves (255) whereas 0 indicates empty grooves. Data presented as mean ± SD for n=8 repeat grooves on 1 alumina sample.

Based on this result, 20 laser passes was adopted for the manufacturing of microchannel electrode arrays as it yielded the most reliable and consistent screen-printing results.

4.2.2 Manufacturing of microchannel electrode arrays by the laser-structured alumina method

The laser-structured alumina method was used to create the microchannel electrode array design (refer to Materials and Methods chapter, section 2.2.8.1). Figure 4.4 depicts the processing steps of this manufacturing method. However, a number of challenges were encountered and the method was not successfully replicated in all samples.

First, the manual passage of a squeegee to remove excess paste from screen printed samples resulted in some paste being removed from solder pads (figure 4.5A) therefore, causing a discontinuity in the electrically conductive path. To overcome this challenge the solder pads were redesigned to feature smaller squares, thus creating a smaller surface area that resulted in the successful retention of the paste ink in the solder pads once the excess paste was removed (figure 4.5B).

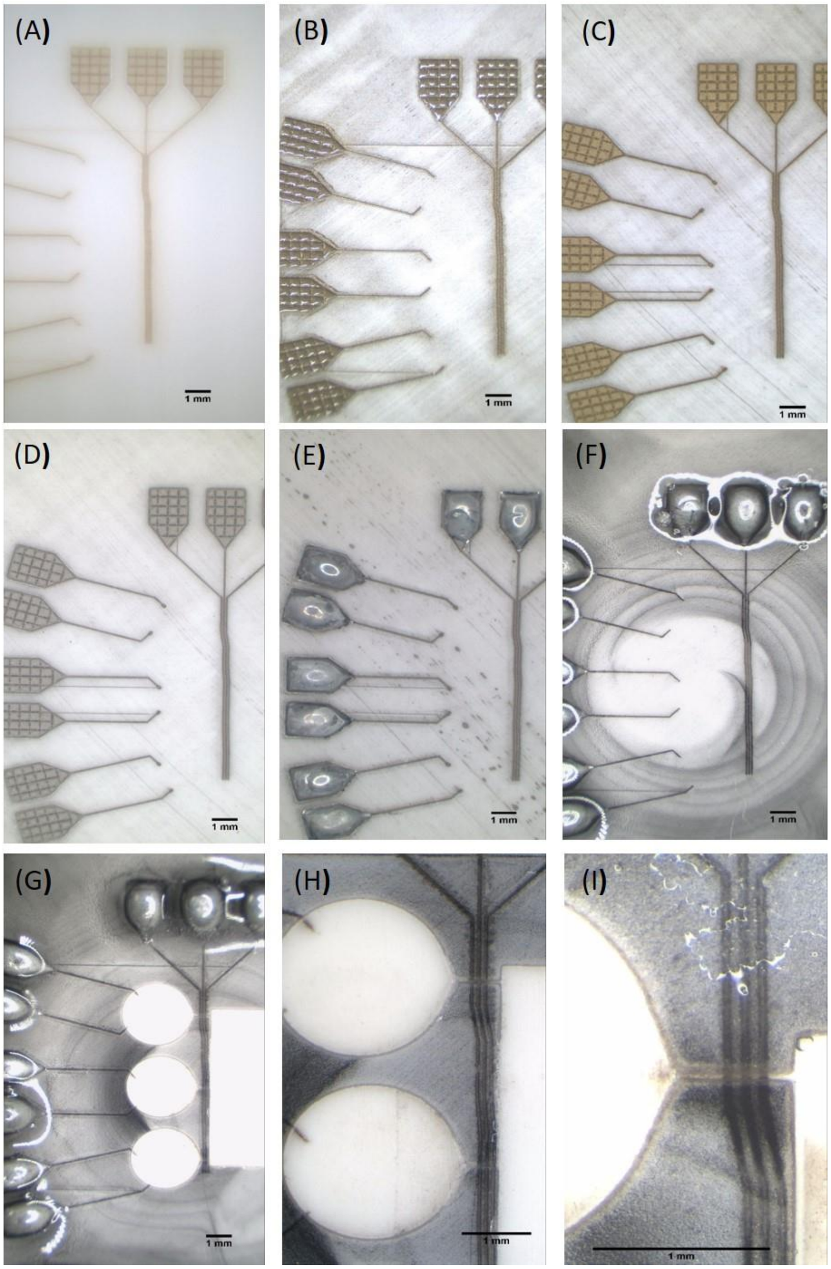

Figure 4.4 Light micrographs of processing steps in the laser-structured alumina manufacturing method

Representative images depicting each step in the manufacturing of microchannel electrode arrays. (A) Laser ablated alumina showing the tripolar recoding electrodes and 6 stimulating electrode tracks, (B) screen-printed Pt/Au paste. Excess paste removed, (C) Pt/Au paste dried, (D) Pt/Au paste sintered, (E) Pads soldered and samples cleaned in and ultrasonic bath, (F) Layer of black silicone spin-coated. Excess silicone not removed, (G) Laser cut silicone and areas of interest manually removed to expose cell-seeding reservoirs and electrode sites, (H) Two cell-seeding reservoirs with exposed stimulation electrodes and track of recording electrodes arranged in a tripolar configuration, (I) Microchannel with exposed recording electrode sites. Errors introduced by the laser resulted in additional lines added to the electrode array design*. Representative images from different samples manufactured at various stages.

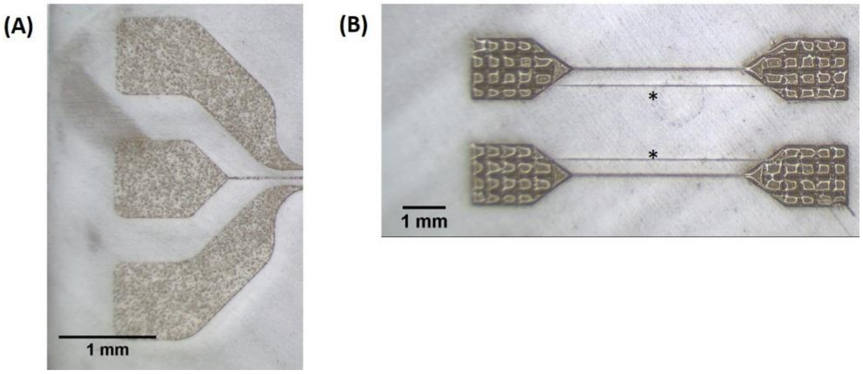

Figure 4.5 Light micrographs of screen-printed solder pads following excess paste removal

Solder pads following excess paste removal by the passage of a squeegee. (A) Discontinuity in electrically conductive path as a result of excess paste removed from areas within solder pads. (B) Redesigned solder pads feature smaller squares, decreasing surface area and leading to retention of metal paste following removal of excess paste with the manual passage of a squeegee.

In spite of successfully manufacturing electrode arrays after overcoming issues, the process was found not suitable as it could not be consistently replicated across all samples in a batch. Once manufacturing was completed and pads soldered, samples were cleaned in an ultrasonic bath (see section 2.2.9.1) to remove flux residues generated during soldering. Following the cleaning process, parts of the Pt/Au detached from the alumina causing discontinuity in the electrically conductive path (figure 4.6).

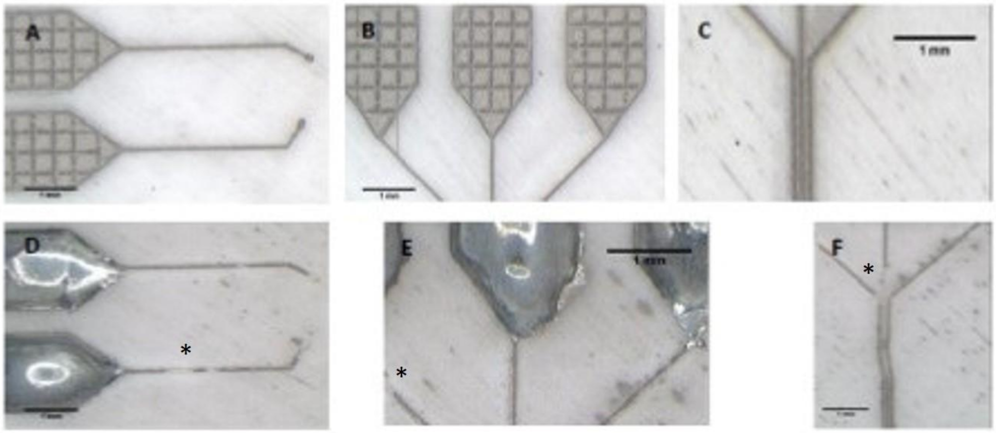

Figure 4.6 Light micrographs of electrode arrays manufactured using the laser-structured alumina method before and after cleaning in ultrasonic bath

The top panel shows different areas of microchannel electrode arrays after Pt/Au sintering and bottom panel depicts the same areas following cleaning in ultrasonic bath. (A and D) Pair of stimulation electrodes; (B and E) Recording tripole solder pads; (C and F) Recording tripole tracks. * indicate areas of Pt/Au detachment. Scale bars = 1 mm.

To investigate the cause of this detachment, the interface between the alumina and the Pt/Au layer was investigated using SEM. A single track with solder pads at both ends was manufactured using the laser-structured alumina method (figure 4.7). Some samples were screen printed with Pt/Au paste, dried and sintered while others were laser ablated with the electrode design and used as controls to explore the effect of laser ablation on the alumina surface. Both control and screen-printed samples were cleaned in an ultrasonic bath as previously described. SEM results of the control samples (figure 4.7A) show differences in the appearance of unmodified alumina compared to those areas that were exposed to laser ablation. Moreover, SEM micrographs of screen printed samples show the presence of voids at the interface between alumina and metal paste (figure 4.7B). In order to improve adherence issues, the manufacturing process was modified. First, the metal paste was dried at a lower temperature (i.e. 50 ^{o}C) for a longer time period (i.e. overnight), however, detachment was still observed in some samples (refer to Materials and Methods chapter, section 2.2.9.1 for details on conventional manufacturing process). To address the possibility of entrapped air bubbles forming voids at the alumina surface, hindering adherence of the paste, samples were placed under vacuum in a pressurised chamber set at approximately 1.5 bar immediately after screen-printing and dried in an oven following the conventional manufacturing process (i.e. 125 ^{o}C for 15 minutes) or the modified manufacturing process (i.e. 50 ^{o}C overnight). Fewer voids were observed on SEM images of vacuumed samples dried following the conventional and the modified manufacturing process (figure 4.7). Nevertheless, detachment of the metal layer was still a persistent issue.

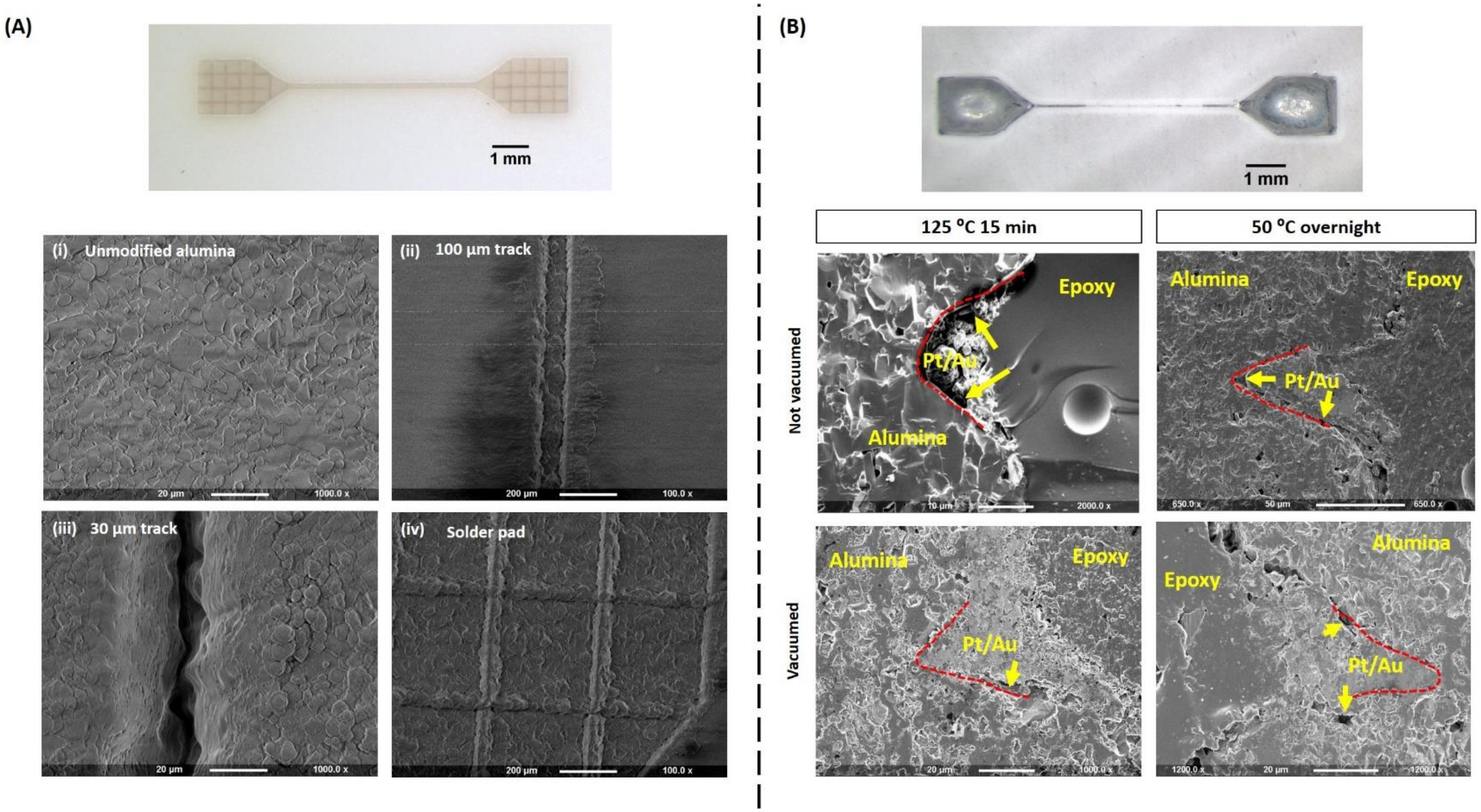
(A)
1 mm
(i) Unmodified alumina
20 µm
1000.0 x
(ii) 100 µm track
200 µm
100.0 x
(iii) 30 µm track
20 µm
1000.0 x
(iv) Solder pad
200 µm
100.0 x
(B)
1 mm
125 °C 15 min
50 °C overnight
Not vacuumed
Vacuumed
Epoxy
Pt/Au
Alumina
Alumina
Epoxy
Pt/Au
Alumina
Epoxy
Pt/Au
Epoxy
Alumina
Pt/Au

Figure 4.7 SEM micrographs of laser-ablated alumina with and without screen-printed Pt/AU

(A) Representative light microscopy image of laser-ablated alumina design analysed under SEM. (i) Area of alumina that was not laser-ablated with grains visible at the surface. Scale bar = 20 µm. (ii) 100 µm wide laser-ablated track, a heat-affected or resintered zone can be seen for approximately 200 µm either side of the track. Scale bar = 200 µm. (iii) 30 µm wide laser-ablated track, resintered alumina creating lips at the side of the track can be seen. Scale bar = 20 µm. (iv) Laser-ablated solder pad. Scale bar = 200 µm (B) Representative light microscopy image of Pt/Au screen-printed electrode manufactured on laser-ablated alumina (v) Cross-section of Pt/Au paste dried at 125 ^{o}C for 15 min. Scale bar = 10 µm (vi) Cross-section of paste baked at 50 ^{o}C overnight. Scale bar = 50 µm (vii) Cross-section of sample vacuumed and paste dried at 125 ^{o}C for 15 min. Scale bar = 20 µm (viii) Cross-section of sample vacuumed and paste dried at 50 ^{o}C overnight. Scale bar = 20 µm .Epoxy resin, Pt/Au and alumina layers labelled. Yellow arrows indicate voids present between substrate and metal.

In light of these results, the unmodified alumina manufacturing process was implemented from this point forwards to develop all electrode arrays presented in this body of work. In adopting this fabrication method, a compromise was made between achieving fine details and the advantage of a more level top surface, for a more reliable and robust manufacturing process.

4.2.3 Manufacturing of microchannel electrode arrays by unmodified alumina method

The unmodified alumina manufacturing process (refer to Materials and Methods chapter, section 2.2.9.2) was successfully used to manufacture the microchannel electrode arrays. In contrast to the manufacturing process previously reported, microchannel electrode arrays produced using the unmodified alumina method did not detach from the alumina surface following cleaning in an ultrasonic bath (figure 4.8). Cross sections of screen-printed alumina substrates were taken for SEM analysis (figure 4.9) to compare the substrate/metal interface between both manufacturing methods.

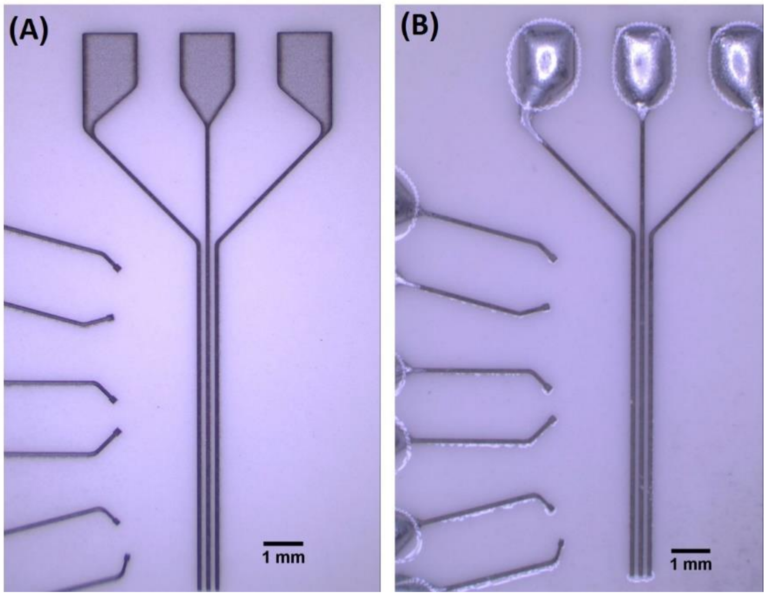

Figure 4.8 Light micrographs of electrode arrays manufactured using the unmodified alumina method before and after soldering and cleaning in ultrasonic bath

(A) Pt/Au sintered and microchannel electrode array design ablated on alumina substrate (B) Electrode array following soldering and cleaning in ultrasonic bath. Scale bars = 1 mm

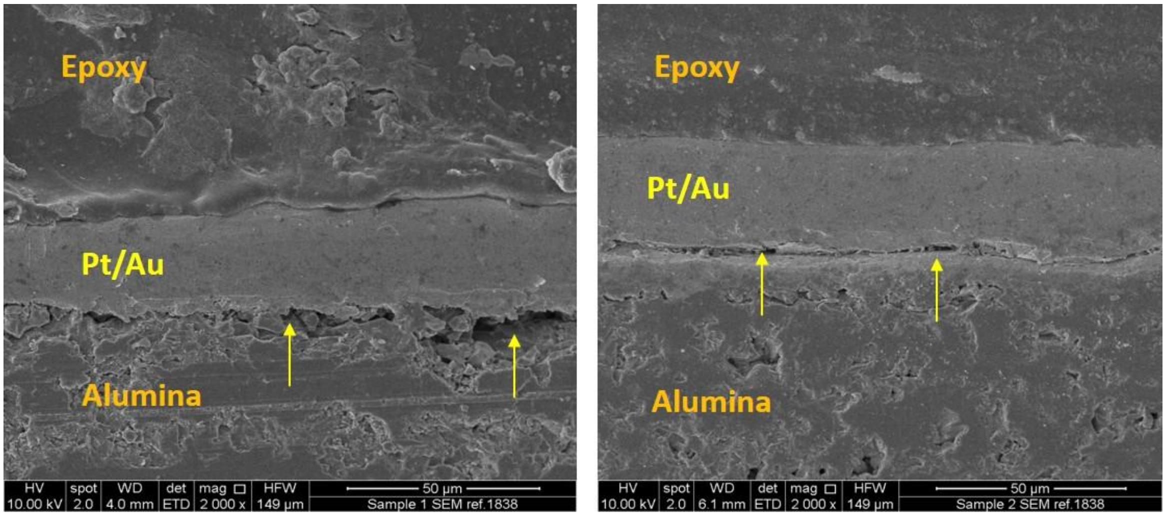

Figure 4.9 SEM micrographs of unmodified alumina substrate with screen-printed Pt/AU

Representative SEM images of individual Pt/Au screen-printed samples on unmodified alumina substrate. Epoxy resin, Pt/Au and alumina layers labelled. Yellow arrows indicate voids present between substrate and metal. Scale bars = 50 µm. Representative images for n = 2.

In a similar manner to the laser-structured alumina manufacturing method, SEM micrographs of screen-printed samples using the unmodified alumina method show the presence of voids at the interface between alumina and metal (figure 4.9). However, this manufacturing technique was robust and reproducible across batches; therefore, it was adopted for the development of all further electrode designs (i.e. the optimised design for *in vitro* experiments and the implantable device prototype).

The next line of investigation consisted of exploring the incorporation of MN like cells onto cell-seeding reservoirs of microchannel electrode arrays. To this end, electrode arrays were leached in IPA for 48 hours to remove any uncured silicone and curing by-products and autoclaved ready to use for cell culture experiments.

4.2.4 Exploring cell growth and neurite extension of NG108 cells on microchannel electrode arrays

The following section investigates cell growth and neurite extension on microchannel electrode arrays. Specifically, it explores whether cells seeded on laser-structured alumina reservoirs are capable of elongating neurites along microchannel structures adjacent to the reservoirs in response to the topographical cues provided by this design. This could allow for the simultaneous stimulation of cells located on reservoirs and recording of neural activity from neurites extending over tripolar recording electrodes. In initial experiments, NG108-15 cells, a cell line with cholinergic motor neuron-like characteristics (Pun *et al*., 1997) was chosen to test cell growth and neurite extension on electrode arrays for initial biocompatibility tests.

First, the optimal coating of electrode arrays for NG108-15 cell attachment was investigated. NG108-15 cells were cultured on cell-seeding reservoirs of microchannel electrode arrays (see Materials and Methods chapter, figure 2.4A) uncoated or coated with PLL (100 µg/ml), collagen type I (2 mg/ml) or laminin I (20 µg/ml) and cell density, total number of neurites and neurite extension were quantified. Cells were cultured on arrays for 5 days, fixed and stained to detect βIII-Tubulin in order to visualise neurites (figure 4.10). Cell density, number of neurites and neurite length were quantified to determine coating of choice to promote cell growth and neurite extension of NG108-15 cells (figure 4.11A, 4.11B and 4.11C, respectively). There was a trend towards there being more cells per field of view in all of the coated samples compared to the uncoated, although only the PLL coating (211 ± 83 cells counted per array on PLL coated samples compared to 18 ± 3 cells counted per array on uncoated samples) and collagen (141 ± 18 cells counted per collagen coated array) coating showed significant differences. Furthermore, there was substantial variability between repeats in the PLL and laminin groups (figure 4.11A).

There was a general trend for the number of neurites detected to be greater in all coated samples compared to uncoated reservoirs (1 ± 0.2 neurites counted per uncoated array). Although this was only statistically significant in the PLL (11 ± 2 neurites counted per array) and collagen (17 ± 4 neurites counted per array) groups (figure 4.11B).

With regards to neurite length, this parameter obeyed the same trend as previously described. Specifically, NG108-15 cells seeded on coated reservoirs extended longer neurites than those seeded on uncoated reservoirs (11 ± 8 µm long neurites measured per uncoated array). Furthermore, PLL and laminin coating favoured NG108-15 neurite extension (144 ± 48 and 147 ± 55 µm long neurites measured per array, respectively) compared to the uncoated group. This increase in neurite length was statistically significant (figure 4.11C).

Based on the data here reported, PLL (100 µg/ml) was chosen as the coating of choice to grow NG108 cells on the microchannel electrode arrays as it resulted in the highest cell density, and similar number of neurites and neurite length as compared to collagen and laminin.

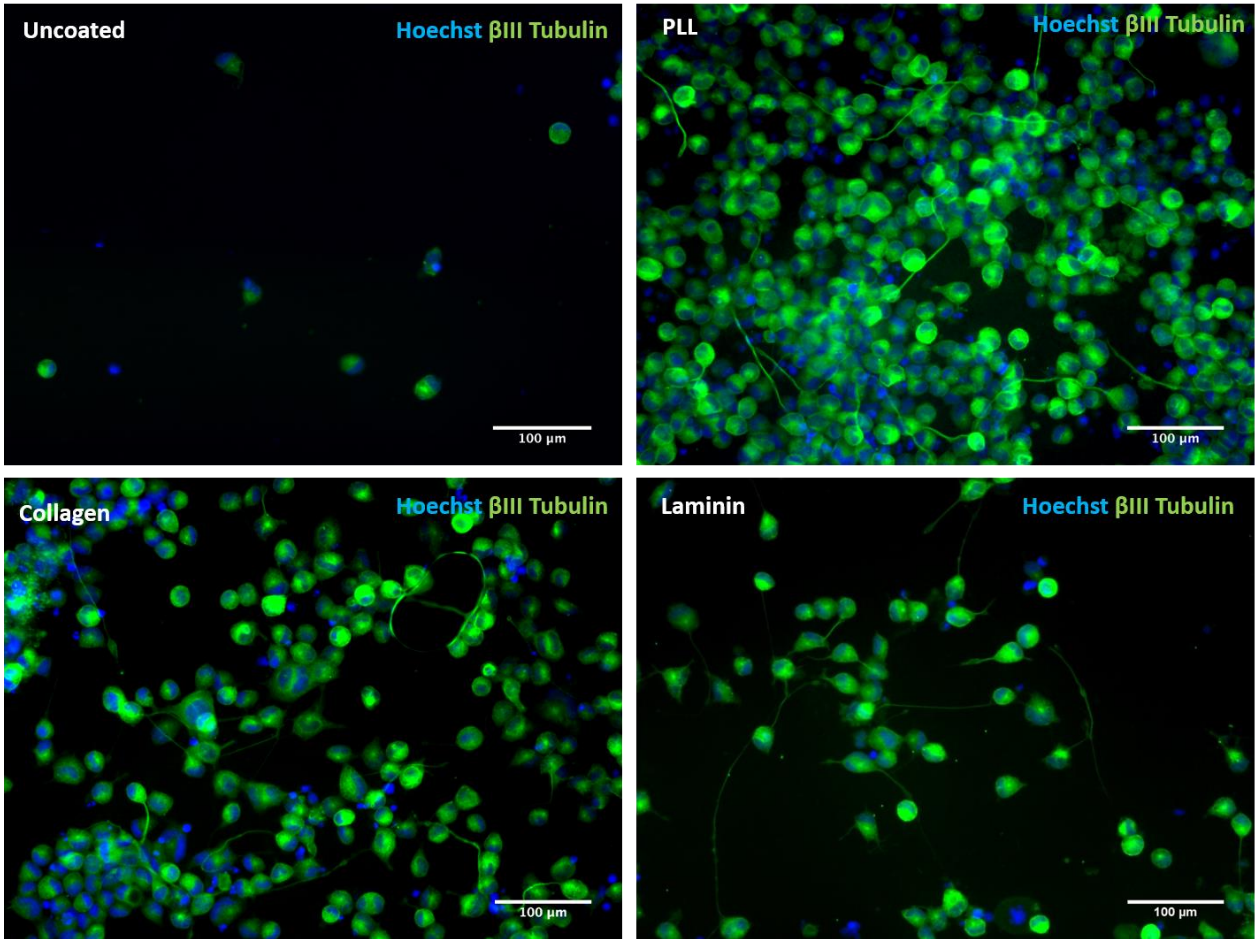
Uncoated
Hoechst βIII Tubulin
100 µm
PLL
Hoechst βIII Tubulin
100 µm
Collagen
Hoechst βIII Tubulin
100 µm
Laminin
Hoechst βIII Tubulin
100 µm

Figure 4.10 NG108-15 cells seeded on microchannel electrode arrays coated with different molecules

Representative fluorescence microscopy images showing NG108 cells cultured on cell-seeding reservoirs of microchannel electrode arrays for 5 days. Cells were fixed at day 5 before staining to detect βIII-Tubulin (green) and Hoechst (blue). Scale bars = 100 µm.

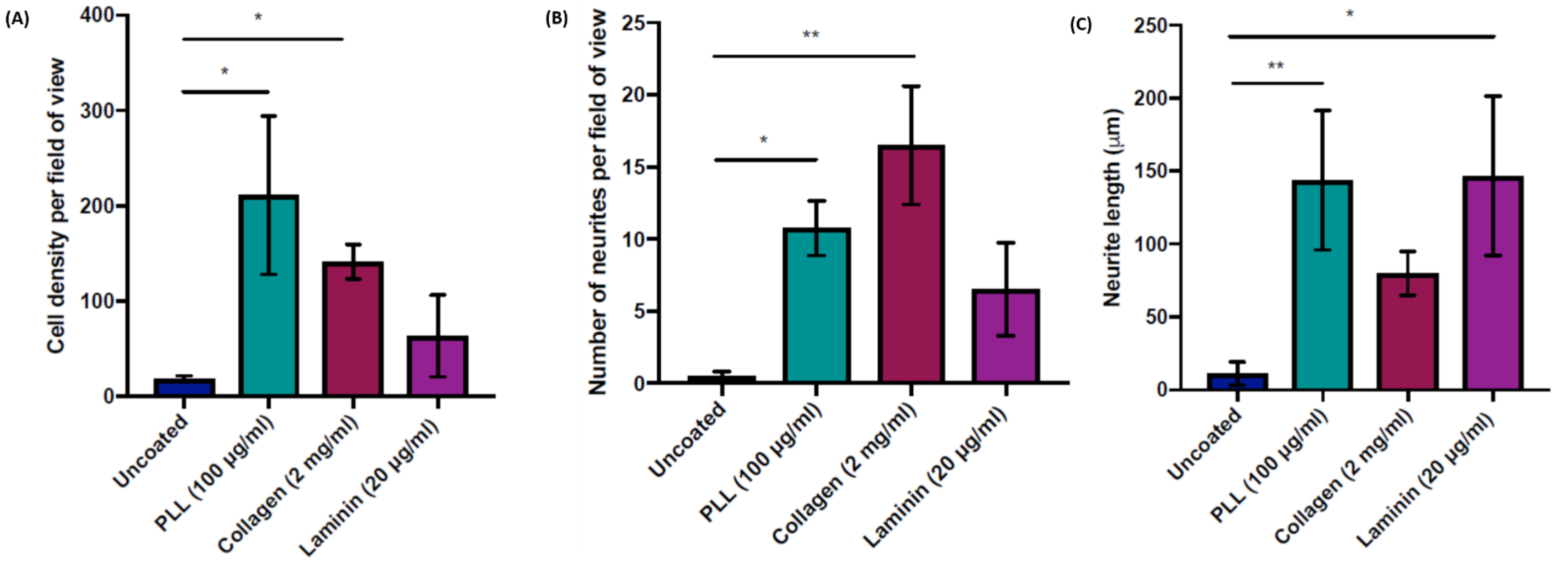

Figure 4.11 Quantification of NG108-15 cell density, neurite density and neurite length of cells seeded on microchannel electrode arrays coated with different molecules

Quantification of cell (A) and neurite (B) density after 5 days in culture. The number of nuclei (Hoechst stain) was quantified to determine the total number of cells per field of view and the number of neurites (βIII-Tubulin) quantified to determine neurite density per field of view (C) Neurite length per field of view was measured on ImageJ by tracing neurite processes of cells stained to detect βIII-Tubulin^{+}. One field of view = 0.003 cm^{2}. Data presented as means ± SD for n=4 microchannel electrode arrays, 5 regions sampled per reservoir (3 reservoirs per electrode array).*$p < 0.05$, **$p<0.01$ Kruskal-Wallis test with Dunn’s post-test.

Next, NG108-15 cells seeded on PLL-coated electrode arrays (figure 4.12A) were cultured *in vitro* for 5 days and immunostained to detect βIII-Tubulin in order to trace neurite outgrowth. Cell bodies were observed in one of the microchannels of the electrode array (figure 4.12B), however, no neurites were detected in the microchannels and the result could not be replicated in subsequent experiments.

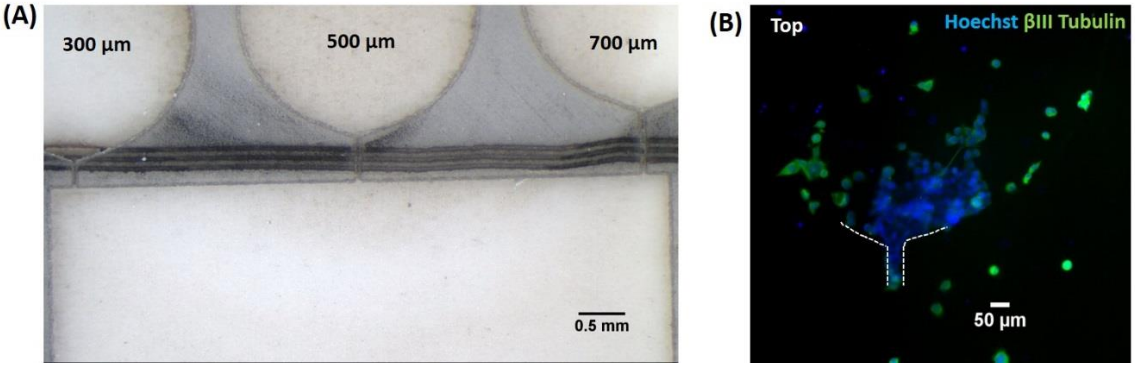

Figure 4.12 NG108-15 cells seeded on PLL-coated microchannel electrode arrays after 5 days *in vitro*

(A) Representative image of cell-seeding reservoirs and microchannels of microchannel electrode array. Microchannels are 30 µm wide and 300, 500 and 700 µm long. Scale bar = 0.5 mm. (B) Representative fluorescence microscopy images showing NG108-15 cell bodies located inside the 700 µm long microchannel. Cells were fixed at day 5 before staining to detect βIII-Tubulin (green) and Hoechst (blue). Scale bar = 50 µm. Representative image of the only occurrence of cells inside the microchannel in 4 repeats.

The next line of investigation focused on exploring growth and neurite extension of differentiated SPC-01 cells seeded on microchannel electrode arrays.

4.2.5 Exploring cell growth and neurite extension of differentiated SPC-01 cells on microchannel electrode arrays

The following experiment tested whether the manufactured microchannel electrode arrays could support growth and neurite extension of MN-like cells generated from differentiation of SPC-01 cells (see Chapter 3 for more details on cell differentiation). Moreover, it also explored whether microchannel structures could serve to guide growing SPC-01 cell neurites over tripolar recording electrodes.

After a 14-day differentiation protocol (see Materials and Methods chapter, section 2.2.1.2), SPC-01 cells were dissociated from tissue culture flasks and seeded on laminin-coated reservoirs of microchannel electrode arrays at the appropriate density. No preliminary tests using different coating molecules were performed as SPC-01 cells are routinely cultured on laminin-coated surfaces (Amemori *et al*., 2013, Cocks *et al*., 2013). Once seeded, cells were grown on electrode arrays for 5 days (figure 4.13A), at which point samples were fixed and cells immunostained to detect βIII-Tubulin (figure 4.13C). In order to compare neurite outgrowth, differentiated SPC-01 cells seeded on laminin-coated coverslips were included in the experiment as a control (figure 4.13B). The mean neurite length of cells seeded on electrode arrays (155 ± 36 µm long neurites measured per array) was comparable to that of the control group (141 ± 39 µm long neurites measured per coverslip). Moreover, in a similar manner to NG108-15 cells, no neurite extension was observed within microchannel structures.

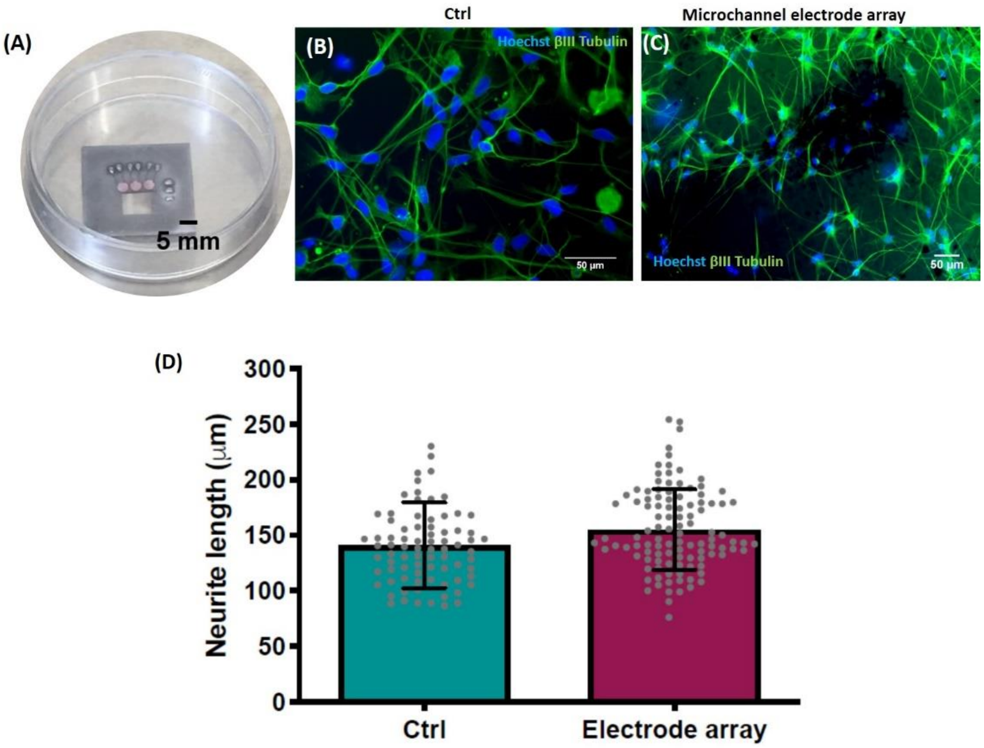

Figure 4.13. Differentiated SCP-01 cells seeded on microchannel electrode arrays.

(A) Representative image depicting the microchannel electrode array with cells seeded on reservoirs inside a petri dish. (B) Representative fluorescence microscopy images showing SPC-01 cells cultured on coverslips and (C) on cell-seeding reservoirs of microchannel electrode arrays for 5 days. Cells were fixed at day 5 before staining to detect βIII-Tubulin (green) and Hoechst (blue). Scale bar = 50 µm; (D) Neurite length per field of view as measured on ImageJ by following neurite traces of cells stained to detect βIII-Tubulin. One field of view = 0.003 cm^2. Data presented as mean ± SD for n=3 microchannel electrode arrays, 5 regions sampled per reservoir (3 reservoirs per electrode array). Individual neurite measurements are displayed.

In light of these results, the electrode design was simplified to feature a single cell-seeding reservoir with three stimulation electrodes. The new optimised design for *in vitro* experiments included laser-ablated microgrooves within the reservoir as a mean of providing topographical cues that could direct neurite outgrowth and encourage longer neurite extension.

4.2.6 Optimised design for *in vitro* experiments

A new electrode array was designed with the purpose of achieving longer neurite extension and directionality (figure 4.14A). This design is herein referred to as the optimised design for *in vitro* experiments. This electrode array consists of three stimulation electrodes and a single cell-seeding reservoir (figure 4.14B) with laser-ablated microgrooves that extend towards the end of the reservoir (figure 4.14C). Microgrooves were designed as parallel lines with a width equal to the laser spot size (30 µm), inter-space of 10 µm and depth of approximately 12 µm (5 laser passes). To avoid cutting over electrode sites when ablating microgrooves, 150 µm spacing was designed between electrode sites and microgrooves. These microgroove-free zones within the reservoir also served to test whether cells seeded on these electrode arrays would favour growing on microgrooves or would avoid these topographical cues.

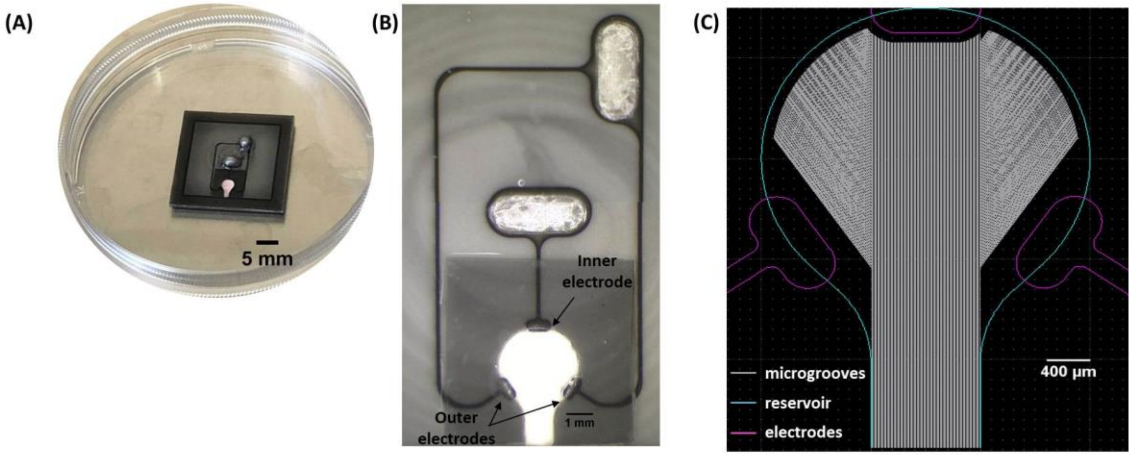

Figure 4.14 Optimised design for *in vitro* experiments

Micrographs of the optimised design for *in vitro* experiments electrode arrays. (A) Representative image of electrode arrays with differentiated SPC-01 cellular solution in the reservoir. Scale bar = 5 mm. (B) Electrode design with inner and outer electrodes labelled (note laser ablated-microgrooves are not visible at this magnification). Outer electrodes total GSA = 0.005 cm^2, Inner electrode GSA = 0.0025 cm^2. Scale bar = 1 mm. (C) Electrode design depicting microgrooves. Each line on the design is separated by 10 µm. Laser ablation of each line resulted in 30 µm wide grooves (laser spot size) and approximately 12 µm depth (5 laser passes). Scale bar = 400 µm.

4.2.7 Investigating the effect of microgrooves on neurite length and directionality

To investigate the effectiveness of microgrooves in directing neurite extension towards the end of the reservoir, differentiated SPC-01 cells were cultured on arrays with laminin-coated reservoirs for 5 days. The hypotheses tested in this experiment were two-fold: first, seeding cells in direct contact with microgrooves would encourage neurite guidance from the reservoir towards the end of the arrays and second, that small diameter microgrooves would confine the space available for cells to grow, thus, restricting meandering neurite outgrowth and promoting linear neurite extension. As a by-product of linear outgrowth neurites would grow over longer distances in a specific period of time.

Coverslips and unmodified alumina samples coated with laminin were included as controls to explore the effect of microgrooves on promoting longer neurite outgrowth. After 5 days in culture, electrode arrays were fixed, stained to detect βIII-Tubulin (figure 4.15) and neurite length quantified. Mean neurite length of cells seeded on unmodified alumina substrate (188 ± 40 µm long neurites per alumina sample) was slightly higher compared to that of cells growing on electrode array reservoirs (161 ± 63 µm long neurites per array) and cells seeded on coverslips (117 ± 32 µm long neurites per coverslip) (figure 4.16A), however there was considerable overlap between the populations in the different groups. Moreover, cells seeded on electrode array reservoirs were identified to grow at the edge of reservoirs where no microgrooves were laser-ablated (outside microgrooves) as well as within the microgroove pattern (figure 4.15). In order to assess whether this topographical cue promoted longer neurite extension, neurite length of cells growing within these two distinct reservoir areas was quantified. Mean neurite length of cells growing on microgrooves (161 ± 63 µm long neurites per array) was equivalent to that obtained on microgroove-free zones (155 ± 45 µm long neurites per array), although slightly more variability was detected on the former group (figure 4.16B). The length of the longest neurite was assessed and compared between all four groups (figure 4.16C). The mean longest neurite was detected on unmodified alumina (381 ± 24 µm long). Furthermore, the mean longest neurite was found on microgrooves (370 ± 50 µm long) compared to microgroove-free zones (299 ± 24 µm long).

To determine whether cells favoured growing on microgrooves or outside microgrooves, cell density on these two distinct zones was quantified. To account for differences in dimensions of each area, the number of cells per field of view was normalised to the area of each region. A 0 hrs experiment, in which samples were fixed after cell attachment, usually 30 min after cell-seeding, was included to explore the possibility of cell migration between different areas. No difference was detected in the proportion of cells present on microgrooves at 0 hrs (33 % ± 10 of cells on microgrooves) and after 5 days (38 % ± 24 percent of cells on microgrooves), therefore, suggesting there was no net cell migration between these two distinct areas. At both time points however, the proportion of cells located outside microgrooves was higher than that observed on the microgroove pattern (figure 4.16D).

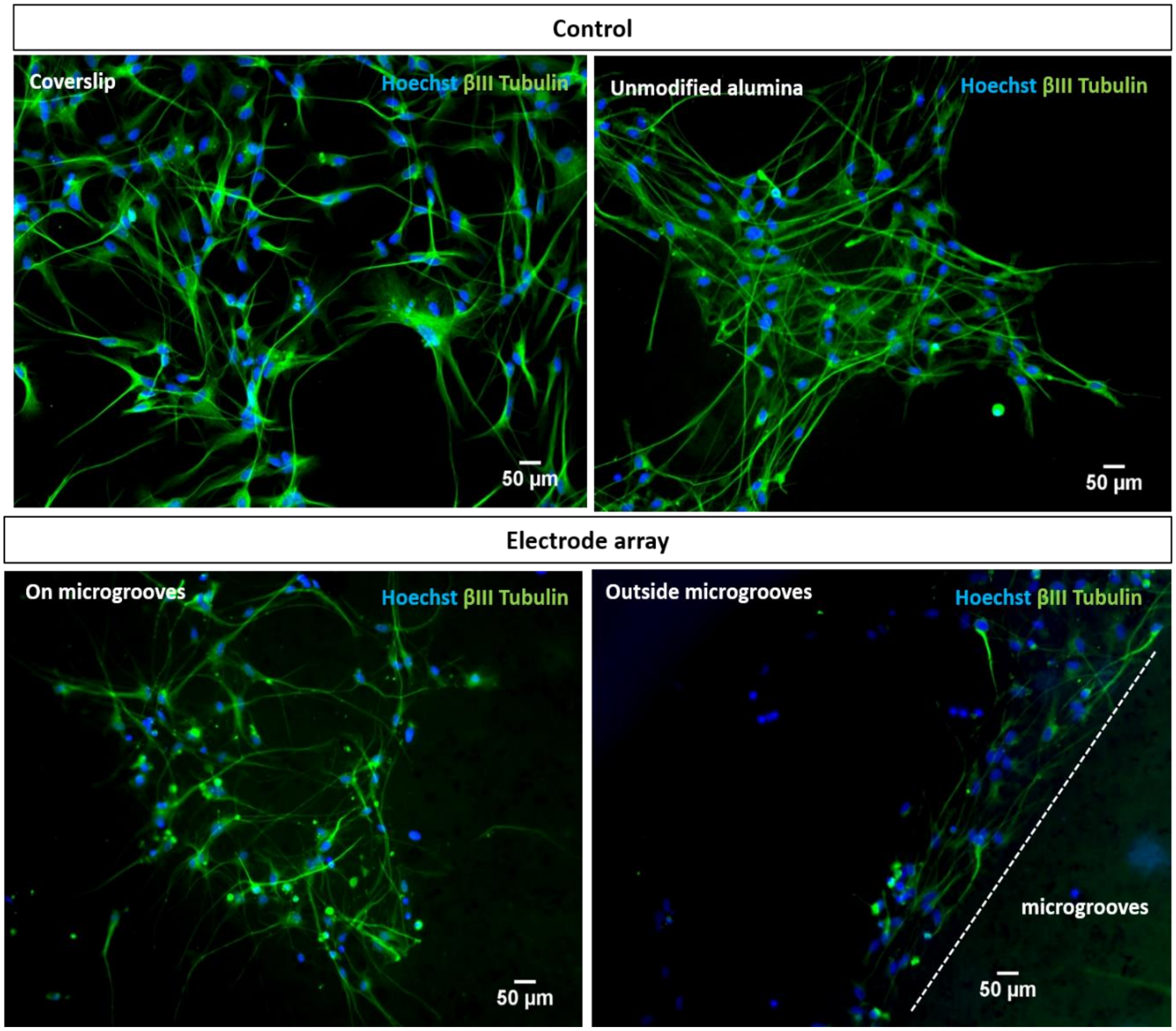
Control
Coverslip
Hoechst βIII Tubulin
50 µm
Unmodified alumina
Hoechst βIII Tubulin
50 µm
Electrode array
On microgrooves
Hoechst βIII Tubulin
50 µm
Outside microgrooves
Hoechst βIII Tubulin
microgrooves
50 µm

Figure 4.15 Differentiated SPC-01 cells cultured on the optimised design for *in vitro* experiments

Representative fluorescence microscopy images showing differentiated SPC-01 cells cultured on coverslips (ctrl), unmodified alumina and cells seeded on reservoir of electrode arrays growing on microgrooves or outside microgrooves for 5 days. Cells were fixed at day 5 before staining to detect βIII-Tubulin (green) and Hoechst (blue). Dashed line depicts the division between the microgrooves and microgroove-free zones. Scale bars = 50 µm

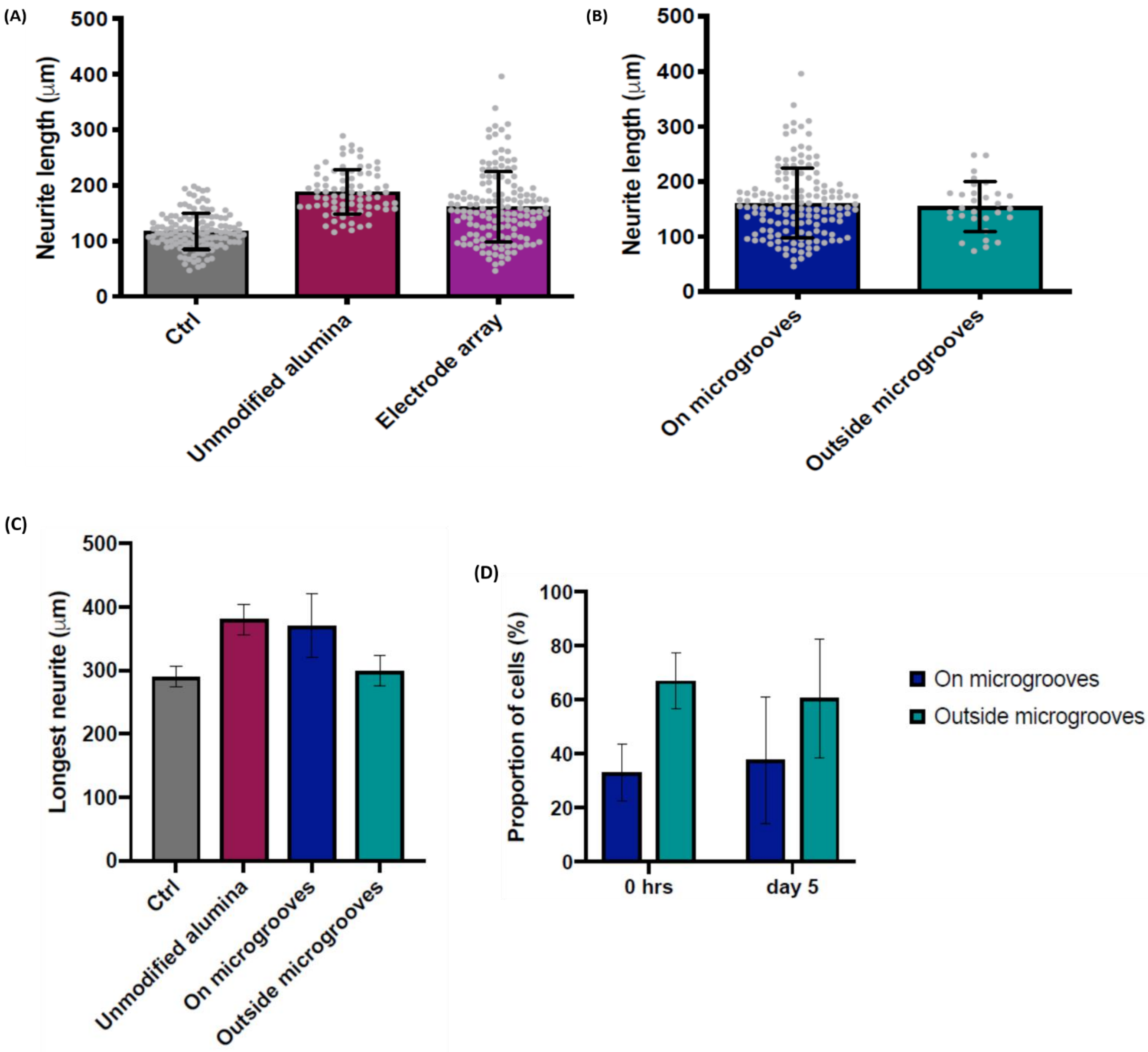

Figure 4.16 Assessment of microgrooves on differentiated SPC-01 cells density and neurite extension

(A) Neurite length of cells growing on coverslips, unmodified alumina and electrode array reservoirs. ImageJ was used to trace neurites of cells stained to detect βIII-Tubulin. (B) Neurite length of cells detected on microgrooves and cells detected outside microgrooves of electrode array reservoirs and (C) length of longest neurite measured on each condition. To explore the preference of cells towards growing in one of these two distinct zones, the number of cells detected on microgrooves and outside microgrooves, immediately following cell attachment to reservoirs (0 hrs) and after 5 days in culture was quantified and results normalised to the area of each region (D). One field of view = 0.003 cm^2. Data presented as mean ± SD for n=3 individual electrode arrays, 5 regions sampled per array. Individual neurite measurements displayed as grey dots.

These data suggest incorporating microgrooves of 30 µm pitch separated by 10 µm did not improve neurite length or provide directionality to differentiated SPC-01 cells growing on electrode arrays. Indeed, neurite length on reservoirs lacking microgrooves (figure 4.13D) was not statistically significantly different from that of cells growing on microgrooves. Furthermore, the morphology of cells seeded on microgrooves is indicative of dying cells. This is further supported by a smaller cell density compared to microgrooves free zones and fewer neurites elongated from cells growing on microgrooves compared to those growing outside microgrooves (figure 4.15). In light of these results, laser-ablated microgrooves were not incorporated on any other electrode array designs herein reported.

The results described in this chapter so far, show that thick-film manufactured electrode arrays support differentiated SPC-01 cell growth and neurite extension. The next line of investigation focused on exploring whether these microelectrodes were suitable for effective neural stimulation. To this end, electrochemical techniques were employed. Thus far, SPC-01 cells have been routinely cultured on laminin-coated surfaces. Therefore, the next experiments focused on characterising the electrochemical properties of manufactured electrodes and the effect of laminin on these properties.

4.2.8 Exploring the effect of laminin coating on electrochemical properties of the optimised electrode arrays designed for *in vitro* experiments.

Electrochemical properties of electrode arrays were characterised using cyclic voltammetry (CV) and electrical impedance spectroscopy (EIS) (refer to Materials and Methods chapter, section 2.2.10.2). EIS was implemented to assess impedance and CV used to measure charge storage capacity (CSC) of electrodes. In order to assess the effect of coating electrodes with laminin (10 µg/ml), both parameters were measured on electrode arrays as manufactured (before laminin) and following laminin coating (after laminin). Each sample consisted of 3 electrodes (2 outer electrodes connected to 1 solder pad - herein referred to as outer electrodes - and 1 inner electrode connected to a single solder pad – herein referred to as inner electrode) (see figure 4.14B). To account for the differences in geometric areas, each electrode was tested individually.

Impedance results are presented as bode plots for electrode arrays as manufactured (before laminin) and following laminin coating (after laminin) (figure 4.17A-D). The results at low (20 Hz), medium (1 kHz) and high (100 kHz) frequencies were compared (table 4.1). Impedance of electrodes coated with laminin was lower than uncoated electrodes at all frequencies measured.

CV responses to a 50 mV/s sweep were measured with either inner or outer electrode as the working electrode. Voltammograms normalised to electrode geometric area, before and after laminin coating, are shown in figure 4.18. Charge storage capacity (CSC) and cathodic CSC (cCSC) were calculated from the CV responses (table 4.2). Slight increases in both cathodic and CSC of inner and outer electrodes were observed following laminin coating.

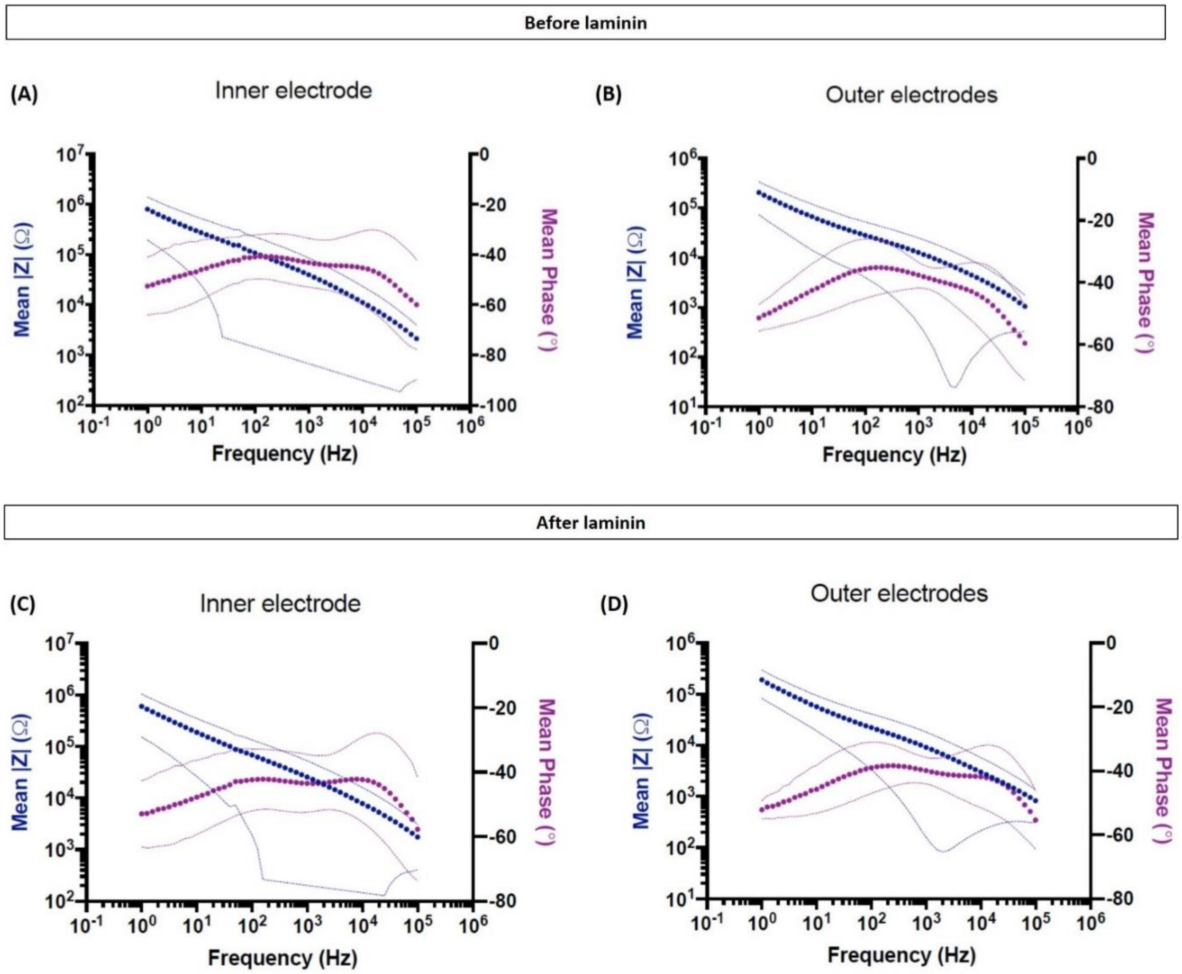

Figure 4.17 Bode plots of frequency-dependent impedance of the optimised design for *in vitro* experiments electrode arrays before and after laminin

Impedance Magnitude |Z| and phase (°) of electrodes tested at different frequencies ranging from 1 Hz to 100 kHz. Inner (A and C) and outer (B and D) electrodes were tested as manufactured (A and B) and following laminin coating (C and D). Data presented as mean ± SD (dashed lines) for n = 5 individual electrode arrays.

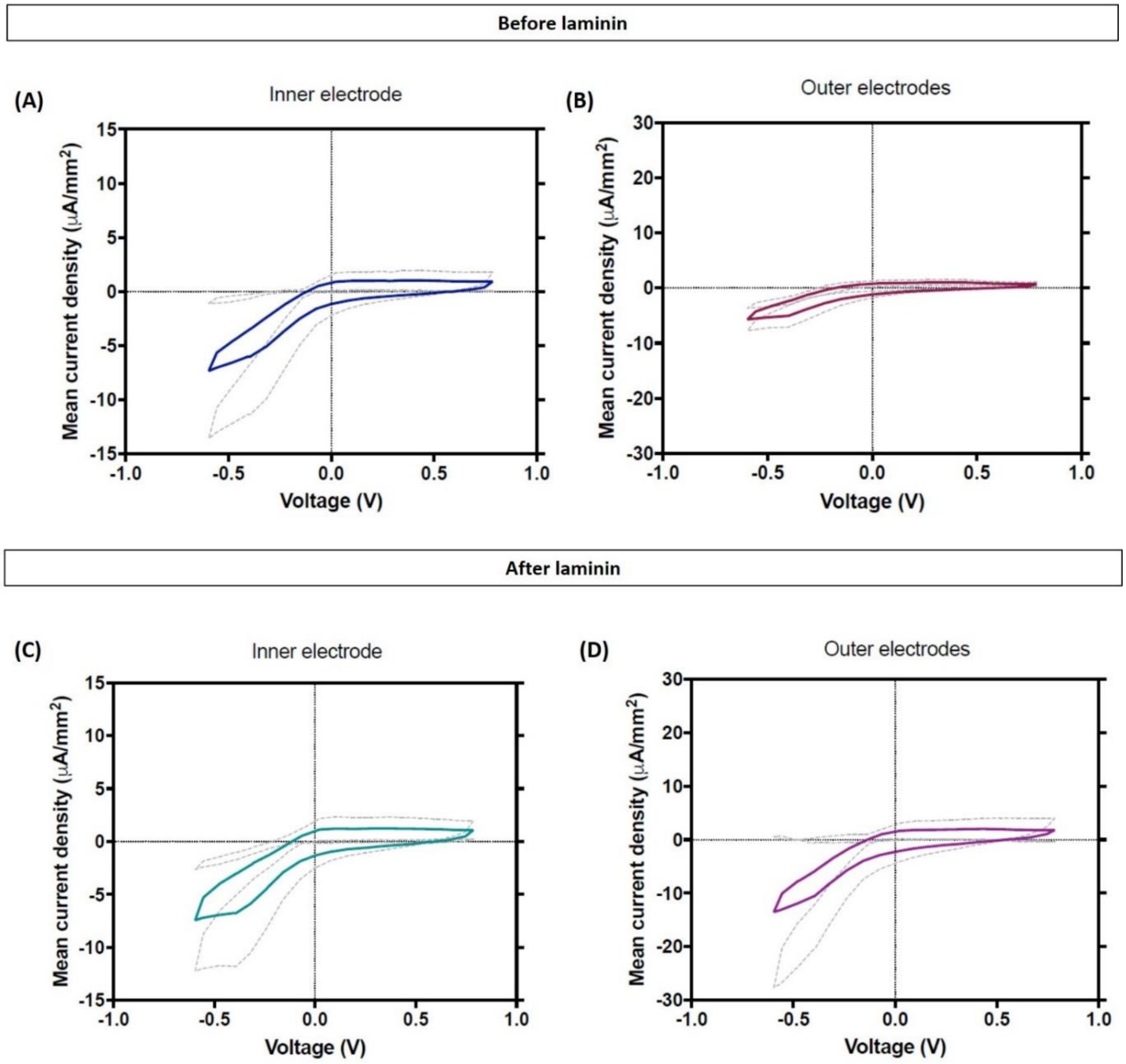

Figure 4.18 Cyclic voltammograms of the optimised electrode array design for *in vitro* experiments as manufactured (before laminin) and following laminin coating (after laminin)

CV responses of electrodes as manufactured and following laminin coating. A potential between -0.6 and +0.8 V w.r.t reference (Ag/AgCl) was swept at a scan rate of 50 mV/s. Responses of inner electrode before (A) and after (C) laminin and outer electrodes before (B) and after (D) laminin were normalised to their respective geometric areas. Data presented as mean ± SD (dashed curves) for n = 5 electrode arrays.

Table 4.1 Impedance (|Z|, in kΩ) of thick film Pt/Au electrode arrays manufacured using the unmodified alumina method to create the optimsised design for *in vitro* experiments

Impedance values reported for inner and outer electrodes tested at low (20 Hz), medium (1 kHz) and high frequencies (100 kHz) before and after laminin-coating. Data presented as mean ± S.D for n = 5 individual electrode arrays. ns, paired t-test.

	Impedance (in kΩ)			
Frequency	**Inner electrode**		**Outer electrodes**	
	Before laminin	*After laminin*	*Before laminin*	*After laminin*
20 Hz	205.55 ± 199.24	136.8 ± 123.24	50.24 ± 40.62	41.61 ± 29.73
1 kHz	39.65 ± 45.75	25.45 ± 27.20	12.76 ± 12.29	9.17 ± 9.01
100 kHz	2.12 ± 1.80	1.75 ± 1.34	1.05 ± 0.72	0.83 ± 0.52

Table 4.2 Charge storage capacity (CSC) and cathodic CSC (cCSC) of thick film Pt/Au electrode arrays manufactured using the unmodified alumina method to create the optimised design for *in vitro* experiments

CSC and cCSC values for inner and outer electrodes before and after laminin coating. Charge values are normalised to electrode geometric area. Data presented as mean ± S.D for n = 5 individual electrode arrays. ns, paired t-test.

	Inner electrode		**Outer electrodes**	
	Before laminin	*After laminin*	*Before laminin*	*After laminin*
CSC (mC/ cm^2)	4.68 ± 3.83	5.08 ± 4.62	4.21 ± 2.59	4.31 ± 2.42
cCSC (mC/ cm^2)	2.99 ± 2.69	3.24 ± 2.98	2.67 ± 1.80	2.76 ± 1.70

Overall, these results suggest coating electrode arrays with laminin at a concentration of 10 µg/ml has a small impact on their impedance and CSC. Because the difference in electrochemical properties between coated and uncoated electrodes seems to be smaller than the inherent difference between samples, it can be ignored for the purpose of this work, therefore allowing the use of laminin to promote attachment of SPC-01 cells cultured in the cell-seeding reservoirs of electrode arrays.

4.3 Discussion

Over the last few decades, microfabrication technologies for neural stimulation and recording have advanced in terms of ease of manufacturability, topographical precision, miniaturisation and multi-functionality. This progress has allowed the unprecedented possibilities to assess electrophysiological behaviour of dynamic neural networks *in vitro* and ultimately inform the manufacturing of neural prosthetic devices.

Here, the suitability of thick-film technology to manufacture electrode arrays for culturing of differentiated SPC-01 cells was investigated. The results presented suggest this fabrication technique allows the production of customisable electrode arrays with features in the micrometre scale. Furthermore, laser-micromachining can be implemented in these electrode arrays to incorporate topographical features in the order of microns. Robustness and reproducibility of electrodes manufactured using thick-film technology was only achieved using unmodified alumina substrates. Laser-micromachining alumina substrates prior to screen-printing the conductor paste resulted in poor adherence of Pt/Au paste to the substrate as indicated by metal detachment from samples once cleaned in an ultrasonic bath. Initial SEM results of screen-printed laser-structured alumina substrates revealed the presence of voids at the interface between alumina and metal layer. To minimise voids and, in an attempt to improve adherence of Pt/Au to the substrate, alterations in the manufacturing protocol were made. Although some improvements in metal retention following cleaning of samples were achieved, the manufacturing protocol was still not reproducible across all electrode arrays. In contrast, screen-printing of Pt/Au onto unmodified alumina substrates, was found to be robust and reproducible across all samples. SEM cross-sections of samples manufactured using this method, showed the presence of voids between substrate and Pt/Au layer; however, these devices did not fail by Pt/Au detachment, thus indicating a lack of correlation between Pt/Au detachment and voids at the interface between substrate and metal.

The findings reported by Fiedler *et al*. (2013), however, differ from the results obtained in this body of work. In that paper, the researchers described successful screen-printing of Pt/Au paste onto laser-structured alumina to manufacture ceramic adaptors. Although Fiedler *et al*. (2013) used the same alumina substrate (96% alumina), Pt/Au paste and Nd:YAG laser of equal wavelength, the differences in Pt/Au attachment may be attributed to two factors: first, different laser parameters used to structure the alumina substrate and second implementing different temperatures to sinter the Pt/Au paste. With regards to the first point, it has been previously documented that thermal stress generated by laser ablation induces structural changes in alumina. Previous work, using Nd:YAG lasers with pulse duration in the micro and millisecond range to generate cavities in alumina, reported the formation of a glassy layer as a consequence of the melting phase involved in removing the material (Knowles *et al*., 2007) . Re-solidification of melt material and formation of a recast layer have also been observed when micromachining alumina with an Nd:YAG laser of the same wavelength as the one used in this body of work (N. Nedialkov *et al*., 2003). Indeed, a recast layer can be observed in the SEM micrographs of laser-structured alumina. Here, deposition of melt material is apparent inside and surrounding the ablated cavities. This is comparable to the SEM micrographs shown by N. Nedialkov *et al*. (2003). The adherence of screen-printed Pt/Au paste to alumina is known to be strong (Fiedler *et al*., 2013). Furthermore, adhesion of Pt/Au to alumina requires a glass binder during the sintering process. Although the glassy layer here described could be compared to the glass binder material in the paste, one key difference that could explain the differences in outcome is temperature. Indeed, the glass binder creates an adhesive layer to the unmodified alumina substrate under high temperatures (850°C). There is a possibility that sintering Pt/Au paste screen-printed onto laser structured alumina may require higher temperatures to promote successful binding of the paste onto a substrate that has undergone structural changes as a by-product of laser ablation. The increased temperature could improve interdiffusion between the glass binder and the glassy layer on the substrate. In line with this argument, Fiedler *et al*. (2013) reported sintering of Pt/Au screen-printed samples on laser micromachined alumina at 1000 ^{o}C.

Overall, laser micromachining of alumina should be performed under optimal parameters as otherwise structural changes could be induced on the substrate, therefore causing poor binding of Pt/Au to alumina. To obtain the highest quality results, it is often desirable to achieve ablation with a minimal degree of melting. In this respect, lasers with short duration pulses are suitable. For example, Knowles *et al*. (2007) observed no evidence of melting when using laser pulses of short wavelengths and duration in the nanosecond range to micromachined alumina.

To achieve reproducibility of electrode array manufacturing using the laser-structured alumina manufacturing method, future experiments should investigate adherence of Pt/Au onto alumina micromachined with various laser processing parameters. For example, the following adjustments may produce robust electrode arrays: (1) lowering laser power to decrease the thermal stress induced to alumina; (2) decreasing the duration of laser pulses used for ablation would reduce the amount of time that the laser beam is in contact with the alumina, thus, shortening the ablation effects on the material; (3) using a laser with shorter wavelength, which has been shown to produce high-quality micromachining in ceramics (Knowles *et al*., 2007), may diminish the structural changes associated with melting and re-casting that could hinder Pt/Au adherence. Knowles *et al*. (2007) used 355 nm (near ultraviolet) harmonic Nd:YAG and 532 nm (green) frequency doubled Nd:YAG lasers, in contrast to the 1064 nm (near infrared) fundamental wavelength Nd:YAG laser in this work; (4) sintering the Pt/Au thick film paste at a higher temperature could help to improve the bond between metal alloy and substrate.

The next line of investigation in this chapter consisted of exploring NG108-15 cell growth on microchannel electrode arrays and assessing whether microchannels can successfully guide neurite extension of cells across tripolar electrodes, therefore providing a multi-functional platform that supports simultaneous stimulation and recording of cells. First, to support growth of NG108-15 cells cultured on cell-seeding reservoirs of electrode arrays, various protein coatings were investigated. Results show PLL-coated samples supported higher NG108-15 cell density, promoted neurite sprouting comparable to that seen on collagen and laminin-coated surfaces and induced neurite outgrowth of similar lengths to those quantified in laminin-coated electrode arrays after 5 days *in vitro*. This finding is in agreement with previously published research reporting PLL-functionalised surfaces, in contrast to other coatings and uncoated surfaces promote NG108-15 neurite sprouting and induce longer neurite outgrowth after 5 days in culture (Hopper *et al*., 2014). In light of this result, PLL was implemented as the coating of choice for growing NG108-15 cells on cell-seeding reservoirs of microchannel electrode arrays. Although neurite outgrowth was observed on cell-seeding reservoirs, directed outgrowth of single neurites down microchannels was not observed in either of the different microchannel lengths tested. Cell bodies were observed in the 700 µm long microchannel as a single occurrence out of 4 repeats; however, these cells did not extend observable neurites and the result was not replicated in subsequent experiments. When culturing differentiated SPC-01 cells on microchannel electrode arrays the same trend was observed. Various plausible hypotheses can be proposed to account for lack of neurite outgrowth along microchannels: first, the distance between cell-seeding reservoir and microchannel may have prevented neurites from reaching microchannels after 5 days in culture. Decreasing size of reservoirs may better support neurite extension towards opening of microchannels. Indeed, the cell-plating area in previous microgrooved surfaces is immediately adjacent to these topographical cues (Zahavi *et al*., 2015, Honegger *et al*., 2016b). Second, in the absence of topographical cues on reservoirs neurites extended in various different directions. This in turn decreased the proportion of neurites growing towards the microchannel and the overall likelihood of neurites encountering the microchannel. Moreover, to induce contact guidance it is essential that growing neurites encounter the imposed topographical feature (edge or wall). It has been shown that the direction of growth following contact is highly dependent on the angle at which the approaching neurite contacts the feature (Li and Folch, 2005). A perpendicular angle at the point of contact results in neurites preserving their direction of growth and crossing over the feature, whereas neurites approaching at a more parallel angle tend to change their direction of growth by a small angle and align to the feature. Based on this, meandering neurites that encountered the reservoir edge at a parallel angle may have turned to align to this edge. However, in the absence of a delineating path provided by a parallel wall or edge, neurites are expected to continue a meandering pattern. Furthermore, the possibility of uncoated microchannels cannot be ruled out, as the hydrophobic nature of the surface may have prevented the flow of coating solution down the narrow microchannels. If indeed, microchannels remained uncoated, the absence of proteins like PLL or laminin that promote cell attachment and growth may have led NG108-15 and differentiated SPC-01 cells to favour growing on coated reservoirs rather than uncoated microchannels. This hypothesis is supported by previous research showing patterning surfaces with PLL (Oliva *et al*., 2003) and laminin (Staii *et al*., 2009) promotes cell body adhesion and neurite extension over coated rather than uncoated areas. More recently, Orlowska *et al*. (2017) reported a two-fold enhanced neurite outgrowth of PC12 cells when seeded on a double-coated PLL/laminin surface compared to single coatings and uncoated surfaces. Interestingly, Bas *et al*. (2019) found that laminin-coated cochlear implants inserted in rats attracted host Schwann cells and promoted neurite extension and guidance 1 months post-implantation. This lead to improved survival of host ganglion neurons following electrode insertion trauma compared to uncoated implants.

Challenges in achieving directional growth through microchannels that could allow simultaneous stimulation and recording from neurons, shifted the focus towards the fabrication of electrode arrays that would support neural stimulation only. To this end, the initial design was simplified to include a single cell-seeding reservoir with three stimulation electrodes and laser-ablated microgrooves of 30 µm diameter, 10 µm pitch and ~ 12 µm deep. By seeding differentiated SPC-01 cells in direct contact with microgrooves it was hypothesised that these topographical features would direct neurite extension towards the end of the array. The results obtained suggest microgrooved surfaces did not enhance neurite length and no evidence of alignment was observed upon visual inspection of cells on microgrooves. Overall, longer neurites were detected on unmodified alumina compared to all other groups. This suggests unmodified alumina substrate is better at supporting neurite elongation of differentiated SPC-01 cells. In line with this finding, previous research has reported enhanced neurite extension on porous surfaces compared to non-porous surfaces. The mouse neuroblastoma cell line, N2a, was found to elongate longer neurites when cultured on anodic porous alumina with pore sizes between 60 and 100 nm compared to flat smooth native-oxide-coated aluminium (El Merhie *et al*., 2019).

Further, these MN-like cells favoured growing on microgroove-free regions of cell-seeding reservoirs of electrode arrays. These findings reject the hypothesis formulated and are in disagreement with previous literature reporting neurite guidance and longer neurite outgrowth of cells in direct contact with microgrooves. Asides from the literature previously discussed (see section 4.1.2). More recently, these results have been reported for iPSCs (Abagnale *et al*., 2017) and iPSC-derived cortical neurons (Terryn *et al*., 2018). The microfabrication technique implemented to create microgrooves may be key in accounting for these confounding results. Ablating features as small as the laser spot size with a 10 µm pitch may have increased the inaccuracy of the ablation process, most likely causing overlaps between laser pulses. This effect has been previously documented by Mohammed *et al*. (2018) using the same laser type (Nd:YAG) to micromachine alumina. The researchers concluded that optimising parameters like intensity and scanning speed can improve dimensional accuracy. In addition, it is likely that the melting effect observed within ablated features as well as in the surrounding areas compromised the shape of microgrooves. A key area that warrants further investigation is the assessment of these microgrooves in detail, either through SEM imaging or atomic force microscopy (AFM) in order to get a better insight into the shape and dimensions of these features and better understand how melting affected their structure. The synergistic effect of decreased accuracy and structural changes due to thermal stress when ablating features as small as the laser spot size, may have resulted in a surface lacking microgrooves of defined shape. Because the present parameters were optimised for cutting through alumina, rather than patterning the surface, future studies should identify optimal parameters to improve ablation accuracy. As a starting point, increasing spacing between microgrooves should improve the ablation of defined microgrooves onto alumina substrates (Mohammed *et al*., 2018). Alternatively, in light of the results here presented, a desirable solution for future experiments is to incorporate microchannels onto unmodified alumina. To this end, narrower and deeper microchannels than the ones herein reported, can be laser-ablated on PDMS substrate and bonded onto an unmodified alumina substrate where cells are seeded, thus avoiding laser-ablation of PDMS coated alumina which may alter the structure of this substrate as part of the PDMS removal process.

Although directional guidance of neurites was not achieved, the findings reported here show that thick-film electrode arrays manufactured on an alumina substrate support growth and neurite extension of differentiated SPC-01 cells, which is paramount for the success of this biohybrid approach. Previous literature has reported the use of glass substrates (commonly implemented in the manufacturing of MEAs) to support growth of the mouse MN-like hybrid cell line, NSC 34, (Sabitha *et al*., 2016), mouse ESCs (Jenkinson *et al*., 2017) and hiPSCs (Hofrichter *et al*., 2017) to mention a few. Furthermore, PDMS is also a substrate commonly reported for culturing cells in microfluidic studies. In line with this, embryonic rat hippocampal neurons have been shown to extend neurites down PDMS channels (Cheng *et al*., 2017). Osaki *et al*. (2018) has also reported successful growth of human embryonic stem-derived MN spheroids on PDMS substrate.

The last section of this chapter focused on characterising the electrochemical properties of these electrodes to assess their ability to support effective neural stimulation.

The electrical impedance spectroscopy results show high variability between electrode arrays across the whole frequency range measured. This high variability in impedance magnitude poses a challenge when comparing EIS results to other studies reporting electrodes of similar size. A possible explanation to account for this result is the possibility of laser offset and variability in laser focus between samples. This would have led to differences in laser ablation of the PDMS layer to expose the reservoir and electrode sites, therefore altering electrode size between samples. Nevertheless, in line with the literature, impedance values increase as the size of electrodes decreases and fall within the range reported by other studies (Green *et al*., 2012, Carnicer-Lombarte *et al*., 2017). In a similar manner, CSC and cCSC values are highly variable between electrode arrays. Nevertheless, they fall within the range reported by Carnicer-Lombarte *et al*. (2017) on thick-film Pt/Au electrodes, Pt foil electrodes roughened by laser-micromachining (Green *et al*., 2012) and smooth Pt foil electrodes (Green *et al*., 2013c). In the context of neural stimulation, it has been shown that artificial retinal devices require a charge injection of 0.016–0.879 µC per phase for a visual percept to be observed (Mahadevappa *et al*., 2005). Green *et al*. (2012), estimate the above amount of charge corresponds to 0.008–0.448 mC/cm^2 if stimulated with electrodes of similar dimensions to the ones reported here. Based on CSC values of electrodes as manufactured and once coated with laminin, the amount of charge that can be stored is over 10 times greater than the largest value needed to stimulate retinal neurons. However, it is important to note that CSC is normally used as an estimate of how much charge can be stored and is not an accurate measure of the amount of charge which can be injected during stimulation. Because these measurements are performed under slow rates of potential change (e.g. 50 mV/s), electrochemical reactions have more time to be completed before water electrolysis occurs. Therefore, the values obtained are higher than the charge injection limit and not an accurate representation of how much charge can be safely delivered by electrodes during physiological stimulation (Hudak *et al*., 2017).

It is well documented that voltammograms are highly dependent on the electrode material, electrolyte composition and the parameters used during CV measurements. Indeed, two voltammograms of electrodes of the same material may look very different due to difference in experimental set-up, electrolyte, the number of cycles and the scan rate implemented (Cogan, 2008, Hudak *et al*., 2010). The high heterogeneity in these parameters poses a challenge for the direct comparison of voltammograms. The most direct comparison that can be established between the results reported here and the literature is the findings obtained by (Carnicer-Lombarte *et al*., 2017) (figure 4.19). The authors used the same manufacturing techniques and materials implemented in this body of work. Furthermore CV measurements were performed with the same parameters and similar set-up as previously described (refer to Materials and Methods chapter, section 2.2.10.2). Although somewhat comparable, the voltammogram reported in that paper shows peaks characteristic of oxidation and reduction reactions which are not observed in the voltammograms presented in this chapter. Notably, it is important to highlight that in that study, laser micromachining was not implemented to manufacture thick-film Pt/Au electrodes (Carnicer-Lombarte *et al*., 2017). The effects of laser-micromachining on electrochemical properties of Pt are indisputable (Green *et al*., 2012), therefore, it is possible that voltammograms of laser-micromachined Pt/Au are different to those of unmodified Pt/Au, thus accounting for the lack of peaks observed in the voltammograms presented here compared to those reported by Carnicer-Lombarte *et al*. (2017) (figure 4.19). Hudak *et al*. (2017) have previously reported that in order to fully detect electrochemical reactions, in particular hydrogen adsorption and desorption, platinum electrodes must be subjected to a ‘cleaning’ procedure. This will ensure that all platinum surface sites are exposed for hydrogen adsorption to take place. The term cleaning within this context refers to repeated cycling over the two potential limits for water electrolysis. After 50 and 100 cycles the authors observed new hydrogen adsorption-desorption related peaks not present during early cycles. Notably however, the electrochemical behaviour of an electrode under physiological stimulation, most likely resembles the appearance of early cycles rather than those obtained after repeated cycling. This is due to protein adsorption to implanted electrodes blocking sites on the electrode surface for charge transfer to occur (Hudak *et al*., 2017). Therefore, although not physiologically accurate, ‘cleaning’ of electrodes through repeated cycling, serves to explore the electrochemical properties of electrodes. It is possible that differences in the voltammograms compared arise from differences in ‘cleaning’ of electrodes. Moreover, another important factor to take into consideration is the electrolyte composition implemented by Hudak *et al*. (2017) (0.15 M H_2SO_4) compared to the one used in this study (0.05 M PBS). The effect of alloying Pt on its electrochemical properties cannot be discarded. Indeed, voltammograms of Au electrodes are very different to those of Pt electrodes. In line with this, the lack of peaks observed in the CV measurements here reported are comparable to those of flat Au electrodes tested in PBS (Ji *et al*., 2019) (figure 4.20).

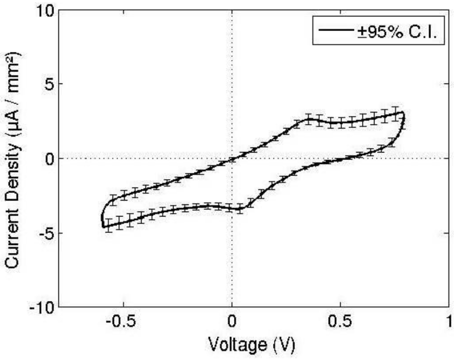

Figure 4.19 Cyclic voltammetry response of thick-film Pt/Au electrode in nitrogen-purged PBS

Voltammogram of Pt/Au electrode as manufactured in nitrogen purged-PBS. Voltage w.r.t a saturated calomel electrode, using a scan rate of 50 mV/sec. Data presented as mean ± 95% confidence intervals for n = 10 (Carnicer-Lombarte *et al*., 2017).

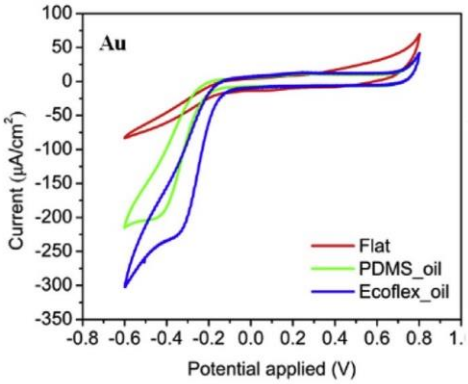

Figure 4.20 Cyclic voltammetry response of Au electrode in PBS

Voltammogram of Au electrode as manufactured (flat, red), wrinkled with oil penetrated PDMS (PDMS oil, green) and Ecoflex substrate (Ecoflex oil, blue). Voltage w.r.t a saturated calomel electrode, using a scan rate of 100 mV/sec (Ji *et al*., 2019).

Overall, these findings show that laminin-coating implemented to promote differentiated SPC-01 cell attachment to electrode arrays had a negligible impact on electrode impedance and CSC. The slight decrease in impedance and increase in CSC detected after laminin-coating may be attributed to repeated cycling exposing more electrode surface sites for charge exchange to occur.

In summary, the results presented in this chapter highlight the ability to manufacture customisable electrode arrays of micrometre scale features using the simple and cost-effective fabrication technique of thick-film printing. Furthermore, electrode arrays manufactured using commercially available materials were shown to support growth and neurite elongation of the MN-like cell line NG108-15 and the human-derived MN-like cells SPC-01.

Additionally, laser-micromachining can be implanted to incorporate topographical cues on these electrode arrays for cell culture studies; however, careful selection of laser-processing parameters is essential to create surfaces that provide directional guidance to extending neurites. Finally, the electrodes manufactured here have low impedance and sufficient CSC to provide effective neural stimulation. Notably, to fully characterise neural electrodes and provide a more accurate expectation of electrode performance during neural stimulation, charge injection limit needs to be considered. This parameter will be presented in Chapter 5, where the biohybrid device for muscle stimulation is discussed.

In conclusion, this chapter presents a simple, versatile and cost-effective technique to manufacture electrode arrays suitable for: supporting differentiated SPC-01 cells, supporting neurite elongation and guiding neurite outgrowth *in vitro*. Furthermore, electrochemical characterisation of manufactured electrodes shows their suitability for effective stimulation of differentiated SPC-01 cells

5.0 Design, development and optimisation of an implantable biohybrid device to stimulate denervated muscles

5.1 Introduction

A novel paradigm in the field of neuroprostheses is the adoption of a biohybrid approach to develop implantable devices. Biohybrid approaches consist of incorporating living cells within implantable electronic devices with the aim of establishing a more biologically relevant interface to the nervous system (Thomas *et al*., 1972). Although this approach is in early, experimental stages, advances in the field will offer unprecedented opportunities towards closer integration of biology and electronics potentially blurring the boundary between living and artificial systems.

The adoption of biohybrid strategies, as reported in the literature thus far, has served two main functions: first, and most commonly reported, to improve the integration of implants with the host environment by increasing biocompatibility. Second, and the main goal of the biohybrid approach described in this thesis, to replace or restore some tissue or organ function following injury.

Overall, the development and functional assessment of biohybrid devices *in vitro* has been met with some degree of success. The most challenging aspect of biohybrid strategies, which still requires further investigation, is the transfer of these devices from the *in vitro* into the *in vivo* environment. At this stage, difficulties encountered centre on the implantation of the device and the long-term survival of the transplanted cells. Such challenges remain largely unsolved at present.

The following section discusses biohybrid approaches adopted to interface with the nervous system and musculoskeletal tissue.

5.1.1 Biohybrid devices to improve implant integration with the host environment

The long-term functionality of implanted electrodes is severely affected by the host inflammatory reaction in response to the foreign implant (Lotti *et al*., 2017). The initial acute inflammatory response triggered by tissue damage during implantation, is followed by a long-term response that results in fibrotic tissue encapsulating the device. The electrical insulation of the implant caused by this fibrotic tissue, leads to a progressive increase in the electrode-tissue impedance, therefore negatively affecting quality of recordings and increasing the amount of charge required for stimulation, consequently increasing power consumption of the device (Green *et al*., 2013b).

Injecting higher amounts of charge can be unsafe, such as where levels breach the electrochemical charge injection limit. Where this level is exceeded, electrochemical reactions at the electrode-tissue interface lead to pH changes, evolution of gasses, and dissolution of electrode material (Cogan, 2008). These irreversible reactions cause tissue damage and implant failure, therefore, limiting the long-term use of implants which evoke a large fibrotic response. As the fibrotic layer increases in thickness, the impact on stimulation and recordings becomes more pronounced. Different approaches have been reported to reduce the host immune response to implants. For example: reducing device size to minimise damage caused during implantation (Kozai *et al*., 2012); using untethered or flexible implants to minimise the impact of tissue movement (Ersen *et al*., 2015); using soft materials that more closely resemble the mechanical properties of the host tissue (Lacour *et al*., 2016) and drug-delivery from the implant to combat the inflammatory response (Boehler *et al*., 2017). Furthermore, a biohybrid approach has been proposed to support long-term functionality of implanted electrodes. The rationale behind this approach is that a cell layer integrated with the surface of implantable electrode arrays will form an indistinct border between the implant and surrounding tissue, minimising or eliminating scar tissue formation and improving integration of the synthetic device with the host environment. Neurons constitute the preferred cell of choice to incorporate into these devices as biohybrids consisting of neurons have been shown to be better tolerated by the host with increased survival as opposed to glial cells which elicit a strong host immune response (Dayawansa *et al*., 2014).

Purcell *et al*. (2009) developed parylene-based biohybrid devices consisting of mouse neural progenitors encapsulated in alginate hydrogels. The device was implanted in rodent brains and immune response monitored at different time points spanning 3 months. The results showed sparing of host neurons and mitigation of the host immune response in the biohybrid group compared to controls (device only and device with acellular alginate gels) after 1 week of implantation. However, this pattern was reversed by 6 weeks post implantation, which the authors attribute to cell death on the biohybrid device and scaffold degradation (Purcell *et al*., 2009). Richter *et al*., (2011a), reported the incorporation of rat glandular stem cells into polyimide probes. Glandular stem cells were chosen due to their ability to differentiate into neural lineages and their ease of accessibility (e.g. sweat glands and submandibular tissue). The authors found seeding these cells in two different types of polyimide probes and protecting them with a fibrin hydrogel, did not alter their survival, growth or ability to differentiate into neural lineages *in vitro* (Richter *et al*., 2011a). Green *et al*. (2013d) adopted a similar approach, but implementing two different hydrogels in their design. First, platinum (Pt) electrodes are coated with a conductive hydrogel formed using a blend of the conductive polymer

PEDOT and poly (vinyl alcohol) (PVA). This blend allowed the release of molecules from the hydrogel (e.g. anti-inflammatory agents) while remaining electrically conductive. An overlying biodegradable gel layer was then used to encapsulate neuronal and glial cells providing biochemical and mechanical support. So far, the authors have published a proof of concept study *in vitro* on the feasibility of developing such a biohybrid device using PC-12 cell line (Green *et al.*, 2013c) and more recently using primary mixed glia and neural progenitors derived from rats (Goding *et al.*, 2017). They reported comparable electrochemical properties between this biohybrid device and bare Pt electrodes. Furthermore, encapsulation of primary cells in the biodegradable hydrogel showed good viability of glia but not neural progenitor cells *in vitro*. In spite of published reports on the feasibility of this approach with certain types of cells, no data has been shown on whether this approach is successful at addressing the issue of scar tissue encapsulation of implanted devices. De Faveri *et al*. (2014) adopted a similar strategy by coating electrodes with autologous hippocampal neurons or astrocytes and encapsulating the device in a fibrin hydrogel in a bid to disguise the implant from the host immune system and match the brain's mechanical properties. Tests in rat cortex showed this approach was biocompatible, did not alter electrochemical properties of the implant, allowed for good quality recordings and reduced the tissue inflammatory reaction over a period of 30 days post-implantation. Roemer *et al*. (2016) reported incorporation of patient-derived mononuclear cells obtained from bone marrow tissue into cochlear implants by using fibrin adhesive to promote attachment of the cells onto silicone-based electrodes. The choice of cells was justified by their immunomodulatory properties and ability to repair tissue following trauma. These biohybrid electrodes were implanted into three patients, meeting safety standards and demonstrating the feasibility of incorporating autologous progenitor cells into cochlear implants. Moreover, the authors compared the performance of the biohybrid device to that of the standard non-coated implant placed in the other ear. They reported all three patients had satisfactory speech perception with similar impedance on both electrodes (Roemer *et al*., 2016). In addition, Kim *et al*. (2016a) reported a multi-functional biohybrid device allowing electrophysiological recording and electrical and/or optical stimulation treatment of skeletal muscles. The hybrid is composed of a sheet of the muscle cell line, C2C12, on transparent graphene electrodes. Results showed the ability of C2C12 to proliferate and differentiate *in vitro* in response to electrical stimulation. Furthermore, implantation of the device into the hind limb muscle of mice showed proliferation of C2C12 cells into native muscle, therefore suggesting integration of the implanted cells with the host tissue. Moreover, the authors also reported the enhancement of angiogenesis near the site of implantation after 7 days, which was attributed to local repair, and showed suppressed recruitment of CD68 macrophages, overall corroborating the therapeutic effect of the cell-sheet graphene hybrid (Kim *et al*., 2016a).

Furthermore, the field of cochlear implants has adopted a biohybrid approach for cell-based drug delivery to the inner ear of hearing disabled patients. This biohybrid approach focuses on the release of neurotrophic factors (NTFs) from human bone marrow-derived MSCs. Briefly, the authors tested feasibility of implantation of an alginate-coated electrode containing genetically modified MSCs in an artificial human cochlea model. They reported reduced insertion forces of the coated device compared to the uncoated device and good stability of the coating after first insertion. Although, the paper did not assess viability of coated MSCs or release of NTFs from these cells, the researchers concluded a biohybrid approach to functionalising electrode arrays offers great promise for the long-term delivery of NTFs from an endogenous source for inner ear therapy (Hugl *et al*., 2019) .

5.1.2 Biohybrid devices to restore tissue function

An alternative application of biohybrid devices is that of partially restoring a tissue or organ function lost as a result of injury or disease. The basis of this approach is to replace native cells with cells on the device. As such, it relies on the formation of synaptic connections between cells on the device and the target tissue. Essentially, if functional connections can be made in this fashion between device and target tissue, this approach offers the potential to change the way in which neuroprostheses operate and the paradigm of electrical stimulation of excitable tissue. So far, proof of concept has been reported; however, several challenges remain to be solved, before such a technology can be feasible (Goding *et al*., 2018).

In 2002, Stieglitz and colleagues reported the development of titanium-gold microprobes using thin-film technology, designed to house cells and to integrate with the PNS. Meyer and colleagues (2002) adopted this device to incorporate an oligodendrocyte cell line of rat origin (OLN-93). These cells were genetically modified to increase their resistance to apoptosis, therefore improving their chances of survival *in vivo*. The authors reported adherence and increased proliferation of OLN-93 cells seeded on the microprobe *in vitro*. However, only a microprobe lacking the cellular component was implanted into the proximal stump of rat sciatic nerve, not the complete biohybrid device. This paper concluded the device remained fixed to the initial position 11 months after implantation and as expected, immunoreactivity to the implant was seen at least 6 months after implantation (Meyer *et al*., 2002). Some efforts have been made towards adopting a biohybrid approach for retinal implants. A prototype of this device comprising neurons cultured on implantable electronics interfaced to an artificial optic nerve prepared from Schwann cells, has been developed in order to guide neurons on the device to the visual cortex, thus connecting the device to the CNS (Yagi *et al.*, 2005, Yagi, 2009). No further development of this biohybrid device has been reported by the authors. Similarly, a biohybrid approach has been developed to incorporate dorsal root ganglion (DRG) neurons with mechanically stretch-grown axons onto MEAs as a mean of interfacing implantable electrodes with regenerating peripheral nerves (Pfister *et al.*, 2006, Kameswaran *et al.*, 2008, Cullen *et al.*, 2011b). DRGs were seeded on flexible MEAs and induced to stretch-growth at a rate of 1 mm/day for 5 days *in vitro*. The neuroelectrode construct was then embedded in agarose hydrogels and the construct placed inside resorbable tubes (NeuraGen) for structural support and consequently sutured to the proximal stump of rat sciatic nerves. This approach may allow for direct interfacing with the transected nerve, therefore avoiding the need to decode complex neural signals from the CNS. Kameswaran *et al*. (2008) reported signs of vascularisation on the device after 2 weeks *in vivo.* Later on, Huang *et al*. (2009) employed this allogeneic biohybrid device to repair a 1.2-1.3 cm rat sciatic nerve gap. Results showed the transplanted device maintained its structure after 16 weeks *in vivo*, host axon regeneration into intimate contact with microelectrodes was observed and axons from the device penetrated into the host nerve. Additionally, a similar paradigm is being actively developed for the CNS. This approach consists of creating long, encapsulated axonal tracks by seeding neuronal cells in hydrogel micro-columns. The technology, known as micro-tissue-engineered neural networks (micro-TENNs) can be paired with less invasive electrodes such as electrocorticography (EoCG) electrode arrays. Essentially, only the biological component of the device is implanted in the brain while the electrical portion remains externalised on the brain or dura surface (Adewole *et al.*, 2018, Adewole *et al.*, 2019). Micro-TENNs consisting of cerebral cortical neurons or DRGs of rodent origin were implanted into the brain of rats. Results showed the implanted neurons survived and preserved their long axonal architecture after 1 month *in vivo*. Furthermore, extension of neurons from micro-TENNs into the host and the formation of synaptic connections was reported (Struzyna *et al.*, 2015).

Overall, the upcoming field of neurological biohybrid devices has reached proof of concept stage. While extensive research is still required to develop this technology, it offers the potential to re-establish functional connections. Moreover, as a result of improved integration between device and host, the foreign body response can potentially be reduced. Ultimately, the success of this technology has the potential to cause a paradigm shift in the field of bioelectronics medicine and usher unprecedented opportunities to treat a diversity of injuries and nervous system disorders.

5.1.3 The use of hydrogels in bioelectronics and biohybrid devices

Hydrogels are polymer networks infiltrated with water that retain their three-dimensional (3D) structure due to physical or chemical cross-linking of individual polymer chains (Chai *et al*., 2017). Their soft and flexible nature resembles that of biological tissue, therefore minimising mechanical mismatch with the *in vivo* environment. Furthermore, their high water content allows for an ion-rich environment, thus increasing the gel's conductivity. Notably, this increased conductivity effect is highly dependent on the degree of cross-linking (Kaklamani *et al*., 2018).

Conductive hydrogels (CH), a hybrid between a conductive polymer and a hydrogel, have been successfully implemented to dampen the mechanical properties of hard implants and to improve the electrical properties of electrodes. Fundamentally, the hydrogel component swells when in aqueous solution increasing the influx of ions and forming a 3D surface through which charge transfer occurs. This enables electrodes to inject greater amounts of charge in the presence of a CH than an uncoated metal electrode of the same geometric surface area (Hassarati *et al*., 2014). For example, it has been recently reported that Pt electrode arrays encapsulated with a thin poly (3,4-ethylenedioxythiophene):poly(styrenesulfonate) (PEDOT:PSS) CH film have a current injection density, approximately 30 times higher than that of uncoated Pt electrodes (Liu *et al*., 2019).

Not surprisingly, hydrogels have drawn a great deal of attention in the bioelectronics field. Their properties have been exploited not only to overcome safe charge injection limits but also as a strategy to achieve seamless integration between biology and electronics. Indeed, in the endeavour of minimising immunoreactivity to implants, PEG-coated neural implants have been shown to reduce scarring and macrophage activation compared with uncoated implants of identical diameters when implanted into the rodent brain (Spencer *et al*., 2017).

With respect to biohybrid devices, hydrogels can be used for cellular encapsulation of the biological component of this hybrid approach. Fundamentally, hydrogels provide a 3D environment that is supportive of cell survival and growth within the confined space of implantable devices (Mahoney and Anseth, 2006). Furthermore, hydrogel encapsulation ensures cell bodies remain in close proximity to electrode sites on the device, while allowing axons to migrate into the host environment. Indeed, for this approach to be successful, migration of host cells out of the implanted device must be prevented (Navarro *et al*., 2005). Moreover, hydrogels can act as a protective barrier against the mechanical forces cells are exposed to during device implantation (De Faveri *et al*., 2014). Of particular relevance to allogeneic (and other non-autologous) biohybrid devices, is the protection hydrogels can provide to implanted cells to prevent immune recognition.

The choice of hydrogel polymer is dependent on the primary function of the device. For example, it may be desirable to use degradable materials that provide a temporary benefit, while other applications will use non-degradable materials to provide long-term effects and permanence. To this end, various polymers (both, natural and synthetic) have been implemented. When using biodegradable hydrogels, two considerations should be taken into account when choosing the polymer and the nature of cross-linking. First, the kinetics of degradation and second the biocompatibility of the polymer and its degradation products. With respect to the former, it is desirable to synchronise the rate of degradation with the development of cellular networks, so the hydrogel degradation process is replaced with the extracellular matrix (ECM) deposition by the cells on the implant or from the host tissue. Failure to do so could results in cells on the implant dying due to loss of mechanical and biological support from the hydrogel (early degradation) or, alternatively, inhibition of differentiation and development of implanted cells (late degradation) (Goding *et al*., 2018). Regarding biocompatibility, the degradation process entails release of products into the local environment, therefore, it is important to ensure such products are biocompatible with the cells on the implant as well as with the native tissue. Failure to do so, could elicit an inflammatory or immune response against the device (Goding *et al*., 2018).

Common natural materials employed to fabricate hydrogels include: collagen, fibrin, agarose and alginate, while most synthetic hydrogels are made with polyethylene glycol (PEG), polyvinyl alcohol (PVA) and polyacrylamide. Although many different types of hydrogels have been used for tissue engineering purposes, only a few have been implemented in the field of biohybrid devices. Table 5.1 summarises the hydrogels employed in the development of biohybrid devices aimed at improving implant integration with the host environment, and table 5.2 summarises the hydrogels employed in the development of biohybrid devices aimed at restoring tissue function.

Study	Material	Type	Choice rationale	Concentration of polymer on the gel	Cells	Purpose of hydrogel	Model	Findings
(Purcell *et al*., 2009)	Alginate	Natural	- Biocompatible - Used to encapsulate secretory cells - Provide immune-isolating barriers	1% w/v	Embryonic mouse cortical neural stem cells	Encapsulate cells and device	Rat CNS	Alginate was stable during the first week *in vivo*. By 6-weeks post-implantation alginate hydrogels significantly degraded, leaving cells vulnerable to immune rejection and leading to inflammation.
(Richter *et al*., 2011b)	Fibrin	Natural	- Biodegradable - Easily applicable - Native coverage - Highly definable - Clinically approved	1.5 mg/ml	Rat pancreatic stem cells	Encapsulate cells and device to protect cells during implantation	*In vitro*	Fibrin hydrogel did not affect cell differentiation potential or metabolism.
(Green *et al*., 2013b)	Poly-vinyl-alcohol (PVA)/ Sericin (silkworm protein)	Biosynthetic	- Degradable in 21 days - Supports cell proliferation and differentiation	9 % w/v PVA 1% w/v sericin	PC-12 neuronal-like cell line	Encapsulate cells to provide biochemical and mechanical support	*In vitro*	Excellent cell viability and neurite extension at day 12. Cells integrated with polymer strands of hydrogel. No degradation observed after 12 days and further improvement of electrical and mechanical properties of device is reported.

Study	Material	Type	Choice rationale	Concentration of polymer on the gel	Cells used	Purpose of hydrogel	Model	Findings
(Goding *et al.*, 2017)	PVA / gelatin / Sericin	Biosynthetic	- Degradable in 21 days - Supports cell proliferation and differentiation - Gelatin supports cell spreading and survival	98% w/v PVA 1% w/v gelatin 1% w/v sericin	Rat primary glia and neural progenitors	Encapsulate cells to provide biochemical and mechanical support	*In vitro*	Decreased in neural progenitor cells viability after 24 hrs. Good viability of encapsulated glial cells.
(De Faveri *et al.*, 2014)	Fibrin	Natural	- Controllable thickness - Does not affect electrochemical properties of electrode - Biodegradable Moderate swelling	Not stated	Rat primary hippocampal neurons and astrocytes	Encapsulate cells and device to minimise mechanical mismatch and protect cells during implantation	Rat CNS	Reduction in astrocyte reaction in fibrin-coated devices after 7 and 30 days *in vivo* compared with uncoated devices. Good viability of astrocytes and neurons encapsulated in fibrin. Hydrogel degraded after 7 days *in vivo.*
(Roemer *et al.*, 2016)	Fibrin	Natural	Not stated	Not stated	Human bone marrow autologous mononuclear cells (BM-MNCs)	Encapsulate cells and device to prevent cells from migrating from device surface	Human cochlea	BM-MNCs survived within the fibrin coating for 3 weeks *in vitro* and died thereafter

Table 5.1 Hydrogels used in the development of biohybrid devices to improve implant integration with the host environment

This table summarises selected studies reporting the use of hydrogels on biohybrid device. Hydrogel material, rational for material used, its concentration, cells encapsulated, purpose of encapsulating cells. Model used to test device and the findings reported, are presented.

Table 5.2 Hydrogels used in the development of biohybrid devices to restore tissue function

This table summarises selected studies reporting the use of hydrogels on biohybrid device. Hydrogel material, rational for material used, its concentration, cells encapsulated, purpose of encapsulating cells. Model used to test device and the findings reported, are presented.

Study	Material	Type	Choice rationale	Concentration of polymer on the gel	Cells used	Purpose of hydrogel	Model	Findings
(Kameswaran *et al*., 2008)	Agarose	Natural	Not stated	Not stated	Rat DRG explants	Support stretch grown axons	Rat PNS	Device maintained its position and structure after 2 weeks *in vivo*
(Huang *et al*., 2009)	Collagen type I	Natural	Not stated	3 mg/ml	Rat DRG neurons	Support stretch grown axons	Rat PNS	Device maintained its position and structure after 16 weeks *in vivo*. Migration of host axons into the device and vice versa was observed
(Struzyna *et al*., 2015)	- Outer gel: Agarose - Inner gels: Collagen Collage-laminin Fibrin	Natural	Not stated	Agarose: 1-4 % w/v Collagen (3 mg/ml) Collagen-laminin (1 mg/ml each) Fibrin (1 mg/ml)	Rat DRG neurons and cortical neurons	Outer hydrogel: provide mechanical support Inner hydrogels: Control movement of cell bodies, support neural survival and extension	*In vitro* and Rat CNS	Collagen-laminin blend and fibrin, but not collagen supported survival and neurite extension of cortical neurons after 7 days *in vitro.* 3-4 % w/v agarose induced healthier neurites than 1-2% w/v. Thinning of agarose hydrogel by day 28 *in vivo.*

Study	Material	Type	Choice rationale	Concentration of polymer on the gel	Cells used	Purpose of hydrogel	Model	Findings
(Hugl *et al.*, 2019)	Alginate	Natural	- Biocompatibility, stability and flexibility - Low immunogenicity - Migration of host regenerating neurites into the hydrogel	0.65 % w/v (ultra-high viscosity alginate)	Human bone marrow-derived MSCs	Encapsulate cells and device to prevent cells migrating from device and shield cells from host immune system	*In vitro* human cochlea model	Cell viability was not assessed, however, alginate reduced insertion forces upon implantation compared with uncoated electrodes

5.1.4 Hydrogel used for the implantable biohybrid device in this study

Here, alginate-based hydrogels were used to cover human neural stem cell-derived motor neuron cells growing on the reservoir of electrode arrays. In choosing a hydrogel material, the following desirable properties were considered: biocompatibility, low immunogenicity, minimal to no biological interaction with cells on the device, non-degradable and ease of gelation.

Alginate is a naturally occurring polysaccharide extracted from brown algae (Andersen *et al*., 2015). This linear polymer is comprised of blocks of mannuronic acid (M) and guluronic acid (G), the concentration ratio of which influences material properties including purity and endotoxin levels (Lee and Mooney, 2012). Formation of an alginate hydrogel is achieved by ionic cross-linking of G blocks. Following cross-linking, a hydrogel with a higher G:M ratio will be stiffer, whereas a lower G:M ratio will produce softer hydrogels with increased porosity (Ramos *et al*., 2018). Alginate is a biocompatible, non-toxic and low-immunogenic polymer (Lee and Mooney, 2012). Its hydrated structure prevents the influx of immune system cells while allowing diffusion of oxygen and nutrients (Meiser *et al*., 2013). Moreover, the lack of suitable mammalian cell adhesion molecules and low protein adsorption characteristic of this polymer, translates into low capacity for cell interaction (Zhang *et al*., 2015). Another desirable property of alginate-based hydrogels for the application described here, is their inability to be degraded by mammalian enzymes. Instead, their degradation occurs over longer periods of time due to the slow diffusion of Ca^{2+} ions out of the gel (Lee and Mooney, 2012).

Taking into account electrical considerations of incorporating a hydrogel onto electrode arrays, previous research has reported alginate can be combined with conductive polymers to enhance electrochemical properties. Indeed, Ferlauto *et al*. (2018) reported the development of a conductive alginate hydrogel by mixing PEDOT, PSS and alginate. The researchers reported this coating improved electrochemical properties of Pt electrodes leading to lower noise recordings from the visual cortex of mice compared with uncoated electrodes.

Although the biocompatibility of this natural polymer has been extensively documented in the literature, some controversy exists based on the type of alginate implemented. Fibrosis and immunoreactivity has been documented for most commercial alginates when implanted *in vivo* (Tam *et al*., 2006), this response is linked to high levels of impurities and endotoxins associated with the polymer. As fibrotic tissue accumulates, the diffusion of oxygen and nutrients becomes restricted (Orive *et al*., 2005). In contrast, little or no immune response to alginate implants has been reported when using high purity polymers (Sondermeijer *et al*., 2016). In light of this, the response of differentiated SPC-01 cells to two types of alginate was studied. A non-purified commercial alginate (herein referred to as Sigma alginate) and an ultrapure alginate manufactured according to good manufacturing practice (GMP) standards (herein referred to as NovaMatrix alginate).

5.1.5 Objectives of this chapter

The aims of this chapter were three-fold. First, to provide proof-of-concept of the development of an implantable biohybrid device with electrochemical properties that effectively supports stimulation of neuronal cells. Second, to assess the feasibility of implanting this device into the rodent muscle denervation model used elsewhere in this body of work. Third, to explore the incorporation of a protective hydrogel to shield human-derived MN-like cells from the host immune system. This was tested by a series of experiments with the following objectives:

(i) To manufacture an implantable device adapted to the dimensions of rat sciatic nerve branches;

(ii) To explore gold rivet bonding as a mean of establishing electrical interconnections with the implantable device;

(iii) To electrochemically characterise manufactured electrodes by CV and EIS;

(iv) To monitor growth of differentiated SPC-01 cells on the biohybrid device and assess reproducibility of fabricating devices with consistent cell densities;

(v) To implant the biohybrid device in a muscle denervation model and explore the fate of differentiated SPC-01 cells on the device;

(vi) To investigate the effect of two types of alginate hydrogels on the metabolic activity of differentiated SPC-01 cells.

5.2 Results

5.2.1 Manufacture of the prototype implantable device

A miniaturised version of the optimised design for *in vitro* experiments (see Chapter 4) was designed and adopted as the implantable device prototype. The size of the device was chosen to meet anatomical requirements of the sciatic nerve branches of rats. Furthermore, as a result of miniaturisation, the cost-effectiveness of the manufacturing process was improved, as 24 individual implantable device prototypes were manufactured from each alumina substrate sample (1” x 1”) (figure 5.1A).

Implantable device prototypes were successfully manufactured using the unstructured alumina manufacturing method (refer to Materials and Methods, section 2.2.9). A number of challenges were encountered during the fabrication process: first, laser misalignment was a common issue when ablating the PDMS layer to expose sites of interest. The process of spin-coating an insulating PDMS layer on top of the sintered Pt/Au electrode arrays, caused non-uniform PDMS deposition across the alumina substrate. As a result, differences in the areas ablated between individual electrode arrays were observed. This issue was more severe when laser ablating electrode arrays located towards the edges of the alumina substrate, where the PDMS layer was thickest. To overcome this challenge approximately 1 mm of PDMS around the edges of the alumina substrate was manually removed using a scalpel before laser-ablating areas of interest. This improved reproducibility in electrode site exposure across samples. Moreover, to accommodate for laser misalignments and minimise these effects across implantable device prototype samples, the initial design (figure 5.1A) consisting of 2 outer electrodes (100 µm x 150 µm), was modified to one outer electrode (400 µm x 150 µm) (figure 5.1B). Having an outer electrode of equal width to the cell-seeding reservoir, served to minimise laser misalignments when exposing electrode sites, therefore, improving reproducibility of electrode site dimensions across individual electrode arrays.

In addition, tearing of the PDMS during separation of individual electrode arrays at the end of fabrication was an issue commonly encountered. Guidelines delineating individual electrode arrays (figure 5.1B) were included in the design and laser-ablated to allow snapping the alumina to separate individual electrode arrays. Snapping alumina also caused tearing of the PDMS layer. To overcome this issue, PDMS covering guidelines between each sample were manually removed using a scalpel before snapping alumina (figure 5.1E).

Connecting copper wires to electrodes was a challenge due to the small size of solder pads. To improve ease of fabrication, ball bumping (refer to Materials and Methods chapter, section 2.2.9.6) was implemented to connect solder pads on the electrode array to external stainless steel pads with dimensions more suitable for soldering. The strength of the bond formed when ball bumping Au onto sintered Pt/Au (figure 5.1B) was very low, therefore, sintered Pt/Au samples were polished using a fiberglass brush. This polished surface (figure 5.1C) improved Au bonding onto Pt/Au. The stainless steel foil was carefully aligned with respect to the solder pads on the electrode array. Two gold bumps were created on the surface of the Pt/Au solder pads. The stainless steel foil was then placed over the gold bumps and a second bond was performed in order to secure the stainless steel pads in place. However, the second bond resulted in detachment of the first gold bond from the Pt/Au pads. Modifications to the bonding parameters were made. Specifically, the force implemented to perform the second bond was decreased to avoid detachment of the first bond and stainless steel pads; however, secure bonding of external pads onto the implantable device prototype was not achievable. Consequently, soldering (refer to Materials and Methods chapter, section 2.2.9.5) was successfully implemented to connect Pt/Au solder pads to insulated copper wires on samples used for electrochemical characterisation. In light of these findings, the microrivet bonded external stainless steel pads were not incorporated on the implantable device.

Finally, the implantable device prototype was mounted onto a PDMS sheet and all sharp alumina corners covered with PDMS, ready for implantation (figure 5.1F).

The following section explores the electrochemical properties of manufactured implantable devices.

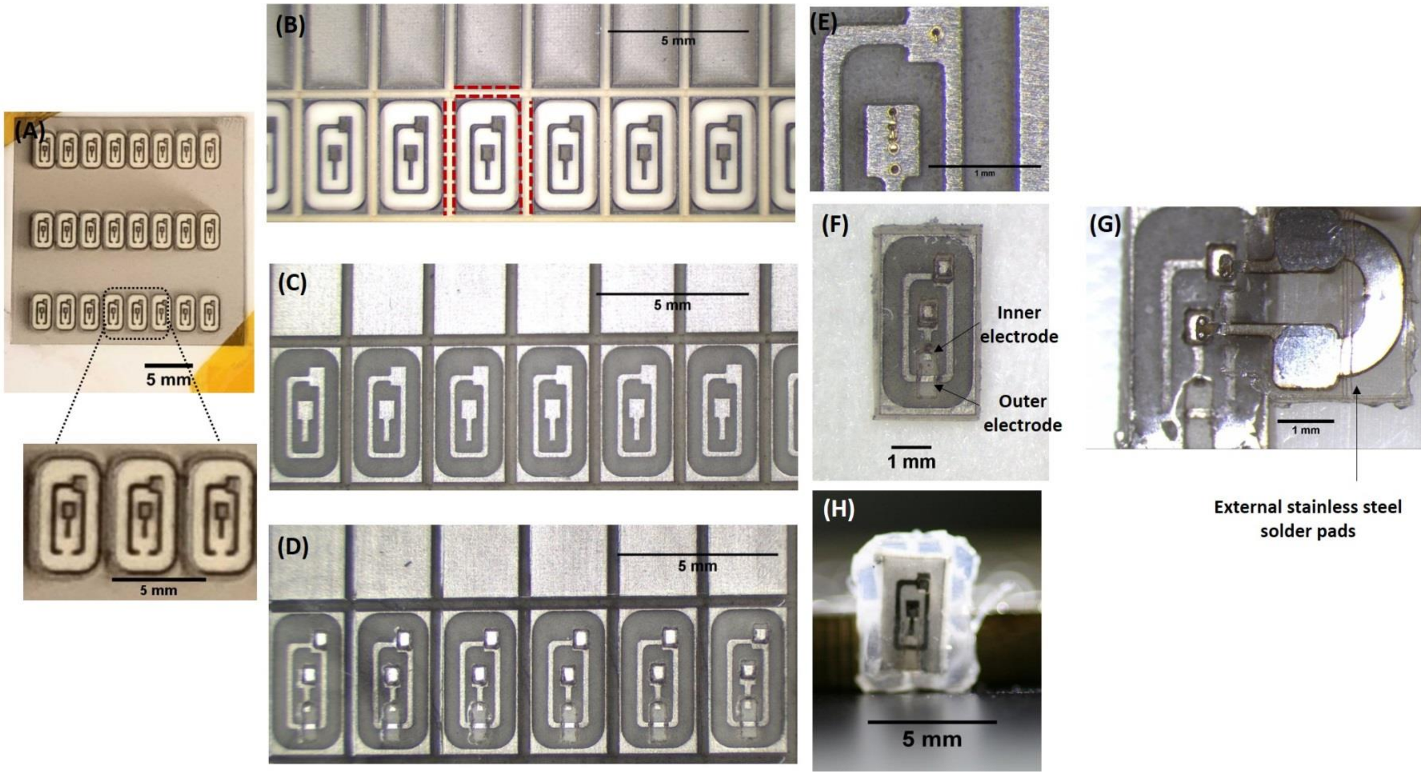

Figure 5.1 Light micrographs of the processing steps in the optimisation and manufacturing of the implantable device prototype

Representative images depicting steps involved in the fabrication of the implantable device prototype. (A) Laser-ablation of 24 individual implantable devices on sintered Pt/Au alumina substrate. Inset shows the initial design consisting of 2 outer electrodes. (B) Laser-ablation of guidelines (shown in dashed red lines) delineating individual implantable devices. (C) Polishing of sintered Pt/Au surface to improve gold ball bumping of Pt/Au solder pads. (D) Laser-ablated PDMS layer to expose electrode sites and solder pads. (E) Gold ball bumping test on polished sintered Pt/Au surface. Scale bar = 1 µm (F) Implantable device prototype following alumina snapping. Inner electrode GSA = 0.0003 cm^2, outer electrode GSA = 0.0006 cm^2. Scale bar = 1 mm. (G) External stainless steel solder pads aligned onto Pt/Au solder pads of implantable device. Scale bar = 1 µm. (H) Sharp corners of device coated in silicone ready for implantation and a support silicone layer added around the reservoir for suturing.

5.2.2 Electrochemical characterisation of implantable device prototype

Electrochemical properties of electrode arrays were characterised using cyclic voltammetry (CV) and electrical impedance spectroscopy (EIS) (refer to Materials and Methods chapter, section 2.2.10.2). EIS was implemented to assess impedance and CV used to measure charge storage capacity (CSC) of electrodes. Each sample consisted of 2 electrodes (referred to as outer electrode and inner electrode) (see figure 5.1F). To account for the differences in geometric areas, each electrode was tested individually.

Impedance results are presented as bode plots for electrode arrays as manufactured (figure 5.2). The results at low (20 Hz), medium (1 kHz) and high (100 kHz) frequencies were compared (table 5.3). As expected, impedance of the larger outer electrodes at the three frequencies compared was lower than that of the inner electrodes.

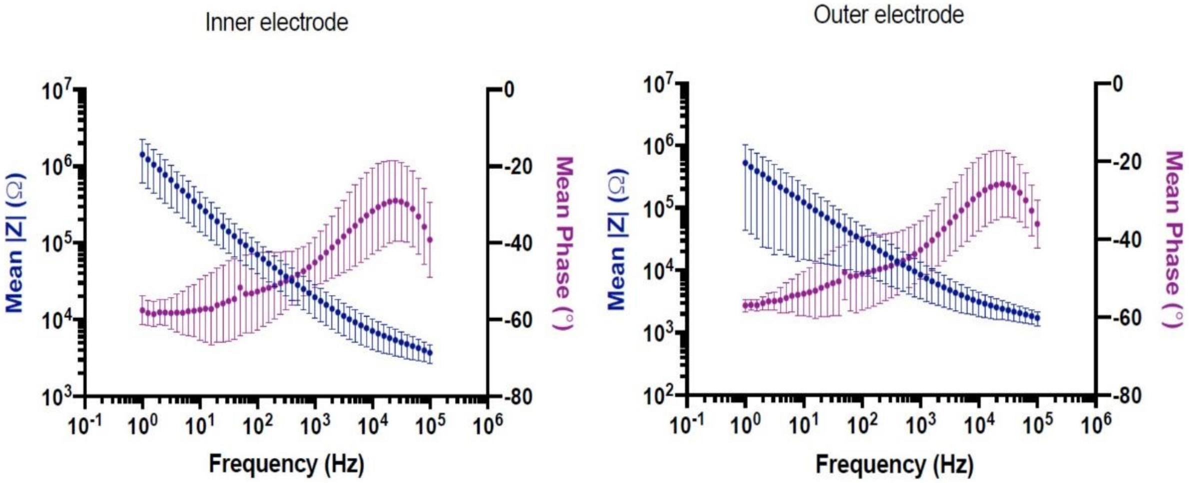

Figure 5.2 Bode plots of frequency-dependent impedance of implantable device prototype as manufactured

Impedance Magnitude |Z| and phase (^{0}) of electrodes tested at different frequencies ranging from 1 Hz to 100 kHz in phosphate buffered saline. Inner and outer electrodes were tested as manufactured. A small deviation in phase angle is apparent at 50 Hz due to power line interference. Data presented as mean ± SD for n = 5 individual electrode array constructs.

CV responses to a 50 mV/s sweep were measured with either the inner or outer electrode as the working electrode. Voltammograms normalised to electrode geometric area are shown in figure 5.3. Charge storage capacity (CSC) and cathodic CSC (cCSC) were calculated from the CV responses. Furthermore, charge injection capacity (Q_{inj}) was assessed using charge controlled biphasic waveforms with a pulse width of 4 ms and implementing maximum negative and positive potentials within the water window (i.e. -0.6 V to + 0.8 V) (table 5.4).

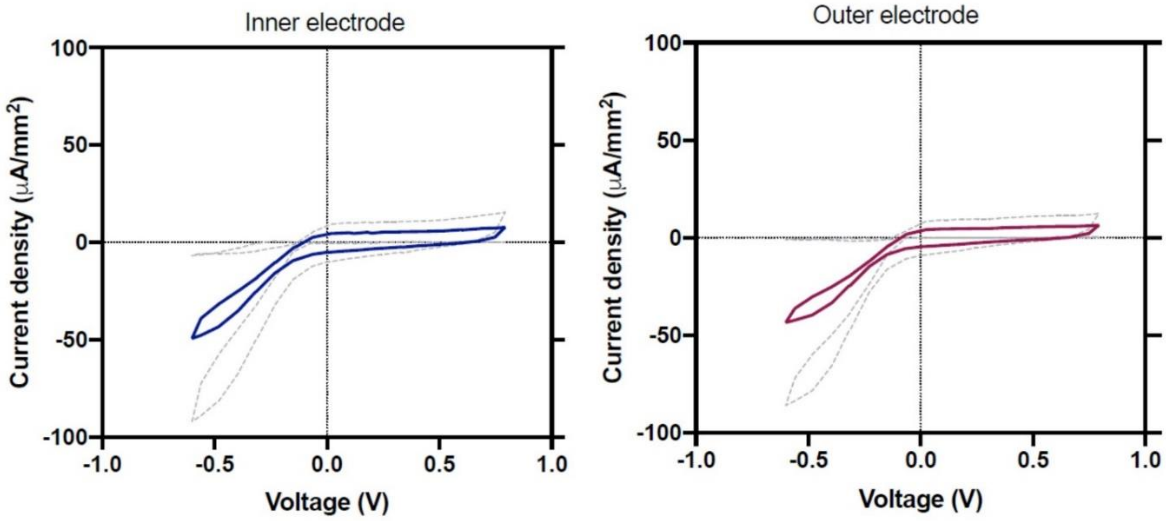

Figure 5.3 Cyclic voltammograms of implantable device prototype as manufactured

A potential between -0.6 and +0.8 V w.r.t reference was swept at a scan rate of 50 mV/s in phosphate buffered saline. Responses of inner electrode and outer electrode were normalised to their respective geometric areas. Data presented as mean ± SD (dashed curves) for n = 5 electrode array constructs.

Table 5.3 Impedance (|Z|, in kΩ) of thick film Pt/Au electrode arrays manufactured using the unmodified alumina method to create implantable device prototypes

Impedance values reported for inner and outer electrode tested at low (20 Hz), medium (1 kHz) and high frequencies (100 kHz). Data presented as mean ± SD for n = 5 individual electrode arrays.

	Impedance (kΩ)	
Frequency	**Inner electrode**	**Outer electrode**
20 Hz	190.82 ± 95.39	79.95 ± 66.74
1 kHz	19.57 ± 9.10	8.43 ± 4.98
100 kHz	3.69 ± 1.04	1.72 ± 0.44

Table 5.4 Charge storage capacity (CSC), cathodic CSC (cCSC) and charge injection capacity (Q_{inj}) of thick film Pt/Au electrode arrays manufactured using the unmodified alumina method to create implantable device prototypes

CSC and cCSC values for inner and outer electrode. All values are normalised to electrode geometric area. Data presented as mean ± SD for n = 5 individual electrode array constructs.

	Inner electrode	**Outer electrode**
CSC (mC/cm^2)	8.02 ± 5.21	20.63 ± 14.59
cCSC (mC/cm^2)	3.62 ± 2.07	10.63 ± 7.91
Q_{inj} per cathodic phase 0.187 ± 0.018 mC/cm^2		

In order to compare the effect of polishing the surface of electrodes with a fiberglass brush, the impedance and CSC values here obtained were compared to those reported for unpolished electrodes (optimised design for *in vitro* experiments) (see Chapter 4, section 4.2.9). To account for differences in electrode size between both designs, impedance values were normalised to GSA. Normalised impedance of unpolished outer electrodes at all frequencies compared was statistically significantly higher than that of polished outer electrodes. At a low frequency (20 Hz) impedance of unpolished electrodes was 251.4 Ω ± 203.3 measured per electrode compared with 48.0 Ω ± 40.4 measured per unpolished electrode (figure 5.4A). Impedance of unpolished electrodes at a medium frequency (1 kHz) was 64.0 Ω ± 61.4 measured per electrode compared with 3×10^6 Ω ± 2.59×10^6 measured per unpolished electrode. At a high frequency (100 kHz) impedance of unpolished electrodes was 5.4 Ω ± 3.7 measured per electrode compared with 1.0 Ω ± 0 measured per polished electrode (figure 5.4A). The same trend was observed when comparing normalised impedance of inner electrodes. At 20 Hz an increase was detected in unpolished electrodes (514 Ω ± 498.1 measured per electrode) compared with polished electrodes (57.2 Ω ± 29 measured per electrode). This increase was statistically significant at 100 kHz frequency (5.2 Ω ± 4.4 measured per unpolished electrode compared with 1.0 Ω ± 0 measured per polished electrode) and at 1 kHz (99.2 Ω ± 114.2 measure per unpolished electrode compared with 5.8 Ω ± 2.9 measured per polished electrode) (figure 5.4B).

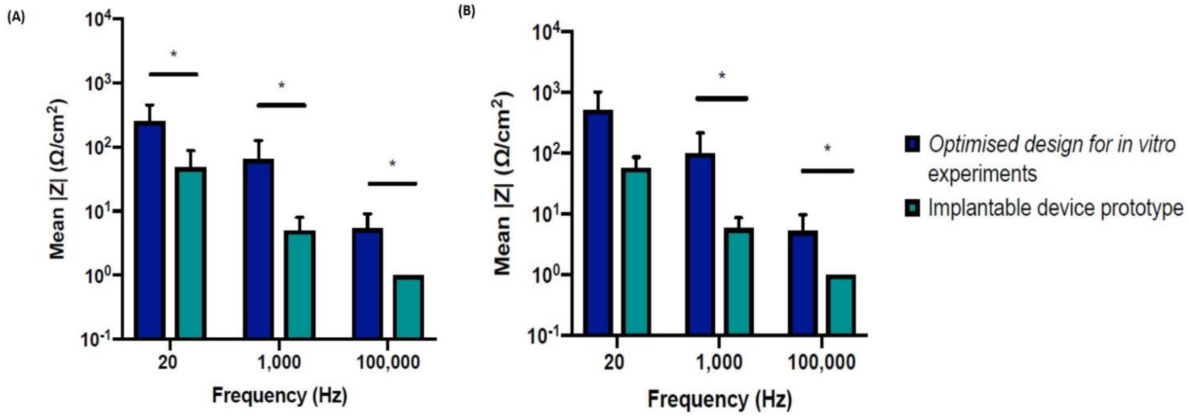

Figure 5.4 Impedance of outer and inner electrodes of unpolished sintered Pt/Au (optimised design for in vitro experiments) and polished sintered Pt/Au (implantable device prototype)

Impedance at low, medium and high frequencies of outer (A) and inner (B) electrodes of the optimised design for *in vitro* experiments (unpolished sintered Pt/Au) compared to that of the implantable device prototype (polished sintered Pt/Au). To account for differences in electrode size between both designs, impedance values were normalised to electrode GSA. Data presented as mean ± SD for n = 5 individual electrode arrays. *$p < 0.05$, Mann Whitney test. Impedance at each frequency was analysed separately.

Comparison of CSC between electrodes showed the opposite trend. Greater CSC per area was obtained with polished sintered Pt/Au electrodes compared with unpolished sintered Pt/Au electrodes. This trend was observed for both, inner (8.02 mC/cm^2 ± 5.21 measured per polished electrode compared with 4.68 mC/cm^2 ± 3.83 measured per unpolished electrode) and outer electrodes, where a statistically significant increase was detected (20.63 mC/cm^2 ± 14.59 measured per polished electrode compared with 4.22 mC/cm^2 ± 2.59 measured per unpolished electrode) (figure 5.5).

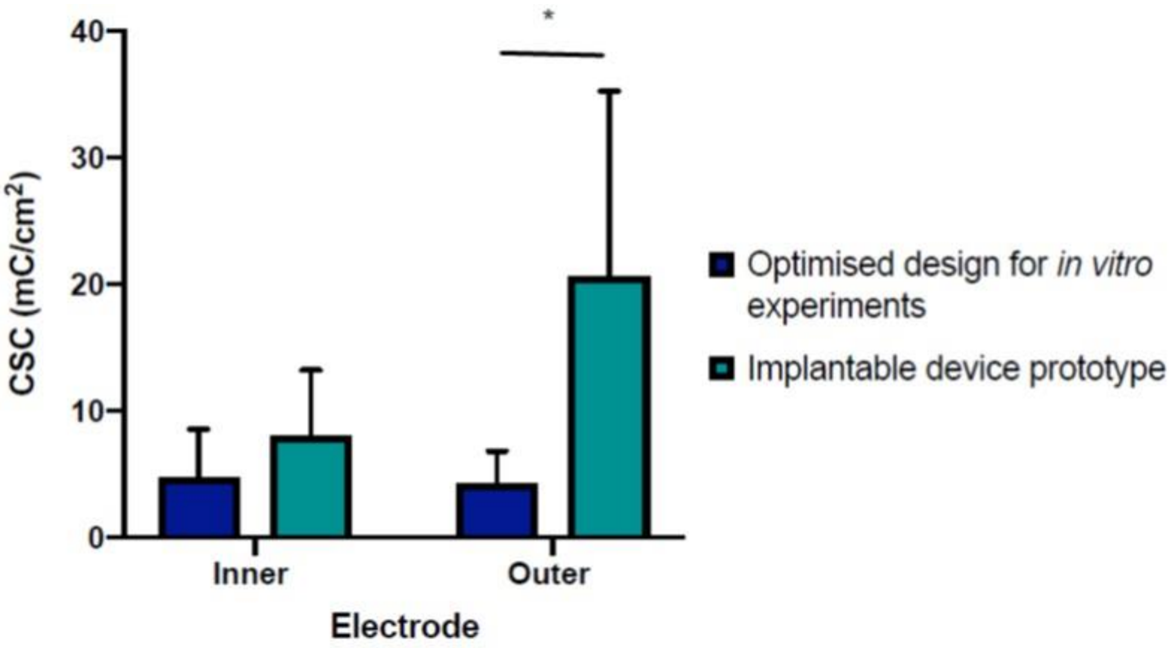

Figure 5.5 CSC of inner and outer electrodes of unpolished sintered Pt/Au (optimised design for in vitro experiments) and polished sintered Pt/Au (implantable device prototype)

CSC of inner and outer electrodes of polished and unpolished samples. To account for differences in electrode size between designs, inner and outer electrodes were normalised to GSA. Data presented as mean ± SD for n = 5 individual electrode arrays. $^*p < 0.05$, unpaired t-test.

Overall, these data suggest polishing the surface of electrodes causes an increase in impedance, however, the values here reported along with CSC and Q_{inj} are adequate to support effective stimulation. The next line of investigation focused on incorporating MN-like cells onto implantable electrodes to assemble a biohybrid device.

5.2.3 Exploring incorporation of differentiated SPC-01 cells on prototype implantable electrode arrays to create a biohybrid device

The following experiment assessed the incorporation of differentiated SPC-01 cells on cell-seeding reservoirs of implantable electrode arrays. Due to the small dimensions of reservoirs in this design (0.4 x 1 mm), approximately 3×10^3 cells diluted in 3 µl of media were seeded per device. To assess uniform seeding of cells between implantable devices and to monitor the growth of cells on these electrode arrays, devices were fixed at different time points and cell density per device quantified (figure 5.6). A 0 hrs time point was included to determine initial seeding density. Following cell attachment, 626 ± 195 cells per implantable device were quantified. Cell density increased after 2 and 7 days *in vitro*. This increase was statistically significant in the day 7 group (993 ± 161 cells per implantable device) (figure 5.7).

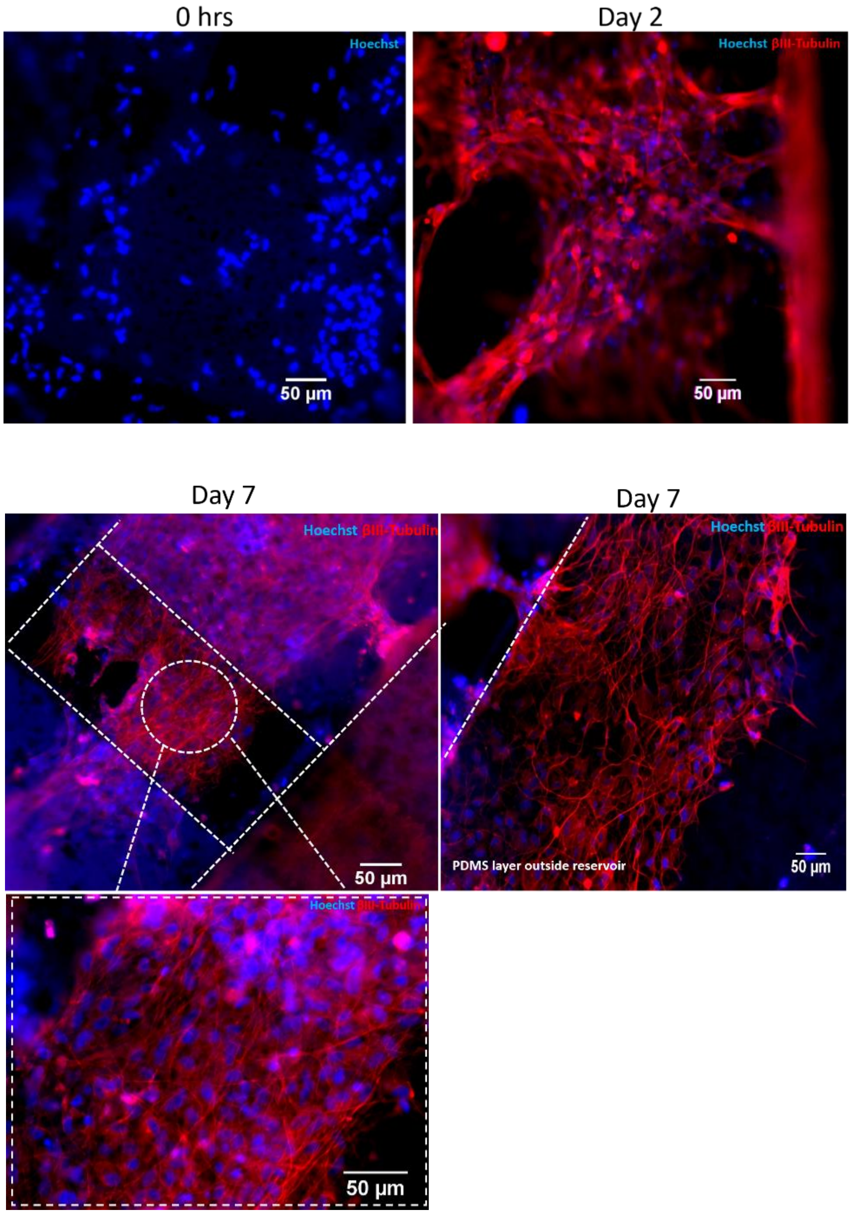

0 hrs

Day 2

Day 7

Day 7

Hoechst
Hoechst βIII-Tubulin
Hoechst βIII-Tubulin
Hoechst βIII-Tubulin
Hoechst βIII-Tubulin
PDMS layer outside reservoir
50 µm

Figure 5.6 Differentiated SPC-01 cells seeded on implantable device prototypes

Representative fluorescence microscopy images showing differentiated SPC-01 cells cultured on reservoir of electrode arrays after seeding (0 hrs), at day 2 and day 7 *in vitro.* High power image of cells growing on reservoir at day 7 seven is shown. Cells growing outside the reservoir are also shown. Cells were fixed before staining to detect βIII-Tubulin (red) and Hoechst (blue). Dashed lines delineate reservoir edges and outer electrode (day 7). Scale bars = 50 µm.

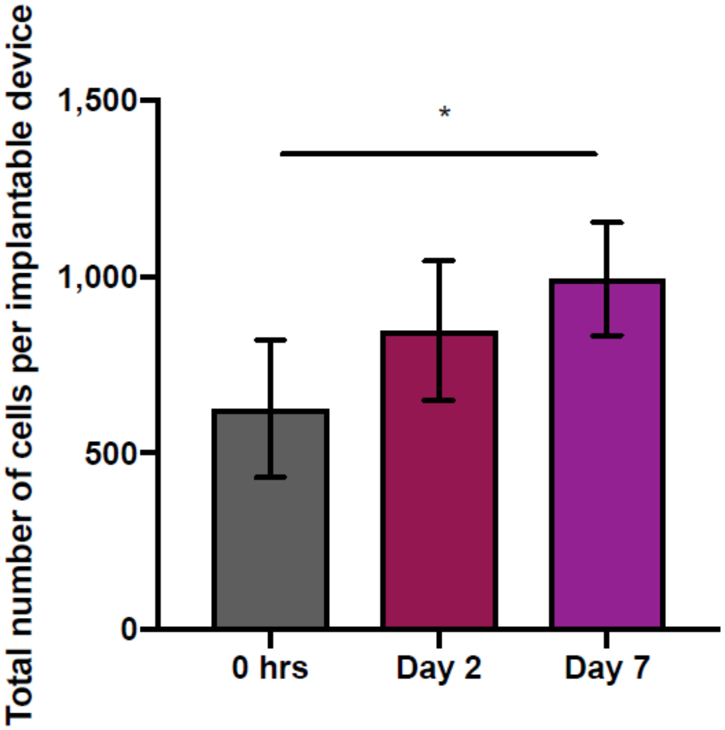

Figure 5.7 Quantification of differentiated SPC-01 cell density per seeded implantable device prototype

Total number of cells per implantable electrode array was assessed by quantifying Hoechst stained nuclei. Intended cell density was 3x10^3 cells per array. Data presented as mean ± SD for n=4 individual electrode constructs at each time point. *$p < 0.05$, one-way ANOVA with Dunnett's post-test.

The results described thus far show the ability to manufacture an implantable device of dimensions suitable for implantation in a rat muscle denervation model. Moreover, electrochemical characterisations of implantable electrode arrays show low impedance and adequate CSC and Q_{inj} to support stimulation of neurons (Palanker *et al.*, 2005, Sekirnjak *et al.*, 2008). Finally, *in vitro* data suggest successful seeding and growth of differentiated SPC-01 cells on implantable electrode arrays after 7 days, thus, indicating the ability to manufacture a biohybrid device suitable for implantation.

In light of the above, the next experiment explored the feasibility of interfacing this biohybrid device to the distal stump of a sciatic nerve branch – an injury model that successfully induces denervation of the gastrocnemius muscle in rats (see Chapter 3, section 3.2.6).

5.2.4 Implantation of biohybrid device *in vivo:* a pilot experiment

Four implantable devices (see figure 5.1H) were used for this experiment. Briefly, $3x10^3$ differentiated SPC-01 cells were seeded on each implantable electrode array. Three of these biohybrid devices were cultured *in vitro* to monitor cell growth and one was implanted *in vivo* after three days *in vitro* culture.

The sciatic nerve was exposed at the level of trifurcation, branches identified, separated and the common peroneal nerve used to interface with the biohybrid device. In order to achieve complete muscle denervation, the common peroneal nerve was transected approximately 5 mm distal from the trifurcation point and the proximal stump reflected proximally and ligated to the biceps femoris muscle to avoid spontaneous reinnervation. The distal stump of the common peroneal nerve was sutured onto the cell-seeding reservoir of the biohybrid device (figure 5.8).

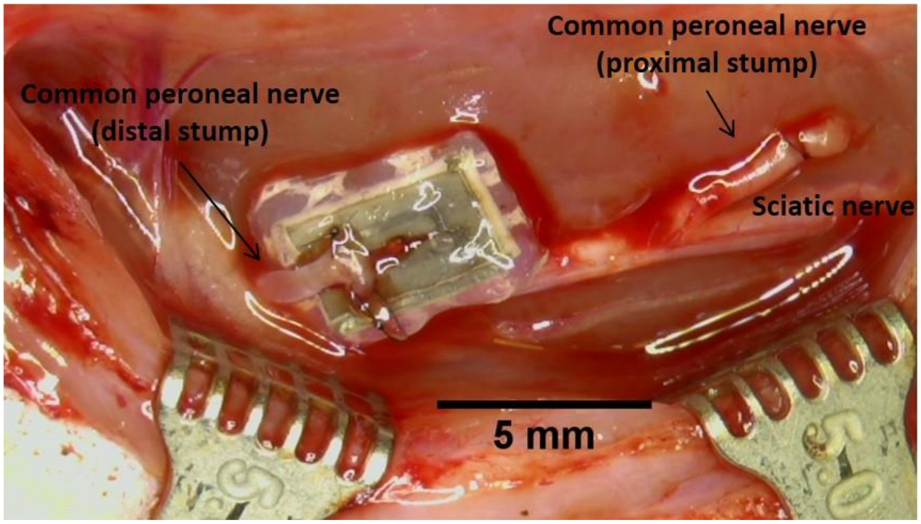

Figure 5.8 Implantation of biohybrid device in a rat muscle denervation model

Intraoperative image of the biohybrid device with a cell density of approximately $3x10^3$ differentiated SPC-01 cells, interfaced with the distal stump of the common peroneal nerve in a muscle denervation model. Scale bar = 5 mm

The biohybrid device remained sutured to the distal stump of the common peroneal nerve. Upon visual inspection, fibrotic tissue was observed around muscle sutures, where the muscle incision was made during surgery, as well as surrounding the distal and proximal stumps of the transected common peroneal nerve. However, no fibrotic encapsulation was observed around the biohybrid device (figure 5.9). After 6 days of implantation, the biohybrid device was removed for histological analysis.

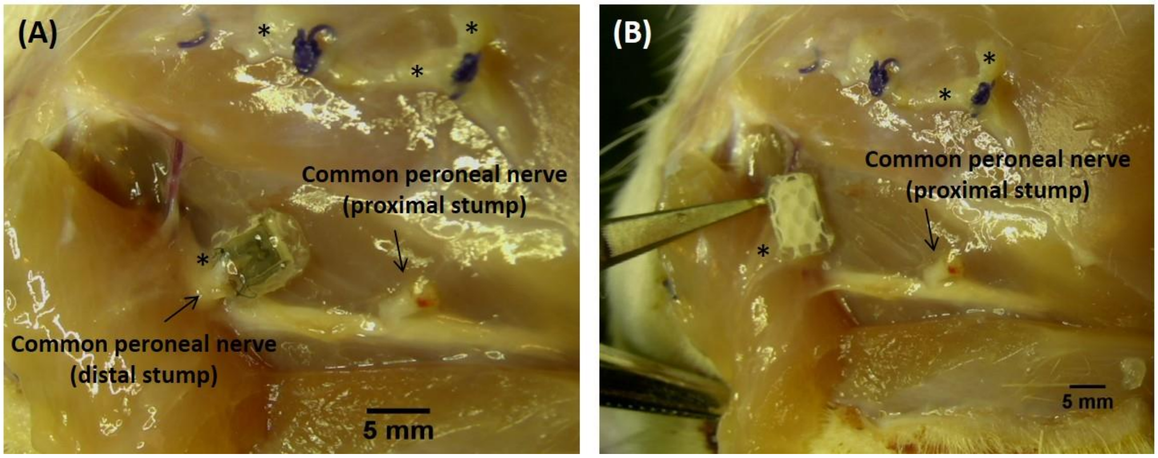
(A)
*
*
*
Common peroneal nerve (proximal stump)
*
Common peroneal nerve (distal stump)
5 mm
(B)
*
*
Common peroneal nerve (proximal stump)
*
5 mm

Figure 5.9 Visual inspection of the nerve-implant interface after 6 days of surgery showing no fibrotic encapsulation around the biohybrid device

Representative images of nerve-implant interface at day 6 post-implantation. Front (A) and back (B) side of the biohybrid device attached to the distal stump of the common peroneal nerve. * depict areas where fibrosis was observed. Scale bars = 5 mm.

5.2.5 Histological analysis of implanted biohybrid device

The biohybrid device was removed from the animal and stained to detect human-specific Nestin, in order to explore the fate of differentiated SPC-01 cells. Nestin$^+$ cells were present, localised in cell-seeding reservoirs of the biohybrid device, however, no neurites were detected. In order to identify the presence of neurites, the device was co-stained to detect βIII-Tubulin. Immunocytochemical results indicate no neurite extension from differentiated SPC-01 cells after 6 days *in vivo*. Furthermore, the absence of Nestin$^-$ Hoechst$^+$ cells, suggests that cells identified on the device were of human origin and that no cell migration from the host into the device occurred (figure 5.10).

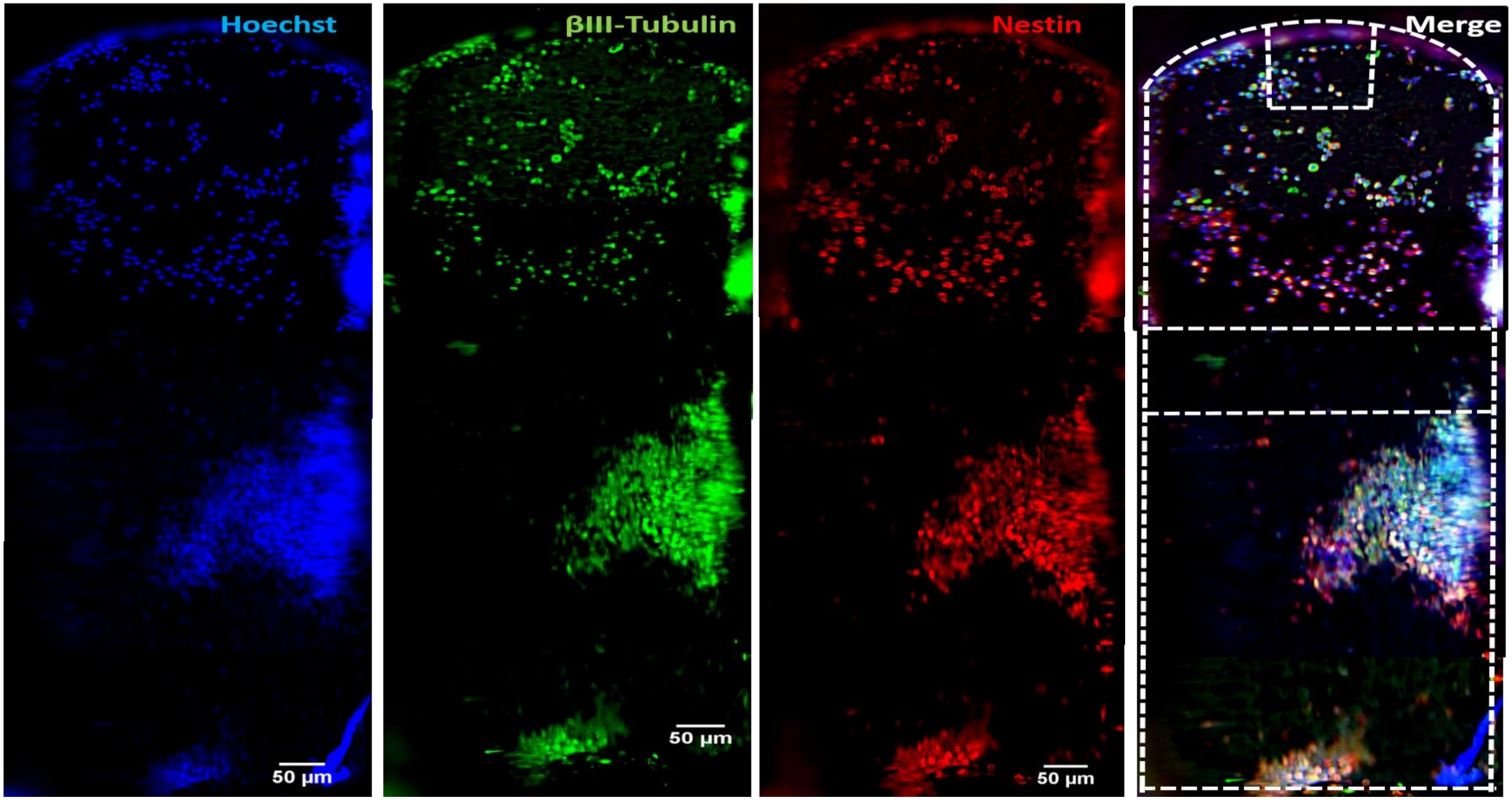

Figure 5.10 Differentiated SPC-01 cells identified on cell-seeding reservoir of biohybrid device 6 days post-implantation

Fluorescence microscopy images of the cell-seeding reservoir depicting differentiated SPC-01 cells. The biohybrid device was stained to detect Hoechst (blue) to allow quantification of total number of cells, βIII-Tubulin (green) to identify presence of neurites and Nestin (red) to distinguish cells of human origin (SPC-01 cells) from host cells. Dashed lines (white) delineate edges of reservoir and inner and outer electrode. Scale bars = 50 µm. Representative images for n = 1.

In order to compare differentiated SPC-01 cells on the implanted biohybrid device to those cultured *in vitro*, biohybrid devices (herein referred to as control biohybrid devices) incubated at 37 ^{o}C, 5% CO_2 were fixed following cell attachment (0 hrs), on the day of implantation (3 days *in vitro*) and at the end of the experiment when the implanted biohybrid device was removed (9 days *in vitro*). Control biohybrid devices were stained to detect βIII-Tubulin in order to assess neurite elongation and nestin to establish a direct comparison between control biohybrid devices and the implanted biohybrid device (figure 5.11). At 0 hrs, 875 differentiated SCP-01 cells were detected on the cell-seeding reservoir of control biohybrid device. On the day of surgery, following 3 days of incubation *in vitro*, 1055 differentiated SPC-01 cells were observed on the control device. Cell density obtained after 9 days *in vitro* was lower than that observed at earlier time points and comparable to the number of cells on the implanted biohybrid device (467 differentiated SPC-01 cells on control biohybrid device compared to 612 differentiated SCP-01 cells on implanted biohybrid device). Furthermore, neurite elongation was observed in control biohybrid devices at the time of implantation and at the end of the *in vivo* experiment (figure 5.12).

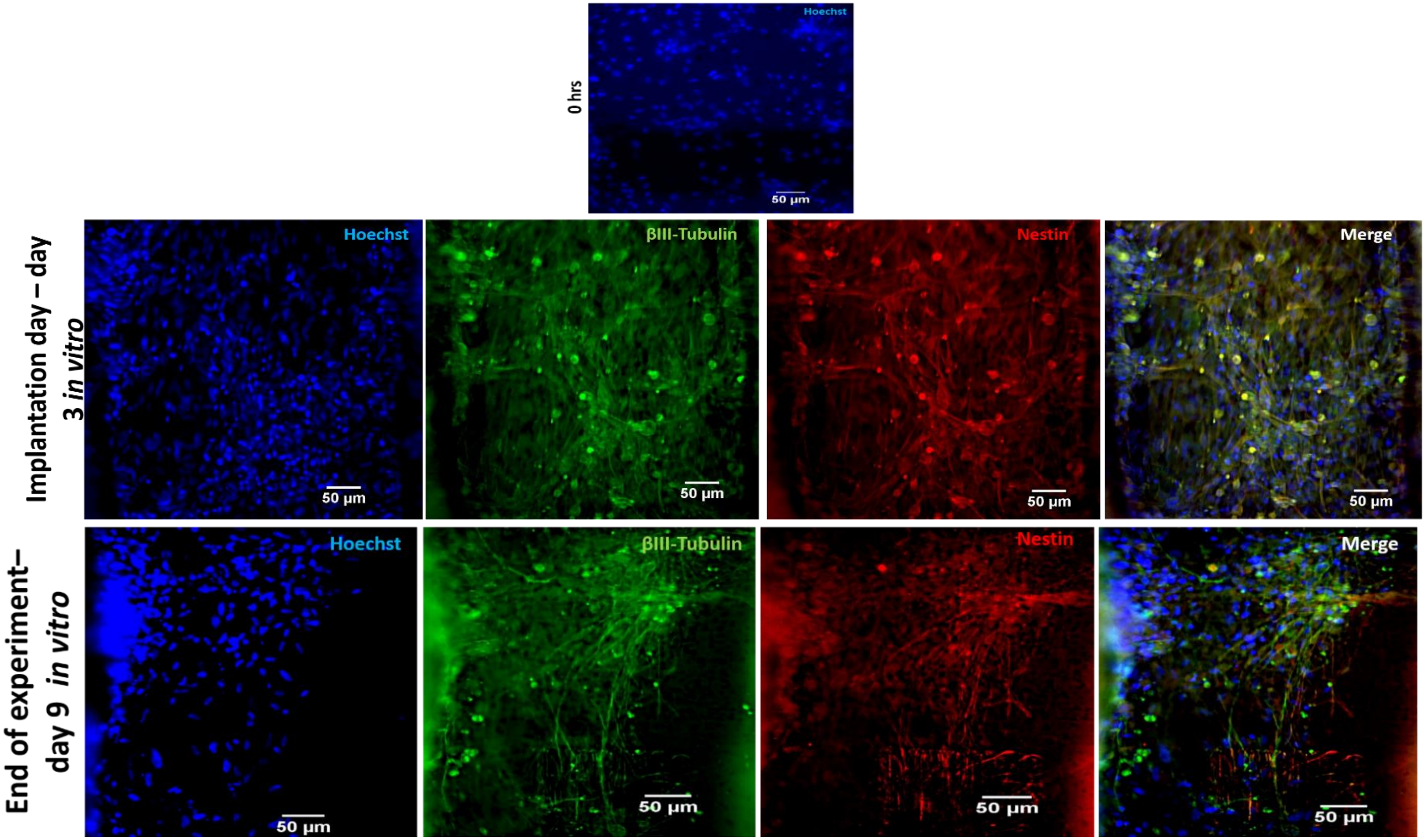
0 hrs
Hoechst
50 µm
Implantation day – day 3 *in vitro*
Hoechst
βIII-Tubulin
Nestin
Merge
50 µm
End of experiment– day 9 *in vitro*
Hoechst
βIII-Tubulin
Nestin
Merge
50 µm

Figure 5.11 Differentiated SPC-01 cells on control biohybrid devices at 3 different time points

Representative fluorescence microscopy images showing SPC-01 cells seeded on implantable electrode arrays incubated for 3 and 9 days *in vitro* (control biohybrid devices). Cells stained to detect βIII-Tubulin (green), Nestin (red) and Hoechst (blue). Scale bars = 50 µm

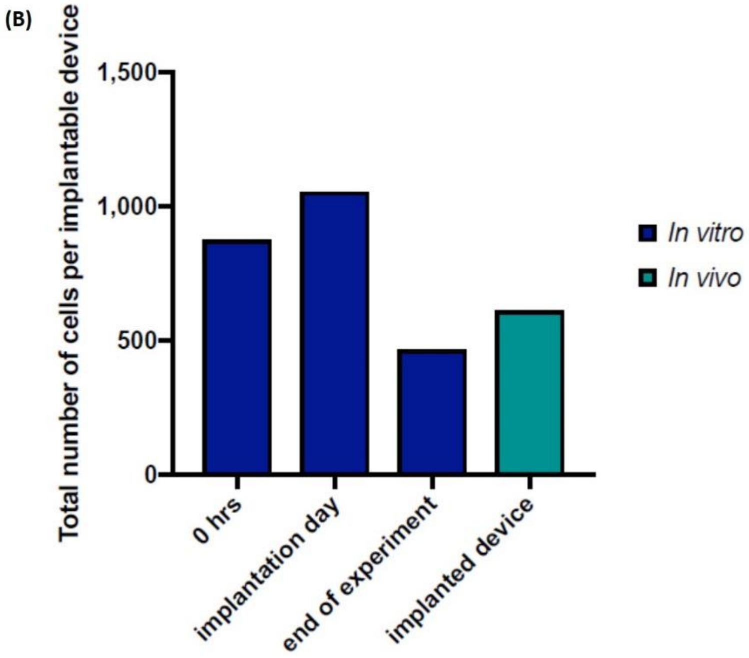

Figure 5.12 Differentiated SPC-01 cell density on control biohybrid devices at 3 different time points

Quantification of total number of cells identified on reservoirs of control biohybrid devices post-seeding (0 hrs), on the day of implantation (3 days *in vitro*), at the end of the experiment (9 days *in vitro*) and on the implanted biohybrid device. The number of nuclei (Hoechst$^+$ cells) was quantified to determine the total number of cells. Data presented for n=1.

The presence of neurites on control biohybrid devices indicates the ability of these implantable electrode arrays to support differentiated SPC-01 cell neurite extension *in vitro*. In contrast, the round morphology and lack of neurites observed on differentiated SPC-01 cells on the implanted biohybrid device at the same time point, is indicative of reduced viability and regenerative potential, therefore, suggesting the host environment is not supportive of cell survival and neurite growth to the same extent seen *in vitro*.

In order to explore ways in which survival of differentiated SPC-01 cells could be improved for future development of this type of biohybrid device, alginate hydrogels were tested as a potential method to protect the cells whilst allowing exchange of oxygen and nutrients.

The following sections examine the feasibility of incorporating alginate hydrogels to cover differentiated SPC-01 cells

5.2.6 Exploring the use of protective hydrogels to shield differentiated SPC-01 cells on electrode arrays from the host immune system

In order to protect differentiated SPC-01 cells from the host immune system, alginate hydrogels were manufactured to cover cells growing on reservoirs of electrode arrays.

First, the effect of acellular alginate hydrogels on metabolic activity of differentiated SPC cells was explored. Prior to testing the effect of alginate, two different metabolic assay approaches were compared (Appendix fig. 8.1, 8.2 and 8.3)

Metabolic activity of differentiated SPC-01 cells was tested using CT-Glo assay. A standard curve using 4 different cell densities was performed (figure 5.13). Luminescence readings were recorded at 24 hrs, 48 hrs and 72 hrs. At the three time points tested, metabolic activity was higher with higher cell densities. A decrease of 26% in luminescence between 24 and 48 hrs (10,056 ± 2,956 RLU per well at 24 hrs compared with 7,409 ± 1,323 RLU per well at 48 hrs) was recorded in the 3,000 cells/well group. Similarly, a 22% decrease in luminescence between 24 and 48 hrs (16,530 ± 4,141 RLU per well at 24 hrs compared with 12,906 ± 3,113 RLU per well at 48 hrs) was obtained with a cell density of 5,000 cells/well. Metabolic activity of 10,000 cells/well decreased by 27% after 48 hrs (26,366 ± 5,940 RLU per well at 24 hrs compared with 19,337 ± 6,350 RLU per well at 48 hrs). Finally, a drop of 30% in luminescence was recorded after 48 hrs in cells seeded at a density of 15,000 cells/well (34,860 ± 8,879 RLU per well at 24 hrs compared with 24,335 ± 11,342 RLU per well at 48 hrs). By 72 hrs, the final luminescence reading, showed a slight decrease in metabolic activity for all densities, except 15,000 cells/well, where luminescence increased from 24,335 ± 11,342 RLU per well to 26,757 ± 12,184 RLU per well tested. For all other densities, however, a further decrease of approximately 17 % was recorded. Statistical significance between groups was not detected (figure 5.13).

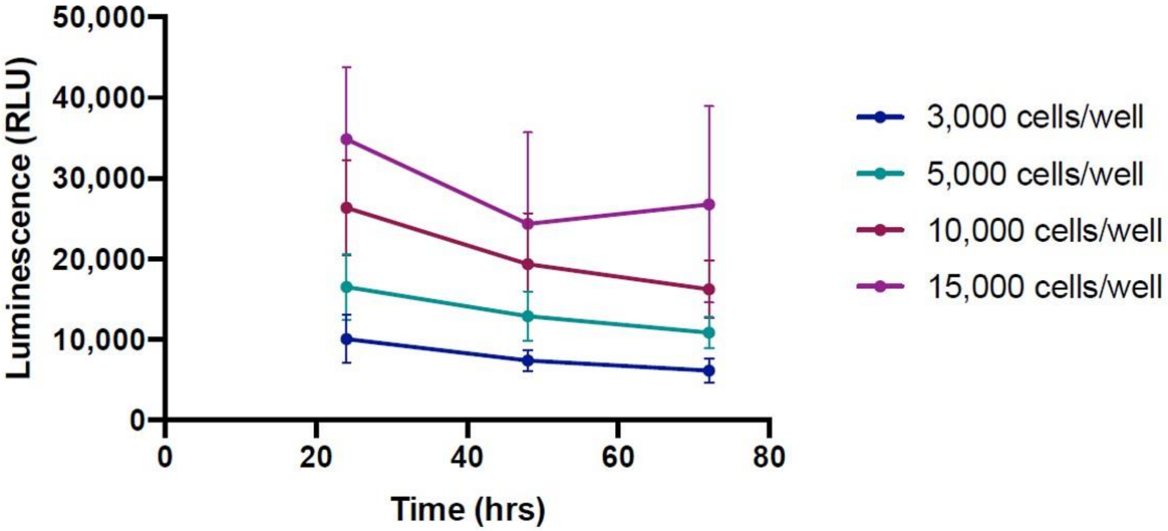

Figure 5.13 Standard curve of differentiated SPC-01 cells metabolic activity using CT Glo assay

Standard curve of metabolic activity of differentiated SPC-01 cells recorded at 3 different time points (24, 48 and 72 hrs) after seeding. Four different cell densities were tested in order to identify the most appropriate density to perform this assay. 3,000 cells/well (blue), 5,000 cells/well (cyan), 10,000 cells/well (magenta) and 15,000 cells/well (purple). Cells were incubated at 37 ^{o}C, 5% CO_2 until each time point. Data presented as mean ± SD for n = 4. ns, two-way ANOVA with Dunnett's post-test. All time points compared to initial reading (24 hrs).

Metabolic activity of differentiated SPC-01 cells incubated for 48h in the presence or absence of alginate hydrogels was tested. Alginate from two different suppliers were tested at two different % formulations (figure 5.14).

There was a slight decrease in luminescence in the alginate hydrogel groups compared to the control groups. This drop was greatest in cells covered by a 2% w/v Sigma alginate hydrogel (14,614 ± 2,501 RLU per hydrogel well compared with 18,043 ± 3,305 RLU per control well). Smaller differences in luminescence were obtained when using the lowest concentrations of alginate hydrogels. In specific, metabolic activity of cells covered with a 1 % w/v NovaMatrix alginate hydrogel was 16,884 ± 2,062 RLU per hydrogel well compared with the control (18.802 ± 1,566 RLU per well). Furthermore, a 1.5 % w/v Sigma alginate hydrogel was found to cause the smallest decrease in metabolic activity (14,506 ± 2,748 RLU per hydrogel well vs 16,158 ± 2,184 RLU per control well) (figure 5.14).

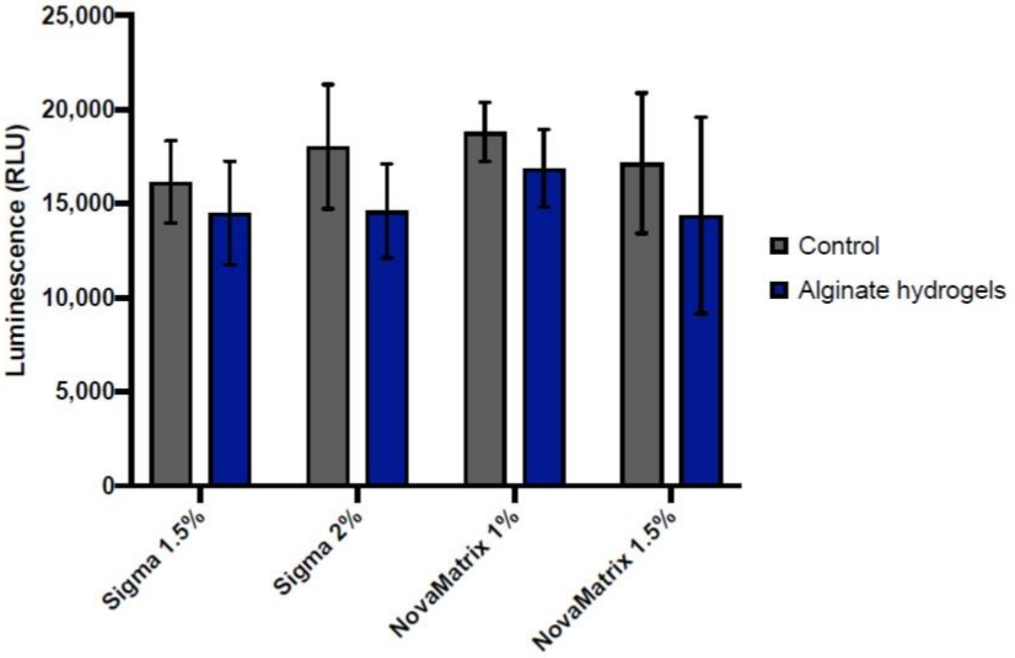

Figure 5.14 Metabolic activity of differentiated SPC-01 cells in the presence of different acellular alginate hydrogels of different concentrations assessed by CT-Glo assay

Metabolic activity of 5,000 differentiated SPC-01 cells per well covered with acellular alginate hydrogels at 48 hrs. The effect of four alginate hydrogel formulations - Sigma alginate 1.5%, Sigma alginate 2%, NovaMatrix alginate 1% and NovaMatrix alginate 1.5% - on metabolic activity of these cells was tested and compared to the control group (cells in the absence of hydrogels; grey bars). Data presented as mean ± SD for n = 3.

Overall, the similar level of luminescence of differentiated SPC-01 cells incubated with alginate hydrogels and in control conditions suggests incorporation of an alginate hydrogel onto biohybrid devices as a mean of shielding transplanted cells from the host environment, is unlikely to affect the metabolic activity of these putative MNs.

5.3 Discussion

The field of biohybrid devices aims to address two unmet needs. One is to restore tissue function in a more physiological manner by bridging electronic devices with biological tissue through a cellular component. The other proposed function is to mitigate the foreign body response to implantable electrodes by mimicking the mechanical properties and biological composition of the host tissue. Both aims seek to establish connections between cells on the device and the target tissue, therefore allowing for neural networks to be developed or host structures to be maintained. Although both strategies were presented separately, they are somewhat complementary. Fundamentally, synaptic connections between host neurons and biohybrid device neurons can be used to relay electrical stimulation to target tissues or to provide sensory feedback to the brain (Cullen *et al*., 2011a, Cullen *et al*., 2011b, Cullen and Smith, 2012). A by-product of seamless integration between device and host is the mitigation of the immune response against the device.

Here, a proof-of-concept biohybrid device was designed, developed and implanted in a rodent muscle denervation model. The results presented, suggest thick-film manufactured electrode arrays can be customised to meet the anatomical dimensions of rat sciatic nerve branches, while retaining electrochemical properties suitable for safe and effective stimulation of neuronal cells.

The miniaturisation of the device resulted in some manufacturing challenges. Of these, the most prominent was connecting circuitry to the device to allow passing of electrical current through the electrode arrays. Microrivet bonding, a form of wire bonding, was explored as an alternative solution to directly soldering copper wires onto the small solder pads. Using ball bump bonding, the aim was to bond larger stainless steel pads to the sintered Pt/Au pads on the electrode arrays. Copper wires could then be soldered to these external stainless steel pads. The wire bonding machine used, is operated using gold wire. It has been previously documented in the literature that inadequate surface smoothness and flatness can interfere with bonding gold bumps onto thick-film Pt (Guenther *et al*., 2011). In light of this, sintered Pt/Au pads were polished using a fibreglass brush. This improved bonding of gold bumps onto Pt/Au compared to unpolished pads, however, a failure to successfully bond stainless steel foil by placing a second gold bump onto carefully aligned external pads prevented the adoption of this method. The most plausible explanation to account for this result is related to the strength of the bond between Pt/Au and Au. Although polishing the Pt/Au surface aids in the bonding of gold bumps, the polishing effect may not have created a sufficiently smooth and flat surface to allow for a strong bonding of the two metals. Therefore, the force applied when placing the second gold bump, resulted in removal of the first bump. Decreasing the force applied to create the second bump helped to improve the consecutive bonding of two gold bumps in the absence of stainless steel foil pads. However, this method was not robust enough to be replicated across samples, thus suggesting adherence-related issues between Au and Pt/Au. In light of this result, soldering of copper wires onto Pt/Au pads was successfully implemented to connect electrode arrays, although with some difficulty. Future experiments and further optimisation of this implantable biohybrid device should focus on establishing electrical interconnections through microrivet bonding. This is a highly desirable approach to form reliable interconnections between electrode arrays and a power source for current supply. Fundamentally, implantable devices are required to have reduced size, weight and power consumption compared to external electronics. As such, the need for device integration is imperative. An integrated circuit (IC), programmed to deliver current pulses to the device, can be bonded to the alumina substrate of the implantable device described in this body of work. To this end, strengthening the bond between Pt/Au and Au is essential. Future experiments should explore polishing sintered Pt/Au pads using diamond and silicon carbide as a polishing substrate to improve flatness and decreased surface roughness of the pads (Guenther *et al*., 2011).

The electrical impedance spectroscopy results showed less variability between electrode arrays than that observed with the previous electrode array design (see Chapter 4, figure 4.13). The reproducibility in frequency-dependent impedance measures between implantable electrode array samples is most likely attributed to polishing of electrodes. Guenther and colleague (2011) reported polishing sintered Pt, helped decrease variability in thickness of thin-film Pt paste. Moreover, this process also removes contaminants deposited on the metal as a product of sintering in a furnace without directed air or inert gas flow. It is also likely that polishing removes debris deposited on the metal during laser-micromachining and possibly improves removal of the PDMS coating by laser ablation from the smoother Pt/Au. Although polishing offers the advantage of consistent and reproducible electrochemical properties, the process of improving surface smoothness may come at the expense of increased impedance due to the decrease in porosity. Porosity determines the surface area over which charge transfer may occur. Increasing total surface area causes a decrease in double-layer capacitance and a reduction in the electrode’s impedance and an increase in charge storage capacity (Franks *et al*., 2005). Here, comparing impedance of unpolished sintered Pt/Au electrodes (optimised design for *in vitro* experiments) to that of polished sintered Pt/Au electrodes (implantable device prototype) at three different frequencies showed increased impedance in the porous unpolished electrodes compared to the polished electrodes. These confounding results may be explained by the complete removal of contaminants, debris and PDMS from the surface of electrode sites, thus leading to an increase in the area available for charge transfer to occur. These results indicate polishing electrodes increases consistency and reproducibility of manufactured thick-film Pt/Au electrodes without compromising the desirable decrease in impedance provided by the inherent porosity and roughness of thick-film metal pastes.

Notably, CSC results are in agreement with the hypothesis formulated above to explain impedance data. Values measured for electrodes of the implantable device prototype (polished surface) were greater than those reported for electrodes of the optimised design for *in vitro* experiments (unpolished surface). It was initially expected that polishing the electrode surface would decrease porosity and decrease CSC. Indeed, it is well documented that roughened Pt electrodes with similar GSA to Pt foil electrodes have greater CSC due to an increase in ESA, thus providing a greater surface area for charge transfer to occur (Green *et al.*, 2014). In a similar manner to impedance, the results described here may be explained by an increase in surface area of implantable device prototype electrodes due to the cleaning effect of polishing the surface. By removing contaminants and debris from the electrode surface, the area available for charge transfer to occur may have increased. Moreover, a smoother Pt/Au surface may have led to more effective laser-ablation of silicone, causing an overall increase in CSC. Electrodes from the optimised design for *in vitro* experiments were cleaned in an ultrasonic bath before assessment of their electrochemical properties, however, it is possible that the cleaning process was not thorough enough; therefore contaminants and debris generated through the manufacturing process may have remained on the electrode surface.

Q_{inj} of polished Pt/Au electrodes of the implantable device prototype are in line with those reported for sintered Pt electrodes on alumina (0.21 to 0.24 mC/cm^2 for pulse widths of 0.2 to 0.8 ms (Green *et al.*, 2013d)) and Pt foil electrodes roughened by laser micromachining on alumina (0.13 to 0.36 mC/cm^2 for pulse widths of 0.1 to 0.8 ms (Green *et al.*, 2014)). However they are slightly lower than those reported by Carnicer-Lombarte *et al.* (2017) for sintered Pt/Au electrodes (0.3 mC/cm^2 for pulse widths of 0.1 ms) but higher than those documented for Pt foil electrodes (0.02 to 0.03 mC/cm^2 for pulse widths of 0.1 to 0.8 ms (Green *et al.*, 2014)). This is indicative of a polished surface that retains a certain degree of porosity inherent to the thick-film paste. In the context of electrical stimulation of excitable tissue, the charge injection density the electrodes on this implantable device can safely deliver is in line with that reported for retinal implants used to stimulate neurons in blind individuals (Palanker *et al.*, 2005). Sekirnjak *et al.* (2008) reported electrical stimulation with Pt electrodes of macaque retinal ganglion cells with an average charge density of 0.05 mC/cm^2, the lowest charge density required to stimulate these cells was 0.018 mC/cm^2 and the highest was 0.099

mC/cm^2. This suggests that the implantable device developed here should be able to stimulate neurons (e.g. differentiated SPC-01 cells) safely.

In a similar manner to the electrodes of the optimised design for *in vitro* experiments, voltammograms of the electrodes of the implantable device prototype do not reflect the peaks expected for Pt electrodes. Instead, they resemble voltammograms of gold electrodes tested in PBS, therefore, reflecting the effect of paste alloying on voltammogram shape (see Chapter 4, figure 4.16 for a Au voltammogram measurement obtained in PBS).

The next line of investigation focused on exploring the incorporation of differentiated SPC-01 cells within implantable device prototypes to fabricate biohybrid devices. Because of the small size of cell-seeding reservoirs (0.004 cm^2), cells were seeded at a low density of 3 x 10^3 cells per device. Cell density quantified 45 minutes post-seeding (0 hrs) showed a 31% variability in seeding efficiency between samples. Furthermore, an increase in the number of cells quantified was observed in biohybrid devices analysed 2 and 7 days after seeding. This increase in cell numbers may be possibly accounted for by the variability expected with low cell densities rather than cell proliferation. This is further strengthened by the cell-proliferation results previously described (Chapter 3, figure 3.4) which showed after 2 weeks of differentiation, only 3% of SPC-01 cells expressed Ki67. Moreover, seeding accuracy – actual cell density compared to target cell density - was lower than expected. This may be explained by a lack of structural barrier around cell-seeding reservoirs of the implantable device prototype. As a result, the cell suspension was not contained within the reservoir area, therefore, some of the cells seeded attached to the PDMS outside. Although, some degree of variability in cell density was observed between samples, overall, reproducibility of the number of cells between biohybrid devices was considered adequate. Too many cells may hamper cell survival and neurite extension. Equally, too few cells may negatively impact cell survival. Here the minimum number of cells detected was 402 cells in one array and the maximum was 1,215 cells in one array. Notably, what constitutes too few and too many regarding cell density was not explored.

In light of these results, the next experiment explored the feasibility of implanting biohybrid devices using the muscle denervation model previously implemented to transplant differentiated SPC-01 cells (see Chapter 3, section 3.2.6). This pilot in vivo experiment (n=1) showed manufactured biohybrid devices were of adequate dimensions to be interfaced with transected sciatic nerve branches (figure 5.7). Furthermore, the device retained its position at 6 days post-implantation despite free movement by the animal, therefore, indicative of stability and firm attachment to the nerve. Visual inspection of the biohybrid device upon its removal, revealed no sign of encapsulation due to fibrotic tissue, even though fibrosis was observed surrounding the transected nerve and around the muscle fascia that was injured during surgical implantation. However, without additional histological and immunohistochemical analyses of the device and surrounding area, a foreign body immune response cannot be completely ruled out. Indeed, Wurth *et al*. (2017) implanted intraneural electrodes in the sciatic nerve of rats and assessed the immune response at different time points. They reported macroscopic observation of connective tissue at the entry and exit sites of the implant in all groups (from day 17 to day 165 post-surgery) except for the acute and short term groups (up to 7 days post-implantation). However, upon microscopic inspection of the implanted nerve they observed a capsule developing around the implant of approximately 100 µm composed of monocytes and fibroblasts within the first week after surgery. Based on this, 6 days post-implantation may have been too early to detect the presence of fibrotic tissue around the biohybrid device upon visual inspection. de la Oliva *et al*. (2018) reported the formation of a capsule around longitudinal intrafascicular electrodes (LIFE) implanted in the tibial nerve of rats as early as 2 days after surgery, however, the capsule thickness was approximately 9 µm and slightly increased to 12 µm by day 4. By two weeks, the thickness of the connective tissue surrounding the device reached its maximum (30 µm thick), and a slight decrease and compaction was observed thereafter until the end of the study (8 months). Both studies indicate a foreign body response to implanted devices is observable at least as early as 2 days post-implantation, however histological analysis and high magnification microscopy are required to detect it. Notably, there is discrepancy in the size of the capsule reported by both studies. This is most likely due to differences in the degree of disruption to the microstructure of the nerve caused during implantation. Wurth *et al*. (2017) reported axon swelling and myelin breakdown 1 day after implantation, whereas de la Oliva *et al*. (2018) reported no functional damage to the nerves caused by their longitudinal intraneural electrodes, therefore accounting for a milder immune response to the implant. The approach presented here, whereby the nerve is transected and the distal stump is sutured to the device, is expected to cause a severe inflammatory response due to the severity of damage caused to the nerve. In addition, the mismatch in mechanical properties of the device and the *in vivo* environment are expected to exacerbate this response. Future experiments should increase the number of samples and include enough animals to assess the time course of the host tissue response over a period of weeks to months. Moreover, histological analysis such as H&E stain to detect fibrotic tissue alongside immunohistochemical staining to detect macrophages and fibroblasts should be performed. To fully assess the FBR elicited by the device it is important to include appropriate control groups that will allow the experimenter to distinguish an immune reaction from the inflammatory response due to surgery. To this end, a sham group that undergoes the same surgical procedures - nerve transection and suturing of the device to the distal stump - but in which biohybrid devices are immediately removed, should be included in the experiment. Furthermore, a second control group in which nerves remain intact would also be beneficial. This experimental set up will allow cellular characterisation of the FBR by comparing number of macrophages and fibroblasts in the treated group to that of both control groups.

The biohybrid device was removed after 6 days *in vivo* and stained to detect the fate of transplanted human-derived differentiated SPC-01 cells. Nestin$^+$ cells were detected throughout the cell-seeding reservoir of the implanted device (figure 5.9). A co-stain to detect βIII-tubulin revealed round cell bodies and no neurite outgrowth, thus indicative of reduced viability and regenerative potential. Control biohybrid devices, cultured *in vitro* and stained at different time points to monitor cell growth and neurite extension, showed neurite elongation of differentiated SPC-01 cells on the day of implantation and at the end of the *in vivo* experiment when the device was removed. This finding suggests the poor viability of differentiated SPC-01 cells observed on the implanted biohybrid device was caused by the *in vivo* environment. Assessment of the total number of cells by quantification of Hoechst-stained nuclei showed all cells present on the reservoir of the implanted device were Nestin$^+$, therefore indicating they were of human origin and that host cells did not migrate into this area of the device. This finding suggests of the poor growth of differentiated SPC-01 cells was not obviously attributable to migration of host immune cells into the device. As such, the lack of oxygen and nutrients in the *in vivo* environment may have been the main cause of reduced transplanted cell viability. In line with this hypothesis, it is well documented that the injured tissue microenvironment is usually associated with ischaemia, ECM degradation, oxidative stress and inflammation (Sart *et al*., 2014). This environment is detrimental to cell survival, consequently transplanted cells display low retention rates and limited survival at the injury site. To improve survival and retention of transplanted cells at the injury site, increased resistance against oxygen and nutrient deprivation is proposed. Indeed, genetic modification of brain-derived NSCs to overexpress anti-apoptotic and antioxidant proteins have proven successful in increasing retention of transplanted cells in an *in vivo* model of ischaemic stroke in mice (Sakata *et al*., 2012). An alternative, and even more desirable approach, is the non-genetic preconditioning of cells to a similar environment before transplantation. With this in mind, various studies have explored the effects of chronic exposure of cells to hypoxic environments *in vitro* with the aim to simulate the stress cells experience in damaged tissue. They have found beneficial effects of this pre conditioning paradigm in the form of increased cell resistance *in vivo* (reviewed in (Sandvig *et al*., 2017)). Future experiments should explore preconditioning of biohybrid devices in hypoxic conditions *in vitro* prior to *in vivo* implantation and assess whether differentiated SPC-01 cells adapt to this microenvironment and successfully graft when implanted in the injured PNS.

Another strategy to improve cell survival and enhance engraftment is minimising the immune response triggered by transplanted cells. To this end, implementing hydrogels to encapsulate cells has been widely adopted by most researchers developing biohybrid devices (see tables 5.1 and 5.2 for a summary of these studies). Here, the incorporation of alginate hydrogels atop of differentiated SPC-01 cells was explored, ultimately for use as a means of shielding cells from the host immune system. In the first instance, metabolic activity in the presence of hydrogels was tested in order to ensure cell viability was not compromised. The data showed a slight decrease in viability in all hydrogels tested compared with the control group. Out of the four hydrogels assessed, the smaller decreases in viability were obtained with the lower concentrations of the Sigma and NovaMatrix alginate, although the effects were small and there were insufficient data to conduct robust statistical tests. It has been previously reported that high alginate concentrations cause an increase in the stiffness and a decrease in pore size of hydrogels, consequently leading to high mechanical cell constraints and limited nutrient diffusion compared with lower concentration gels (Meiser *et al*., 2013, Jia *et al*., 2014, Espona-Noguera *et al*., 2018). The factor of stiffness and its correlation with nutrient diffusion could account for the small differences observed in viability between high and low alginate concentrations. Indeed, covering differentiated SPC-01 cells with 2 % w/v and 1.5 % w/v alginate hydrogels may have affected the influx of oxygen and nutrients through the gels and outflow of waste products generated by the cells, consequently impacting their viability. Alternatively, the presence of a hydrogel may have interfered with the assay itself as it may have taken longer for the reagents and metabolites in the assay to interact with the cells. Relying solely on a metabolic assay to assess viability of differentiated SPC-01 cells in the presence of hydrogels has limitations. Future experiments should therefore perform live/dead assays as well as increase number of repeats. Overall, however, this result suggest alginate could be incorporated onto biohybrid devices as they have a negligible impact on differentiated SPC-01 viability.

This initial development of the biohybrid device focused on keeping cells in direct contact with the alumina and electrode sites, as the data obtained throughout this body of work suggests this substrate is supportive of differentiated SPC-01 cells growth and neurite extension. In light of this, hydrogels were incorporated to cover cells on the substrate, rather than fully encapsulating them. Future experiments should assess whether this approach is sufficient to mitigate the immune response against these cells or if they need to be encapsulated fully in order to improve their survival and function *in vivo*.

In summary, the results presented in this chapter highlight the successful development of electrode arrays suitable for implantation in a rodent model of muscle denervation. Furthermore, Au bonding techniques can be implemented on this small electrode arrays to incorporate an IC onto the device for the delivery of current pulses, however, optimisation of techniques to polish sintered Pt/Au surfaces as well as bump bonding parameters is required. The results showed that polishing electrodes with a fibreglass brush did not impair their abilities to support effective stimulation. Indeed, charge density of these electrodes is in line with that reported for retinal neuroprostheses.

Additionally, this chapter also provides proof-of-concept of the development of a biohybrid device comprised of implantable electrode arrays with human-derived MN-like cells, capable of growth and neurite extension *in vitro*. Moreover, this biohybrid device can be interfaced to branches of the sciatic nerve in rodents retaining its position and structure after 6 days of implantation.

Notably, a critique of the *in vivo* work here presented is the implantation of the biohybrid device immediately after performing nerve axotomy. The severity of the nerve injury caused would have elicited a severe inflammatory response. Indeed, Sart *et al*. (2014) documented events such as ischaemia, ECM degradation, oxidative stress and severe inflammation in the injured tissue micro-environment. Injury-related inflammation creates a hostile environment for the newly transplanted cells, therefore minimising their potential of grafting and surviving *in vivo*. Future experiments should add a time window of approximately 7 days between nerve injury to replicate muscle denervation and implantation of the biohybrid device. This time point is generally accepted as a suitable therapeutic window for the inflammatory response to take place. After a week, inflammation decreases and the glial scar that prevents implant and host tissue integration has not yet developed (Nakamura and Okano, 2013, de la Oliva et al., 2018).

This work highlights the need to identify causes of reduced MN-like cell viability *in vivo* and ways to improve cell survival and neurite growth. To this end, incorporation of a protective alginate hydrogel atop MN-like cells on biohybrid devices is proposed. The preliminary data presented here show covering MN-like cells with low concentration alginate hydrogels has a marginal impact on cell viability, therefore suggesting incorporation of alginate hydrogels onto this biohybrid device is feasible and warrants further investigation in the quest of improving cell survival *in vivo*.

In conclusion, the results here presented provide proof-of-concept of the development of an implantable biohybrid device with electrochemical properties that effectively supports stimulation of neuronal cells. Moreover, this device can be implanted into the rodent muscle denervation model used elsewhere in this body of work.

6.0 General discussion and proposed future work

This chapter summarises the key findings and conclusions derived from this thesis. In addition, immediate and long-term future work are presented

The aim of this thesis was to design and develop an implantable biohybrid device for muscle stimulation following lower motor neuron injuries.

Chapter 1 presented an overview of complete *cauda equina* and *conus medullaris* lesions, clinical symptoms associated with these injuries, the current rehabilitation therapy used in these patients and the limitations of this approach. The main issue of this rehabilitation therapy is the side effects and discomfort generated by the high electrical current required to stimulate denervated muscles. A potential solution to reduce the amount of current required to elicit muscle contraction, is to stimulate denervated muscles via neuromuscular interaction. To this end, a biohybrid approach was proposed; incorporating motor neurons onto implantable electrode arrays, therefore providing a cellular intermediate between the electrical stimulus and the muscle. This approach has the potential to overcome the issues associated with direct electrical stimulation of muscle, as the allogeneic motor neurons associated with the implant will require substantially less injected current to generate action potentials compared with direct stimulation of the target muscle. Stimulating muscle in this manner could mitigate atrophy and degeneration characteristic of chronic denervation and the secondary health related complications associated with lower limb paralysis.

The challenges and considerations related to developing a biohybrid device were discussed. A central issue related to miniaturisation of implantable devices is the inherent increase in impedance and limit on charge injection capacity of electrodes. Therefore, the appropriate conductive materials and modification of electrode surface must be implemented to compensate for the negative impact on electrochemical properties of electrodes. Incorporation of topographical cues on the substrate to provide guidance for neurite extension on the device has been adopted as a means of directing implanted cells towards endogenous target tissue. Furthermore, material considerations are centred around biocompatibility of all elements incorporated within the device, including any degradable hydrogels and their byproducts.

With regards to the cellular components of this biohybrid approach, cell source, developmental stage at which cells are implanted and survival of cells within the host environment required careful assessment. Cells with therapeutic potential: must be available in sufficient quantity, reliability and repeatability; must be obtained from a source with minimal to no ethical concerns and must mitigate the risks of tumorigenicity once implanted. Moreover, if allogeneic cells are implemented, these must be protected from the host immune system. Potential strategies to protect allogeneic cells from the host immune response thus far reported include encapsulation within hydrogels, local release of anti-inflammatory agents and pre-conditioning of cells to the *in vivo* environment before implantation. Given the various considerations to develop the optimal biohybrid device, it is expected that the best match will have some limitations.

Chapter 3 focused on exploring the potential of a therapeutically relevant human neural stem cell line, SPC-01, to differentiate into motor neuron-like cells. SPC-01 is a conditionally immortalised cell line of human origin, originally derived from spinal cord tissue. Results obtained showed the development of an efficient (24% yield) and rapid (14 days) differentiation protocol to generate MN-like cells as assessed by the expression of the motor neuron marker, Isl-1. One of the concerns with cell therapies is the risk of uncontrolled cell division and resulting tumour formation. Results presented in chapter 3 show that after 2 weeks of differentiation the expression of the proliferation marker Ki67 is near to none. Overall, the differentiation assessment of SPC-01 cells, suggest these motor-neuron like cells have therapeutic potential to be implemented as the cellular component of this biohybrid device.

Finally, initial assessment of transplantation of MN- like cells *in vivo* was explored in this chapter. Results presented in Chapter 3 suggest tibial nerve transection is a suitable model to induce denervation in rodents and cell therapy candidates can be delivered successfully via injection. Immediate future work should seek to improve upon the histological characterisation implemented in this thesis by using at least 2 or 3 motor neuron markers (e.g. Hb9 in combination with Isl1/Isl2, or ChAT) to increase reliability of the differentiation of SPC-01 cells into motor neurons. As part of an overall histological characterisation, markers for other cells types should be implemented. More specifically, markers expressed by astrocytes, oligodendrocytes and interneurons (GFAP, Olig-2 and Chx10, respectively).

Furthermore, the immunostaining protocol described throughout this thesis should be improved by the addition of negative and positive controls, whenever possible. This will ensure positive stains accurately represent presence of the specific protein in the cells as opposed to non-specific staining.

Relying solely on a histological approach to assess efficiency of differentiation has limitations. Therefore, the electrophysiological properties of these cells warrant investigation as they must be electrically active to give the desired therapeutic effect. To this end, techniques such as calcium imaging or patch clamping must be implemented to determine whether these differentiated cells are capable of evoking action potentials in response to stimulation. In order to validate the equivalence of these MN- like cells to their *bona fide* counterparts, exploring the formation of neuromuscular junctions is of essence. Co-culture with muscle cells *in vitro* could be employed to assess the formation and function of neuromuscular junctions. This can be further validated by transplanting these cells *in vivo*. A nerve transection model similar to the one proposed in chapter 3 with local injection of cells in the distal stump will be a suitable model to assess muscle reinnervation. Indeed, upon stimulation of the nerve a muscle contraction will only be detected if the transplanted cells formed neuromuscular junctions with the host muscle. Muscle and nerve should be excised for histological analysis to identify neuromuscular interaction.

In line with the development of a biohybrid device, chapter 4 explored the design and manufacturing of electrode arrays suitable for supporting growth and neurite extension of motor neuron-like cells. Key findings of chapter 4 highlighted the successful implementation of thick film technology, a simple and low-cost fabrication technique, to manufacture versatile electrodes with features in the micrometre scale suitable for rodent pre-clinical studies. Pt/Au electrode arrays screen printed onto alumina substrate and encapsulated in an insulating layer of medical grade PDMS, were shown to support growth and extension of both NG108-15, a cell line with cholinergic motor-neuron like characteristics, and SPC-01-derived motor neuron-like cells. Microgrooves were laser-ablated onto the cell-seeding reservoir to provide cell guidance and increase neurite length; however, results suggested neither guidance nor increased neurite outgrowth was achieved. Further engineering optimisation is required to achieve directional growth of these cells. Indeed, for this approach to be successful the MN-like cells incorporated on the device need directional guidance to grow towards the target muscle tissue. Immediate future work should characterise the microgrooves described in chapter 4. SEM or atomic force microscopy (AFM) techniques could be implemented to gain an insight into the features ablated by the laser and better understand whether the lack of directionally and straight neurite outgrowth observed was due to a lack of definition between edges separating individual microgrooves. It was hypothesised that ablating features as small as the laser spot size (30 µm diameter) with a 10 µm pitch may have increased the inaccuracy of the ablation process (Mohammed *et al*., 2018). Moreover, the parameters used to ablate these features may have caused the formation of a recast layer that disrupted the well-defined edges separating individual microgrooves. A potential solution to mitigate the effect of laser offset on the features ablated is to increase the space between microgrooves. Furthermore, optimisation of laser parameters to minimise the melting and recast layer formed following ablation, is highly desirable. Finally, electrochemical characterisation techniques were employed to assess whether thick film technology produced electrodes suitable for effective neural stimulation. Data reported in chapter 4 show that impedance values and charge storage capacity are in line with those reported in the literature for Pt/Au electrodes (Carnicer-Lombarte *et al*., 2017) and roughened Pt electrodes (Green *et al*., 2012), therefore indicative of electrode arrays supportive of effective neural stimulation. Moreover, laminin-coating can be implemented on these arrays to promote the attachment of MN-like cells without affecting the inherent electrochemical properties of electrodes. A key finding reported in this chapter is centred on the consequences of laser offset in the manufacturing of these electrode arrays. As well as its potential impact on microgrooves, it is hypothesised that the high variability in electrochemical properties detected between samples may be attributed to this effect. Overall, future work should focus on optimising ablation of microgrooves on alumina substrate to provide well-defined topographical cues for neurite guidance. Additionally, further optimisation of laser parameters is essential to minimise the effects of laser offset on the electrochemical properties of electrodes.

The work presented in chapters 3 and 4 described the generation of motor neuron-like cells with therapeutic potential and the manufacturing of electrode arrays supportive of cell growth and neurite extension *in vitro*. Subsequently, the aim in chapter 5 was to combine the cellular and electronic components to develop a biohybrid device with dimensions suitable for *in vivo* implantation.

Results presented in chapter 5 show thick-film electrode arrays can be customised to meet the anatomical dimensions of the rodent *in vivo* environment, while retaining electrochemical properties suitable for safe and effective stimulation of cells. Indeed, the charge injection capacity of these electrodes was found to be in line with that reported for retinal implants used to stimulate neurons in blind patients (Palanker *et al*., 2005) . Further studies should focus on applying current pulses to electrode arrays to stimulate MN-like cells seeded on this device. This will allow electrophysiological activity of these cells to be determined (using recording techniques previously mentioned) as well as assessing stimulation pulse parameters required for the safe generation of APs in these cells.

Furthermore, chapter 5 explored Au rivet bonding as a mean of establishing electrical interconnects with implantable electrode arrays. Data presented suggests further optimisation of bonding parameters and polishing of the Pt/Au surface are required for the successful implementation of this technique. As part of the engineering optimisation of this device, an area of priority should centre around incorporating rivet bonding or microwire bonding to connect electrode arrays to an application specific integrated circuit (ASIC). Fundamentally, as implantable electronics are required to have reduced size, the need for integrated electronics becomes imperative. Bonding techniques offer the possibility to incorporate an ASIC within the implantable device, to deliver current pulses to the electrodes with minimal external connections and may provide for a completely wireless approach.

Regarding incorporation of MN-like cells into prototype implantable devices, data presented in this chapter shows miniaturised electrode arrays support growth and neurite extension of these cells *in vitro*. Identifying the appropriate density of MN-like cells to incorporate on devices warrants further investigation. Experimental data thus far obtained shows some degree of variability in cell density between samples. However, overall reproducibility of the number of cells between biohybrid devices was considered adequate. It is important to determine what constitutes too few or too many cells as these parameters may affect cell survival, neurite extension, and the ability of the biohybrid device to establish functional connections with muscle. To this end, multiple cell-seeding densities should be tested on implantable devices across various time periods to identify low and high limits.

Furthermore, transplanting MN-like cells at different densities in the *in vivo* model previously described, offers the possibility to determine the quantity of cells required to achieve electrophysiological activity in the rodent gastrocnemius muscle. This will serve to provide guidance on the minimum cell density necessary to test the potential of this biohybrid approach to maintain muscle viability in denervating injuries.

Overall, the results presented in the first half of chapter 5 provide proof-of-concept of manufacturing an implantable biohybrid device. In light of this, the rest of the chapter assessed the feasibility of implanting this device in the rodent muscle denervation model and the incorporation of hydrogels to protect MN-like cells from the host immune response.

Preliminary *in vivo* findings showed electrode arrays were of adequate dimensions to interface with rodent sciatic nerve branches. Furthermore, the device retained its position after 6 days *in vivo* despite free movement by the animal, therefore, indicative of stability and firm attachment to the nerve. Preliminary data in this chapter showed the absence of fibrotic tissue around the device upon its removal and visual inspection, even though fibrosis was observed around tissue injured during surgical implantation.

A thorough microscopic investigation and immunocytochemical analysis of the device is warranted in order to completely rule out a foreign body response. Moreover, it is highly desirable to fully characterise the following: (1) the extent of the foreign body response elicited by the electrode arrays, (2) the immune response elicited by MNs of human origin and (3) the inflammatory reaction caused by tissue damage during surgical insertion. To this end, immediate future experiments should focus on improving the *in vivo* methods and analysis used in this thesis.

First, it is important to allow an appropriate time window between nerve axotomy and implantation of the biohybrid device in order to allow for the inflammatory response caused by injury to decrease. It is generally agreed that after 7 days, inflammation decreases and the glial scar tissue formed due to injury has not yet developed (Amemori et al., 2013, de la Oliva et al., 2018). Implanting the biohybrid device at day 7 post- surgery will likely give the transplanted cells a better chance of survival in another wise hostile in-vivo environment.

Second, it is highly desirable to assess the host immune response to human-derived differentiated SCP-01 cells. Previous research by Santos Roballo et al. (2019) characterised the density of key immune cell players at different time points following a nerve allograft in rats. They reported T-helper and cytotoxic T-cell levels peaking between 7 and 14 days following nerve allograft surgery and declining by day 28. Future *in vivo* work should evaluate the presence of a host immune reaction in response to differentiated SPC-01 cells between day 7 and 14 after implantation of the biohybrid device.

In this work, transplanted human MN-like cells were identified on the device after 6 days *in vivo.* However, the lack of neurite sprouting, and cell morphology observed were indicative of reduced viability and regenerative potential.

In order to improve MN-like cell viability *in vivo*, the incorporation of a ‘protective’ hydrogel atop of the device was explored. Initial experiments consisted of fabricating alginate hydrogels of different formulations and assessing their impact on MN-like cell metabolic activity. There was a marginal decrease in MN-like cell metabolic activity in the presence of alginate hydrogels, suggesting that these types of hydrogels can be incorporated into biohybrid devices. The potential of this strategy to increase cell viability on biohybrid devices implanted *in vivo* warrants investigation. To this end, T-cell assays could be implemented *in vitro* to assess proliferation of these immune cells. If indeed, covering human MN-like cells with an alginate hydrogel is an effective strategy to protect these cells, one would expect to see decreased rodent T-cell proliferation in a hydrogel coated group compared with a non-alginate hydrogel control group. Alternatively, if this protective hydrogel approach is not effective, future experiments should explore MN-like cell pre-conditioning before implantation or hydrogel encapsulation of the entire device.

In summary, this project provides proof-of-concept of the development of a biohybrid device for muscle stimulation (Cullen *et al*., 2011a, Green *et al*., 2013c) . The work presented here established the possibility of implementing a low-cost, customisable manufacturing technique using commercially available, biocompatible materials to manufacture implantable electrode arrays that support cell growth and neurite extension.

Furthermore, electrochemical characterisation showed electrodes manufactured using this technique are likely to be supportive of safe and effective stimulation and can inject charges comparable that those currently used in visual prosthesis to stimulate retinal neurons in blind patients. Additionally, a therapeutically relevant cell source was implemented, and a differentiation protocol developed to generate motor neuron-like cells. These therapeutic cells were successfully incorporated onto manufactured electrode arrays to produce biohybrid devices. Preliminary *in vivo* studies, showed the feasibility of implanting biohybrid devices in a rodent muscle denervation model and initial steps were taken to improve viability and facilitate integration of the cellular component of this approach *in vivo.* The implementation of biohybrid devices to stimulate denervated muscles in patients with complete lower motor neuron injuries, could have a profound impact on mitigating the secondary complications of bone, skin and cardiovascular function associated with these injuries. Although this approach is still in early experimental stages, advances in this field offer unprecedented opportunities to replace some of the lost tissue and organ function following injury or disease, thus revolutionising the field of neuroprostheses and the way we treat patients.

7.0 References

A AL-SANABANI, F., MADFA, A. & H AL-QUDAIMI, N. 2014. Alumina ceramic for dental applications: A review article. *American Journal of Materials Research,* 1**,** 26-34.

ABAGNALE, G., SECHI, A., STEGER, M., ZHOU, Q., KUO, C. C., AYDIN, G., SCHALLA, C., MULLER-NEWEN, G., ZENKE, M., COSTA, I. G., VAN RIJN, P., GILLNER, A. & WAGNER, W. 2017. Surface Topography Guides Morphology and Spatial Patterning of Induced Pluripotent Stem Cell Colonies. *Stem Cell Reports,* 9**,** 654-666.

ABIDIAN, M. R., KIM, D. H. & MARTIN, D. C. 2006. Conducting-Polymer Nanotubes for Controlled Drug Release. *Adv Mater,* 18**,** 405-409.

ADEEB, N., DEEP, A., HOSE, N., REZAEI, M., FARD, S. A., TUBBS, R. S., YASHAR, P., LIKER, M. A., KATEB, B. & MORTAZAVI, M. M. 2015. Stem cell therapy for spinal cord injury: The use of oligodendrocytes and motor neurons derived from human embryonic stem cells. *Translational Research in Anatomy,* 1**,** 17-24.

ADEWOLE, D. O., SERRUYA, M. D., WOLF, J. A. & CULLEN, D. K. 2019. Bioactive Neuroelectronic Interfaces. *Frontiers in Neuroscience,* 13**,** 269.

ADEWOLE, D. O., STRUZYNA, L. A., HARRIS, J. P., NEMES, A. D., BURRELL, J. C., PETROV, D., KRAFT, R. H., CHEN, H. I., SERRUYA, M. D., WOLF, J. A. & CULLEN, D. K. 2018. Optically-Controlled “Living Electrodes” with Long-Projecting Axon Tracts for a Synaptic Brain-Machine Interface. *bioRxiv***,** 333526.

AGARWAL, S., KOBETIC, R., NANDURKAR, S. & MARSOLAIS, E. B. 2003. Functional electrical stimulation for walking in paraplegia: 17-year follow-up of 2 cases. *J Spinal Cord Med,* 26**,** 86-91.

AGUADO, B. A., MULYASASMITA, W., SU, J., LAMPE, K. J. & HEILSHORN, S. C. 2012. Improving viability of stem cells during syringe needle flow through the design of hydrogel cell carriers. *Tissue Eng Part A,* 18**,** 806-15.

AHUJA, C. S., WILSON, J. R., NORI, S., KOTTER, M. R. N., DRUSCHEL, C., CURT, A. & FEHLINGS, M. G. 2017. Traumatic spinal cord injury. *Nat Rev Dis Primers,* 3**,** 17018.

ALLEN, P., YEOH, J., MCCOMBE, M., HERIOT, W., LUU, C. & AYTON, L. 2013. Bionic Vision Australia - implantation of a suprachoroidal retinal prosthesis - Results for the first participants. *Invest Ophthalmol Vis Sci,* 54.

AMEMORI, T., ROMANYUK, N., JENDELOVA, P., HERYNEK, V., TURNOVCOVA, K., PROCHAZKA, P., KAPCALOVA, M., COCKS, G., PRICE, J. & SYKOVA, E. 2013. Human conditionally immortalized neural stem cells improve locomotor function after spinal cord injury in the rat. *Stem Cell Research & Therapy,* 4**,** 68.

AMER, M. H., ROSE, F., SHAKESHEFF, K. M., MODO, M. & WHITE, L. J. 2017. Translational considerations in injectable cell-based therapeutics for neurological applications: concepts, progress and challenges. *NPJ Regen Med,* 2**,** 23.

AMER, M. H., WHITE, L. J. & SHAKESHEFF, K. M. 2015. The effect of injection using narrow-bore needles on mammalian cells: administration and formulation considerations for cell therapies. *The Journal of pharmacy and pharmacology,* 67**,** 640-650.

AMOROSO, M. W., CROFT, G. F., WILLIAMS, D. J., O'KEEFFE, S., CARRASCO, M. A., DAVIS, A. R., ROYBON, L., OAKLEY, D. H., MANIATIS, T., HENDERSON, C. E. & WICHTERLE, H. 2013. Accelerated high-yield generation of limb-innervating motor neurons from human stem cells. *J Neurosci,* 33**,** 574-86.

ANDERSEN, T., AUK-EMBLEM, P. & DORNISH, M. 2015. 3D Cell Culture in Alginate Hydrogels. *Microarrays (Basel),* 4**,** 133-61.

ANSSELIN, A. D. & POLLARD, J. D. 1990. Immunopathological factors in peripheral nerve allograft rejection: Quantification of lymphocyte invasion and major histocompatibility complex expression. *Journal of the Neurological Sciences,* 96**,** 75-88.

APEL, P. J., ALTON, T., NORTHAM, C., MA, J., CALLAHAN, M., SONNTAG, W. E. & LI, Z. 2009. How age impairs the response of the neuromuscular junction to nerve transection and repair: An experimental study in rats. *J Orthop Res,* 27**,** 385-93.

AQRAWE, Z., MONTGOMERY, J., TRAVAS-SEJDIC, J. & SVIRSKIS, D. 2018. Conducting polymers for neuronal microelectrode array recording and stimulation. *Sensors and Actuators B: Chemical,* 257**,** 753-765.

ARBER, S., HAN, B., MENDELSOHN, M., SMITH, M., JESSELL, T. M. & SOCKANATHAN, S. 1999. Requirement for the Homeobox Gene Hb9 in the Consolidation of Motor Neuron Identity. *Neuron,* 23**,** 659-674.

AREGUETA-ROBLES, U. A., LIM, K. S., MARTENS, P. J., LOVELL, N. H., POOLE-WARREN, L. A. & GREEN, R. 2015. Producing 3D neuronal networks in hydrogels for living bionic device interfaces. *Conf Proc IEEE Eng Med Biol Soc,* 2015**,** 2600-3.

AREGUETA-ROBLES, U. A., WOOLLEY, A. J., POOLE-WARREN, L. A., LOVELL, N. H. & GREEN, R. A. 2014. Organic electrode coatings for next-generation neural interfaces. *Front Neuroeng,* 7**,** 15.

BADIA, J., BORETIUS, T., ANDREU, D., AZEVEDO-COSTE, C., STIEGLITZ, T. & NAVARRO, X. 2011. Comparative analysis of transverse intrafascicular multichannel, longitudinal intrafascicular and multipolar cuff electrodes for the selective stimulation of nerve fascicles. *J Neural Eng,* 8**,** 036023.

BAGHER, Z., KAMRAVA, S. K., ALIZADEH, R., FARHADI, M., ABSALAN, M., FALAH, M., FAGHIHI, F., ZARE-SADEGHI, A. & KOMEILI, A. 2018. Differentiation of neural crest stem cells from nasal mucosa into motor neuron-like cells. *J Chem Neuroanat,* 92**,** 35-40.

BAMFORD, J. A. & MUSHAHWAR, V. K. 2011. Chapter 17 - Intraspinal microstimulation for the recovery of function following spinal cord injury. *In:* SCHOUENBORG, J., GARWICZ, M. & DANIELSEN, N. (eds.) *Progress in Brain Research.* Elsevier.

BAREKET-KEREN, L. & HANEIN, Y. 2012. Carbon nanotube-based multi electrode arrays for neuronal interfacing: progress and prospects. *Front Neural Circuits,* 6**,** 122.

BAS, E., ANWAR, M. R., GONCALVES, S., DINH, C. T., BRACHO, O. R., CHIOSSONE, J. A. & VAN DE WATER, T. R. 2019. Laminin-coated electrodes improve cochlear implant function and post-insertion neuronal survival. *Neuroscience,* 410**,** 97-107.

BATT, J., BAIN, J., GONCALVES, J., MICHALSKI, B., PLANT, P., FAHNESTOCK, M. & WOODGETT, J. 2006. Differential gene expression profiling of short and long term denervated muscle. *Faseb j,* 20**,** 115-7.

BATT, J. A. E. & BAIN, J. R. 2013. Tibial nerve transection - a standardized model for denervation-induced skeletal muscle atrophy in mice. *Journal of visualized experiments : JoVE***,** e50657-e50657.

BIANCHI, F., MALBOUBI, M., LI, Y., GEORGE, J. H., JERUSALEM, A., SZELE, F., THOMPSON, M. S. & YE, H. 2018. Rapid and efficient differentiation of functional motor neurons from human iPSC for neural injury modelling. *Stem Cell Res,* 32**,** 126-134.

BIAZAR, E., KHORASANI, M. T., MONTAZERI, N., POURSHAMSIAN, K., DALIRI, M., REZAEI, M., JABARVAND, M., KHOSHZABAN, A., HEIDARI, S., JAFARPOUR, M. & ROVIEMIAB, Z. 2010. Types of neural guides and using nanotechnology for peripheral nerve reconstruction. *Int J Nanomedicine,* 5**,** 839-52.

BOEHLER, C., KLEBER, C., MARTINI, N., XIE, Y., DRYG, I., STIEGLITZ, T., HOFMANN, U. G. & ASPLUND, M. 2017. Actively controlled release of Dexamethasone from neural microelectrodes in a chronic in vivo study. *Biomaterials,* 129**,** 176-187.

BORSCHEL, G. H., KIA, K. F., KUZON, W. M. & DENNIS, R. G. 2003. Mechanical properties of acellular peripheral nerve. *Journal of Surgical Research,* 114**,** 133-139.

BROCKER, D. T. & GRILL, W. M. 2013. Chapter 1 - Principles of electrical stimulation of neural tissue. *In:* LOZANO, A. M. & HALLETT, M. (eds.) *Handbook of Clinical Neurology.* Elsevier.

BROUWERS, E., VAN DE MEENT, H., CURT, A., STARREMANS, B., HOSMAN, A. & BARTELS, R. 2017. Definitions of traumatic conus medullaris and cauda equina syndrome: a systematic literature review. *Spinal Cord,* 55, 886-890.

BRUNTON, E., BLAU, C. W. & NAZARPOUR, K. Multichannel cuff electrodes for peripheral nerve stimulation and recording. 2016 IEEE International Conference on Systems, Man, and Cybernetics (SMC), 9-12 Oct. 2016 2016. 003223-003227.

BRYSON, B. J., BARCELLOS MACHADO, C., CROSSLEY, M., STEVENSON, D., BROS-FACER, V., BURRONE, J., GREENSMITH, L. & LIEBERAM, I. 2014. Optical Control of Muscle Function by Transplantation of Stem Cell-Derived Motor Neurons in Mice. *Science,* 344, 94-97.

BURNETT, M. G. & ZAGER, E. L. 2004. Pathophysiology of peripheral nerve injury: a brief review. *Neurosurg Focus,* 16, E1.

BUSSCHER, H. J., VAN DER MEI, H. C., SUBBIAHDOSS, G., JUTTE, P. C., VAN DEN DUNGEN, J. J., ZAAT, S. A., SCHULTZ, M. J. & GRAINGER, D. W. 2012. Biomaterial-associated infection: locating the finish line in the race for the surface. *Sci Transl Med,* 4, 153rv10.

C. L, L. & M. R, P. 2008. Functional Electrical Stimulation. *IEEE Control Systems Magazine,* 28, 40-50.

CALDWELL, D. J., OJEMANN, J. G. & RAO, R. P. N. 2019. Direct Electrical Stimulation in Electrocorticographic Brain–Computer Interfaces: Enabling Technologies for Input to Cortex. *Frontiers in Neuroscience,* 13.

CARLSON, B., B. BORISOV, A., DEDKOV, E., DOW, D. & KOSTROMINOVA, T. 2002. The biology and restorative capacity of long-term denervated skeletal Muscle. *Basic and Applied Myology,* 12, 247-254.

CARLSON, B. M. 2014. The Biology of Long-Term Denervated Skeletal Muscle. *European Journal of Translational Myology,* 24, 5-11.

CARNICER-LOMBARTE, A., LANCASHIRE, H. T. & VANHOESTENBERGHE, A. 2017. In vitrobiocompatibility and electrical stability of thick-film platinum/gold alloy electrodes printed on alumina. *Journal of Neural Engineering,* 14, 036012.

CARRARO, U. & KERN, H. 2016. Severley atrophic human muscle fibers with a nuclear displacement surive many years of permanent denervation. *European Journal of Translational Myology,* 2.

CATHARYN, T., LIVERMAN, B. M., ALTEVOGT, J. E., JOY, T. & RICHARD, T. 2005. *Spinal Cord Injury: Progress, Promise, and Priorities,* Washington, DC, The National Academies Press.

CEDERNA, P., NGHIEM, B., HU, Y., SANDO, I. & URBANCHEK, M. 2015. Sensory protection to enhance functional recovery following proximal nerve injuries: current trends. *Plastic and Aesthetic Research,* 2, 202.

CHAI, Q., JIAO, Y. & YU, X. 2017. Hydrogels for Biomedical Applications: Their Characteristics and the Mechanisms behind Them. *Gels,* 3.

CHAN, G. & MOONEY, D. J. 2008. New materials for tissue engineering: towards greater control over the biological response. *Trends Biotechnol,* 26, 382-92.

CHEN, L., YAN, C. & ZHENG, Z. 2018a. Functional polymer surfaces for controlling cell behaviors. *Materials Today,* 21, 38-59.

CHEN, Y., KIM, Y. S., TILLMAN, B. W. & YEO, W. H. 2018b. Advances in Materials for Recent Low-Profile Implantable Bioelectronics. 11.

CHENG, M. Y., HO, H. H., HUANG, T. K., CHUANG, C. F., CHEN, H. Y., CHUNG, H. W., LEONG, W. C., YANG, W. C., FU, C. C., HSU, Y. H. & CHANG, Y. C. 2017. A compartmentalized culture device for studying the axons of CNS neurons. *Anal Biochem,* 539, 11-21.

CHUNG, T.-W., HUANG, C.-N., CHEN, P.-C., NODA, T., TOKUDA, T. & OHTA, J. 2018. Fabrication of Iridium Oxide/Platinum Composite Film on Titanium Substrate for High-Performance Neurostimulation Electrodes. *Coatings,* 8, 420.

CISNAL, A., FRAILE, J. C., PEREZ-TURIEL, J., MUNOZ-MARTINEZ, V., MULLER, C. & F, R. I. 2018. A Measurement Setup and Automated Calculation Method to Determine the Charge Injection Capacity of Implantable Microelectrodes. *Sensors (Basel),* 18.

COCKS, G., ROMANYUK, N., AMEMORI, T., JENDELOVA, P., FOROSTYAK, O., JEFFRIES, A. R., PERFECT, L., THURET, S., DAYANITHI, G., SYKOVA, E. & PRICE, J. 2013. Conditionally immortalized stem cell lines from human spinal cord retain regional identity and generate functional V2a interneurons and motorneurons. *Stem Cell Research & Therapy,* 4**,** 69.

COGAN, S. F. 2008. Neural Stimulation and Recording Electrodes. *Annual Review of Biomedical Engineering,* 10**,** 275-309.

COGAN, S. F., EHRLICH, J., PLANTE, T. D., SMIRNOV, A., SHIRE, D. B., GINGERICH, M. & RIZZO, J. F. 2009. Sputtered iridium oxide films for neural stimulation electrodes. *J Biomed Mater Res B Appl Biomater,* 89**,** 353-61.

CORTEC. 2017. *Hermectic Encapsulation* [Online]. Cortec. Available: https://cortec-neuro.com/?s=Hermetic+Encapsulation [Accessed 16 August 2019].

COWLEY, A. & WOODWARD, B. 2011. A Healthy Future: Platinum in Medical Applications. *Platinum Metals Review,* 55**,** 98-107.

CULLEN, D. K. & SMITH, D. H. 2012. Bionic Connections. *Scientific American,* 308**,** 52-57.

CULLEN, D. K., WOLF, J. A., SMITH, D. H. & PFISTER, B. J. 2011a. Neural tissue engineering for neuroregeneration and biohybridized interface microsystems in vivo (Part 2). *Crit Rev Biomed Eng,* 39**,** 241-59.

CULLEN, D. K., WOLF, J. A., VERNEKAR, V. N., VUKASINOVIC, J. & LAPLACA, M. C. 2011b. Neural tissue engineering and biohybridized microsystems for neurobiological investigation in vitro (Part 1). *Crit Rev Biomed Eng,* 39**,** 201-40.

CUMMINGS, B. J., UCHIDA, N., TAMAKI, S. J., SALAZAR, D. L., HOOSHMAND, M., SUMMERS, R., GAGE, F. H. & ANDERSON, A. J. 2005. Human neural stem cells differentiate and promote locomotor recovery in spinal cord-injured mice. *Proc Natl Acad Sci U S A,* 102**,** 14069-74.

CURTIS, A. & WILKINSON, C. 1997. Topographical control of cells. *Biomaterials,* 18**,** 1573-83.

DASARI SHAREENA, T. P., MCSHAN, D., DASMAHAPATRA, A. K. & TCHOUNWOU, P. B. 2018. A Review on Graphene-Based Nanomaterials in Biomedical Applications and Risks in Environment and Health. *Nanomicro Lett,* 10.

DAVIS-DUSENBERY, B. N., WILLIAMS, L. A., KLIM, J. R. & EGGAN, K. 2014. How to make spinal motor neurons. *Development,* 141**,** 491-501.

DAYAWANSA, S., WANG, E. W., LIU, W., MARKMAN, J. D., GELBARD, H. A. & HUANG, J. H. 2014. Allotransplanted DRG neurons or Schwann cells affect functional recovery in a rodent model of sciatic nerve injury. *Neurol Res,* 36**,** 1020-1027.

DE FAVERI, S., MAGGIOLINI, E., MIELE, E., DE ANGELIS, F., CESCA, F., BENFENATI, F. & FADIGA, L. 2014. Bio-inspired hybrid microelectrodes: a hybrid solution to improve long-term performance of chronic intracortical implants. *Front Neuroeng,* 7**,** 7.

DE LA OLIVA, N., NAVARRO, X. & DEL VALLE, J. 2018. Time course study of long-term biocompatibility and foreign body reaction to intraneural polyimide-based implants. *J Biomed Mater Res A,* 106**,** 746-757.

DEL VALLE, J. & NAVARRO, X. 2013. Chapter Two - Interfaces with the Peripheral Nerve for the Control of Neuroprostheses. *In:* GEUNA, S., PERROTEAU, I., TOS, P. & BATTISTON, B. (eds.) *International Review of Neurobiology.* Academic Press.

DESHPANDE, D. M., KIM, Y. S., MARTINEZ, T., CARMEN, J., DIKE, S., SHATS, I., RUBIN, L. L., DRUMMOND, J., KRISHNAN, C., HOKE, A., MARAGAKIS, N., SHEFNER, J., ROTHSTEIN, J. D. & KERR, D. A. 2006. Recovery from paralysis in adult rats using embryonic stem cells. *Ann Neurol,* 60**,** 32-44.

DOHERTY, J. G., BURNS, A. S., O'FERRALL, D. M. & DITUNNO, J. F., JR. 2002. Prevalence of upper motor neuron vs lower motor neuron lesions in complete lower thoracic and lumbar spinal cord injuries. *J Spinal Cord Med,* 25**,** 289-92.

DONNELLY, E. M., LAMANNA, J. & BOULIS, N. M. 2012. Stem cell therapy for the spinal cord. *Stem Cell Research & Therapy,* 3**,** 24.

DU, Z. W., CHEN, H., LIU, H., LU, J., QIAN, K., HUANG, C. L., ZHONG, X., FAN, F. & ZHANG, S. C. 2015. Generation and expansion of highly pure motor neuron progenitors from human pluripotent stem cells. *Nat Commun,* 6**,** 6626.

DUSART, P., FAGERBERG, L., PERISIC, L., CIVELEK, M., STRUCK, E., HEDIN, U., UHLEN, M., TREGOUET, D. A., RENNE, T., ODEBERG, J. & BUTLER, L. M. 2018. A systems-approach reveals human nestin is an endothelial-enriched, angiogenesis-independent intermediate filament protein. *Sci Rep,* 8**,** 14668.

EL-AKABAWY, G., RATTRAY, I., JOHANSSON, S. M., GALE, R., BATES, G. & MODO, M. 2012. Implantation of undifferentiated and pre-differentiated human neural stem cells in the R6/2 transgenic mouse model of Huntington's disease. *BMC Neuroscience,* 13**,** 97.

EL MERHIE, A., SALERNO, M., TOCCAFONDI, C. & DANTE, S. 2019. Neuronal-like response of N2a living cells to nanoporous patterns of thin supported anodic alumina. *Colloids Surf B Biointerfaces,* 178**,** 32-37.

ERB, D. E., MORA, R. J. & BUNGE, R. P. 1993. Reinnervation of Adult Rat Gastrocnemius Muscle by Embryonic Motoneurons Transplanted into the Axotomized Tibial Nerve. *Experimental Neurology,* 124**,** 372-376.

ERSEN, A., ELKABES, S., FREEDMAN, D. S. & SAHIN, M. 2015. Chronic tissue response to untethered microelectrode implants in the rat brain and spinal cord. *J Neural Eng,* 12**,** 016019.

ESPONA-NOGUERA, A., CIRIZA, J., CANIBANO-HERNANDEZ, A., FERNANDEZ, L., OCHOA, I., SAENZ DEL BURGO, L. & PEDRAZ, J. L. 2018. Tunable injectable alginate-based hydrogel for cell therapy in Type 1 Diabetes Mellitus. *Int J Biol Macromol,* 107**,** 1261-1269.

FARAVELLI, I., BUCCHIA, M., RINCHETTI, P., NIZZARDO, M., SIMONE, C., FRATTINI, E. & CORTI, S. 2014. Motor neuron derivation from human embryonic and induced pluripotent stem cells: experimental approaches and clinical perspectives. *Stem cell research & therapy,* 5**,** 87-87.

FERLAUTO, L., D'ANGELO, A. N., VAGNI, P., AIRAGHI LECCARDI, M. J. I., MOR, F. M., CUTTAZ, E. A., HEUSCHKEL, M. O., STOPPINI, L. & GHEZZI, D. 2018. Development and Characterization of PEDOT:PSS/Alginate Soft Microelectrodes for Application in Neuroprosthetics. *Front Neurosci,* 12**,** 648.

FERRO, M. D. & MELOSH, N. A. 2018. Electronic and Ionic Materials for Neurointerfaces. *Advanced Functional Materials,* 28**,** 1704335.

FIEDLER, E., ORDONEZ, J. S. & STIEGLITZ, T. 2013. Laser-structured ceramic adapters for reliable assembly of flexible thin-film electrodes. *Biomed Tech (Berl),* 58 Suppl 1.

FORTIN, J. M., AZARI, H., ZHENG, T., DARIOOSH, R. P., SCHMOLL, M. E., VEDAM-MAI, V., DELEYROLLE, L. P. & REYNOLDS, B. A. 2016. Transplantation of Defined Populations of Differentiated Human Neural Stem Cell Progeny. *Sci Rep,* 6**,** 23579.

FRANK-KAMENETSKY, M., ZHANG, X. M., BOTTEGA, S., GUICHERIT, O., WICHTERLE, H., DUDEK, H., BUMCROT, D., WANG, F. Y., JONES, S., SHULOK, J., RUBIN, L. L. & PORTER, J. A. 2002. Small-molecule modulators of Hedgehog signaling: identification and characterization of Smoothened agonists and antagonists. *Journal of biology,* 1**,** 10-10.

FRANKS, W., SCHENKER, I., SCHMUTZ, P. & HIERLEMANN, A. 2005. Impedance Characterization and Modeling of Electrodes for Biomedical Applications. *IEEE Transactions on Biomedical Engineering,* 52**,** 1295-1302.

FREEMAN, F. E. & KELLY, D. J. 2017. Tuning Alginate Bioink Stiffness and Composition for Controlled Growth Factor Delivery and to Spatially Direct MSC Fate within Bioprinted Tissues. *Sci Rep,* 7**,** 17042.

FURRER, R. & HANDSCHIN, C. 2019. Muscle Wasting Diseases: Novel Targets and Treatments. *Annual Review of Pharmacology and Toxicology,* 59**,** 315-339.

GABAY, T., BEN-DAVID, M., KALIFA, I., SORKIN, R., ABRAMS, Z. R., BEN-JACOB, E. & HANEIN, Y. 2007. Electro-chemical and biological properties of carbon nanotube based multi-electrode arrays. *Nanotechnology,* 18**,** 035201.

GAZDIC, M., VOLAREVIC, V., HARRELL, C. R., FELLABAUM, C., JOVICIC, N., ARSENIJEVIC, N. & STOJKOVIC, M. 2018. Stem Cells Therapy for Spinal Cord Injury. *Int J Mol Sci,* 19.

GEORGE, S. M., GAYLOR, J. D., LEADBITTER, J. & GRANT, M. H. 2011. The effect of betacyclodextrin and hydroxypropyl betacyclodextrin incorporation into plasticized poly(vinyl chloride) on its compatibility with human U937 cells. *J Biomed Mater Res B Appl Biomater,* 96**,** 310-5.

GHOLMIEH, G., SOUSSOU, W., HAN, M., AHUJA, A., HSIAO, M. C., SONG, D., TANGUAY, A. R., JR. & BERGER, T. W. 2006. Custom-designed high-density conformal planar multielectrode arrays for brain slice electrophysiology. *J Neurosci Methods,* 152**,** 116-29.

GODING, J., GILMOUR, A., ROBLES, U. A., POOLE-WARREN, L., LOVELL, N., MARTENS, P. & GREEN, R. 2017. A living electrode construct for incorporation of cells into bionic devices. *MRS Communications,* 7**,** 487-495.

GODING, J. A., GILMOUR, A. D., AREGUETA-ROBLES, U. A., HASAN, E. A. & GREEN, R. A. 2018. Living Bioelectronics: Strategies for Developing an Effective Long-Term Implant with Functional Neural Connections. *Advanced Functional Materials,* 28**,** 1702969.

GOMEZ, N., LU, Y., CHEN, S. & SCHMIDT, C. E. 2007. Immobilized nerve growth factor and microtopography have distinct effects on polarization versus axon elongation in hippocampal cells in culture. *Biomaterials,* 28**,** 271-84.

GREEN, R. & ABIDIAN, M. R. 2015. Conducting Polymers for Neural Prosthetic and Neural Interface Applications. *Adv Mater,* 27**,** 7620-37.

GREEN, R., TOOR, H., DODDS, C. & LOVELL, N. 2012. Variation in Performance of Platinum Electrodes with Size and Surface Roughness. *Sensors and Materials,* 24**,** 165-180.

GREEN, R. A., GUENTHER, T., JESCHKE, C., JAILLON, A., YU, J. F., DUECK, W. F., LIM, W. W., HENDERSON, W. C., VANHOESTENBERGHE, A., LOVELL, N. H. & SUANING, G. J. 2013a. Integrated electrode and high density feedthrough system for chip-scale implantable devices. *Biomaterials,* 34**,** 6109-18.

GREEN, R. A., LIM, K. S., HENDERSON, W. C., HASSARATI, R. T., MARTENS, P. J., LOVELL, N. H. & POOLE-WARREN, L. A. 2013b. Living electrodes: tissue engineering the neural interface. *Conf Proc IEEE Eng Med Biol Soc,* 2013**,** 6957-60.

GREEN, R. A., LOVELL, N. H. & POOLE-WARREN, L. A. 2010. Impact of co-incorporating laminin peptide dopants and neurotrophic growth factors on conducting polymer properties. *Acta Biomater,* 6**,** 63-71.

GREEN, R. A., MATTEUCCI, P. B., DODDS, C. W., PALMER, J., DUECK, W. F., HASSARATI, R. T., BYRNES-PRESTON, P. J., LOVELL, N. H. & SUANING, G. J. 2014. Laser patterning of platinum electrodes for safe neurostimulation. *J Neural Eng,* 11**,** 056017.

GREEN, R. A., MATTEUCCI, P. B., HASSARATI, R. T., GIRAUD, B., DODDS, C. W., CHEN, S., BYRNES-PRESTON, P. J., SUANING, G. J., POOLE-WARREN, L. A. & LOVELL, N. H. 2013c. Performance of conducting polymer electrodes for stimulating neuroprosthetics. *J Neural Eng,* 10**,** 016009.

GREEN, R. A., MATTEUCCI, P. B., HASSARATI, R. T., GIRAUD, B., DODDS, C. W. D., CHEN, S., BYRNES-PRESTON, P. J., SUANING, G. J., POOLE-WARREN, L. A. & LOVELL, N. H. 2013d. Performance of conducting polymer electrodes for stimulating neuroprosthetics. *Journal of Neural Engineering,* 10**,** 016009.

GREIG, C. A. & JONES, D. A. 2016. Muscle physiology and contraction. *Surgery (Oxford),* 34**,** 107-114.

GRUMET, A. E., WYATT, J. L., JR. & RIZZO, J. F., 3RD 2000. Multi-electrode stimulation and recording in the isolated retina. *J Neurosci Methods,* 101**,** 31-42.

GUENTHER, T., MINTRI, A., LIM, W. W., JUNG, L. H., LEHMANN, T., LOVELL, N. H. & SUANING, G. J. Laser-micromachined, chip-scaled ceramic carriers for implantable neurostimulators. 2011 Annual International Conference of the IEEE Engineering in Medicine and Biology Society, 30 Aug.-3 Sept. 2011 2011. 1085-1088.

GULATI, A. K. 1998. Immune Response and Neurotrophic Factor Interactions in Peripheral Nerve Transplants. *Acta Haematologica,* 99**,** 171-174.

HABIBEY, R., LATIFI, S., MOUSAVI, H., PESCE, M., ARAB-TEHRANY, E. & BLAU, A. 2017. A multielectrode array microchannel platform reveals both transient and slow changes in axonal conduction velocity. *Sci Rep,* 7**,** 8558.

HAGEN, E. M. 2015. Acute complications of spinal cord injuries. *World Journal of Orthopedics,* 6**,** 17.

HANDSCHIN, C. & SPIEGELMAN, B. M. 2008. The role of exercise and PGC1alpha in inflammation and chronic disease. *Nature,* 454**,** 463-469.

HARRIS, K. D., QUIROGA, R. Q., FREEMAN, J. & SMITH, S. L. 2016. Improving data quality in neuronal population recordings. *Nat Neurosci,* 19**,** 1165-74.

HASSARATI, R. T., DUECK, W. F., TASCHE, C., CARTER, P. M., POOLE-WARREN, L. A. & GREEN, R. A. 2014. Improving cochlear implant properties through conductive hydrogel coatings. *IEEE Trans Neural Syst Rehabil Eng,* 22**,** 411-8.

HE, W., MCCONNELL, G. C. & BELLAMKONDA, R. V. 2006. Nanoscale laminin coating modulates cortical scarring response around implanted silicon microelectrode arrays. *J Neural Eng,* 3**,** 316-26.

HELLENBRAND, D. J., KAEPPLER, K. E., EHLERS, M. E., THOMPSON, C. D., ZURKO, J. C., BUCHHOLZ, M. M., SPRINGER, A. R., THOMPSON, D. L., IBRAHIM, R. K. & HANNA, A. 2016. Immunohistochemical assessment of rat nerve isografts and immunosuppressed allografts. *Neurol Res,* 38**,** 1094-1101.

HENDRICKSON, M. L., RAO, A. J., DEMERDASH, O. N. & KALIL, R. E. 2011. Expression of nestin by neural cells in the adult rat and human brain. *PLoS One,* 6**,** e18535.

HEUSCHKEL, M. O., FEJTL, M., RAGGENBASS, M., BERTRAND, D. & RENAUD, P. 2002. A three-dimensional multi-electrode array for multi-site stimulation and recording in acute brain slices. *J Neurosci Methods,* 114**,** 135-48.

HO, C. H., TRIOLO, R. J., ELIAS, A. L., KILGORE, K. L., DIMARCO, A. F., BOGIE, K., VETTE, A. H., AUDU, M. L., KOBETIC, R., CHANG, S. R., CHAN, K. M., DUKELOW, S., BOURBEAU, D. J., BROSE, S. W., GUSTAFSON, K. J., KISS, Z. H. & MUSHAHWAR, V. K. 2014. Functional electrical stimulation and spinal cord injury. *Phys Med Rehabil Clin N Am,* 25**,** 631-54, ix.

HODGKIN, A. L. & HUXLEY, A. F. 1952. A quantitative description of membrane current and its application to conduction and excitation in nerve. *The Journal of physiology,* 117**,** 500-544.

HOFER, C., MAYR, W., STOHR, H., UNGER, E. & KERN, H. 2002. A stimulator for functional activation of denervated muscles. *Artif Organs,* 26**,** 276-9.

HOFFMAN-KIM, D., MITCHEL, J. A. & BELLAMKONDA, R. V. 2010. Topography, cell response, and nerve regeneration. *Annu Rev Biomed Eng,* 12**,** 203-31.

HOFRICHTER, M., NIMTZ, L., TIGGES, J., KABIRI, Y., SCHROTER, F., ROYER-POKORA, B., HILDEBRANDT, B., SCHMUCK, M., EPANCHINTSEV, A., THEISS, S., ADJAYE, J., EGLY, J. M., KRUTMANN, J. & FRITSCHE, E. 2017. Comparative performance analysis of human iPSC-derived and primary neural progenitor cells (NPC) grown as neurospheres in vitro. *Stem Cell Res,* 25**,** 72-82.

HONEGGER, T., THIELEN, M. I., FEIZI, S., SANJANA, N. E. & VOLDMAN, J. 2016a. Microfluidic neurite guidance to study structure-function relationships in topologically-complex population-based neural networks. *Scientific Reports,* 6.

HONEGGER, T., THIELEN, M. I., FEIZI, S., SANJANA, N. E. & VOLDMAN, J. 2016b. Microfluidic neurite guidance to study structure-function relationships in topologically-complex population-based neural networks. *Scientific Reports,* 6**,** 28384.

HOPPER, A. P., DUGAN, J. M., GILL, A. A., FOX, O. J., MAY, P. W., HAYCOCK, J. W. & CLAEYSSENS, F. 2014. Amine functionalized nanodiamond promotes cellular adhesion, proliferation and neurite outgrowth. *Biomed Mater,* 9**,** 045009.

HU, B. Y. & ZHANG, S. C. 2009. Differentiation of spinal motor neurons from pluripotent human stem cells. *Nat Protoc,* 4**,** 1295-304.

HU, F. & STRITTMATTER, S. M. 2004. Regulating axon growth within the postnatal central nervous system. *Seminars in Perinatology,* 28**,** 371-378.

HU, J. J. 1998. Application of thick film technology in mass production of biosensors. *Ann N Y Acad Sci,* 864**,** 305-8.

HUANG, C.-W., HUANG, W.-C., QIU, X., FERNANDES FERREIRA DA SILVA, F., WANG, A., PATEL, S., NESTI, L. J., POO, M.-M. & LI, S. 2017. The Differentiation Stage of Transplanted Stem Cells Modulates Nerve Regeneration. *Scientific reports,* 7**,** 17401-17401.

HUANG, J. H., CULLEN, D. K., BROWNE, K. D., GROFF, R., ZHANG, J., PFISTER, B. J., ZAGER, E. L. & SMITH, D. H. 2009. Long-term survival and integration of transplanted engineered nervous tissue constructs promotes peripheral nerve regeneration. *Tissue Eng Part A,* 15**,** 1677-85.

HUDAK, E., T MORTIMER, J. & MARTIN, H. 2010. *Platinum for neural stimulation: Voltammetry considerations*.

HUDAK, E. M., KUMSA, D. W., MARTIN, H. B. & MORTIMER, J. T. 2017. Electron transfer processes occurring on platinum neural stimulating electrodes: calculated charge-storage capacities are inaccessible during applied stimulation. *J Neural Eng,* 14**,** 046012.

HUGL, S., SCHEPER, V., GEPP, M. M., LENARZ, T., RAU, T. S. & SCHWIEGER, J. 2019. Coating stability and insertion forces of an alginate-cell-based drug delivery implant system for the inner ear. *J Mech Behav Biomed Mater,* 97**,** 90-98.

HYNEK WICHTERLE, I. L., JEFFERY A. PORTER, THOMAS M. JESSELL 2002. Directed Differentiation of Embryonic

Stem Cells into Motor Neurons. *Cell,* 110**,** 385-397.

INGULLI, E. 2010. Mechanism of cellular rejection in transplantation. *Pediatr Nephrol,* 25**,** 61-74.

IVANHOE, C. B. & REISTETTER, T. A. 2004. Spasticity: the misunderstood part of the upper motor neuron syndrome. *Am J Phys Med Rehabil,* 83**,** S3-9.

JANG, S., KANG, Y. H., ULLAH, I., SHIVAKUMAR, S. B., RHO, G. J., CHO, Y. C., SUNG, I. Y. & PARK, B. W. 2018. Cholinergic Nerve Differentiation of Mesenchymal Stem Cells Derived from Long-Term Cryopreserved Human Dental Pulp In Vitro and Analysis of Their Motor Nerve Regeneration Potential In Vivo. *Int J Mol Sci,* 19.

JENDELOVÁ, P., HERYNEK, V., URDZÍKOVÁ, L., GLOGAROVÁ, K., KROUPOVÁ, J., ANDERSSON, B., BRYJA, V., BURIAN, M., HÁJEK, M. & SYKOVÁ, E. 2004. Magnetic resonance tracking of transplanted bone marrow and embryonic stem cells labeled by iron oxide nanoparticles in rat brain and spinal cord. *Journal of Neuroscience Research,* 76**,** 232-243.

JENKINSON, S. P., GRANDGIRARD, D., HEIDEMANN, M., TSCHERTER, A., AVONDET, M.-A. & LEIB, S. L. 2017. Embryonic Stem Cell-Derived Neurons Grown on Multi-Electrode Arrays as a Novel In vitro Bioassay for the Detection of Clostridium botulinum Neurotoxins. *Frontiers in Pharmacology,* 8**,** 73.

JHA, B. S., RAO, M. & MALIK, N. 2014. Motor Neuron Differentiation from Pluripotent Stem Cells and Other Intermediate Proliferative Precursors that can be Discriminated by Lineage Specific Reporters. *Stem Cell Reviews and Reports,* 11**,** 194-204.

JI, B., WANG, M., GE, C., XIE, Z., GUO, Z., HONG, W., GU, X., WANG, L., YI, Z., JIANG, C., YANG, B., WANG, X., LI, X., LI, C. & LIU, J. 2019. Flexible bioelectrodes with enhanced wrinkle microstructures for reliable electrochemical modification and neuromodulation in vivo. *Biosens Bioelectron,* 135**,** 181-191.

JIA, J., RICHARDS, D. J., POLLARD, S., TAN, Y., RODRIGUEZ, J., VISCONTI, R. P., TRUSK, T. C., YOST, M. J., YAO, H., MARKWALD, R. R. & MEI, Y. 2014. Engineering alginate as bioink for bioprinting. *Acta Biomater,* 10**,** 4323-31.

KAKLAMANI, G., KAZARYAN, D., BOWEN, J., IACOVELLA, F., ANASTASIADIS, S. H. & DELIGEORGIS, G. 2018. On the electrical conductivity of alginate hydrogels. *Regen Biomater,* 5**,** 293-301.

KALLADKA, D., SINDEN, J., POLLOCK, K., HAIG, C., MCLEAN, J., SMITH, W., MCCONNACHIE, A., SANTOSH, C., BATH, P. M., DUNN, L. & MUIR, K. W. 2016. Human neural stem cells in patients with chronic ischaemic stroke (PISCES): a phase 1, first-in-man study. *The Lancet,* 388**,** 787-796.

KAMESWARAN, N., CULLEN, D. K., PFISTER, B. J., RANALLI, N. J., HUANG, J. H., ZAGER, E. L. & SMITH, D. H. 2008. A novel neuroprosthetic interface with the peripheral nervous system using artificially engineered axonal tracts. *Neurol Res,* 30**,** 1063-7.

KANG, E., JEONG, G. S., CHOI, Y. Y., LEE, K. H., KHADEMHOSSEINI, A. & LEE, S. H. 2011. Digitally tunable physicochemical coding of material composition and topography in continuous microfibres. *Nat Mater,* 10**,** 877-83.

KAPETANAKIS, S., CHANIOTAKIS, C., KAZAKOS, C. & PAPATHANASIOU, J. V. 2017. Cauda Equina Syndrome Due to Lumbar Disc Herniation: a Review of Literature. *Folia Med (Plovdiv),* 59**,** 377-386.

KAROVA, K., WAINWRIGHT, J. V., MACHOVA-URDZIKOVA, L., PISAL, R. V., SCHMIDT, M., JENDELOVA, P. & JHANWAR-UNIYAL, M. 2019. Transplantation of neural precursors generated from spinal progenitor cells reduces inflammation in spinal cord injury via NF-kappaB pathway inhibition. *J Neuroinflammation,* 16**,** 12.

KARUMBAYARAM, S., NOVITCH, B. G., PATTERSON, M., UMBACH, J. A., RICHTER, L., LINDGREN, A., CONWAY, A. E., CLARK, A. T., GOLDMAN, S. A., PLATH, K., WIEDAU-PAZOS, M., KORNBLUM, H. I. & LOWRY, W. E. 2009. Directed differentiation of human-induced pluripotent stem cells generates active motor neurons. *Stem Cells,* 27**,** 806-11.

KATO, S., KURIMOTO, S., NAKANO, T., YONEDA, H., ISHII, H., MITA-SUGIURA, S. & HIRATA, H. 2015. Successful transplantation of motoneurons into the peripheral nerve depends on the number of transplanted cells. *Nagoya journal of medical science,* 77**,** 253-263.

KEEFER, E. W., BOTTERMAN, B. R., ROMERO, M. I., ROSSI, A. F. & GROSS, G. W. 2008. Carbon nanotube coating improves neuronal recordings. *Nat Nanotechnol,* 3**,** 434-9.

KEIFER, O. P., JR., RILEY, J. P. & BOULIS, N. M. 2014. Deep brain stimulation for chronic pain: intracranial targets, clinical outcomes, and trial design considerations. *Neurosurg Clin N Am,* 25**,** 671-92.

KERN, H., HOFER, C., LOEFLER, S., ZAMPIERI, S., GARGIULO, P., BABA, A., MARCANTE, A., PICCIONE, F., POND, A. & CARRARO, U. 2017. Atrophy, ultra-structural disorders, severe atrophy and degeneration of denervated human muscle in SCI and Aging. Implications for their recovery by Functional Electrical Stimulation, updated 2017. *Neurol Res,* 39**,** 660-666.

KERN, H., HOFER, C., MÖDLIN, M., FORSTNER, C., MAYR, W. & RICHTER, W. 2002a. Functional Electrical Stimulation (FES) of Long-Term Definervated Muscles in Humans: Clinical Observations and Laboratory Findings. *Basic and Applied Myology,* 12**,** 291-299.

KERN, H., HOFER, C., MODLIN, M., FORSTNER, C., RASCHKA-HOGLER, D., MAYR, W. & STOHR, H. 2002b. Denervated muscles in humans: limitations and problems of currently used functional electrical stimulation training protocols. *Artif Organs,* 26**,** 216-8.

KERN, H., HOFER, C., STROHHOFER, M., MAYR, W., RICHTER, W. & STOHR, H. 1999. Standing up with denervated muscles in humans using functional electrical stimulation. *Artif Organs,* 23**,** 447-52.

KERN, H., STRAMARE, R., MARTINO, L., ZANATO, R., GARGIULO, P. & CARRARO, U. 2010. Permanent LMN denervation of human skeletal muscle and recovery by h-b FES: management and monitoringHelmut Kern (1), Roberto Stramare (2), Leonora Martino (2), Riccardo Zanato (2), Paolo Gargiulo (3), Ugo Carraro (4). *Basic and applied myology: BAM,* 22**,** 91-104.

KHAZAEI, M., AHUJA, C. S. & FEHLINGS, M. G. 2016. Induced Pluripotent Stem Cells for Traumatic Spinal Cord Injury. *Front Cell Dev Biol,* 4**,** 152.

KIL, D., DE VLOO, P., FIERENS, G., CEYSSENS, F., HUNYADI, B., BERTRAND, A., NUTTIN, B. & PUERS, R. 2018. A foldable electrode array for 3D recording of deep-seated abnormal brain cavities. *Journal of Neural Engineering,* 15**,** 036029.

KIM, S., JANG, L. K., JANG, M., LEE, S., HARDY, J. G. & LEE, J. Y. 2018a. Electrically Conductive Polydopamine-Polypyrrole as High Performance Biomaterials for Cell Stimulation in Vitro and Electrical Signal Recording in Vivo. *ACS Appl Mater Interfaces,* 10**,** 33032-33042.

KIM, S. J., CHO, K. W., CHO, H. R., WANG, L., PARK, S. Y., LEE, S. E., HYEON, T., LU, N., CHOI, S. H. & KIM, D.-H. 2016a. Stretchable and Transparent Biointerface Using Cell-Sheet-Graphene Hybrid for Electrophysiology and Therapy of Skeletal Muscle. *Advanced Functional Materials,* 26**,** 3207-3217.

KIM, T., CHO, M. & YU, K. J. 2018b. Flexible and Stretchable Bio-Integrated Electronics Based on Carbon Nanotube and Graphene. *Materials (Basel),* 11.

KIM, Y. H., KIM, G. H., PARK, J. & JUNG, S. Highly efficient nanoporous gold-modified multi-electrode arrays for in vitro extracellular recording and stimulation performance. 2016 IEEE Nanotechnology Materials and Devices Conference (NMDC), 9-12 Oct. 2016 2016b. 1-2.

KNOWLES, M. R. H., RUTTERFORD, G., KARNAKIS, D. & FERGUSON, A. 2007. Micro-machining of metals, ceramics and polymers using nanosecond lasers. *The International Journal of Advanced Manufacturing Technology,* 33**,** 95-102.

KOZAI, T. D. Y., LANGHALS, N. B., PATEL, P. R., DENG, X., ZHANG, H., SMITH, K. L., LAHANN, J., KOTOV, N. A. & KIPKE, D. R. 2012. Ultrasmall implantable composite microelectrodes with bioactive surfaces for chronic neural interfaces. *Nature Materials,* 11**,** 1065.

KUMSA, D. W., BHADRA, N., HUDAK, E. M., KELLEY, S. C., UNTEREKER, D. F. & MORTIMER, J. T. 2016. Electron transfer processes occurring on platinum neural stimulating electrodes: a tutorial on thei(Ve) profile. *Journal of Neural Engineering,* 13**,** 052001.

KURIMOTO, S., KATO, S., NAKANO, T., YAMAMOTO, M., TAKANOBU, N. & HIRATA, H. 2016. Transplantation of embryonic motor neurons into peripheral nerve combined with functional electrical stimulation restores functional muscle activity in the rat sciatic nerve transection model. *J Tissue Eng Regen Med,* 10**,** E477-E484.

LACOUR, S. P., COURTINE, G. & GUCK, J. 2016. Materials and technologies for soft implantable neuroprostheses. *Nature Reviews Materials,* 1**,** 16063.

LACOUR, S. P., FITZGERALD, J. J., LAGO, N., TARTE, E., MCMAHON, S. & FAWCETT, J. 2009. Long micro-channel electrode arrays: a novel type of regenerative peripheral nerve interface. *IEEE Trans Neural Syst Rehabil Eng,* 17**,** 454-60.

LAMB, D. R. 1984. *Physiology of Exercise: Responses and Adaptations,* New York, Macmillan Publishing Co. Inc.,.

LANCASHIRE, H. T., VANHOESTENBERGHE, A., PENDEGRASS, C. J., AJAM, Y. A., MAGEE, E., DONALDSON, N. & BLUNN, G. W. 2016. Microchannel neural interface manufacture by stacking silicone and metal foil laminae. *J Neural Eng,* 13**,** 034001.

LAVY, C., JAMES, A., WILSON-MACDONALD, J. & FAIRBANK, J. 2009. Cauda equina syndrome. *BMJ,* 338**,** b936.

LEE, C. D., HUDAK, E. M., WHALEN, J. J., PETROSSIANS, A. & WEILAND, J. D. 2018. Low-Impedance, High Surface Area Pt-Ir Electrodeposited on Cochlear Implant Electrodes. *Journal of The Electrochemical Society,* 165**,** G3015-G3017.

LEE, H., SHAMY, G. A., ELKABETZ, Y., SCHOFIELD, C. M., HARRSION, N. L., PANAGIOTAKOS, G., SOCCI, N. D., TABAR, V. & STUDER, L. 2007. Directed differentiation and transplantation of human embryonic stem cell-derived motoneurons. *Stem Cells,* 25**,** 1931-9.

LEE, H. J., KIM, K. S., AHN, J., BAE, H. M., LIM, I. & KIM, S. U. 2014. Human Motor Neurons Generated from Neural Stem Cells Delay Clinical Onset and Prolong Life in ALS Mouse Model. *PLOS ONE,* 9**,** e97518.

LEE, K. H., CHUNG, K., CHUNG, J. M. & COGGESHALL, R. E. 1986. Correlation of cell body size, axon size, and signal conduction velocity for individually labelled dorsal root ganglion cells in the cat. *J Comp Neurol,* 243**,** 335-46.

LEE, K. Y. & MOONEY, D. J. 2012. Alginate: properties and biomedical applications. *Prog Polym Sci,* 37**,** 106-126.

LI, J., MCNALLY, H. & SHI, R. 2008. Enhanced neurite alignment on micro-patterned poly-L-lactic acid films. *J Biomed Mater Res A,* 87**,** 392-404.

LI, N. & FOLCH, A. 2005. Integration of topographical and biochemical cues by axons during growth on microfabricated 3-D substrates. *Exp Cell Res,* 311**,** 307-16.

LIU, Y., LIU, J., CHEN, S., LEI, T., KIM, Y., NIU, S., WANG, H., WANG, X., FOUDEH, A. M., TOK, J. B. & BAO, Z. 2019. Soft and elastic hydrogel-based microelectronics for localized low-voltage neuromodulation. *Nat Biomed Eng,* 3**,** 58-68.

LOTTI, F., RANIERI, F., VADALA, G., ZOLLO, L. & DI PINO, G. 2017. Invasive Intraneural Interfaces: Foreign Body Reaction Issues. *Front Neurosci,* 11**,** 497.

MAGOWN, P., RAFUSE, V. F. & BROWNSTONE, R. M. 2017. Microcircuit formation following transplantation of mouse embryonic stem cell-derived neurons in peripheral nerve. *J Neurophysiol,* 117**,** 1683-1689.

MAHADEVAPPA, M., WEILAND, J. D., YANAI, D., FINE, I., GREENBERG, R. J. & HUMAYUN, M. S. 2005. Perceptual thresholds and electrode impedance in three retinal prosthesis subjects. *IEEE Trans Neural Syst Rehabil Eng,* 13**,** 201-6.

MAHONEY, M. J. & ANSETH, K. S. 2006. Three-dimensional growth and function of neural tissue in degradable polyethylene glycol hydrogels. *Biomaterials,* 27**,** 2265-74.

MAHONEY, M. J., CHEN, R. R., TAN, J. & MARK SALTZMAN, W. 2005. The influence of microchannels on neurite growth and architecture. *Biomaterials,* 26**,** 771-778.

MARTIN, R., SADOWSKY, C., OBST, K., MEYER, B. & MCDONALD, J. 2012a. Functional Electrical Stimulation in Spinal Cord Injury: From Theory to Practice. *Topics in Spinal Cord Injury Rehabilitation,* 18**,** 28-33.

MARTIN, R., SADOWSKY, C., OBST, K., MEYER, B. & MCDONALD, J. 2012b. Functional electrical stimulation in spinal cord injury:: from theory to practice. *Top Spinal Cord Inj Rehabil,* 18**,** 28-33.

MATTHEWS, G. G. & MATTHEWS, G. G. 2013. Neural Control of Muscle Contraction. *In:* MATTHEWS, G. G. (ed.) *Cellular Physiology of Nerve and Muscle.*

MAYR, W., HOFER, C., RAFOLT, D., BIJAK, M., LANMUELLER, H., REICHEL, M., SAUERMANN, S., UNGER, E. & KERN, H. 2004. The European FP5- project RISE: FES of denervated degenerated musculature. *9th Annual Conference of the International FES Society.* Bournemouth, UK.

MCINTYRE, C. C. & GRILL, W. M. 2000. Selective microstimulation of central nervous system neurons. *Ann Biomed Eng,* 28**,** 219-33.

MEISER, I., MÜLLER, S. C., EHRHART, F., SHIRLEY, S. G. & ZIMMERMANN, H. 2013. A new validation method for clinical grade micro-encapsulation: quantitative high speed video analysis of alginate capsule. *Microsystem Technologies,* 21**,** 75-84.

MERRILL, D. R., BIKSON, M. & JEFFERYS, J. G. 2005. Electrical stimulation of excitable tissue: design of efficacious and safe protocols. *J Neurosci Methods,* 141**,** 171-98.

MEYER, J., STIEGLITZ, T., RUF, H. H., ROBITZKI, A., DABOURAS, V., WEWETZER, K. & BRINKER, T. A biohybrid microprobe for implanting into the peripheral nervous system. 2nd Annual International IEEE-EMBS Special Topic Conference on Microtechnologies in Medicine and Biology. Proceedings (Cat. No.02EX578), 2-4 May 2002 2002. 265-268.

MILES, G. B. 2004. Functional Properties of Motoneurons Derived from Mouse Embryonic Stem Cells. *Journal of Neuroscience,* 24**,** 7848-7858.

MOBASSERI, A., FARONI, A., MICHAEL MINOGUE, B., DOWNES, S., TERENGHI, G. & REID, A. 2014. *Polymer Scaffolds with Preferential Parallel Grooves Enhance Nerve Regeneration*.

MOE, J. & POST, H. 1962. Functional electrical stimulation for ambulation in hemiplegia. *Lancet,* 82**,** 285-288.

MOHAMMED, M. K., UMER, U., REHMAN, A. U., AL-AHMARI, A. M. & EL-TAMIMI, A. M. 2018. Microchannels Fabrication in Alumina Ceramic Using Direct Nd:YAG Laser Writing. *Micromachines (Basel),* 9.

N. NEDIALKOV, N., A. ATANASOV, P., SAWCZAK, M. & SLIWINSKI, G. 2003. Ablation of ceramics with ultraviolet, visible, and infrared nanosecond laser pulses. *XIV International Symposium on Gas Flow, Chemical Lasers, and High-Power Lasers.*

NAGATA, I., KAWANA, A. & NAKATSUJI, N. 1993. Perpendicular contact guidance of CNS neuroblasts on artificial microstructures. *Development,* 117**,** 401-8.

NAKAMURA, M. & OKANO, H. 2013. Cell transplantation therapies for spinal cord injury focusing on induced pluripotent stem cells. *Cell Research,* 23**,** 70-80.

NAVARRO, X., KRUEGER, T. B., LAGO, N., MICERA, S., STIEGLITZ, T. & DARIO, P. 2005. A critical review of interfaces with the peripheral nervous system for the control of neuroprostheses and hybrid bionic systems. *J Peripher Nerv Syst,* 10**,** 229-58.

NGUYEN-VU, T. D., CHEN, H., CASSELL, A. M., ANDREWS, R. J., MEYYAPPAN, M. & LI, J. 2007. Vertically aligned carbon nanofiber architecture as a multifunctional 3-D neural electrical interface. *IEEE Trans Biomed Eng,* 54**,** 1121-8.

NGUYEN, J. K., PARK, D. J., SKOUSEN, J. L., HESS-DUNNING, A. E., TYLER, D. J., ROWAN, S. J., WEDER, C. & CAPADONA, J. R. 2014. Mechanically-compliant intracortical implants reduce the neuroinflammatory response. *J Neural Eng,* 11**,** 056014.

NIKITINA, V., ASTRELINA, T., NUGIS, V., OSTASHKIN, A., KARASEVA, T., DOBROVOLSKAYA, E., USUPZHANOVA, D., SUCHKOVA, Y., LOMONOSOVA, E., RODIN, S., BRUNCHUKOV, V., LAUK-DUBITSKIY, S., BRUMBERG, V., MACHOVA, A., KOBZEVA, I., BUSHMANOV, A. & SAMOILOV, A. 2018. Clonal chromosomal and genomic instability during human multipotent mesenchymal stromal cells long-term culture. *PLoS One,* 13**,** e0192445.

NIKKHAH, M., EDALAT, F., MANOUCHERI, S. & KHADEMHOSSEINI, A. 2012. Engineering microscale topographies to control the cell-substrate interface. *Biomaterials,* 33**,** 5230-46.

NORLIN, A., PAN, J. & LEYGRAF, C. 2005. Investigation of Electrochemical Behavior of Stimulation⁄Sensing Materials for Pacemaker Electrode Applications. *Journal of The Electrochemical Society,* 152**,** 7-15.

O'ROURKE, C., DAY, A. G. E., MURRAY-DUNNING, C., THANABALASUNDARAM, L., COWAN, J., STEVANATO, L., GRACE, N., CAMERON, G., DRAKE, R. A. L., SINDEN, J. & PHILLIPS, J. B. 2018. An allogeneic 'off the shelf' therapeutic strategy for peripheral nerve tissue engineering using clinical grade human neural stem cells. *Scientific Reports,* 8**,** 2951.

OBIEN, M. E., DELIGKARIS, K., BULLMANN, T., BAKKUM, D. J. & FREY, U. 2014. Revealing neuronal function through microelectrode array recordings. *Front Neurosci,* 8**,** 423.

OLIVA, A. A., JAMES, C. D., KINGMAN, C. E., CRAIGHEAD, H. G. & BANKER, G. A. 2003. Patterning Axonal Guidance Molecules Using a Novel Strategy for Microcontact Printing. *Neurochemical Research,* 28**,** 1639-1648.

ORDONEZ, J., SCHUETTLER, M., BOEHLER, C., BORETIUS, T. & STIEGLITZ, T. 2012. Thin films and microelectrode arrays for neuroprosthetics. *MRS Bulletin,* 37**,** 590-598.

ORIVE, G., CARCABOSO, A. M., HERNÁNDEZ, R. M., GASCÓN, A. R. & PEDRAZ, J. L. 2005. Biocompatibility Evaluation of Different Alginates and Alginate-Based Microcapsules. *Biomacromolecules,* 6**,** 927-931.

ORLOWSKA, A., PERERA, P. T., AL KOBAISI, M., DIAS, A., NGUYEN, H. K. D., GHANAATI, S., BAULIN, V., CRAWFORD, R. J. & IVANOVA, E. P. 2017. The Effect of Coatings and Nerve Growth Factor on Attachment and Differentiation of Pheochromocytoma Cells. *Materials (Basel, Switzerland),* 11**,** 60.

OSAKI, T., SIVATHANU, V. & KAMM, R. D. 2018. Engineered 3D vascular and neuronal networks in a microfluidic platform. *Scientific Reports,* 8**,** 5168.

PALANKER, D., VANKOV, A., HUIE, P. & BACCUS, S. 2005. Design of a high-resolution optoelectronic retinal prosthesis. *J Neural Eng,* 2**,** S105-20.

PARK, H. W., CHO, J. S., PARK, C. K., JUNG, S. J., PARK, C. H., LEE, S. J., OH, S. B., PARK, Y. S. & CHANG, M. S. 2012. Directed induction of functional motor neuron-like cells from genetically engineered human mesenchymal stem cells. *PLoS One,* 7**,** e35244.

PARK, S., KIM, J. Y., MYUNG, S., JUNG, N., CHOI, Y. & JUNG, S. C. 2019. Differentiation of Motor Neuron-Like Cells from Tonsil-Derived Mesenchymal Stem Cells and Their Possible Application to Neuromuscular Junction Formation. *Int J Mol Sci,* 20.

PATANI, R. 2016. Generating Diverse Spinal Motor Neuron Subtypes from Human Pluripotent Stem Cells. *Stem Cells Int,* 2016**,** 1036974.

PATANI, R., HOLLINS, A. J., WISHART, T. M., PUDDIFOOT, C. A., ALVAREZ, S., DE LERA, A. R., WYLLIE, D. J., COMPSTON, D. A., PEDERSEN, R. A., GILLINGWATER, T. H., HARDINGHAM, G. E., ALLEN, N. D. & CHANDRAN, S. 2011. Retinoid-independent motor neurogenesis from human embryonic stem cells reveals a medial columnar ground state. *Nat Commun,* 2**,** 214.

PATTON, K. T. 2012. *Laboratory Manual for Seeley's Essentials of Anatomy and Physiology*, McGraw-Hill Education.

PENDERGRASS, K. D., BOOPATHY, A. V., SESHADRI, G., MAIELLARO-RAFFERTY, K., CHE, P. L., BROWN, M. E. & DAVIS, M. E. 2013. Acute preconditioning of cardiac progenitor cells with hydrogen peroxide enhances angiogenic pathways following ischemia-reperfusion injury. *Stem Cells Dev,* 22**,** 2414-24.

PEPPER, J. P., WANG, T. V., HENNES, V., SUN, S. Y. & ICHIDA, J. K. 2017. Human Induced Pluripotent Stem Cell-Derived Motor Neuron Transplant for Neuromuscular Atrophy in a Mouse Model of Sciatic Nerve Injury. *JAMA Facial Plast Surg,* 19**,** 197-205.

PETROSSIANS, A., WHALEN, J. J. & WEILAND, J. D. 2016. Improved electrode material for deep brain stimulation. *Conf Proc IEEE Eng Med Biol Soc,* 2016**,** 1798-1801.

PFISTER, B. J., IWATA, A., TAYLOR, A. G., WOLF, J. A., MEANEY, D. F. & SMITH, D. H. 2006. Development of transplantable nervous tissue constructs comprised of stretch-grown axons. *J Neurosci Methods,* 153**,** 95-103.

PIEBER, K., HERCEG, M., PATERNOSTRO-SLUGA, T. & SCHUHFRIED, O. 2015. Optimizing stimulation parameters in functional electrical stimulation of denervated muscles: a cross-sectional study. *Journal of NeuroEngineering and Rehabilitation,* 12**,** 51.

PODNAR, S. 2006. Bowel dysfunction in patients with cauda equina lesions. *Eur J Neurol,* 13**,** 1112-7.

POLLOCK, K., STROEMER, P., PATEL, S., STEVANATO, L., HOPE, A., MILJAN, E., DONG, Z., HODGES, H., PRICE, J. & SINDEN, J. D. 2006. A conditionally immortal clonal stem cell line from human cortical neuroepithelium for the treatment of ischemic stroke. *Experimental Neurology,* 199**,** 143-155.

POMEROY, J. E., HOUGH, S. R., DAVIDSON, K. C., QUAAS, A. M., REES, J. A. & PERA, M. F. 2016. Stem Cell Surface Marker Expression Defines Late Stages of Reprogramming to Pluripotency in Human Fibroblasts. *Stem Cells Transl Med,* 5**,** 870-82.

PRANTI, A. S., SCHANDER, A., BÖDECKER, A. & LANG, W. 2018. PEDOT: PSS coating on gold microelectrodes with excellent stability and high charge injection capacity for chronic neural interfaces. *Sensors and Actuators B: Chemical,* 275**,** 382-393.

PREUSCH, F., ADELMANN, B. & HELLMANN, R. 2014. Micromachining of AlN and Al2O3 Using Fiber Laser. *Micromachines,* 5**,** 1051-1060.

PUN, S., YANG, J. F., NG, Y. P. & TSIM, K. W. K. 1997. NG108-15 cells express neuregulin that induces AChR α-subunit synthesis in cultured myotubes. *FEBS Letters,* 418**,** 275-281.

PURCELL, E. K., SEYMOUR, J. P., YANDAMURI, S. & KIPKE, D. R. 2009. In vivo evaluation of a neural stem cell-seeded prosthesis. *J Neural Eng,* 6**,** 026005.

QU, Q., LI, D., LOUIS, K. R., LI, X., YANG, H., SUN, Q., CRANDALL, S. R., TSANG, S., ZHOU, J., COX, C. L., CHENG, J. & WANG, F. 2014. High-efficiency motor neuron differentiation from human pluripotent stem cells and the function of Islet-1. *Nature Communications,* 5.

QUAILE, A. 2019. Cauda equina syndrome—the questions. *International Orthopaedics,* 43**,** 957-961.

RAGNARSSON, K. T. 2008. Functional electrical stimulation after spinal cord injury: current use, therapeutic effects and future directions. *Spinal Cord,* 46**,** 255-74.

RAJNICEK, A., BRITLAND, S. & MCCAIG, C. 1997. Contact guidance of CNS neurites on grooved quartz: influence of groove dimensions, neuronal age and cell type. *J Cell Sci,* 110 (Pt 23)**,** 2905-13.

RAMOS, P. E., SILVA, P., ALARIO, M. M., PASTRANA, L. M., TEIXEIRA, J. A., CERQUEIRA, M. A. & VICENTE, A. A. 2018. Effect of alginate molecular weight and M/G ratio in beads properties foreseeing the protection of probiotics. *Food Hydrocolloids,* 77**,** 8-16.

RAMOT, Y., SCHIFFENBAUER, Y. S., AMOUYAL, N., EZOV, N., STEINER, M., IZRAEL, M., LAVON, N., HASSON, A., REVEL, M. & NYSKA, A. 2017. Compact MRI for the detection of teratoma development following intrathecal human embryonic stem cell injection in NOD-SCID mice. *Neurotoxicology,* 59**,** 27-32.

REHAB, M. 2018. *ODFS Pace* [Online]. Motion Rehab. Available: http://libraryguides.vu.edu.au/harvard/internet-websites [Accessed 19 September 2019].

REINA, G., GONZALEZ-DOMINGUEZ, J. M., CRIADO, A., VAZQUEZ, E., BIANCO, A. & PRATO, M. 2017. Promises, facts and challenges for graphene in biomedical applications. *Chem Soc Rev,* 46**,** 4400-4416.

RICHTER, A., KRUSE, C., MOSER, A., HOFMANN, U. & DANNER, S. 2011a. Cellular Modulation of Polymeric Device Surfaces: Promise of Adult Stem Cells for Neuro-Prosthetics. *Frontiers in Neuroscience,* 5**,** 114.

RICHTER, A., KRUSE, C., MOSER, A., HOFMANN, U. G. & DANNER, S. 2011b. Cellular modulation of polymeric device surfaces: promise of adult stem cells for neuro-prosthetics. *Front Neurosci,* 5**,** 114.

RIGHI, M., PULEO, G. L., TONAZZINI, I., GIUDETTI, G., CECCHINI, M. & MICERA, S. 2018. Peptide-based coatings for flexible implantable neural interfaces. *Sci Rep,* 8**,** 502.

ROACH, P., PARKER, T., GADEGAARD, N. & ALEXANDER, M. R. 2010. Surface strategies for control of neuronal cell adhesion: A review. *Surface Science Reports,* 65**,** 145-173.

ROEMER, A., KOHL, U., MAJDANI, O., KLOSS, S., FALK, C., HAUMANN, S., LENARZ, T., KRAL, A. & WARNECKE, A. 2016. Biohybrid cochlear implants in human neurosensory restoration. *Stem Cell Res Ther,* 7**,** 148.

ROLSTON, J. D., GROSS, R. E. & POTTER, S. M. 2009. A low-cost multielectrode system for data acquisition enabling real-time closed-loop processing with rapid recovery from stimulation artifacts. *Front Neuroeng,* 2**,** 12.

ROSE, T. L. & ROBBLEE, L. S. 1990. Electrical stimulation with Pt electrodes. VIII. Electrochemically safe charge injection limits with 0.2 ms pulses. *IEEE Trans Biomed Eng,* 37**,** 1118-20.

ROSSI, S. L., NISTOR, G., WYATT, T., YIN, H. Z., POOLE, A. J., WEISS, J. H., GARDENER, M. J., DIJKSTRA, S., FISCHER, D. F. & KEIRSTEAD, H. S. 2010. Histological and functional benefit following transplantation of motor neuron progenitors to the injured rat spinal cord. *PLoS One,* 5**,** e11852.

RUFFIN, V. A., SALAMEH, A. I., BORON, W. F. & PARKER, M. D. 2014. Intracellular pH regulation by acid-base transporters in mammalian neurons. *Front Physiol,* 5**,** 43.

RUGG-GUNN, P. J., FERGUSON-SMITH, A. C. & PEDERSEN, R. A. 2007. Status of genomic imprinting in human embryonic stem cells as revealed by a large cohort of independently derived and maintained lines. *Hum Mol Genet,* 16 Spec No. 2**,** R243-51.

SABITHA, K. R., SANJAY, D., SAVITA, B., RAJU, T. R. & LAXMI, T. R. 2016. Electrophysiological characterization of Nsc-34 cell line using Microelectrode Array. *J Neurol Sci,* 370**,** 134-139.

SAKATA, H., NIIZUMA, K., WAKAI, T., NARASIMHAN, P., MAIER, C. M. & CHAN, P. H. 2012. Neural stem cells genetically modified to overexpress cu/zn-superoxide dismutase enhance amelioration of ischemic stroke in mice. *Stroke,* 43**,** 2423-9.

SALMONS, S. & JARVIS, J. C. 2008. Functional Electrical Stimulation of Denervated Muscles: An Experimental Evaluation. *Artificial Organs,* 32**,** 597-603.

SANCES, S., BRUIJN, L. I., CHANDRAN, S., EGGAN, K., HO, R., KLIM, J. R., LIVESEY, M. R., LOWRY, E., MACKLIS, J. D., RUSHTON, D., SADEGH, C., SAREEN, D., WICHTERLE, H., ZHANG, S.-C. & SVENDSEN, C. N. 2016. Modeling ALS with motor neurons derived from human induced pluripotent stem cells. *Nature Neuroscience,* 16**,** 542-553.

SANDVIG, I., GADJANSKI, I., VLASKI-LAFARGE, M., BUZANSKA, L., LONCARIC, D., SARNOWSKA, A., RODRIGUEZ, L., SANDVIG, A. & IVANOVIC, Z. 2017. Strategies to Enhance Implantation and Survival of Stem Cells After Their Injection in Ischemic Neural Tissue. *Stem Cells Dev,* 26**,** 554-565.

SANTOS ROBALLO, K. C., DHUNGANA, S., JIANG, Z., OAKEY, J. & BUSHMAN, J. S. 2019. Localized delivery of immunosuppressive regulatory T cells to peripheral nerve allografts promotes regeneration of branched segmental defects. *Biomaterials,* 209**,** 1-9.

SART, S., MA, T. & LI, Y. 2014. Preconditioning stem cells for in vivo delivery. *Biores Open Access,* 3**,** 137-49.

SEKIRNJAK, C., HOTTOWY, P., SHER, A., DABROWSKI, W., LITKE, A. M. & CHICHILNISKY, E. J. 2008. High-resolution electrical stimulation of primate retina for epiretinal implant design. *J Neurosci,* 28**,** 4446-56.

SHIMOJO, D., ONODERA, K., DOI-TORII, Y., ISHIHARA, Y., HATTORI, C., MIWA, Y., TANAKA, S., OKADA, R., OHYAMA, M., SHOJI, M., NAKANISHI, A., DOYU, M., OKANO, H. & OKADA, Y. 2015. Rapid, efficient, and simple motor neuron differentiation from human pluripotent stem cells. *Molecular Brain,* 8.

SILVA, N. A., SOUSA, N., REIS, R. L. & SALGADO, A. J. 2014. From basics to clinical: a comprehensive review on spinal cord injury. *Prog Neurobiol,* 114**,** 25-57.

SIMITZI, C., KARALI, K., RANELLA, A. & STRATAKIS, E. 2018. Controlling the Outgrowth and Functions of Neural Stem Cells: The Effect of Surface Topography. 19**,** 1143-1163.

SIMON, J., FLAHAUT, E. & GOLZIO, M. 2019. Overview of Carbon Nanotubes for Biomedical Applications. *Materials (Basel),* 12.

SOHAL, H. S., CLOWRY, G. J., JACKSON, A., O'NEILL, A. & BAKER, S. N. 2016. Mechanical Flexibility Reduces the Foreign Body Response to Long-Term Implanted Microelectrodes in Rabbit Cortex. *PLoS One,* 11**,** e0165606.

SONDERMEIJER, H. P., WITKOWSKI, P., WOODLAND, D., SEKI, T., AANGENENDT, F. J., VAN DER LAARSE, A., ITESCU, S. & HARDY, M. A. 2016. Optimization of alginate purification using polyvinylidene difluoride membrane filtration: Effects on immunogenicity and biocompatibility of three-dimensional alginate scaffolds. *J Biomater Appl,* 31**,** 510-520.

SOUNDARARAJAN, P. 2006. Motoneurons Derived from Embryonic Stem Cells Express Transcription Factors and Develop Phenotypes Characteristic of Medial Motor Column Neurons. *Journal of Neuroscience,* 26**,** 3256-3268.

SPENCER, K. C., SY, J. C., RAMADI, K. B., GRAYBIEL, A. M., LANGER, R. & CIMA, M. J. 2017. Characterization of Mechanically Matched Hydrogel Coatings to Improve the Biocompatibility of Neural Implants. *Sci Rep,* 7**,** 1952.

SRINIVASAN, A., TAHILRAMANI, M., BENTLEY, J. T., GORE, R. K., MILLARD, D. C., MUKHATYAR, V. J., JOSEPH, A., HAQUE, A. S., STANLEY, G. B., ENGLISH, A. W. & BELLAMKONDA, R. V. 2015. Microchannel-based regenerative scaffold for chronic peripheral nerve interfacing in amputees. *Biomaterials,* 41**,** 151-65.

STAII, C., VIESSELMANN, C., BALLWEG, J., SHI, L., LIU, G. Y., WILLIAMS, J. C., DENT, E. W., COPPERSMITH, S. N. & ERIKSSON, M. A. 2009. Positioning and guidance of neurons on gold surfaces by directed assembly of proteins using Atomic Force Microscopy. *Biomaterials,* 30**,** 3397-404.

STEVENSON, G., MOULTON, S. E., INNIS, P. C. & WALLACE, G. G. 2010. Polyterthiophene as an electrostimulated controlled drug release material of therapeutic levels of dexamethasone. *Synthetic Metals,* 160**,** 1107-1114.

STRUZYNA, L. A., WOLF, J. A., MIETUS, C. J., ADEWOLE, D. O., CHEN, H. I., SMITH, D. H. & CULLEN, D. K. 2015. Rebuilding Brain Circuitry with Living Micro-Tissue Engineered Neural Networks. *Tissue Eng Part A,* 21**,** 2744-56.

SU, W. T., LIAO, Y. F., WU, T. W., WANG, B. J. & SHIH, Y. Y. 2013. Microgrooved patterns enhanced PC12 cell growth, orientation, neurite elongation, and neuritogenesis. *J Biomed Mater Res A,* 101**,** 185-94.

TAKAHASHI, K. & YAMANAKA, S. 2006. Induction of pluripotent stem cells from mouse embryonic and adult fibroblast cultures by defined factors. *Cell,* 126**,** 663-76.

TAKAZAWA, T., CROFT, G. F., AMOROSO, M. W., STUDER, L., WICHTERLE, H. & MACDERMOTT, A. B. 2012. Maturation of spinal motor neurons derived from human embryonic stem cells. *PLoS One,* 7**,** e40154.

TAM, S. K., DUSSEAULT, J., POLIZU, S., MÉNARD, M., HALLÉ, J.-P. & YAHIA, L. H. 2006. Impact of residual contamination on the biofunctional properties of purified alginates used for cell encapsulation. *Biomaterials,* 27**,** 1296-1305.

TAVEGGIA, C. 2016. Schwann cells-axon interaction in myelination. *Curr Opin Neurobiol,* 39**,** 24-9.

TERRYN, J., WELKENHUYSEN, M., KRYLYCHKINA, O., FIRRINCIELI, A., ANDREI, A., REUMERS, V., VAN DAMME, P., BRAEKEN, D. & VERFAILLIE, C. 2018. Topographical Guidance of PSC-Derived Cortical Neurons. *Journal of Nanomaterials,* 2018**,** 1-10.

THOMAS, C. A., SPRINGER, P. A., LOEB, G. E., BERWALD-NETTER, Y. & OKUN, L. M. 1972. A miniature microelectrode array to monitor the bioelectric activity of cultured cells. *Experimental Cell Research,* 74**,** 61-66.

THOMPSON, C. H., ZORATTI, M. J., LANGHALS, N. B. & PURCELL, E. K. 2016. Regenerative Electrode Interfaces for Neural Prostheses. *Tissue Eng Part B Rev,* 22**,** 125-35.

TICKNER, J. A., SCHETTLER, T., GUIDOTTI, T., MCCALLY, M. & ROSSI, M. 2001. Health risks posed by use of Di-2-ethylhexyl phthalate (DEHP) in PVC medical devices: a critical review. *Am J Ind Med,* 39**,** 100-11.

TROMPETTO, C., MARINELLI, L., MORI, L., PELOSIN, E., CURRA, A., MOLFETTA, L. & ABBRUZZESE, G. 2014. Pathophysiology of spasticity: implications for neurorehabilitation. *Biomed Res Int,* 2014**,** 354906.

TYLER, D. J. & DURAND, D. M. 2002. Functionally selective peripheral nerve stimulation with a flat interface nerve electrode. *IEEE Trans Neural Syst Rehabil Eng,* 10**,** 294-303.

VENKATRAMAN, S., HENDRICKS, J., KING, Z. A., SERENO, A. J., RICHARDSON-BURNS, S., MARTIN, D. & CARMENA, J. M. 2011. In vitro and in vivo evaluation of PEDOT microelectrodes for neural stimulation and recording. *IEEE Trans Neural Syst Rehabil Eng,* 19**,** 307-16.

VOIGT, M. B. & KRAL, A. 2019. Cathodic-leading pulses are more effective than anodic-leading pulses in intracortical microstimulation of the auditory cortex. *J Neural Eng,* 16**,** 036002.

WADA, T., HONDA, M., MINAMI, I., TOOI, N., AMAGAI, Y., NAKATSUJI, N. & AIBA, K. 2009. Highly efficient differentiation and enrichment of spinal motor neurons derived from human and monkey embryonic stem cells. *PLoS One,* 4**,** e6722.

WALKER, P. A., JIMENEZ, F., GERBER, M. H., AROOM, K. R., SHAH, S. K., HARTING, M. T., GILL, B. S., SAVITZ, S. I. & COX, C. S., JR. 2010. Effect of needle diameter and flow rate on rat and human mesenchymal stromal cell characterization and viability. *Tissue engineering. Part C, Methods,* 16**,** 989-997.

WAN, D., CHEN, D., LI, K., QU, Y., SUN, K., TAO, K., DAI, K. & AI, S. 2016. Gold Nanoparticles as a Potential Cellular Probe for Tracking of Stem Cells in Bone Regeneration Using Dual-Energy Computed Tomography. *ACS Appl Mater Interfaces,* 8**,** 32241-32249.

WANG, K., LIU, C. C. & DURAND, D. M. 2009. Flexible nerve stimulation electrode with iridium oxide sputtered on liquid crystal polymer. *IEEE Trans Biomed Eng,* 56**,** 6-14.

WEI, L., FRASER, J. L., LU, Z. Y., HU, X. & YU, S. P. 2012. Transplantation of hypoxia preconditioned bone marrow mesenchymal stem cells enhances angiogenesis and neurogenesis after cerebral ischemia in rats. *Neurobiol Dis,* 46**,** 635-45.

WEIGEL, S., OSTERWALDER, T., TOBLER, U., YAO, L., WIESLI, M., LEHNERT, T., PANDIT, A. & BRUININK, A. 2012. Surface microstructures on planar substrates and textile fibers guide neurite outgrowth: a scaffold solution to push limits of critical nerve defect regeneration? *PLoS One,* 7**,** e50714.

WEISS, P. 1934. In vitro experiments on the factors determining the course of the outgrowing nerve fiber. *Journal of Experimental Zoology,* 68**,** 393-448.

WEN, Z. & ZHENG, J. Q. 2006. Directional guidance of nerve growth cones. *Curr Opin Neurobiol,* 16**,** 52-8.

WHITE, N. 2017. Thick Films. 1-1.

WICHTERLE, H., LIEBERAM, I., PORTER, J. A. & JESSELL, T. M. 2002. Directed Differentiation of Embryonic Stem Cells into Motor Neurons. *Cell,* 110**,** 385-397.

WIERINGA, P. A., GONCALVES DE PINHO, A. R., MICERA, S., VAN WEZEL, R. J. A. & MORONI, L. 2018. Biomimetic Architectures for Peripheral Nerve Repair: A Review of Biofabrication Strategies. *Adv Healthc Mater,* 7**,** e1701164.

WILSON, A., WEBSTER, A. & GENEVER, P. 2019. Nomenclature and heterogeneity: consequences for the use of mesenchymal stem cells in regenerative medicine. *Regenerative Medicine*.

WONG, A. & POMERANTZ, J. H. 2019. The Role of Muscle Stem Cells in Regeneration and Recovery after Denervation: A Review. *Plast Reconstr Surg,* 143**,** 779-788.

WOODWARD, B. K. 2014. Platinum group metals (PGMs) for permanent implantable electronic devices. 130-147.

WOOLLEY, A. J., DESAI, H. A., STECKBECK, M. A., PATEL, N. K. & OTTO, K. J. 2011. In situ characterization of the brain-microdevice interface using device-capture histology. *J Neurosci Methods,* 201**,** 67-77.

WURTH, S., CAPOGROSSO, M., RASPOPOVIC, S., GANDAR, J., FEDERICI, G., KINANY, N., CUTRONE, A., PIERSIGILLI, A., PAVLOVA, N., GUIET, R., TAVERNI, G., RIGOSA, J., SHKORBATOVA, P., NAVARRO, X., BARRAUD, Q., COURTINE, G. & MICERA, S. 2017. Long-term usability and bio-integration of polyimide-based intra-neural stimulating electrodes. *Biomaterials,* 122**,** 114-129.

WYATT, T. J., ROSSI, S. L., SIEGENTHALER, M. M., FRAME, J., ROBLES, R., NISTOR, G. & KEIRSTEAD, H. S. 2011. Human motor neuron progenitor transplantation leads to endogenous neuronal sparing in 3 models of motor neuron loss. *Stem Cells Int,* 2011**,** 207230.

YAGI, T. 2009. Biohybrid Visual Prothesis for Restoring Blindness. *International Journal of Applied Biomedical Engineering,* 2**,** 1-5.

YAGI, T., WATANABE, M., OHNISHI, Y., OKUMA, S. & MUKAI, T. Biohybrid Retinal Implant: Research and Development Update in 2005. Conference Proceedings. 2nd International IEEE EMBS Conference on Neural Engineering, 2005., 16-19 March 2005 2005. 248-251.

YAN, J., XU, L., WELSH, A. M., HATFIELD, G., HAZEL, T., JOHE, K. & KOLIATSOS, V. E. 2007. Extensive Neuronal Differentiation of Human Neural Stem Cell Grafts in Adult Rat Spinal Cord. *PLoS MEDICINE,* 4**,** e39.

YANG, K., FENG, L., HONG, H., CAI, W. & LIU, Z. 2013. Preparation and functionalization of graphene nanocomposites for biomedical applications. *Nat Protoc,* 8**,** 2392-403.

YIN, J. & LUAN, S. 2016. Opportunities and challenges for the development of polymer-based biomaterials and medical devices. *Regen Biomater,* 3**,** 129-35.

YOHN, D. C., MILES, G. B., RAFUSE, V. F. & BROWNSTONE, R. M. 2008. Transplanted Mouse Embryonic Stem-Cell-Derived Motoneurons Form Functional Motor Units and Reduce Muscle Atrophy. *Journal of Neuroscience,* 28**,** 12409-12418.

YOUSEFI, B., SANOOGHI, D., FAGHIHI, F., JOGHATAEI, M. T. & LATIFI, N. 2017. Evaluation of motor neuron differentiation potential of human umbilical cord blood- derived mesenchymal stem cells, in vitro. *J Chem Neuroanat,* 81**,** 18-26.

YUK, H., LU, B. & ZHAO, X. 2019. Hydrogel bioelectronics. *Chem Soc Rev,* 48**,** 1642-1667.

ZAHAVI, E. E., IONESCU, A., GLUSKA, S., GRADUS, T., BEN-YAAKOV, K. & PERLSON, E. 2015. A compartmentalized microfluidic neuromuscular co-culture system reveals spatial aspects of GDNF functions. *J Cell Sci,* 128**,** 1241-52.

ZENG, P. 2013. Biocompatible alumina ceramic for total hip replacements. *Materials Science and Technology,* 24**,** 505-516.

ZHANG, L. Q., ZHANG, W. M., DENG, L., XU, Z. X., LAN, W. B. & LIN, J. H. 2018. Transplantation of a Peripheral Nerve with Neural Stem Cells Plus Lithium Chloride Injection Promote the Recovery of Rat Spinal Cord Injury. *Cell Transplant,* 27**,** 471-484.

ZHANG, Y., LIU, J., HUANG, L., WANG, Z. & WANG, L. 2015. Design and performance of a sericin-alginate interpenetrating network hydrogel for cell and drug delivery. *Sci Rep,* 5**,** 12374.

ZHENG, X., WOEPPEL, K. M., GRIFFITH, A. Y., CHANG, E., LOOKER, M. J., FISHER, L. E., CLAPSADDLE, B. J. & CUI, X. T. 2019. Soft Conducting Elastomer for Peripheral Nerve Interface. *Adv Healthc Mater,* 8**,** e1801311.

ZHU, Y., MURALI, S., CAI, W., LI, X., SUK, J. W., POTTS, J. R. & RUOFF, R. S. 2010. Graphene and graphene oxide: synthesis, properties, and applications. *Adv Mater,* 22**,** 3906-24.

ZOCHODNE, D. 2008. The intact peripheral nerve tree. *In:* ZOCHODNE, D. W. (ed.) *Neurobiology of Peripheral Nerve Regeneration.* Cambridge: Cambridge University Press.

8.0 Appendix

8.1 Assessing metabolic activity of differentiated SPC-01 cells with RT-Glo metabolic assay

Two different types of alginates at different w/v concentration were tested (see Materials and Methods chapter, section 2.2.5.4). RT-Glo assay was chosen as the most informative assay to be able to monitor metabolic activity of the same cell population over a 72-hr period.

A standard curve using different cell densities was performed to identify the most appropriate density of differentiated SPC-01 cells to use for this assay (figure 8.1). Luminescence readings were performed, at 0 hrs (45 minutes post-seeding allowing for cells to attach to 96-well plate), 1 hr, 24 hrs, 48 hrs and 72 hrs. As expected, viability at 0 hrs was higher in wells with higher cell densities (52,768 ± 3,624 RLU per well containing 15,000 cells compared with 11,617 ± 2,099 RLU per well containing 3,000 cells). A slight drop in luminescence was recorded for all densities after 1 hr, this drop was higher in the 5,000 cells/well group (from 15,999 ± 1,511 RLU per well at 0 hrs to 15,064 ± 1,516 RLU per well at 1 hr). Viability after 24 hrs decreased for all densities, with a more pronounced drop in wells with 15,000 cells. (23,255 ± 6,360 RLU per well) compared with wells containing 3,000 cells (7,993 ± 2,166 RLU per well). By 48 hrs, a decrease in luminescence greater than 50% of the initial value (at 0 hrs) was recorded for all cell densities, with the 5,000 cells/well group showing the least decrease in luminescence (i.e. 61% lower). By 72 hrs the luminescence recorded was comparable between groups. Moreover, compared to initial luminescence readings, after 3 days luminescence in the 3,000 cells/well and 5,000 cells/well groups reduced to 16% and that recorded for the 10,000 cells/well and 15,000 cells/well groups decreased to 10% and 6% of their initial values, respectively (Statistics results are displayed in a table) (figure 8.1)

Overall, the data indicates a significant decrease in metabolic activity of differentiated SPC-01 cells over a period of 72 hours, thus suggesting, cell death. In light of this data, a new population of SPC-01 cells was differentiated and used for the next set of experiments where viability of these cells in the presence of an acellular alginate hydrogel was tested.

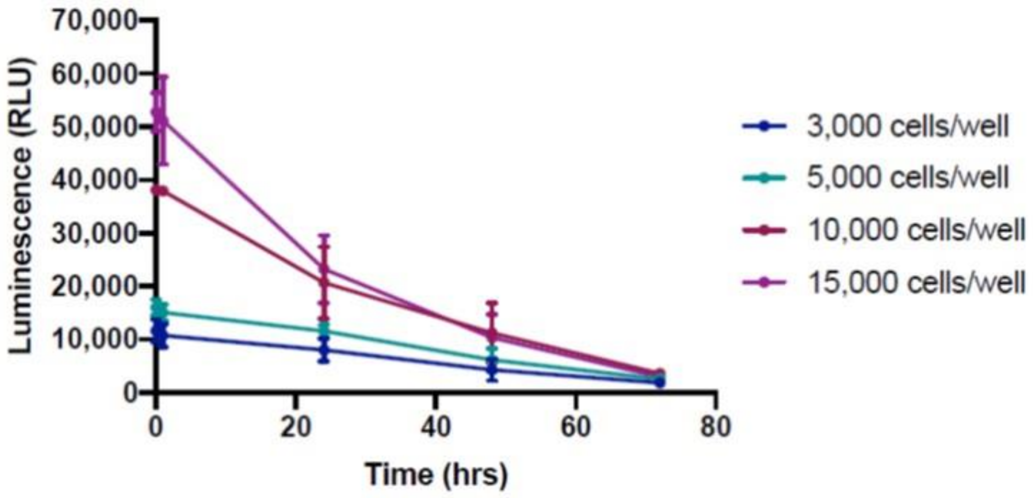

Cell density (per/well) / Time (hrs)	1 hr	24 hrs	48 hrs	72 hrs
3,000 cells	ns	***	**	**
5,000 cells	*	*	***	***
10,000 cells	ns	*	**	****
15,000 cells	ns	**	**	***

Figure 8.1 Standard curve of differentiated SPC-01 cells metabolic activity using RT-Glo assay

Standard curve of cell viability of the same population of differentiated SPC-01 cells monitor at 4 different time points (0, 1, 24, 28 and 72 hrs) over a period of 72 hrs. Four different cell densities were tested in order to identify the most appropriate density to perform this assay. 3,000 cells/well (blue), 5,000 cells/well (cyan), 10,000 cells/well (magenta) and 15,000 cells/well (purple). Cells were placed in incubators at 37 ^{0}C, 5% CO$_2$ between each reading. Data presented as mean ± SD for n = 4. *p <0.05, **p<0.01, ***p<0.001, ****p <0.0001, two-way ANOVA with Dunnett's post-test. All time points compared to initial reading (0 hrs).

Albeit, cell viability decreased in all densities tested, 5,000 cells/well was the density adopted for the next set of experiments as it is low enough to minimise use of cells without compromising seeding accuracy between samples.

8.2 Investigating the effect of Sigma alginate protective hydrogels on differentiated SPC-01 cells in vitro using RT-Glo metabolic assay

Sigma alginate hydrogels were produced at 1.5% and 2% w/v concentration, placed atop differentiated SPC-01 cells and cell viability tested using RT-Glo assay (refer to Materials and Methods chapter section 2.2.5.4). Control wells consisted of the same cell density in the absence of hydrogels. For 1.5% hydrogels at 0 hrs, cell density of controls and hydrogel wells was similar (20,669 RLU compared to 20,552 RLU, respectively). At 1 hr, luminescence recording showed a decrease in metabolic activity on both, control well (15,303 RLU) and the hydrogel well (12,404 RLU). This trend was observed across all time points where luminescence was read. Interestingly, the control group obeyed the same trend, with viability decreasing over time. However, the decreased in the 1.5% sigma alginate hydrogel group was more pronounced than that observed in the control group (figure 8.2A).

With respect to the 2% w/v Sigma alginate hydrogel, cell viability followed a similar trend as the 1.5% w/v hydrogels. However, the decrease in luminescence recorded from cells with a 2% w/v hydrogel atop compared to the control group was more pronounced than that recorded with 1.5% w/v hydrogels. By 48hrs, the viability of cells in the presence of a hydrogel reduced to 10% (from 22,152 RLU at 0 hrs to 2,007 RLU at 48 hrs). A similar trend, albeit less severe, was observed in the control group, where viability decreased overtime. Interestingly, the biggest decrease for both groups was observed within the first 48 hrs (54% reduction in luminescence in the control group and 90% in the hydrogel group). By the last luminescence reading (72 hrs) cell viability in the control group was slightly higher than that of cells in the hydrogel group (3,858 RLU compared with 1,074 RLU) (figure 8.2B).

8.3 Investigating the effect of NovaMatrix alginate protective hydrogels on differentiated SPC-01 viability using RT-Glo assay

A different type of alginate was tested to assess whether viability of cells would improve. Novamatrix alginate is purified and manufactured according to GMP standards (see section 5.1.4). This alginate (herein referred to as NovaMatrix alginate) was used to manufacture hydrogels of 1% and 1.5%

concentration. 2% concentration was not included as the hydrogels produced were too viscous to be expelled through a pipette tip.

A similar pattern as that observed with the Sigma alginate was detected with Novamatrix hydrogels of both concentrations.

First, placing a 1% NovaMatrix acellular alginate hydrogel atop differentiated SPC-01 cells, resulted in a sharp decrease in viability of these cells from 18,513 RLU (0 hrs) to 7,022 RLU at 24 hours. Luminescence continued to decrease up until the last recording at 72 hrs, when the value recorded was 1,353 RLU (7% of the initial value). The control group obeyed a similar trend, albeit at a slower rate (figure 8.2C).

With regards to NovaMatrix 1.5% alginate hydrogels a similar trend in viability of differentiated SPC-01 cells was observed. However, the decrease within the first 24 hours (from 17,908 RLU at 0 hrs to 2,120 RLU at 24 hrs) was more pronounced than that reported for 1% NovaMatrix hydrogels (figure 8.2D).

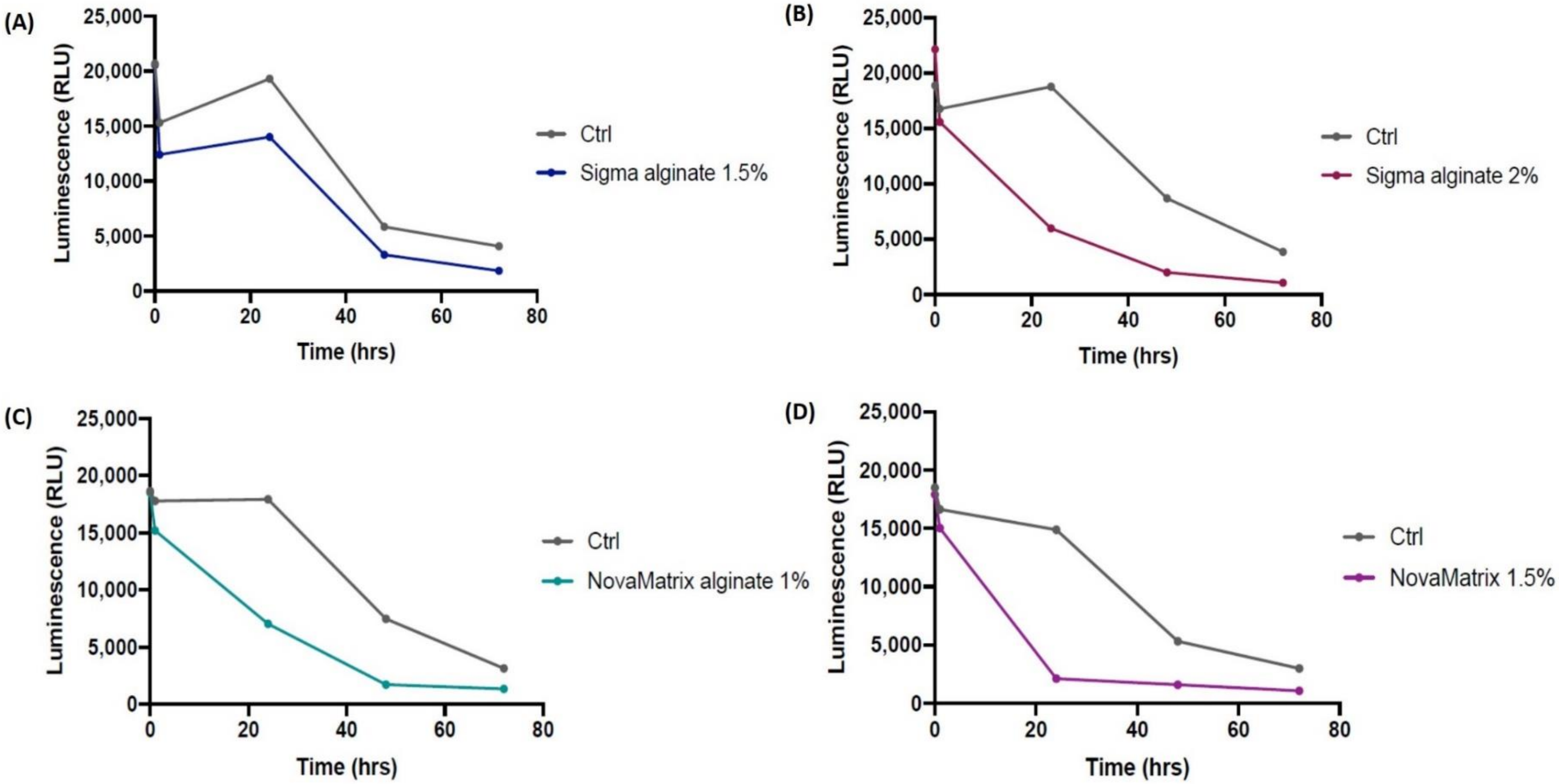

Figure 8.2 Viability of differentiated SPC-01 cells in the presence of different acellular alginate hydrogels of different concentrations assessed by RT Glo assay

Metabolic activity of differentiated SPC-01 cells with acellular alginate hydrogels atop monitor at 4 different time points (0, 1, 24, 48 an d 72 hrs) over a period of 72 hrs. The effect of four alginate hydrogels on metabolic activity of these cells was tested and compared to the control groups (cells in the absence of hydrogels; grey curves). (A) Sigma alginate 1.5%, (B) Sigma alginate 2%, (C) NovaMatrix alginate 1% and (D) NovaMatrix alginate 1.5%. Data presented for n =1.

The results obtained using RT-Glo assay suggest the sharp decrease on metabolic activity may be indicative of cell death. However, given that a new population of differentiated SPC-01 cells was used for this experiment and that control groups (cells in the absence of hydrogels) obeyed the same decreasing trend in metabolic activity with time as hydrogel groups, prompted the use of a different assay to assess metabolic activity.

8.4 Comparison of differentiated SPC-01 cell metabolic activity using RT-Glo and CT-Glo assays

Unlike, RT Glo, CT Glo does not allow continuous luminescence readings from the same cell population. Instead, metabolic activity can be assessed at a single time point on the same cell population. A standard curve using the same cell densities tested with the RT-Glo assay (see section 5.2.5) was performed (see Chapter 5, figure 5.13).

Overall, luminescence recorded from differentiated SPC-01 cells varies greatly between the two metabolic assays used. Figure 8.3 summarises the percentage change in luminescence at 48 and 72 hrs compared to that recorded at 24 hrs for all cell densities using the RT-Glo and CT-Glo assays. At 48 hrs, luminescence of cells seeded at a density of 3,000 cells/well was 52 % ± 18 of the initial value based on the RT-Glo assay. However, when using CT-Glo assay luminescence was 74 % ± 11 of the initial value. Similarly, luminescence readings obtained in the 5,000 cells/group were statistically significantly higher based on the CT-Glo assay than that yielded by the RT-Glo assay (78 % ± 4 of the initial recording compared with 53 % ± 17 of the initial recording, respectively). Both densities, 10,000 cells/well and 15,000 cells/well, obeyed the same trend. In specific, CT-Glo assay showed 72 % ± 13 of the initial luminescence value and 68 % ± 21 of the initial value, respectively. In contrast, luminescence values obtained with the RT-Glo assay at 48 hrs were 52 % ± 17 of the initial reading and 45 % ± 17 of the initial reading, respectively (figure 8.3A).

The difference in percentage change of luminescence between both assays at 72 hrs, becomes more evident, as a statistically significant increase in luminescence across all 4 cell densities tested was detected (figure 8.3B). Using CT-Glo assay, luminescence of 5,000 cells/well was 68 % ± 16 of the initial value, whereas the recording obtained when using RT-Glo assay indicates by 72 hrs luminescence was 22 % ± 4 of the initial value. At a cell density of 10,000 cells/well, the change in luminescence compared to that obtained at 24 hrs was over three times greater using RT-Glo assay (18 % ± 3 of the initial recording) compared to CT-Glo assay (62 % ± 3 of the initial recording). Finally, at the highest cell density tested, luminescence recorded using CT-Glo assay was 75 % ± 24 of the initial value, whereas measurements yielded with the RT-Glo assay reflect 13 % ± 2 of the initial luminescence reading.

Overall, these findings suggest that the sharp decrease in luminescence observed when using RT-Glo assay is most likely explained by a failure of the assay to monitor continuous metabolic activity after a number of readings rather than a decrease in cell viability.

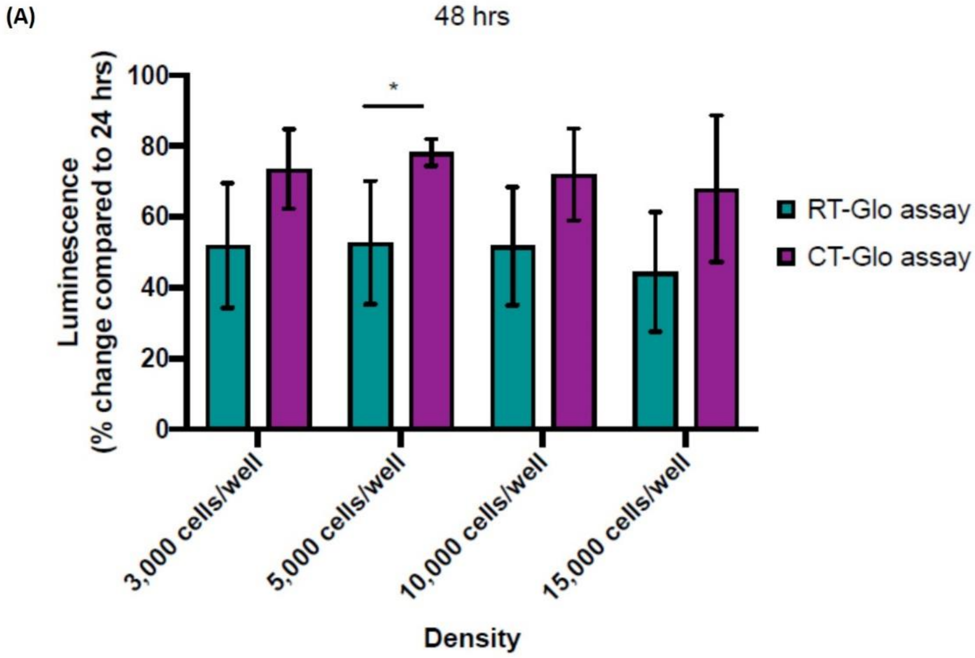

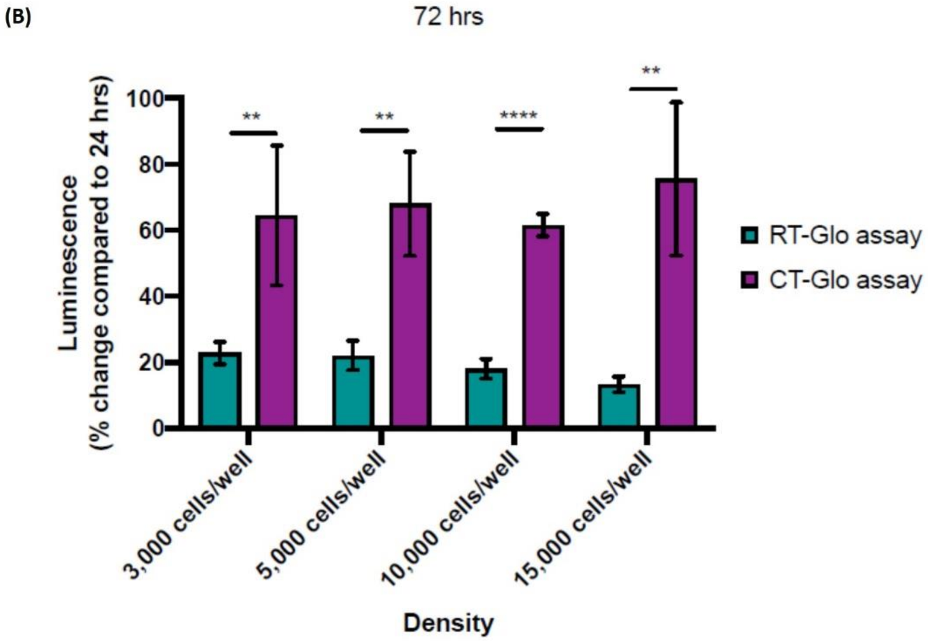

Figure 8.3 Percentage change in luminescence recordings at 48 and 72 hrs compared to 24 hrs

Percentage change in luminescence obtained with the RT-Glo and CT-Glo metabolic assays at 48 hrs (A) and 72 hrs (B) across four cell densities. Percentages were calculated based on luminescence values obtained at 24 hrs. Data presented as mean ± SD for n = 4. *p <0.05, ****p <0.0001, unpaired t-test (each cell density was compared individually).